Chem Soc Rev

REVIEW ARTICLE

View Article Online
View Journal

Cite this: DOI: 10.1039/d5cs00594a

Functional tetrapodal zinc oxide: from synthesis and multiphysics to advanced applications

Mozaffar Abdollahifar, †*[ab] Erik Greve, †[a] Jonas Lumma†[a] and Rainer Adelung *[ab]

Tetrapodal zinc oxide (T-ZnO) represents a distinctive ZnO architecture, characterized by a central core and four tetrahedrally arranged monocrystalline arms. Beyond its role as a conventional particle, T-ZnO is increasingly recognized as a microscopic building block whose three-dimensional geometry governs tightly coupled multiphysics properties. This review critically examines the structural lifecycle of T-ZnO across multiple length scales. We evaluate scalable synthesis methodologies and competing thermodynamic models governing early-stage nucleation, followed by a systematic analysis of structure–property relationships. Structure–property correlations are addressed from the atomic scale of the crystal lattice, through the microscopic scale of individual tetrapodal particles, to the macroscopic aggregation of tetrapods into functional networks. Across these scales, the tetrapodal morphology dictates properties like mechanics, piezoelectricity, and optoelectronics *via* diverse and often competing effects. These properties are typically intertwined, producing physical coupling that generates both performance synergies and fundamental design trade-offs. The utility of this architecture is demonstrated in two principal domains: first, as an active functional particle network leveraging geometric stress concentration and percolation effects for applications such as advanced sensing; and second, as a sacrificial structural template for the fabrication of ultralight, highly porous aeromaterials that decouple the architectural advantages of the network from the intrinsic chemical limitations of ZnO. Ultimately, advancing T-ZnO from empirical optimization to rational technological deployment requires predictive multiphysics computational frameworks capable of guiding the design of its complex functionality.

Received 22nd November 2025

DOI: 10.1039/d5cs00594a

rsc.li/chem-soc-rev

[a] *Chair for Functional Nanomaterials, Department of Materials Science, Faculty of Engineering, Kiel University, Kaiserstr. 2, 24143 Kiel, Germany. E-mail: moza@tf.uni-kiel.de, ra@tf.uni-kiel.de*

[b] *Kiel Nano, Surface and Interface Science (KiNSIS), Kiel University, Kaiserstr. 2, 24143 Kiel, Germany*

† These authors have the same contribution to this work.

Mozaffar Abdollahifar

Mozaffar Abdollahifar earned his doctorate in energy storage materials from National Taiwan University (NTU) in 2018. Currently serving as a Group Leader at Kiel University in Germany, he brings extensive scientific expertise from previous roles at NTU and the Battery LabFactory Braunschweig (BLB, TU Braunschweig). His research focuses on advancing cutting-edge materials for next-generation energy storage. Specifically, he specializes in supercapacitors, Li, Na, and sulfur battery chemistries, anode-free architectures, electrode engineering, and the sustainable recycling of end-of-life batteries.

Erik Greve

Erik Greve is a PhD candidate in materials science at Kiel University (Christian-Albrechts-Universität zu Kiel), Germany. His research focuses on ZnO frameworks and stimuli-responsive interpenetrating composites. He works with tetrapodal ZnO networks as mechanically stable scaffolds that can be combined with soft, functional phases to create adaptive material systems. His main interest lies in understanding structure–property relationships and controlling microstructure to tune mechanical and functional behavior. Through scalable synthesis and systematic characterization, he develops multifunctional composites with potential applications in smart materials and soft robotics.

1. Introduction

Predictive control over functional materials remains one of the foremost challenges in materials science. This problem is deeply rooted in the synthesis-structure–property relationship that governs material performance. Tetrapodal zinc oxide (T-ZnO) exemplifies this challenge. Its functional properties are governed not only by its intrinsic chemistry but also by its distinct morphology (a particle with a central core and four arms extending in different directions at roughly 109.5° angles) and are highly sensitive to its synthesis conditions. The scientific journey of T-ZnO, chronicled over eight decades in Fig. 1, began with the foundational crystallographic description of T-ZnO twinning in 1944.[1] It evolved through the postulation of seminal yet contested growth models, ranging from the simple metastable zinc blende (ZB) nucleus hypothesis (1981)[2] to the complex octatwin (1993)[3] and multi-grain wurtzite (WZ) (2005)[4] theories. Furthermore, the timeline in Fig. 1 marks the transition from fundamental understanding to a dual yet interconnected landscape of technological applications. Early breakthroughs demonstrated its utility as an active material in photocatalysis (2007),[5] single-tetrapod sensors (2009),[6] and as a light-scattering layer in dye-sensitized solar cells (DSSC) (2011).[7] Concurrently, a transformative application emerged with the synthesis of aerographite (2012),[8] as illustrated by the emergence of the blue "template" stream in Fig. 1. This established T-ZnO not just as a functional component, but as a revolutionary sacrificial template for creating entirely new classes of microstructured materials, such as ultralightweight three-dimensionally (3D) interconnected thin films, the so called "aeromaterials".[8,9]

Despite extensive studies on T-ZnO synthesis, the fundamental atomistic mechanisms driving the formation of its characteristic four-armed morphology are still not fully understood.[2,3,10,11] This fundamental uncertainty creates a critical knowledge gap between macroscopic synthesis parameters and atomistic control, limiting the rational and predictive design of T-ZnO. In addition to the knowledge gap regarding its formation, T-ZnO is characterized by structural features such as a defect-rich core, a non-centrosymmetric WZ-lattice in its arms, and high-energy polar facets. These features are often dependent on synthesis conditions, closely related, and can influence each other. For instance, intrinsic defects enable n-type conductivity,[12,13] and the concentration of these defects, directly affects the material's conductivity. These intrinsic defects also influence the piezoelectric properties of the WZ arms through free charge carriers[14,15] and reduce optical efficiency *via* non-radiative recombination centers.[16] Furthermore, structural features such as the core junction, also play an important role.[14] In this junction, the degree of lattice mismatch and the presence of defects further influence the behavior of T-ZnO in various regards. This complex interdependency of the structural features and their effects to the properties needs to be tuned for desired application but also enables multi-terminal functionalities.[17]

The systematic analysis of these interconnected phenomena establishes a foundation for the practical use of T-ZnO in materials science. Crucially, our analysis reveals that T-ZnO acts as a material nexus, uniting functional and structural domains. T-ZnO can be rationally applied in two synergistic modes. First, it can serve as an active material, where its intrinsic properties such as n-type conductivity, piezoelectricity, or photoluminescence (PL) are directly exploited and often enhanced by its tetrapodal structure. Second, T-ZnO can function as a load-bearing structural element, where its morphology enables new properties, such as the formation of three-dimensionally percolating networks with low percolation thresholds. Moreover, the architecture of these networks can be transferred to other materials. In such a templating approach, T-ZnO can imprint its structural properties onto materials like graphene,[18] SiO_2[19] or ceramics,[20] which are otherwise difficult to produce in such a morphology. This strategy effectively decouples morphology from chemistry,

Jonas Lumma

Jonas Lumma studied chemistry and economics at Kiel University and is currently a PhD candidate at the Institute of Materials Science at Kiel University in the research group of Prof. Rainer Adelung. His research focuses on the fabrication of open-porous, low-density structures using tetrapodal ZnO networks as sacrificial templates, as well as on investigating their potential applications in various fields, including electromagnetic shielding and laser light scattering.

Rainer Adelung

Rainer Adelung is Professor of Materials Science and Chair of Functional Nanomaterials at Kiel University, Germany. He studied physics at Kiel University and received his PhD in 2000. In 2001, he joined Case Western Reserve University, USA. After his habilitation in 2007, he was awarded a Heisenberg Professorship at Kiel University and has led the Chair of Functional Nanomaterials since 2010. His research focuses on ZnO-based systems, porous and aeromaterials, and bio- and energy-related applications, bridging fundamental science and technology transfer. He has authored more than 300 peer-reviewed publications, holds around 30 patent applications, and has co-founded several start-up companies.

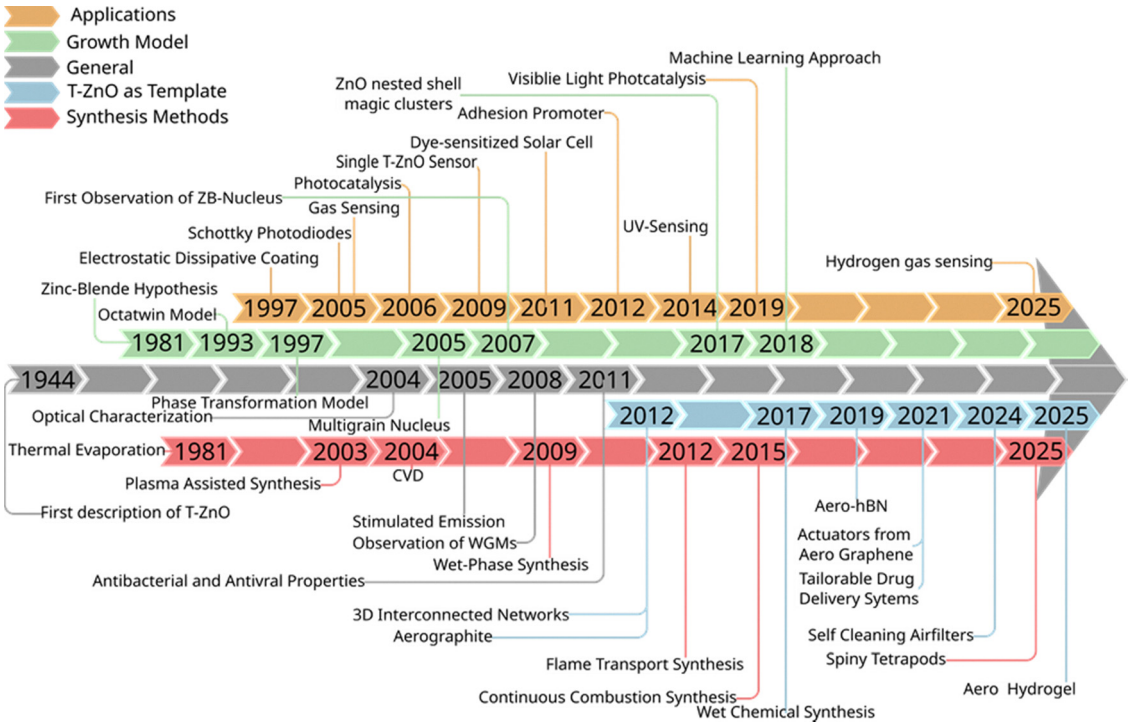

Fig. 1 A timeline illustrating the historical progress of T-ZnO research from 1944 to now. The chart highlights key milestones across five major themes: general discoveries (grey), synthesis methods (red), growth models (green), T-ZnO as a sacrificial template (blue), and applications (orange). The progression shows a clear evolution from foundational crystallographic and synthesis studies toward an expanding landscape of advanced, architecture-driven technologies.

allowing T-ZnO to export its structural benefits to other functional chemistries.

This review provides a critical, multi-scale framework to clarify the current challenges regarding T-ZnO. We begin with a critical assessment of the synthesis and unresolved growth mechanisms of T-ZnO (Section 2). We then trace how these conditions shape the structure–property relationships (Section 3), which govern the material's vast application potential (Section 4). Following the detailed discussion of synthesis, properties and applications of T-ZnO, the review culminates in a forward-looking perspective (Section 5). This section outlines key experimental and theoretical frontiers. Progress in these areas may move T-ZnO from a model system of study toward a blueprint for a new paradigm: the predictive, on-demand design of three-dimensionally microstructured materials.

2. Synthesis and growth mechanisms of T-ZnO

Despite decades of research and a large variety of synthesis routes, the predictable design of T-ZnO with tailored arm morphologies and core structures remains difficult. This challenge stems from the material's distinctive architecture. Unlike zero-dimensional (0D), one-dimensional (1D), or two-dimensional (2D) nanostructures, T-ZnO exhibits a spatially open three-dimensional (3D) tetrapodal morphology. This unique morphology comprises a central core from which four high-aspect-ratio arms extend. This geometric configuration imparts properties that differentiate it from other ZnO forms. Consequently, deviations in morphology directly alter material properties. This structure–property relationship is central to governing T-ZnO's performance across all scales, from individual arms to assembled networks. Consequently, it emphasizes the importance of a combined theoretical and empirical understanding of nucleation and growth.

This section critically assesses the synthesis-mechanism, arguing that a unified growth theory, bridging atomistic nucleation with macroscopic process parameters, is the critical missing link for realizing the full potential of these unique 3D nano-/micromaterials. To address this gap, the section first examines the fundamental growth mechanisms of the nucleus (Section 2.1). Building on this foundation, Section 2.2 develops the underlying thermodynamic principles and general design rules, which are then applied to the primary fabrication methods for T-ZnO in Section 2.3. This creates a rational framework that enables deliberate control over synthesis parameters, shifting the field from empirical recipes to first-principles design.

2.1 Fundamental growth mechanism

2.1.1 The nucleation paradox. A significant scientific paradox lies at the heart of T-ZnO research. While its synthesis is remarkably reproducible, the precise atomistic mechanism governing the nucleation of its four-armed structure remains a subject of intense debate.[21,22] Although most models agree on the idea that growth originates from a central seed from which

the four arms extend,[2,3,11,23–25] the formation and nature of the initial nucleus remains unresolved.

This section traces the evolution of scientific thought on the nature of the T-ZnO nucleus. Early models postulated that a core of a metastable crystal phase, specifically cubic ZB, provides the necessary tetrahedral symmetry.[11] Conversely, later theories argued that the structure could arise entirely from the thermodynamically stable WZ phase through complex twinning and strain accommodation mechanisms. This progression reveals how increasingly sophisticated characterization methods have deepened our understanding of symmetry breaking and crystal growth at the nanoscale.

2.1.1.1 Model A: the epitaxial growth model (1981). The first and most intuitive explanation for the tetrapod morphology, proposed by Shiojiri and Kaito in 1981, is the epitaxial growth model.[11,15] This framework suggests that the tetrapod does not nucleate from the stable WZ phase, but rather from a core composed of the metastable cubic ZB polymorph. The formation of such a metastable phase is theorized to be plausible under the high-supersaturation, non-equilibrium conditions characteristic of vapor-phase synthesis.

In this model, the ZB nucleus forms an octahedron, exposing four energetically equivalent Zn-terminated facets. These surfaces act as a template for the epitaxial growth of WZ arms. As deposition proceeds along the crystallographically equivalent directions, the arms extend to form a structure with ideal tetrahedral symmetry, producing the characteristic tetrapod.[26,27] This epitaxial relationship explains the fourfold symmetry and predicts a tetrahedral arm angle of 109.5°, the ideal tetrahedral angle.[24,28] This model predicts a perfect tetrahedral alignment of WZ arms extending from the ZB octahedral nucleus (Fig. 2a). Direct high-resolution transmission electron microscopy (HRTEM) analysis confirms this ZB core in specific samples, validating the epitaxial relationship between the ZB {111} and WZ ⟨0001⟩ growth directions (Fig. 2b).

While this simplicity makes model A conceptually attractive, it also defines its principal limitations. Several factors limit the applicability of this model: systematic experimental deviations from ideal tetrahedral geometry, the energetic cost of maintaining a coherent ZB–WZ interface, and the rarity of direct ZB-core observations. Collectively, these suggest that this mechanism, if operative, is restricted to a narrow range of synthesis conditions. These shortcomings motivated the development of alternative models that relax the requirement of a perfect crystallographic template and instead incorporate strain, defects, or phase transformation as central elements of tetrapod nucleation.

2.1.1.2 Model B: the octa-twin nucleus model (1993). To address the limitations of the epitaxial model, Iwanaga *et al.* developed the octa-twin model, which rationalizes tetrapod formation entirely within the stable WZ phase.[3,24,25] A crucial advantage of this model is its ability to account for the persistent ∼105° arm angle frequently observed in experiments.[21,29]

This model postulates a nucleus composed of eight trigonal pyramidal WZ sub-crystals. Each sub-crystal exposes three outward-facing {1$\bar{1}$22} facets and one basal plane. All sub-crystals are twinned along the outward facing facets, which are the most energetically favorable twinning planes in the WZ structure. These twinned domains arrange into an octahedron, introducing significant internal strain due to angular mismatches of the twin boundaries.[30] This strain is partially relieved by microcracking or dislocation formation, resulting in a distorted nucleus. Growth then proceeds preferentially from four sub-crystals whose basal planes are oriented along the +*c* direction, producing the characteristic four-armed tetrapod morphology.[25] As the nucleus evolves, it transitions into a hexa-twin configuration (Fig. 3), where mutual accommodation of twin interfaces minimizes interfacial stress.

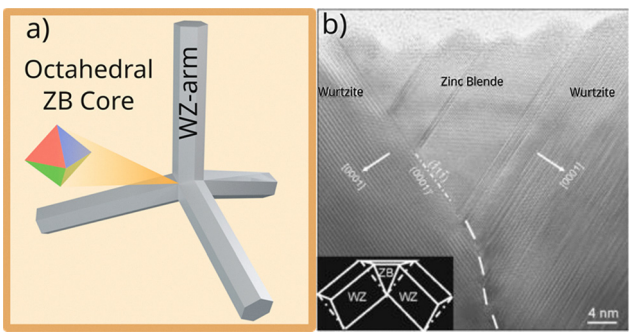

Fig. 2 Epitaxial growth model for tetrapod ZnO. (a) Schematic illustration of a ZB octahedral nucleus (left) and the resulting WZ tetrapod with arms aligned in perfect tetrahedral geometry (right). (b) High-resolution TEM image showing a ZB core enclosed by WZ domains, with the corresponding structural model inset, providing direct evidence for the epitaxial relationship between ZB {111} and WZ {0001} growth directions. (b) Reproduced from ref.10 with permision from AIP Publishing,[10] Copyright 2007.

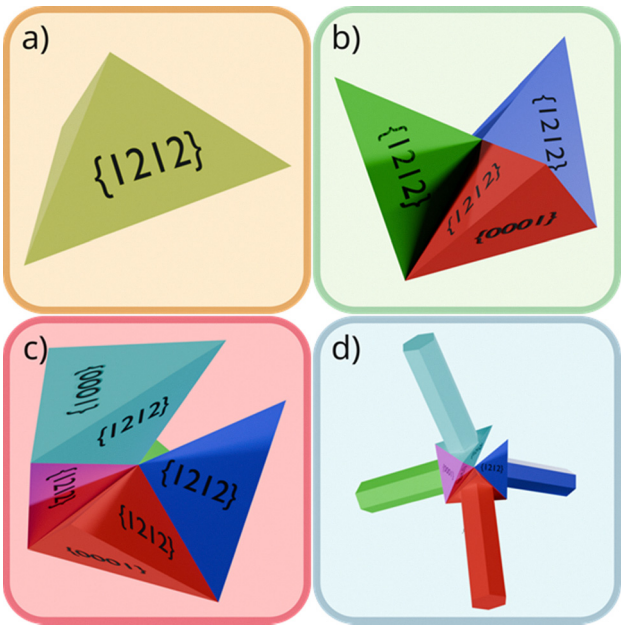

Fig. 3 Twin-mediated nuclei with increasing multiplicity. (a) Single pyramidal twin with an equilateral triangle as base. (b) Three additional twins grown on the {1212} facets of the first twin. (c) Hexa-twin configuration (after Iwanaga *et al.*[25]), in which all twinned interfaces are mutually accommodated, releasing interfacial stress and yielding a distorted tetrahedral arrangement of the c^+ axes; the {0001} facet is indicated. (d) Resulting distorted tetrapod morphology.

In direct contrast to the epitaxial growth model, the octa-twin nucleus model abandons the concept of a predefined symmetry template and instead explains tetrapod formation entirely within the stable WZ phase. Here, the morphology results not from the crystallographic properties but emerges from strain-driven twinning during nucleation. This distinguishes model B from model A and marks the first explicit incorporation of defect-mediated growth.

The octa-twin model offers an explanation for the consistent $\sim 105^\circ$ arm angles seen in experiments, attributing the deviation from 109.5° to the relaxation of the twinned nucleus structure.[25] This interpretation is supported by angular measurements on multiple tetrapods and by indirect TEM evidence suggesting the presence of twinned subdomains, even though direct imaging of a complete eight-domain nucleus remains elusive.[3,24,25] Lastly, the complexity of the proposed nucleus structure and variability in observed tetrapod morphologies suggest this may be one of several possible growth pathways, rather than a universal mechanism for all T-ZnO structures.

2.1.1.3 Model C: the nucleus transformation model (1997). A third growth mechanism proposed by Nishio *et al.*[2] presents a hybrid model that links cubic and hexagonal phases in ZnO tetrapod formation. Growth initiates with a transient ZB nucleus formed under high supersaturation and elevated temperatures typical of vapor-phase synthesis.[2] The metastable ZB phase subsequently undergoes a solid-state transformation into the WZ structure *via* crystallographic slip, accompanied by the formation of stacking faults and twin boundaries. This transformation preserves the octahedral geometry of the original ZB nucleus but produces a multiply twinned WZ core. Depending on the slip system, the core typically consists of either four or six coherently twinned WZ domains. In the six-domain configuration, specific twins form the internal nucleus boundaries, while the remaining domains elongate outward to form the arms. Such a sixfold twinned core cannot be accounted for by the previously proposed octa-twin model. From this multiply twinned nucleus, four WZ domains aligned along the *c*+ direction extends outward to form the characteristic tetrapod arms. Diffraction data confirms the existence of multiply twinned $\{1\bar{1}24\}$ domains (Fig. 4), supporting the transformation-based mechanism by validating the specific orientation of the WZ elements.

This model is primarily supported by Nishio *et al.*'s[2] observation of a six-grained tetrapod, which has not been independently

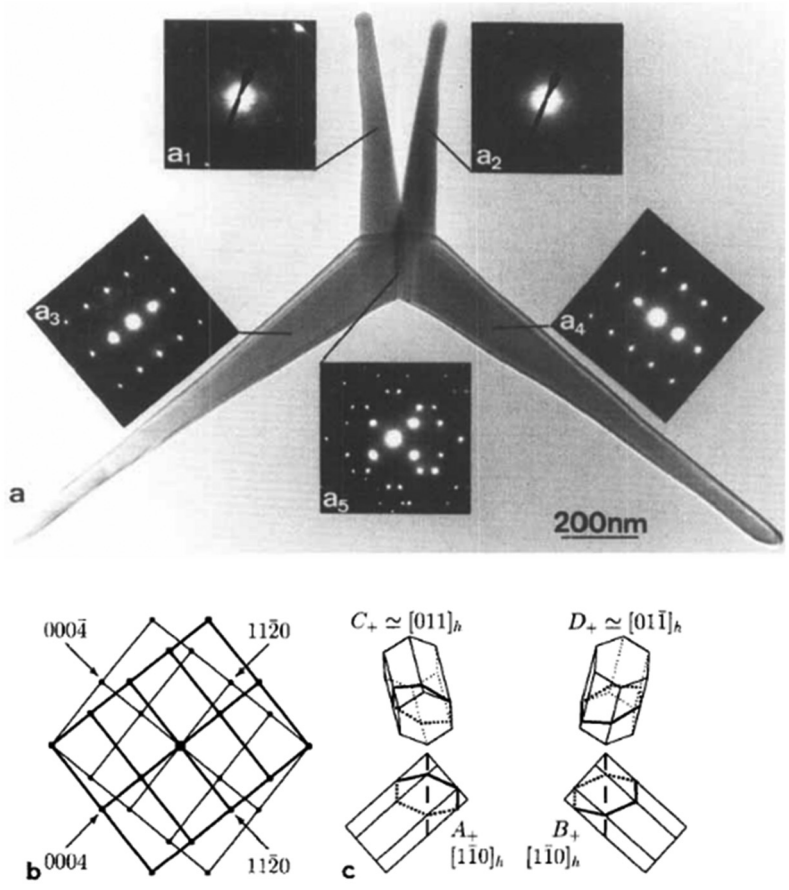

Fig. 4 TEM analysis of a T-ZnO particle with a multiply twinned $\{1\bar{1}24\}$ core. (a) TEM image of a tetrapod with four arms, accompanied by selected-area electron diffraction (ED) patterns for each domain (a_1–a_5). (b) Schematic of the ED pattern highlighting the characteristic reflections of the twinned domains. (c) Crystal orientation models of the four WZ elements (A^+, B^+, C^+, D^+), showing the hexagonal prism geometry and twinning relationships. (a)–(c) Reproduced from ref. 2 with permision from Taylor & Francis,[2] Copyright 1997.

confirmed. It does, however, account for the experimentally observed inter-arm angles.

2.1.1.4 Model D: the multi-grain wurtzite model (2005). Ronning *et al.*[4] proposed an alternative model based on direct HRTEM evidence and supported by density functional theory (DFT) calculations. In this model, the tetrapod core consists of four single-crystalline WZ grains arranged in a distorted tetrahedral geometry, with misfit strain accommodated by a high density of structural defects. They suggest a self-assembly nucleation mechanism resembling a phase transition, similar to that described by Nishio *et al.*[2] Zn vapor initially forms small Zn clusters that oxidize into ZnO spheroids. Upon further growth, these spheroids collapse into a more stable tetrahedral structure. This final structure is composed of four triangular dipyramidal ZnO grains with their *c*-axes pointing toward the apexes (Fig. 5a). High-angle grain boundaries accommodate the internal misfit strain, effectively stabilizing the distorted tetrahedral arrangement (Fig. 5b–e).

The key contribution of this model is its emphasis on nanoscale thermodynamics. Rather than invoking a predefined crystallographic template such as a ZB phase or octa-twin, it describes a dynamic process in which the core structure emerges from energy minimization through particle aggregation and rearrangement. However, it remains unclear whether the initial nucleus originates from Zn condensation, as supersaturation of Zn vapor with respect to metallic Zn is not expected under the relevant conditions,[31] making homogeneous Zn nucleation unlikely.

2.1.2 Critical assessment: why a unified theory remains elusive. Despite the extensive research detailed above, no single, universally accepted growth mechanism for T-ZnO has emerged. To address this lack of consensus, it is necessary to compare these models not as competing truths, but as complementary pathways activated by different synthesis environments and observational limits. A critical assessment reveals three fundamental barriers that prevent a unified conclusion.

2.1.2.1 Condition-dependent pathways (thermodynamic vs. kinetic control). The diversity of synthesis methods implies that a universal nucleation pathway likely does not exist. Instead, the dominant mechanism appears to be dictated by the thermodynamic landscape of the specific synthesis method. Models A and C, which invoke metastable ZB phases, are predominantly supported by data from high-temperature vapor-phase synthesis. Under these far-from-equilibrium conditions, rapid kinetics can stabilize metastable phases before they relax into the equilibrium structure. In contrast, model D (multi-grain WZ) often aligns with wet-chemical or slower oxidation data. Here, slower kinetics allow the system to relax into the thermodynamically stable WZ phase, resolving the tetrapod geometry *via* defect accommodation rather than phase changes. It is physically plausible that distinct nucleation mechanisms operate in parallel, with the dominant pathway determined by local parameters such as temperature, supersaturation, and precursor chemistry.

2.1.2.2 Limits of ex situ characterization. A major obstacle is the temporal disparity between the nucleation event and structural characterization. Nucleation is a transient, non-equilibrium process occurring on rapid timescales at high temperatures. However, current evidence, such as the HRTEM imaging supporting models A and D, is predominantly obtained *ex situ* on mature nanostructures.

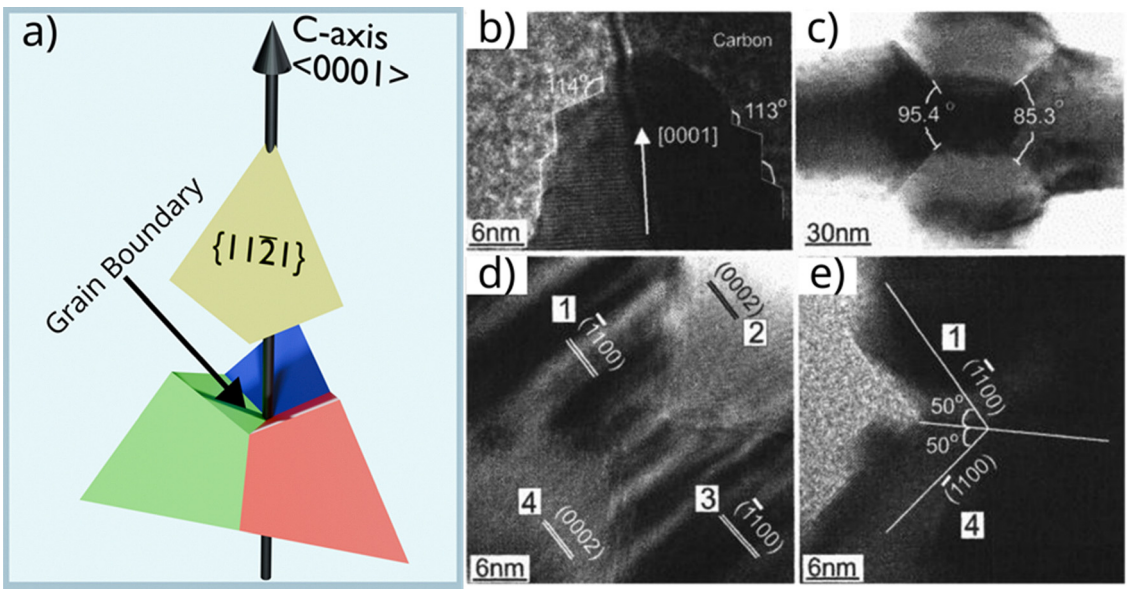

Fig. 5 Structural analysis of the multi-grain wurtzite (WZ) nucleus. (a) Schematic representation of the self-assembled tetrahedral core, comprising four WZ grains bounded by {1$\bar{1}$21} facets with outward-facing *c*-axes. (b) HRTEM image of a leg tip exhibiting 113°–114° growth steps. (c) Low- and (d) high-magnification TEM images of the central core, revealing four distinct hexagonal grains separated by high-angle grain boundaries. (e) HRTEM image of the boundary region detailing the twin relationship between adjacent arms.[4] (b)–(e) Reproduced from ref. 4 with permision from AIP Publishing,[4] Copyright 2005.

Researchers are therefore analyzing the thermodynamically relaxed state of the nucleus rather than the active nucleation complex. Distinguishing between a structure that initiated growth (*e.g.*, a metastable ZB core) and one that formed *via* stress relaxation during cooling (*e.g.*, a multi-grain WZ core) remains a significant analytical challenge. While model A relies on geometric elegance, it lacks broad statistical backing; conversely, model D provides direct imaging evidence but struggles to definitively explain the initial symmetry-breaking event without *in situ* verification.

2.1.2.3 Strain-induced structural reconfiguration. Finally, T-ZnO growth involves a complex coupling of atomistic and mesoscopic scales. The macroscopic morphology is governed by the core's crystallographic defects, such as twin boundaries and inversion domains. However, as the arms extend, they exert retroactive strain on the central core. This feedback loop can induce plastic deformation or defect migration that obscures the original crystallographic signature of the nucleation event. Consequently, the final core structure observed in microscopy may differ significantly from the initial nucleus, complicating efforts to reverse-engineer the mechanism solely from the final morphology.

Summary: evolution of nucleation concepts. The historical progression of T-ZnO nucleation models represents a conceptual evolution from idealized crystallography toward defect-mediated, thermodynamically driven theories. Early hypotheses, such as the epitaxial model (A), were notable for their geometric simplicity, relying on a perfect ZB core to explain the tetrapod's symmetry. However, the persistent experimental observation of non-ideal arm angles ($\sim$105°) necessitated more physically robust descriptions. This drove the development of the octa-twin (B) and multi-grain (D) models, which do not require a perfect template. Instead, these modern models propose that the tetrapod morphology arises from the WZ phase itself, where the core structure is determined by the energetic accommodation of strain *via* defects. Current understanding thus positions T-ZnO nucleation not as a single fixed event, but as a dynamic competition between kinetic trapping and thermodynamic relaxation, as summarized in Table 1.

2.2 Unifying principles: kinetic *vs.* thermodynamic control

The chemical state of the reactor, specifically the degree of supersaturation, acts as the unifying principle that governs the formation of T-ZnO. Synthesis parameters dictate the transport rates, determining whether the system has sufficient energy to overcome activation barriers or if it operates under strict kinetic control. These transport conditions directly dictate the atomic arrangement, determining whether atoms relax into stable lattices or become trapped in metastable states. As illustrated in Fig. 6, these structural differences dictate the final macroscopic shape, separating kinetically trapped products (such as hexagonal prisms) from thermodynamically stable morphologies (such as bipyramids).[32] Therefore, understanding how macroscopic parameters shift the regime between thermodynamic and kinetic control is essential for predictive synthesis.

When a reactor operates at high temperatures but low supersaturation, the system falls under thermodynamic control where the surface diffusion of species exceeds their arrival rate.[32,33] This high atomic mobility allows the atoms to bypass the formation of internal defects and relax into their lowest-energy lattice sites. Consequently, the crystal minimizes its overall surface energy to form compact, low-aspect-ratio prisms or quasi-spherical aggregates.[27,32,34] A clear illustration of this transport behavior is Ostwald ripening, frequently observed in the wet-chemical synthesis of ZnO nanoparticles.[35] As demonstrated by Wong *et al.*[35] smaller, highly curved particles dissolve, releasing species that diffuse and deposit onto larger, more stable particles. This process confirms that thermodynamic control inherently erases high-energy anisotropic features in favor of compact, energetically stable structures.[35]

Conditions of high precursor flux and extreme supersaturation, typical of vapor-phase synthesis, drive the system into strict kinetic control.[27,34] Elevated synthesis temperatures (typically $>$900 °C)

Table 1 A critical comparison of the primary models for T-ZnO growth

Model (first proposed)	Nature of the nucleus	Primary driving force	Key supporting evidence	Key challenges/limitations
A: epitaxial growth (1981)	Metastable ZB crystal core.	Epitaxial growth of WZ arms on the four {111} faces of the ZB seed.	HRTEM/ED showing a distinct ZB core in some rare samples.[10]	• Persistent angle discrepancy ($\sim$105° *vs.* 109.5°) • High energetic cost of ZB/WZ interface • Core is very rarely observed
B: octa-twin nucleus (1993)	A complex, strained WZ octa-twin embryo composed of eight sub-crystals.	Accommodation and release of internal strain to explain the non-ideal ($\sim$105°) arm angles.	Explains the experimentally observed non-ideal ($\sim$105°) arm angles.[25]	• Proposed nucleus is extremely complex • Has not been directly and unambiguously observed
C: nucleus transformation (1997)	An initial, transient ZB crystal that transforms into a twinned WZ structure.	Solid-state phase transformation from metastable ZB to stable, twinned WZ *via* crystallographic slips.	Reconciles evidence for a ZB origin with the final, defect-rich WZ structure, supported by the rare observation of a six-grained core.[2]	• The proposed rapid, solid-state transformation is highly complex • Key observation of a six-grained core has not been independently reproduced
D: multi-grain wurtzite (2005)	Four distinct WZ grains that self-assemble in a twin-like relationship.	Thermodynamic energy minimization by reducing the high surface area of precursor clusters.	Direct HRTEM imaging of a four-grain core; strongly supported by DFT calculations.[4]	Evidence for the final core is strong, but the dynamic self-assembly pathway remains a theoretical assumption

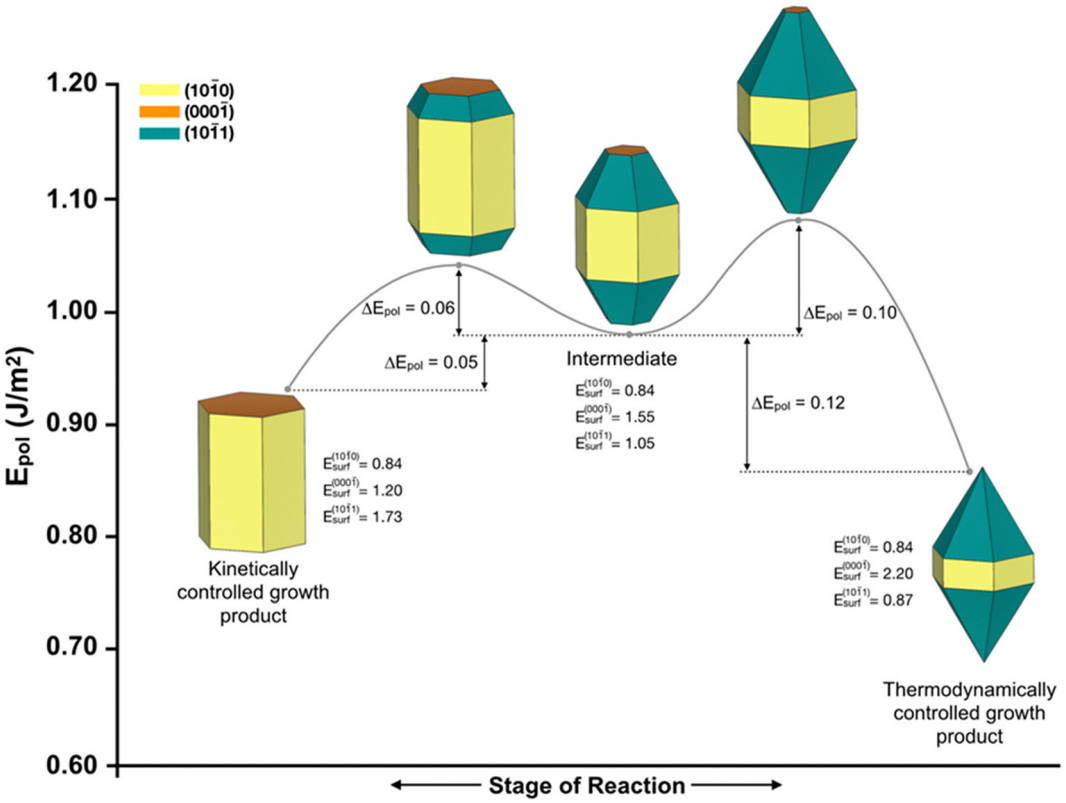

Fig. 6 Quantitative energy landscape governing ZnO morphology. The reaction pathway illustrates the structural transition from a high-energy kinetically controlled product (left) to a surface-energy-minimized thermodynamically controlled product (right). The denoted energy barriers (ΔE_{pol}) represent the activation energy required for these atomic rearrangements. Macroscopic synthesis parameters dictate whether the system overcomes these barriers or remains locked in a metastable morphology. Reproduced from ref. 32 with permision from MDPI,[32] Copyright 2023.

increase the zinc vapor pressure, accelerating the arrival rate of growth species so that it overwhelmingly exceeds the surface diffusion rate.[4,21,36–38] This kinetic arrest forces the system to initially form a nucleus *via* homogeneous nucleation in the gas phase, locking atoms into specific facets before they can relax into equilibrium sites.[39] Subsequently, the rapid accumulation of material restricts growth to the most exposed facets, driving the anisotropic extension of the four arms along the ⟨0001⟩ directions.

Within this highly supersaturated gas phase, the effective nucleation density remains low because most subcritical clusters fail to overcome the critical nucleation barrier.[31] Similar to Ostwald ripening during ZnO annealing,[40] these structurally unstable atomic clusters re-evaporate rather than forming stable defect centers. The resulting zinc and oxygen species are then transported and recycled to feed the rapid elongation of the already established tetrapodal arms. If these intermediate nuclei were stabilized instead, the chemical supersaturation of the reactor would be rapidly depleted. This depletion would remove the driving force for kinetic control, inherently suppressing anisotropic extension and forcing a return to isotropic morphologies.

The temporal dynamics of this process were elucidated by Zhou *et al.*,[41] who demonstrated how the chemical environment drives a two-step growth mechanism. Initially, a slower nucleation step locks the atomic arrangement of the core, after which extreme kinetic control forces arriving species onto specific outward-facing facets.[31,41] This rapid transport sequence ultimately yields the high-aspect-ratio elongation of the tetrapodal arms. However, as demonstrated by the pivotal work of Ali and Winterer[42] and supported by thermodynamic calculations,[31] simply increasing the reactor temperature can raise the equilibrium vapor pressure and inherently reduce the degree of supersaturation. This loss of chemical driving force favors the gas phase, potentially suppressing the initial atomic nucleation event and preventing the required defect center from forming altogether.[31]

These findings provide critical experimental validation: reactor conditions must be deliberately engineered to maintain continuous, high supersaturation in order to sustain strict kinetic control.[31,42] If this transport-driving force is lost, atoms will relax into equilibrium lattices rather than forming structural defects, and the highly anisotropic tetrapodal arms cannot be achieved. To rigorously resolve this causal interplay between the chemical environment and physical transport, it is necessary to quantify the system using the two fundamental dimensionless numbers that govern reactive flows.

To describe the physical transport of species within the highly supersaturated reactor environment, we first employ the Péclet number (Pe). This dimensionless number quantifies the regime of kinetic control by representing the ratio of the advective

transport rate (bulk fluid flow) to the diffusive transport rate. Mathematically, it is expressed as:

$$\mathrm{Pe} = \frac{LU}{D}$$

Here, L is the characteristic length scale, U is the local flow velocity of the precursor vapor or fluid and D is the mass diffusion coefficient of the species in the gas phase. This simple ratio physically captures the essence of the transport environment. When advection dominates ($\mathrm{Pe} \gg 1$), this kinetic control forces arriving atoms to stick to exposed facets rather than diffusing laterally across the lattice structure. Ultimately, this balance directly dictates whether the resulting morphology will remain compact or extend into elongated tetrapodal arms.

In vapor-phase systems typical for T-ZnO synthesis, the mass diffusion coefficient (D) is dynamically governed by the local supersaturation and the surrounding thermal environment. The gas-kinetic dependence of this diffusivity dictates the threshold for kinetic control, which is rigorously described by the Chapman–Enskog equation:

$$D = \frac{1.858 \times 10^{-3} T^{3/2} \sqrt{\frac{1}{M_\mathrm{A}} + \frac{1}{M_\mathrm{B}}}}{P \sigma_{\mathrm{AB}}{}^2 \Omega_\mathrm{D}}$$

In this formulation, T is the absolute temperature, P is the total pressure, $M_{\mathrm{A,B}}$ are the molecular weights of the species, and Ω_D is the temperature-dependent collision integral. By simplifying the material-specific constants within a highly supersaturated environment, we derive the critical scaling law that governs the chemical vapor transport regime. This mathematical relationship dictates the advection rates required to prevent atomic surface relaxation, ultimately setting the boundary conditions for the resulting anisotropic tetrapodal arms:

$$D \propto \left(\frac{T^{1.5}}{P}\right)$$

By applying this specifically to gas-phase transport, we derive the critical scaling law that governs the Péclet regime in chemical vapor transport (CVT):

$$\mathrm{Pe}_{\mathrm{gas}} \propto P$$

This scaling law highlights the critical leverage of reactor pressure within a highly supersaturated environment. Increasing the total pressure (P) directly suppresses gas-phase diffusivity (D), inherently forcing the system into strict kinetic control. Babu *et al.*[43] validated this crossover, demonstrating how these advection-dominated transport rates lock atomic species into gas-phase structural defects rather than allowing them to relax on substrate surfaces. Ultimately, this rapid gas-phase nucleation event serves as the foundation for the emergent, free-standing tetrapodal arms.[43] Independently, increasing the zinc precursor flux elevates the local flow velocity (U), establishing extreme kinetic control by further inflating the Pe.[44] This rapid advective transport outpaces lateral surface diffusion, preventing atoms from assuming equilibrium lattice sites and locking in the required internal defects. Consequently, this sequence yields highly anisotropic, tapered tetrapodal arms instead of compact, thermodynamically stable crystals.[44]

Conversely, fluids in hydrothermal or liquid-phase synthesis are effectively incompressible, meaning pressure cannot be used to tune the chemical supersaturation or D. Therefore, strict kinetic control *via* the Pe in these systems is achieved entirely by manipulating the advective precursor U. Martin *et al.*[45] experimentally demonstrated this transport universality by tuning the flow rate to balance advection and diffusion ($\mathrm{Pe} \sim 1.1$). This specific transport balance allows arriving atoms to arrange into oriented, stable lattices rather than chaotic structural defects, ultimately dictating the uniform morphology of ZnO nanowires.[45] However, as flow velocity increases further ($\mathrm{Pe} > 2$), the extreme kinetic control forces atoms to precipitate too rapidly, preventing proper lattice arrangement and yielding severe macroscopic agglomeration.[45]

Second, to capture the chemical kinetics within a highly supersaturated environment, we introduce the first Damköhler number ($\mathrm{Da_I}$). This dimensionless ratio quantifies kinetic control by comparing the chemical reaction rate to the advective fluid transport rate:

$$\mathrm{Da_I} = \frac{\text{reaction rate}}{\text{advective transport rate}} = \frac{kL}{U}$$

where k is the reaction rate constant. If $\mathrm{Da_I} \ll 1$, advection dominates and reactants are swept away before they can bond. Conversely, if $\mathrm{Da_I} \gg 1$, the extreme chemical reaction rate outpaces fluid transport, forcing precursor atoms to bond instantly upon mixing and forming internal lattice structures before they can reach the substrate.

In complex, high-temperature environments like FTS, a singular metric cannot fully capture the dynamic supersaturation. The reliable formation of T-ZnO requires a strict sequence of kinetic control: first initiating rapid homogeneous gas-phase nucleation, followed by sustained advection to feed the growing facets. To predict this sequential atomic arrangement, first forming a twinned defect core and then extending into a crystalline lattice, we couple the transport (Pe) and kinetic ($\mathrm{Da_I}$) descriptors into a unified master scaling law. By multiplying them, we eliminate the flow velocity (U) and derive the second Damköhler number ($\mathrm{Da_{II}}$), which serves as the ultimate predictor of the final tetrapodal arm morphology:

$$\mathrm{Da_{II}} = \mathrm{Da_I} \times \mathrm{Pe} = \left(\frac{kL}{U}\right) \times \left(\frac{LU}{D}\right) = \frac{kL^2}{D}$$

This unified number ($\mathrm{Da_{II}}$) evaluates the transport balance by representing the intrinsic ratio of the chemical reaction rate to the diffusive mass transfer rate. It serves as the critical determinant of the nucleation locus within a supersaturated system:

2.2.1 The rod/film regime ($\mathrm{Da_{II}} \ll 1$). Here, diffusion dominates ($D \gg kL^2$), allowing precursors to travel to the substrate before reacting. This avoids gas-phase defect formation and aligns with the low-pressure observations of Babu *et al.*,[43] where atoms relax smoothly on the substrate surface to yield a heterogeneous film morphology.

2.2.2 The tetrapod regime ($Da_{II} \gg 1$). Here, the extreme reaction rate dominates ($kL^2 \gg D$), establishing immediate kinetic control. The high supersaturation forces precursors to react instantly in the gas phase, structurally locking atoms into twinned defects before they can reach the reactor walls.[22,43] Ultimately, this localized gas-phase nucleation is the mandatory precursor for the emergence of free-standing tetrapodal arms.

This unified framework mathematically explains the extreme sensitivity of the synthesis environment to temperature. By substituting the Arrhenius dependence for the chemical reaction rate (k) and the Chapman–Enskog dependence for gas-phase diffusion (D) into the second Damköhler equation, we derive the constitutive scaling law that governs strict kinetic control in vapor transport:

$$\mathrm{Da_{II}} \propto \frac{k}{D} \propto P \cdot T^{-1.5} \cdot \mathrm{e}^{\frac{-E_a}{RT}}$$

This mathematical relationship reveals that increasing temperature causes an exponential rise in Da_{II} (*via* the Arrhenius term). While this specific derivation is unique to compressible gases, the resulting transport regimes universally dictate the final atomic arrangement across both gas and liquid phases:

2.2.3 When diffusion dominates ($Da_{II} \ll 1$ or $Pe \ll 1$). The system lacks extreme supersaturation, allowing surface diffusion to outpace the arrival of new material. Atoms have sufficient time to bypass defect formation and relax into stable equilibrium lattices, which drives the ripening of the structure into compact, isotropic particles.[35,45]

2.2.4 When arrival/reaction dominates ($Da_{II} \gg 1$ or $Pe \gg 1$). The highly supersaturated environment pushes the system into strong kinetic control. Rapid convective flux delivers precursor material much faster than it can diffuse laterally across the crystal surface. Consequently, growth species are locked into place exactly where they land, forcing continuous and rapid atomic extension along the polar {0001} facets. This prevention of lattice relaxation ultimately yields the characteristic high-aspect-ratio, tapered tetrapodal arms.[32,33,45,46]

By formally linking these dimensionless transport parameters to their resulting crystallographic structures, this theoretical framework provides a powerful predictive tool for rational synthesis (summarized in Table 2). Crucially, this analysis resolves the apparent paradox of temperature in T-ZnO synthesis. It clarifies that while a high-temperature environment is initially essential to generate the extreme supersaturation required to trigger kinetic control ($Da_{II} \gg 1$) and form the foundational gas-phase defect core, this exact same thermal energy becomes a double-edged sword during the subsequent growth phase.

If the newly formed nuclei are not rapidly transported to a cooler zone, the local environment loses its effective supersaturation. As shown by Saunders *et al.*,[31] the zinc vapor actually becomes undersaturated at these sustained high temperatures. Without rapid quenching to maintain kinetic control (high Pe), the thermodynamic drive to re-evaporate completely overwhelms the advective growth rate.[31] This thermal destruction erases the internal defects and dissolves the emerging tetrapodal arms. Consequently, the rational design of high-quality T-ZnO requires spatially decoupled reactors: an initial high-temperature zone is required to trigger extreme supersaturation and core nucleation (high Da_{II}), followed immediately by a high-velocity, lower-temperature zone to sustain the kinetic control required to rapidly extend the arms (high Pe).[15,41]

The specific compositional gradient in the Zn/O ratio, measured from the core to the arm tip, physically records the fluctuating supersaturation and transport rates experienced by the particle as it traverses the reactor.[45,47] This macroscopic behavior is directly supported by atomistic theory. Specifically, DFT and machine learning (ML) predictions demonstrate how these shifting chemical environments alter the localized energetics of individual

Table 2 A critical analysis of controllable parameters on the unified second Damköhler number (Da_{II}) and Péclet number (Pe). This table distinguishes between universal effects (valid for both vapor and hydrothermal phases) and phase-specific transport laws

Experimental parameter	Mechanistic impact & scaling law (kinetics)	Primary outcome: nucleation (Da_{II} regime)	Secondary trade-off: growth (Pe regime)
Temperature (T) (universal)	Reaction dominates ($k\uparrow\uparrow$): rate constant k rises exponentially (Arrhenius), overwhelmingly outpacing gas-phase diffusion D. $\mathrm{Da_{II}} \propto \mathrm{e}^{\frac{-E_a}{RT}}$	Establishing the defect core: the extreme initial supersaturation drives $Da_{II} \gg 1$, forcing gas-phase atoms to instantly lock into twinned defects rather than relaxing into surface films.[22,31]	Loss of supersaturation: sustained high T eventually undersaturates the environment. If kinetic control is not maintained *via* rapid quenching, atoms re-evaporate and the emerging arms dissolve.[31]
Reactor pressure (P) (vapor-phase specific)	Diffusion suppression ($D\downarrow$): in highly supersaturated compressible gases, diffusivity is strictly suppressed inversely with total pressure ($D \propto 1/P$) (note: in liquid/hydrothermal, P has negligible effect on D).	Transition to gas-phase defect centers increasing P drives $Da_{II} \gg 1$ by trapping reactants, ensuring the rapid formation of structural defects rather than equilibrium substrate lattices.[43]	Anisotropic shaping: high P sustains strict kinetic control (high Pe), preventing lateral lattice relaxation and forcing atoms to extend into sharp, high-aspect-ratio tetrapodal arms.[32]
Flow velocity (U) (universal)	Advection dominates ($Pe\uparrow$): directly establishes kinetic control by overwhelmingly increasing the advective transport rate over lateral surface diffusion. $\mathrm{Pe} = \frac{LU}{D}$	Yielding free-standing cores: rapid advection sweeps precursor species into the fluid stream, preventing them from structurally relaxing onto the reactor walls.	Morphology tuning: extreme kinetic control (high Pe) forces atoms into tapered tetrapodal arms. Conversely, a loss of advection (low Pe) allows atoms to relax into isotropic agglomerations.[45]

atomic fragments. By dynamically tuning the relative stability of specific structural facets, these fundamental changes in kinetic control directly drive the structural transitions in the macroscopic morphology at the nanoscale.[32]

Therefore, the scaling laws summarized in Table 2 offer a predictive pathway for rational reactor engineering. For example, to force the elongation of blunt structures into sharp tetrapodal arms, the system must be pushed deeper into strict kinetic control (Pe $\gg$ 1). In gas-phase reactors, increasing pressure inherently suppresses lateral diffusion; in continuous hydrothermal systems, increasing precursor flow enhances advection. Both actions prevent atoms from relaxing into equilibrium lattices, successfully locking them into the extending tips (note: in static batch reactors where flow is negligible, the lack of advection naturally reverts the system to thermodynamic control, allowing atoms to form stable lattices that yield low-aspect-ratio isotropic prisms). Conversely, to increase the yield of free-standing tetrapods rather than substrate films, the priority shifts to the Da_{II}. A sharp increase in temperature elevates the supersaturation, driving the reaction locus entirely into the gas phase ($Da_{II} \gg 1$). This rapid kinetic control ensures that precursors instantly bond to form twinned defect seeds before they can physically diffuse to the reactor walls. Ultimately, this decoupled transport framework moves the field beyond empirical trial-and-error, enabling the deliberate design of both initial yield and precise final morphology.[21,37,43,45,48] This theoretical foundation provides a direct transition to the applied synthesis methods discussed in the following section.

2.3 Synthesis methods of T-ZnO

Tetrapodal ZnO can be synthesized *via* a variety of routes, which are broadly divided into liquid-phase and vapor-phase methods, which are discussed below. While liquid-phase routes offer potential advantages in low-temperature processing, vapor-phase approaches are the most established, widely utilized, and best understood for producing high-quality crystalline T-ZnO. As such, they will be discussed first.

2.3.1 Vapor phase methods. Vapor-phase approaches remain the dominant and most established routes for T-ZnO synthesis. However, they are not monolithic; instead, they represent a spectrum of techniques defined by a trade-off between manufacturing scalability and morphological precision. Despite differences in technical setup, all vapor-based routes are governed by the same fundamental physicochemical sequence: (i) generation of gas-phase zinc species, (ii) oxidation to form ZnO precursor, (iii) nucleation of ZnO clusters driven by high supersaturation,[22,34] and (iv) anisotropic crystal growth of WZ arms from these nuclei, ultimately producing the characteristic tetrapodal structure.[15]

As established in Section 2.2, these methods rely on generating a high zinc flux to drive the system into the kinetic controlled regime, ensuring the formation of tetrpodal structures rather than compact crystals. Different vapor-phase methods, such as thermal evaporation, chemical vapor deposition (CVD), FTS, plasma-assisted growth, and combustion-based approaches can be distinguished by the zinc precursor, the heat source, and the strategy used to control the vapor pressures. Each method provides a unique way of creating the required non-equilibrium conditions for the self-organized emergence of tetrapodal morphology, each with its own profile regarding cost, scalability, energy consumption, and the precision of morphological control. Each vapor-based method is discussed in detail in the following sections.

2.3.1.1 Thermal evaporation. Thermal evaporation represents the most classical route to synthesize T-ZnO. Thermal evaporation allows for high-throughput synthesis, but only offers limited control over the final morphology. The process relies on the direct thermal oxidation of a metallic zinc source (powder, foil, wires) in an oxygen-containing environment.[4,49] Its key advantage is the simplicity of the setup (often just a tube furnace) which translates to low capital cost. Oxygen can be supplied either by ambient air[4,49,50] or by a controlled atmosphere with a carrier gas such as Ar/N_2.[4,51] However, this simplicity is offset by high operational costs, as the process is energy-intensive, using external heat sources, with typical synthesis temperatures ranging from 650 °C to 1100 °C.[4,21,22,33,52–55] Fig. 7 schematically illustrates the thermal evaporation process. Zinc atoms evaporate and react with oxygen to form ZnO molecules, which nucleate and aggregate into ZnO nuclei. These clusters evolve into crystalline domains, ultimately growing into T-ZnO.

Depending on the setup, the oxidizing atmosphere can be static (sealed batch systems) or utilize a continuous input of oxidizer and/or zinc precursor. The process is most often conducted as a batch-type reaction, where Zn powder, foils or pellets are evaporated inside a tube furnace.[49,51,53,55]

The final dimensions are highly sensitive to the temperature gradient; higher deposition temperatures favor the growth of larger tetrapods with longer arms,[4,27,53] while lower temperatures often yield shorter or irregular arms, as described in Section 2.1. Reaction times vary and exert a significant influence on final dimensions.[4,53] The resulting tetrapods typically exhibit arm lengths between 0.3 and 10 μm and with diameters in the range of 30–650 nm, depending on exact synthesis conditions.[4,49,50,56]

Thermal evaporation enables the rapid and direct synthesis of T-ZnO in comparatively simple setups.[2,52,54,57] This makes it attractive for applications requiring large amounts of material. The primary drawback of this method, however, is the inherent difficulty in precisely controlling these thermal and concentration gradients, leading to inhomogeneous nucleation and growth conditions across the deposition zone, resulting in a product with broad size and morphology distributions.[23,34,56] This lack of monodispersity is a significant limitation for advanced electronic or optical applications where uniformity is paramount. Consequently, post-synthesis processing or selection is often necessary if narrow dimensional control is desired.[52] Overall, thermal evaporation lacks the fine tunability of more advanced techniques like CVD or plasma-assisted processes. However, its low setup cost and proven ability to produce gram-scale quantities[27,52] ensure its continued relevance. It remains particularly useful for mechanistic studies and applications requiring large volumes of material, such as fillers for polymer composites, where precise morphological uniformity is a secondary concern.

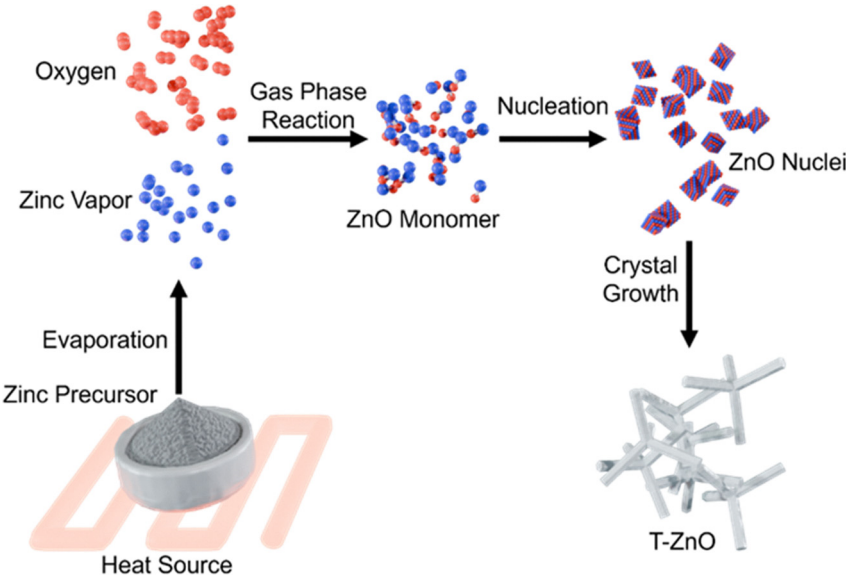

Fig. 7 Schematic overview of the thermal evaporation synthesis route. A heat source vaporizes metallic zinc precursors, which undergo a gas-phase reaction with oxygen to generate ZnO monomers. These monomers aggregate into foundational nuclei and subsequently undergo anisotropic crystal growth to yield the final T-ZnO morphology.

2.3.1.2 Combustion-driven synthesis: flame transport synthesis (FTS) and related methods. Combustion-driven approaches represent a scalable alternative to furnace-based heating, aiming to improve energy efficiency by utilizing the chemical energy of fuels. Among these, FTS is one of the most effective and widely adopted techniques for producing T-ZnO.[12,21,58] Fig. 8 illustrates this process, where a mixture of zinc microparticles and a sacrificial organic component undergoes combustion, generating a highly reactive flame atmosphere that vaporizes zinc and drives the nucleation and growth of T-ZnO. This method occupies a unique space in the synthesis landscape, offering very high throughput and reduced reliance on external energy, but at the cost of precise, steady-state process control.

A mixture of Zn microparticles and a sacrificial organic fuel undergoes combustion, generating a localized high-temperature,

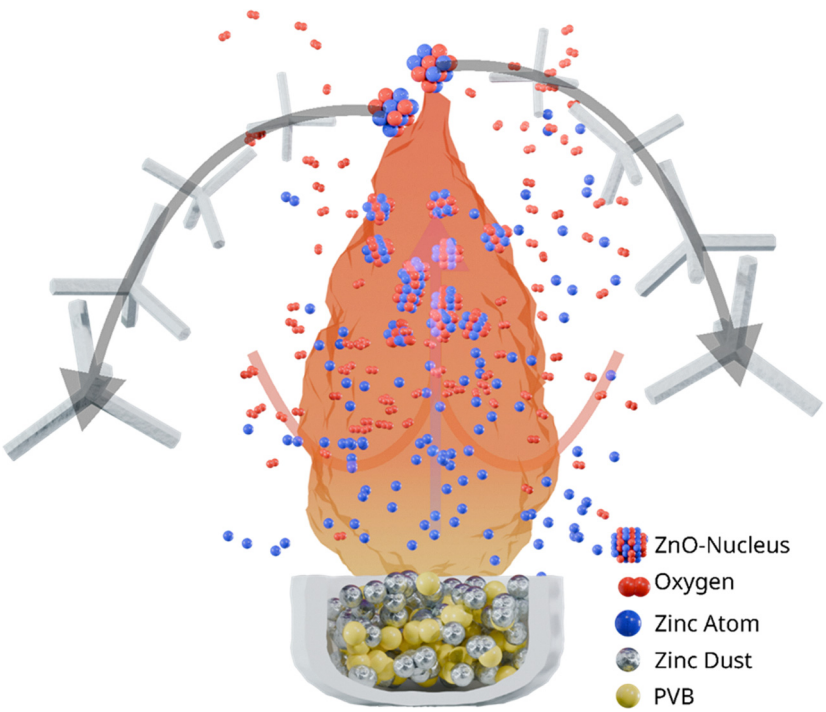

Fig. 8 Schematic of flame transport synthesis (FTS) for tetrapodal ZnO (T-ZnO).

reactive atmosphere. The exothermic flame vaporizes zinc and creates transient Zn/O ratios that drive rapid nucleation and anisotropic growth of ZnO tetrapods.[28,52] In a typical approach, a Zn microparticles: polyvinyl butyral (PVB) mixture is heated in a muffle furnace at ~900–950 °C. The process combines zinc microparticles with a sacrificial organic component, such as PVB or ethanol. Upon combustion, this mixture generates a highly reactive atmosphere.[21,37] Instead of relying entirely on external heating to vaporize the zinc, an external heat source is used to ignite the organic additive. The subsequent exothermic combustion generates a rapid, intense, and localized high-temperature environment that vaporizes zinc and establishes the supersaturation conditions required for tetrapod nucleation and growth.[21,59] The PVB combustion releases Zn vapor along with CO_2, H_2O, and other volatiles.[21]

The advantage of FTS results from its dynamic, self-regulating chemical environment, which directly dictates the final morphology. Initially, the rapid combustion of the polymer consumes local oxygen, creating a transient, Zn-rich atmosphere. Initially, Zn and O atoms combine to form a primary cluster. Additional Zn and O atoms then attach to this cluster at different facets, leading to the formation of a stable nucleus. Once this nucleus is established, subsequent Zn and O atoms drive conventional one-dimensional spike growth along the *c*-axis (0001). Nucleation represents a critical step, while homogeneous nucleation predominantly yields tetrapod-type structures, heterogeneous nucleation can give rise to diverse morphologies, including multipods, flowers, and tree-like architectures.[21,58,59] This intrinsic time-dependence is also seen in variants like ethanol-assisted flame transport synthesis (E-FTS), which yield morphologically distinct tetrapods.[37,60] From a critical perspective, this dynamic nature is both a feature and a flaw. While it allows for the single-step synthesis of complex morphologies and facilitates the incorporation of dopant metals such as Cu, Al, and Sn,[58,61] the lack of steady-state control makes achieving high batch-to-batch reproducibility and morphological uniformity a significant challenge. Furthermore, the use of a sacrificial fuel results in poor atom economy, a key consideration from a green chemistry standpoint.

Other combustion-based strategies have been explored to gain better control over the reaction environment. Xu *et al.*[62] demonstrated counterflow diffusion flame (CDF) synthesis, where zinc substrates are exposed to a methane-air flame. The controlled gradients of temperature and oxygen yield diverse morphologies, including rods, ribbons, flowers, and tetrapods, with morphology being strongly dependent on flame conditions. Chen *et al.*[63] reported a melting-combustion method (MCM), directly igniting molten zinc with an acetylene-oxygen flame to produce high-purity tetrapods without catalysts or volatile precursors. Growth follows a vapor-solid mechanism and occasionally shows bottleneck features along the arm.[63] Offering perhaps the highest energy efficiency, Hwang *et al.*[64] introduced a self-propagating high-temperature synthesis (SHS) approach. In this method, compacted Zn powder with an oxidizer (NH_4NO_4) is ignited by a heating coil in a closed chamber, the exothermic reaction sustains itself, generating mainly tetrapodal ZnO with aspect ratios up to 50 and yields of ~95% under optimized conditions.

Collectively, these methods highlight the versatility of combustion as a scalable energy source for T-ZnO synthesis, though precise morphological control remains a common challenge across all variants. The methods also demonstrate that tetrapod growth is driven by strong advection. The formation of high-quality crystals in this chaotic environment confirms that T-ZnO growth thrives under conditions of strong advection (), where reaction rates dominate over diffusion.

2.3.1.3 Chemical vapor deposition (CVD). Representing the high-precision, moderate-throughput approach to T-ZnO synthesis, CVD and related vapor-transport methods offer a significant leap in morphological control compared to direct evaporation or combustion. Fig. 9 illustrates the principle of this process in a two-zone furnace setup, where Zn-based precursors are converted into a supersaturated Zn vapor that is transported and subsequently nucleates into T-ZnO crystals under controlled conditions. The key advantage of CVD is the spatial decoupling of the precursor source from the growth substrate, typically achieved within a two-zone furnace.[15,53,65–68] This arrangement allows for independent and precise control over vapor generation and crystal nucleation. Consequently, it enables a level of tunability that is difficult to achieve with other methods. In contrast to FTS, which operates in highly turbulent conditions, CVD allows for the independent tuning of reaction temperature and precursor flux and ratio.

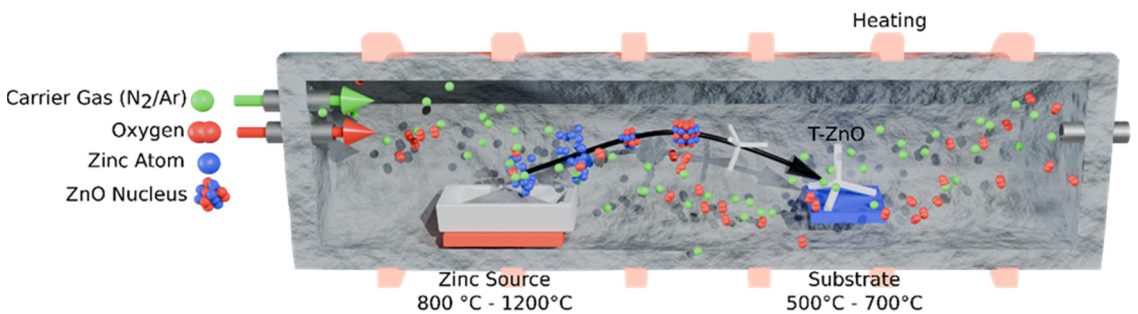

Fig. 9 Schematic representation of T-ZnO synthesis *via* CVD in a two-zone furnace. Zn-based precursors undergo carbothermal reduction to form a supersaturated Zn vapor, which is transported and oxidized under controlled gas atmospheres, leading to nucleation and anisotropic growth of T-ZnO crystals on the substrate.

In a typical approach, carbothermal reduction of Zn-based precursors such as Zn, ZnO, or $ZnCO_3$ with graphite generates a supersaturated Zn vapor that oxidizes under controlled atmospheres in a two-zone furnace.[15,53,65–69] Using this strategy, Yu *et al.*[70] produced high-quality, uniform T-ZnO nanocrystals with arm diameters of 80–100 nm and lengths of 600–1000 nm, guided by NiO nanoparticles that acted as catalytic nucleation sites on substrates held at ~600 °C. Numerous catalyst-free variations have also been reported.[53] For example, Newton *et al.*[15] synthesized tetrapods with arm lengths from 200 nm to 10 μm and diameters between 50 and 500 nm simply by varying the oxygen content (0.5–5%) in the carrier gas, demonstrating the strong influence of Zn/O ratios on growth.[15] This highlights the method's capacity to systematically explore the growth parameter space, where subtle shifts in partial pressure and substrate temperature determine the final morphology.[65]

Alternative variants further expand the accessible parameter space. Self-catalytic growth using zinc mixed with zinc acetate has been shown to promote anisotropic growth through a vapor–liquid–solid mechanism at temperatures as low as 650 °C.[71] Catalyst-free CVD oxidation of pure Zn powders at 940–990 °C in Ar/O_2 atmospheres yields tetrapod arms of 20–100 nm diameter and 1–15 μm length, with O_2 concentration governing not only morphology[67] but also optical properties. Higher oxygen flows enhance visible luminescence (590–610 nm) linked to oxygen vacancies, whereas moderate O_2 favours stronger UV emission (~3.2 eV excitons), directly connecting synthesis conditions to functional behaviour.[67]

Overall, CVD-based routes provide significant tunability, combining the simplicity of thermal evaporation methods with a good morphology control. Despite their advantages, CVD-based methods face several key limitations. They require advanced equipment, including high-temperature furnaces, gas flow controllers, and vacuum systems, which significantly increase both the cost and technical complexity. Additionally, the use of catalysts such as NiO or Zinc acetate, introduces health and environmental hazards.[70,72] Scalability also remains limited by furnace volume and substrate area, making CVD not suitable for mass production of T-ZnO. Finally, the high operating temperatures (600–900 °C) contribute to energy consumption and carbon emissions, limiting the sustainability.

2.3.1.4 Plasma-assisted synthesis of T-ZnO. Plasma-assisted methods exploit highly reactive, non-equilibrium environments to enable rapid ZnO formation while simultaneously offering a pathway to sophisticated defect engineering. The fundamental advantage of plasma lies in its unique chemistry. Fig. 10 illustrates this process, where precursor gases are ionized into a plasma containing energetic ions, electrons, and radicals that drive ultrafast nucleation and growth of T-ZnO. By applying strong electromagnetic fields (microwave, DC), the precursor gases are ionized into a highly energetic state containing ions (Zn^{2+}, O^{2-}), electrons, and reactive radicals ($O^{\bullet}$). These species possess much higher chemical potential than their neutral counterparts in thermal methods, allowing for extremely rapid nucleation and growth at lower overall substrate temperatures. This can also suppress thermal agglomeration, enabling the formation of much finer nanostructures.[73]

Early work by Zhang *et al.*[73] used a microwave plasma furnace (400 W, 4 Torr, Ar/O_2) to produce crystalline tetrapods with fine arms (10–25 nm), showing that plasma conditions can inhibit agglomeration and stabilize anisotropic growth. Lin *et al.*[74] expanded this with a DC plasma reactor, where injected zinc powder was vaporized and oxidized, yielding tetrapods along with rods and nanoplatelets. The tetrapod yield (15–65%) depended on plasma power and particle residence time, and the process scaled up to ~1 kg h^{-1}, though post-processing was required. Lee *et al.*[75] applied a 2.45 GHz microwave plasma (~6500 K) with an N_2/O_2 swirl gas, producing tetrapods (~30 nm diameter, ~250 nm length). Yang *et al.*[46] synthesized

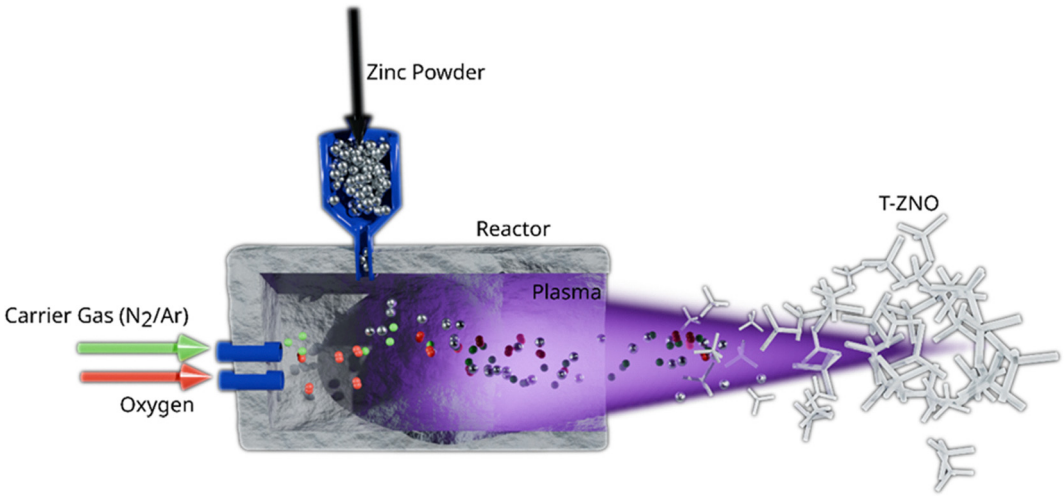

Fig. 10 Schematic of plasma-assisted synthesis of tetrapodal ZnO (T-ZnO). Elemental Zn is injected into a plasma environment where strong electromagnetic fields ionize precursor gases, generating energetic ions, electrons, and radicals. These reactive species enable rapid nucleation and anisotropic growth of ZnO tetrapods at lower substrate temperatures compared to thermal vapor methods.

morphology-controlled ZnO tetrapods using a direct arc plasma discharge, showing that changing oxygen partial pressure-controlled shape and structure.

Recent atmospheric-pressure microwave plasma (APMP) systems allowed for more control. Yang and Jeong[76] demonstrated that adjusting power and collection distance tuned tetrapod size, with larger structures forming at greater distances. Padmanaban *et al.*[29] further showed that RF-powered microplasmas can produce defect-free nanoscale tetrapods (~65 nm arms, ~11 nm diameters).

High plasma powers or reduced oxygen concentrations strongly promote the formation of anisotropic ZnO microstructures, including well-defined tetrapods.[77] While the influence of plasma pressure has not yet been systematically investigated, it is expected that lower pressures would favour the development of more faceted tetrapods. Plasma-assisted methods, however, inherently increase both the complexity and energy demands of synthesis, resulting in higher costs compared even conventional CVD approaches. Despite these drawbacks, certain plasma configurations have demonstrated the ability to produce high-quality T-ZnO with controlled morphology. One important advantage of plasma-based techniques is that they do not require specialized or expensive precursors, instead relying on elemental zinc. The costs increase even further considering the high energy demands for operating the plasma and possible external heat sources. Plasma-based methods demonstrate that extreme non-equilibrium conditions can be achieved by means other than temperature. This allows for the study of precursor ratios independently of thermal effects, offering a unique perspective on the growth mechanism. Table 3 summarizes the geometries and morphologies reported for each vapor-phase synthesis method. It highlights typical ranges in arm length/diameter and key features influencing morphology.

Ultimately, the selection of a vapor-phase synthesis route is a strategic decision dictated by the classic engineering trade-off between production scale, material quality, and cost. The methods discussed represent a spectrum of choices along this continuum.

At one end, thermal evaporation and combustion-based approaches offer pathways to high-throughput, gram-scale production, making them suitable for bulk applications like composites and fillers; however, this scalability is fundamentally coupled with poor morphological homogeneity and, in some cases, high energy consumption or low atom economy. In contrast, CVD provides unparalleled precision, enabling the fabrication of uniform, defect-engineered T-ZnO crystals essential for high-performance devices, albeit with significant penalties in setup complexity and scalability.

Plasma-assisted synthesis emerges as a compelling outlier, a potential paradigm-shifter that promises both extreme speed and fine nanostructure control. However, its very high energy and capital costs currently remain a significant barrier to widespread adoption. The persistent challenge in the field, therefore, is to develop hybrid or novel synthetic routes that unite the scalability of combustion with the precision of CVD in an economically and environmentally sustainable manner.

2.3.2 Wet-phase synthesis of T-ZnO. In stark contrast to the high-energy, non-equilibrium conditions of vapor-phase routes, wet-chemical approaches represent a low-energy, solution-processable frontier for T-ZnO synthesis. These methods, operating at or near room pressure and at significantly lower temperatures (typically <200 °C), are rooted in the principles of green chemistry. They offer the potential for reduced energy costs and compatibility with heat-sensitive substrates like polymers. However, this synthesis paradigm is fundamentally different; instead of being driven by rapid vapor condensation, it relies on controlled, near-equilibrium precipitation from a complex solution, making the underlying chemical mechanisms more subtle and often more challenging to control.

2.3.2.1 Aqueous solution growth. The simplest wet-chemical approach involves direct precipitation from an aqueous solution. Using Zinc sulfate and ammonia, branched rods, crosses, and tetrapods can form within 15 minutes at ~90 °C.[6,78] The chemistry of this process is far more nuanced than the simple addition of

Table 3 Critical comparison of vapor-phase synthesis methods for T-ZnO

Method	Typical conditions	Tetrapod arm size/ morphology	Key advantages	Key limitations
Thermal evaporation	650–1100 °C in a tube furnace; ambient or controlled O_2	Arms 0.3–10 μm; diameters 30–650 nm; sensitive to thermal gradients	Low capital cost, simple setup, high material throughput.	Poor morphological uniformity (broad size distribution), high energy consumption.
Combustion-driven (FTS, SHS, *etc.*)	Ignition of Zn ion fuel/ oxidizer mixture (*e.g.*, PVB, NH_4NO_3); ~900–950 °C	Arms from nm to tens of μm; often features tapered tips due to dynamic gas environment.	High throughput, potentially energy-efficient (exothermic), single-step process.	Poor uniformity and reproducibility due to lack of steady-state control; poor atom economy.
Chemical vapor deposition (CVD)	Carbothermal reduction of ZnO in a 2-zone furnace; controlled gas flow.	Arms 200 nm-10 μm; diameters 20–500 nm; capable of highly uniform, high-quality crystals.	Excellent morphological and dimensional control, allows for *in situ* defect engineering.	Higher capital cost, complex setup, scalability limited by reactor size and deposition rate.
Plasma-assisted synthesis	Microwave/DC/RF plasma; high power density; low- or atmospheric-pressure.	Very fine arms 10–65 nm; can produce defect-free or intentionally engineered crystals.	Extremely rapid growth rates, simultaneous control over morphology and defects.	Very high capital and operational (energy) costs, complex process control.

Zn^{2+} and OH^- ions. In reality, the zinc ions exist as stable coordination complexes (*e.g.*, tetraamminezinc, $[Zn(NH_3)_4]^{2+}$). The growth of ZnO occurs *via* the slow, controlled decomposition of these complexes, which provides a steady supply of the fundamental growth units to the crystal surfaces. The process also relies on the nucleation of a ZnO nucleus, from which arms extend by the addition of Zn^{2+} and OH^- ions in the complex solution.[6] The resulting tetrapods typically display arm lengths of about 5 μm and diameters below 1 μm, with rather good homogeneity.[6] While straightforward, this method's outcome is extremely sensitive to subtle fluctuations in pH, temperature, and concentration, which alter the delicate equilibrium of the zinc complexes, making precise morphological control and reproducibility a significant challenge.

2.3.2.2 Mechanisms of aqueous growth and morphological control. The wet phase synthesis employ Zn^{2+} and OH, for example zinc sulfate, Zinc acetate and ammonia or sodium hydroxide. For the case of ammonium containing solutions, ZnO formation is governed by the equilibria between $[Zn(OH)_3]^{2-}$ and $[Zn(NH_3)_4]^{2+}$, which therefore determines the activity of Zn^{2+}. Thus, they control axial and lateral growth at pH's of 10–11 and temperatures above 75 °C as they decompose to feed anisotropic extension along ⟨0001⟩ directions.[79] Fast nucleation under these conditions yields a ZB nucleus (as described in the Epitaxial growth model, Section 2.2.2) from which four WZ arms grow, leading to the tetrapodal morphology.[6] The exact morphology is further tuned by capping molecules that selectively adsorb on polar or non-polar facets. Ammonia favors axial growth, whereas citrate or PVA can suppress ⟨0001⟩ extension or induce twinning, leading to the growth toward disks or dumbbells *via* facet passivation or bridging at (0001).[80] Accordingly, these outcomes reflect shifts in the surface-energy landscape which can be explained on the basis of Wulff-based morphology maps and how ligands, solvent, and temperature alter relative facet energies to drive branching and arm growth.[32] Integrating supersaturation kinetics with complexation chemistry and targeted facet capping thus enables reproducible wet-chemical synthesis of T-ZnO.

2.3.2.3 Microemulsion-mediated and solvothermal methods. To exert greater control over nucleation and growth, more sophisticated methods have been developed. Microemulsion-mediated hydrothermal methods attempt to address morphology control by confining nucleation and growth within surfactant-stabilized droplets. These droplets act as individual nanoreactors, limiting nucleus size and promoting uniformity. Jiang *et al.*[81] used this approach to produce highly crystalline ZnO nanotetrapods with uniform leg lengths (200–300 nm) at 120 °C for 12 h. The confinement effect of the reverse micelles, together with surfactant interactions with ZnO surfaces, is believed to bias growth along the [0001] axis. This mechanism, however, is still not well understood, and the method depends on a balance of surfactant, co-surfactant, and precursor concentrations.[81]

Alcohol-based wet chemical synthesis has also been described in the literature,[82] where zinc alkoxides or acetates are decomposed in alcohol solutions, sometimes with stabilizers or surfactants. This approach can generate tetrapods with arm diameters below 100 nm and relatively uniform morphologies. The use of organic solvents and stabilizers can provide different coordination environments for the zinc precursor compared to water, offering another lever for controlling growth kinetics. Variants that incorporate dopants such as Mg have been shown to increase yield and improve structural homogeneity.[82] Nevertheless, these alcoholysis routes face similar challenges to hydrothermal methods: they are highly sensitive to precursor chemistry, reaction conditions, and additives, which makes reproducibility and scale-up difficult.

To sum up, wet-chemical synthesis provides a low-cost, low-temperature alternative to vapor-phase methods for T-ZnO, enabling direct formation of nanoscale tetrapods without specialized hardware and offering compatibility with flexible substrates for applications in catalysis and sensing. Compared to vapor-phase approaches, however, these methods often suffer from lower morphological uniformity, high sensitivity to precursor chemistry, and limited reproducibility, which complicates scale-up. Their main practical advantage lies in accessibility and affordability, but they also introduce environmental problems, the solvents, surfactants, and additives contaminate water, requiring removal or disposal. The resulting tetrapods must be thoroughly washed to eliminate residual chemicals. Future progress will depend on greener chemistries and simplified purification strategies that preserve the low-threshold nature of wet synthesis while improving uniformity, scalability, and sustainability.

2.4 Computational and ML-driven insights

The competing experimental growth models highlight the current limitations in capturing nanoscale nucleation events. To overcome these limitations, the field is increasingly turning to advanced computational methods, particularly the integration of first-principles calculations with ML. This approach marks a crucial shift from describing a few plausible-but-unproven models to building a truly predictive framework for nanoparticle formation. This trend is underscored by the 2024 Nobel Prize in Chemistry for breakthroughs in computational protein design.

A prime example of this paradigm is the work by Chen and Dixon,[83] who developed a fragment-based energy decomposition method enhanced with ML to rapidly and accurately predict the stability of ZnO nanoparticles across different sizes and polymorphs. Instead of relying solely on computationally expensive (DFT calculations for each potential structure, they trained a ML model on the energies of small atomic fragments). This allowed them to predict the stability of large, complex nanoclusters with DFT-level accuracy at a fraction of the cost. The insights from this predictive approach are profound because they begin to unify the preceding models:

2.4.1 Bridging precursor chemistry and thermodynamics. The calculations revealed that ultrasmall ZnO clusters (<2 nm) energetically favor cage-like or body-centered tetragonal structures, not WZ. This provides strong theoretical support for the idea that symmetric, non-WZ "magic clusters" could be the initial gas-phase building blocks. This focus on unique cluster stability is directly supported by the work of Dmytruk *et al.*,[84]

who used mass spectrometry and quantum calculations to identify exceptionally stable nested shell clusters. They identified specific clusters, such as $(ZnO)_{60}$ and particularly $(ZnO)_{168}$, as likely nuclei. Their findings suggest that these specific geometries act as templates for the final tetrapod structure.[84] Chen and Dixon's model[83] further predicted that the stable WZ structure only becomes dominant at larger sizes, driven by the minimization of surface energy. This finding aligns perfectly with the thermodynamic self-assembly of WZ grains proposed in earlier models.

2.4.1 Providing a fundamental reason for anisotropic growth. The calculations confirmed that the non-polar WZ surfaces like $\{10\bar{1}0\}$ and $\{11\bar{2}0\}$ are significantly more stable than the polar {0001} faces. This provides a clear energetic explanation for the rapid, anisotropic *c*-axis growth observed in all tetrapod synthesis. These calculations confirm that the arm elongation observed in experiments is the direct result of the kinetic suppression of diffusion to the stable side facets, validating the transport model proposed in Section 2.2.

This predictive link between atomistic surface energetics and macroscopic shape is further strengthened by the work of Gouveia and co-workers.[32] As illustrated in Fig. 11, they combined DFT surface energy calculations with the Wulff construction to generate comprehensive morphology maps. These diagrams successfully reproduce experimentally observed ZnO shapes (from prisms to plates) by simulating how growth conditions (governed by the local Pe) alter the relative stability of the polar and non-polar surfaces.[32]

Ultimately, this computational framework offers a potential pathway to settle the long-standing debate. By simulating the energy landscapes under varied chemical potentials, ML-enhanced models could predict which nucleation pathway. Specifically, they could determine if a ZB core, a twinned WZ embryo, or a multi-grain assembly dominates under specific synthesis conditions. This approach bridges the atomistic world of precursor chemistry with the nanoscale world of crystallography, representing the most promising route toward

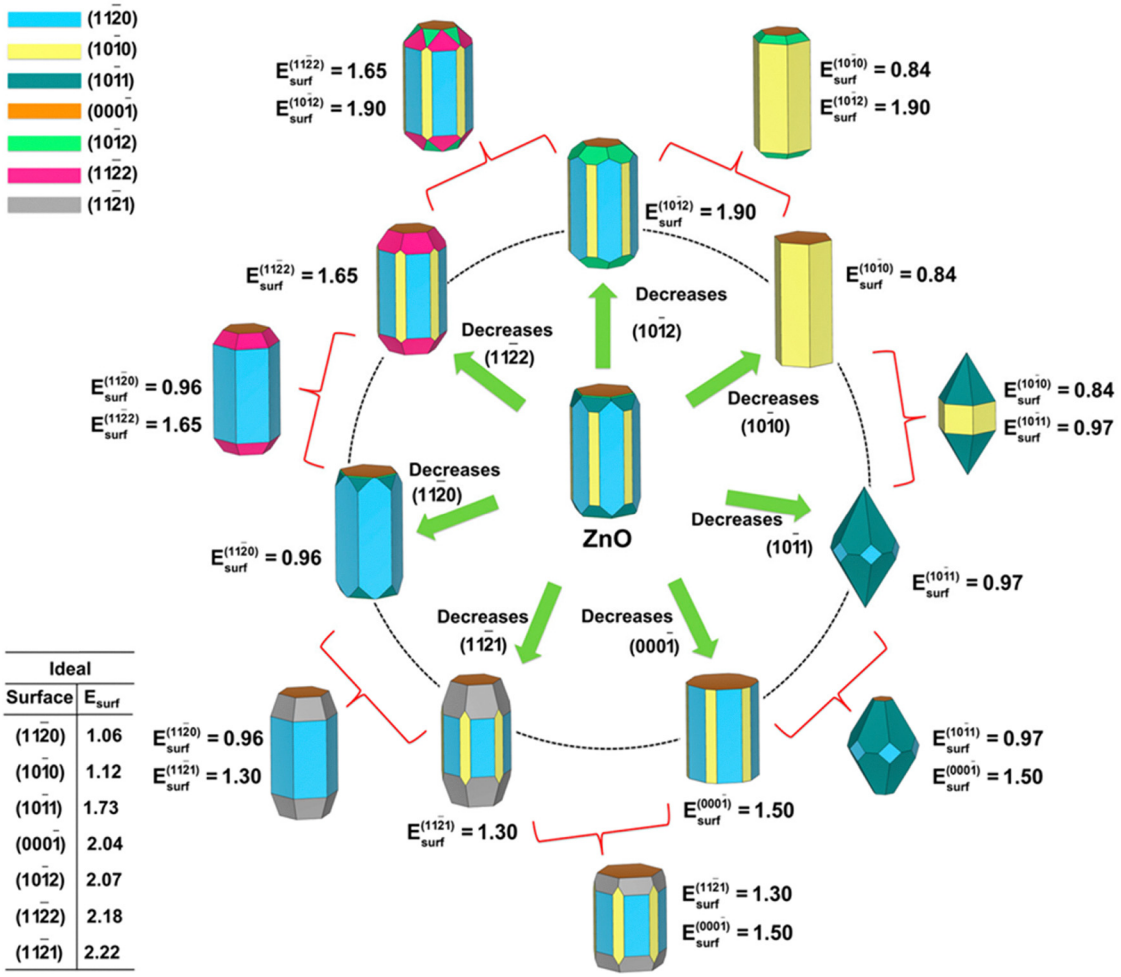

Ideal	
Surface	E_{surf}
(11$\bar{2}$0)	1.06
(10$\bar{1}$0)	1.12
(10$\bar{1}$1)	1.73
(0001)	2.04
(10$\bar{1}$2)	2.07
(11$\bar{2}$2)	2.18
(11$\bar{2}$1)	2.22

Fig. 11 Computational morphology map of wurtzite (WZ) ZnO generated *via* Wulff constructions. The central structure represents the equilibrium morphology based on standard surface energies. The surrounding pathways illustrate how the selective reduction of specific surface energies (*e.g.*, stabilizing the non-polar $\{10\bar{1}0\}$ yellow facets *vs.* the polar {0001} orange facets) drives the morphological transition from compact crystals to elongated prisms or flat plates. Reproduced from ref. 32 with permision from MDPI,[32] Copyright 2023.

a unified, multi-scale understanding that could finally enable the rational, predictive design of T-ZnO morphologies.

2.5 Future frontiers: integrating experiment and theory

The synthesis of T-ZnO is a mature field, yet it remains governed by a fundamental paradox: the remarkable reproducibility of a complex 3D morphology that emerges from a poorly understood, atomistically-contested nucleation event. This review has traced the evolution of this challenge, from the debate over discrete crystallographic models to the practical trade-offs between various synthesis routes. The path forward, however, lies not in finding a single ''winner'' among the historical growth models. Instead, it requires adopting a unified, multi-scale framework. This framework must directly link controllable macroscopic process parameters to the underlying nanoscale physics of nucleation and growth.

The foundation for this framework is now in place. The competition between kinetic and thermodynamic forces, quantified by the Pe and Da_{II}, provides the essential physical language to connect reactor conditions to morphological outcomes. This transport-reaction triad clarifies that complex methods like FTS are not chaotic. Rather, they are governed by definable regimes where the second Damköhler number (Da_{II}) dictates the nucleation locus and the Pe controls the arm extension. Concurrently, the rise of ML-enhanced computational methods provides the predictive engine capable of navigating these vast energy landscapes.

The critical challenge is no longer a lack of plausible theories, but rather the lack of a direct, data-rich feedback loop between synthesis, *in situ* characterization, and predictive simulation. Achieving true synthesis-by-design therefore requires a concerted, three-pronged research initiative. This strategy aims to bridge the gap between macroscopic processing and atomistic control through the following interconnected approaches:

2.5.1 Mapping the parameter space. Future work must utilize automated reactors to generate comprehensive experimental maps. The goal is not merely to optimize yield. Instead, it is to link specific reactor inputs (flow rates, temperature, pressure as detailed in Table 2) to quantitative morphological outputs. This links experimental data directly to their corresponding dimensionless regimes (Da_{II} and Pe). This establishes the ''ground truth'' for predictive models.

2.5.2 Visualizing the nucleation event. While replicating industrial flame conditions inside an electron microscope is unfeasible, two complementary strategies exist to resolve the symmetry-breaking nucleation event:

2.5.2.1 Environmental TEM (ETEM) on model systems. We cannot put a turbulent flame inside a TEM, but we can replicate the chemical potential. By using an ETEM equipped with a specialized micro-electro-mechanical systems (MEMS) heating holder, researchers can replicate the chemical potential of the reactor. This setup allows them to generate the exact same zinc vapor and oxygen supersaturation conditions in a controlled, low-pressure environment. This allows for real-time observation of the crystal's birth, determining if the seed starts as a metastable zinc blende cube, a magic cluster, or a multi-grain assembly, effectively validating the crystallographic pathway without macroscopic turbulence.

2.5.2.2 In situ synchrotron X-ray scattering. To understand the dense, turbulent environments of real-world reactors where electrons cannot penetrate, high-energy synchrotron X-rays (30–100 keV) are required. These hard X-rays can pass through thick reactor walls and flames as if they were transparent. By placing portable flame reactors directly in the beamline, small-angle X-ray scattering (SAXS) can reveal real-time growth rates. Simultaneously, wide-angle X-ray scattering (WAXS) captures the exact millisecond of phase transition from molten Zn to crystalline WZ. This provides kinetic data that ETEM cannot.

2.5.3 Closing the loop with ML. The gap between atomic nucleation and industrial manufacturing is bridged by ML. Data from these *in situ* experiments can train ML models to understand the fundamental constitutive relations of defect formation and growth. These learned physical laws can then be upscaled and embedded into computational fluid dynamics (CFD) simulations of large-scale reactors, enabling the predictive control of macroscopic production based on atomistic insights.

Ultimately, solving the T-ZnO growth puzzle is a model problem for a grander challenge in materials science: the rational design of complex, non-equilibrium 3D nanostructures. The strategies outlined here unite dimensionless physical descriptors with ML-driven simulation and targeted *in situ* validation. They represent a transferable blueprint for moving beyond empirical trial-and-error, guiding the field toward the predictive synthesis of functional materials with unparalleled architectural control.

3 Fundamental properties and structure–property relationships

The scientific relevance of T-ZnO extends beyond its synthesis and arises from the way its distinctive three-dimensional morphology governs and couples a wide range of material properties. Rather than acting as a passive scaffold, the tetrapodal architecture strongly influences how optical, electronic, mechanical, and chemical properties are expressed and interact. Many of the functional characteristics of T-ZnO therefore emerge not from its chemistry alone, but from the combination of intrinsic ZnO properties with geometric confinement, anisotropy, and connectivity across multiple length scales. This section adopts a general, property-centered perspective and aims to clarify how the characteristic architecture of T-ZnO gives rise to coupled physical responses. These couplings are central to understanding why T-ZnO often exhibits behavior that differs markedly from that of simpler ZnO morphologies, such as particles, rods, or films. Understanding these built-in multi-physical interactions is essential for developing rational synthesis strategies. Furthermore, it facilitates the translation of T-ZnO from an empirical material system toward targeted, application-driven design.

To provide a structured framework for these interdependencies, the properties of T-ZnO are discussed hierarchically across three length scales. At the atomic scale, the WZ crystal structure

and the defect landscape define the intrinsic electronic, optical, and piezoelectric properties and their fundamental limits. At the microscale, the single tetrapod geometry introduces additional functionalities, including anisotropic mechanical response, stress concentration, and directional charge transport. At the macroscale, the assembly of tetrapods into interconnected networks leads to emergent properties governed by percolation, porosity, and collective deformation.

Following this hierarchy, the section begins with the crystal structure and defect chemistry of T-ZnO (Section 3.1) and proceeds to discuss its electronic (Section 3.2), optical (Section 3.3), mechanical (Section 3.4), piezoelectric (Section 3.5), and surface chemical properties (Section 3.6). These individual aspects are then brought together in Section 3.7 to highlight overarching structure–property relationships and inherent trade-offs. This integrated view provides the conceptual foundation for the application-oriented discussions in Section 4. To support this multi-scale perspective, Fig. 12 summarizes the key structural and functional domains of T-ZnO and illustrates how atomic-scale characteristics translate into emergent behavior at the network level.

3.1 Crystal structure and defect engineering

The functionality of T-ZnO emerges from the interplay between its macroscopic 3D architecture and atomic-scale imperfections. This section deconstructs the anisotropic WZ arm structure (Section 3.1.1), the structural ambiguity of the central junction (Section 3.1.2), and the resulting intrinsic defect landscape (Section 3.1.3). We then frame defect manipulation as an exercise in applied thermodynamics (Section 3.1.4) and assess the characterization suite required to resolve these features (Section 3.1.5).

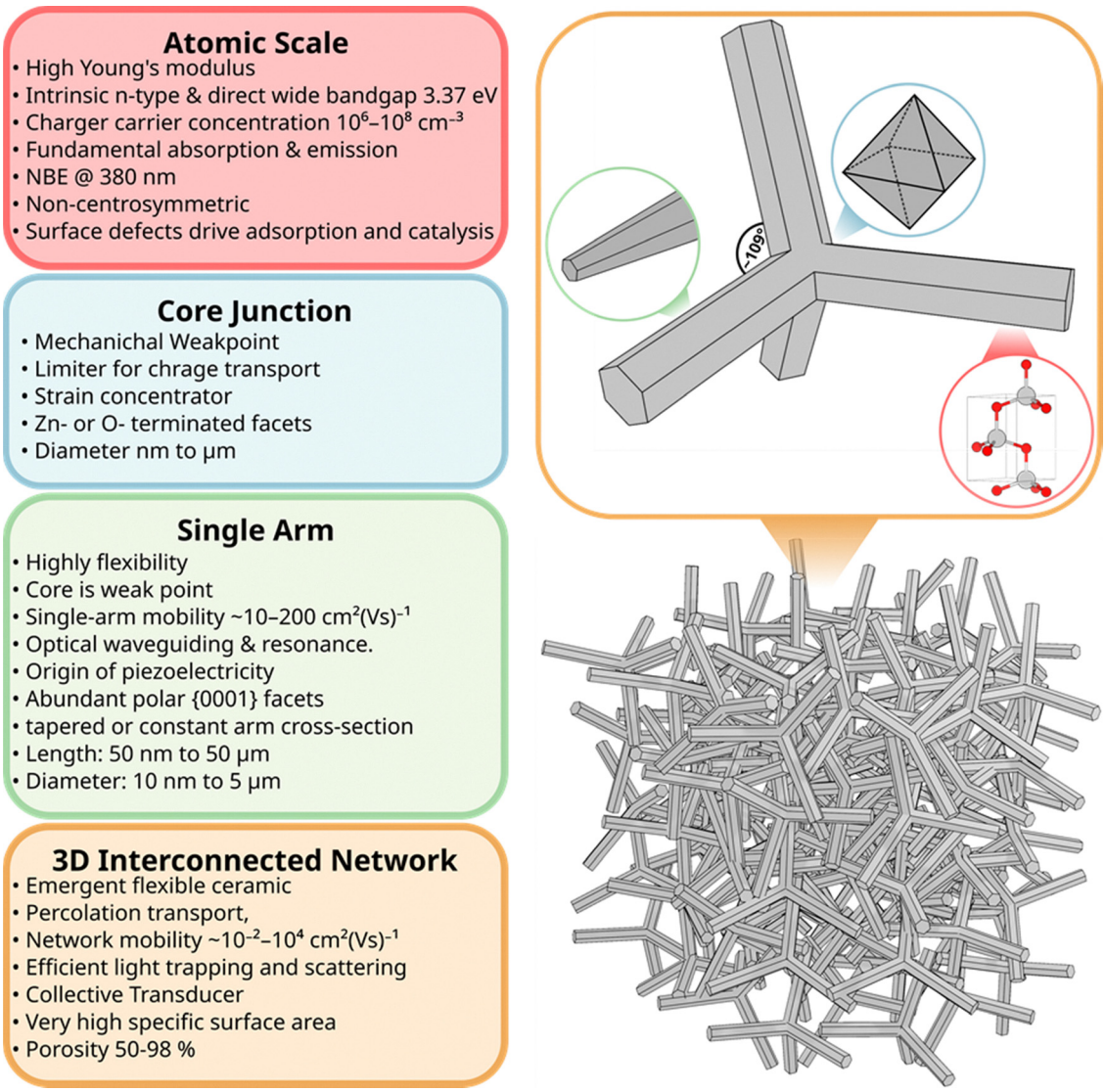

Fig. 12 A schematic overview of the fundamental structural, electrical, optical, mechanical, piezoelectric, and chemical/surface properties of T-ZnO. The central image depicts a typical 3D network of interconnected tetrapods, while the inset highlights the key features of an individual tetrapod, including its core and arm geometry, alongside a WZ unit cell model.

3.1.1 Wurtzite (WZ) structure of arms. Despite divergent theories on the initial nucleus (Section 2.2), there is a consensus that the four extended arms (Fig. 13a–c) consist of the thermodynamically stable hexagonal WZ structure (space group *P*63*mc*).[21,29,36,37,85] The single-crystalline nature of these arms is confirmed *via* X-ray diffraction (XRD), (Fig. 13f),[26,29,38,86,87] Raman spectroscopy (Fig. 13e),[21,37,87–89] and high-resolution imaging (HRTEM/selected area electron diffraction, SAED) (Fig. 13d).[37,38,86] Collectively, these techniques confirm the single-crystalline nature of individual arms.[21,38,86,89] Directional growth along the [0001] *c*-axis is driven by the inherent anisotropy of the WZ unit cell ($a = b = 0.325$ nm and $c = 0.521$ nm).[29,37,38,86,90] During vapor-phase synthesis, kinetic conditions favor rapid deposition on high-energy polar {0001} facets at the arm tips, while suppressing growth on stable, lower-energy non-polar side facets. Beyond simple measurement, subtle XRD-detectable lattice parameter shifts signify lattice strain. This strain, modulated by synthesis parameters like plasma power or intentional alloying (*e.g.*, with titanium[91]), serves as a precision engineering tool.[21,92] By slightly distorting the unit cell, this strain directly modulates the electronic band structure. This provides a mechanism to fine-tune the material's band gap and, consequently, its optical and electronic properties.[29,91,92]

The WZ is inherently non-centrosymmetric due to the tetrahedral coordination of Zn^{2+} and O^{2-} ions.[93,94] This lack of inversion symmetry leads to two primary functional consequences: a net spontaneous polarization along the *c*-direction,[88,95,96] and critically, strong piezoelectric properties.[94,95] This intrinsic electromechanical coupling provides the physical foundation for T-ZnO applications in strain sensing and energy harvesting (Section 3.4). While the arms typically maintain high crystalline perfection,[12,13,29,37,38,86,88,89] they may host planar defects like stacking faults and are often terminated by reactive polar surfaces that act as sinks or sources for point defects.[21,86,88] This relative structural integrity of the arms contrasts sharply with the complex, defect-rich central junction discussed in the following section.

3.1.2 Ambiguity of the central core structure and its functional consequences. While T-ZnO arms consistently exhibit a

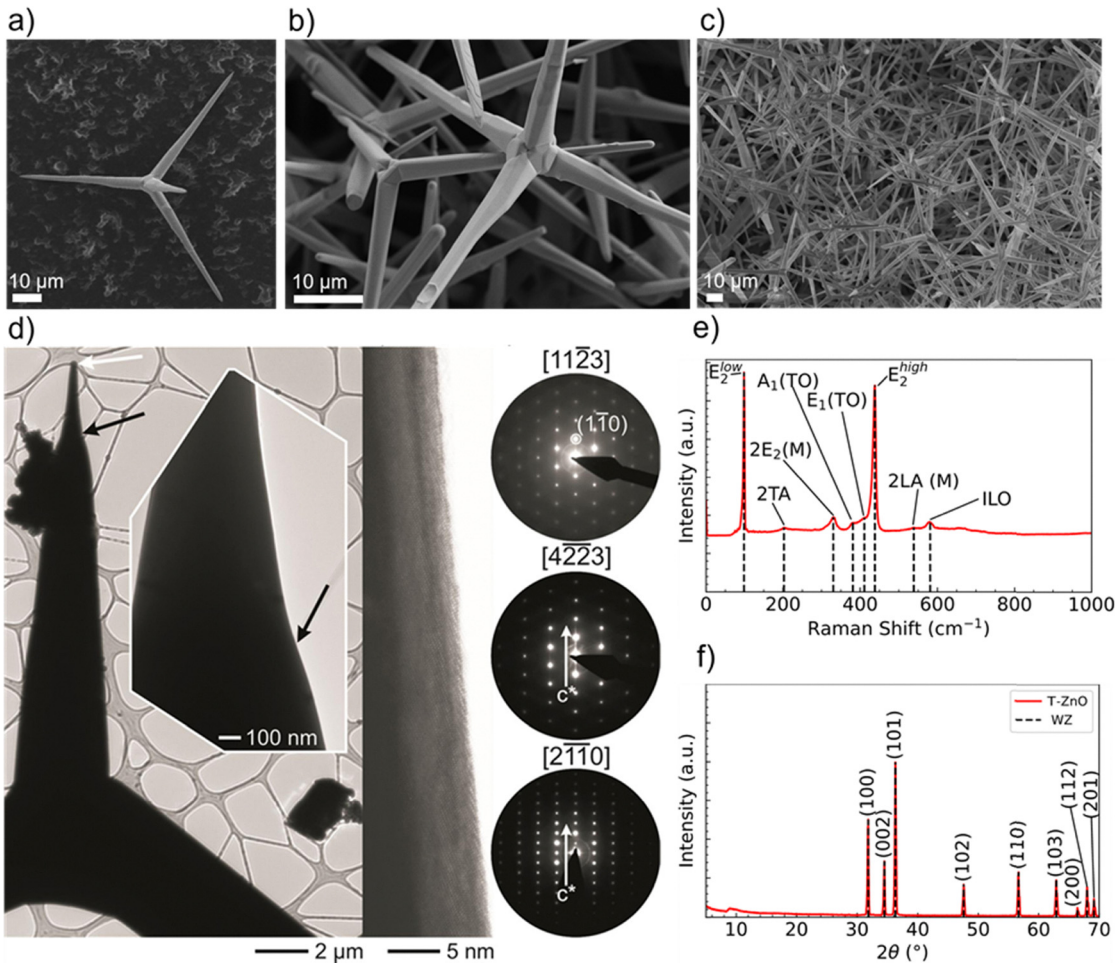

Fig. 13 SEM images of T-ZnO showing its tetrapodal morphology, with (a) a single tetrapod, (b) and (c) in a network at different magnifications. (d) HRTEM and SAED analysis confirming the single-crystalline nature of a T-ZnO arm. A bright-field TEM image, a high-resolution micrograph taken from the arm, revealing the atomic lattice. and a SAED tilting series, which confirms the arm is a single crystal that grew along the *c*-axis. (e) Raman spectrum of T-ZnO and (f) XRD spectrum of T-ZnO synthesized *via* the FTS method. (d) Reproduced from ref. 21 with permision from American Chemical Society,[21] Copyright 2015.

well-defined WZ structure, the atomic arrangement of the central core remains a subject of active debate.[21,37,38,97] This uncertainty stems from the competing growth mechanisms (Section 2.2) and the crystallographic challenge of transitioning from an initial seed to four diverging arms. Two primary hypotheses exist: the first posits a persistent ZB core, as suggested by the epitaxial growth model (model A). This is supported by specific HRTEM observations and theoretical models (Fig. 2b) identifying a cubic phase at the junction center.[11,95,98,99] The second, more widely accepted hypothesis suggests the core is a complex assembly of intricately joined WZ domains, a conclusion shared by the octa-twin nucleus (model B), nucleus transformation (model C), and multi-grain WZ (model D) models. In these scenarios, the final core is composed entirely of WZ domains separated by twin or grain boundaries and associated planar defects.[21,29,38,95]

Defining the T-ZnO core structure is critical, as divergent atomic arrangements produce distinct functional signatures. A persistent ZB core, for instance, would create ZB/WZ polymorphic homojunctions at the arm interfaces. The resulting band offsets likely introduce significant potential energy barriers that act as scattering centers, severely hindering inter-arm charge transport.[12,26,95,97] Conversely, a highly strained, twinned WZ core would serve as a preferential sink for defect accumulation.[21,47,85,97] Local strain fields around twin boundaries can lower the defect formation energy (E^f), driving defects toward the core region.[100] This defect-rich environment influences optical and electronic performance by promoting non-radiative recombination and introducing localized electronic states at internal interfaces[97] (Fig. 14). Furthermore, these defect-laden boundaries function as both mechanical stress concentrators for crack initiation and electronic resistive bottlenecks, ultimately defining the material's failure points and conductivity limits under load.[101]

Beyond electronic and optical effects, the core structure also plays a key role in the mechanical response of T-ZnO. Defect-decorated twin boundaries can serve as stress concentrators and preferential sites for crack initiation under load. Simultaneously, they serve as a resistive bottleneck for charge transport. This dual role inextricably links mechanical deformation to electrical performance. Together, these considerations highlight that the unresolved core structure is a central element in understanding the coupled mechanical, electronic, and optical properties of T-ZnO.[12,21,29,38,85]

3.1.3 The intrinsic defect landscape. While the central core acts as a localized defect "hotspot," the functional properties of T-ZnO are governed by a broader landscape of atomic-scale point defects populating the entire crystal.[12,21,29,36,87,88,97] Rather than being homogeneously distributed, these imperfections form a dynamic and complex defect landscape characterized by spatial heterogeneity and the formation of defect complexes.[92,102,103] The type and concentration of these defects are dictated by the thermodynamic driving forces established during high-temperature, non-equilibrium synthesis (Section 2).[104] This landscape must be understood as a collection of primary point defects and their subsequent higher-order interactions.

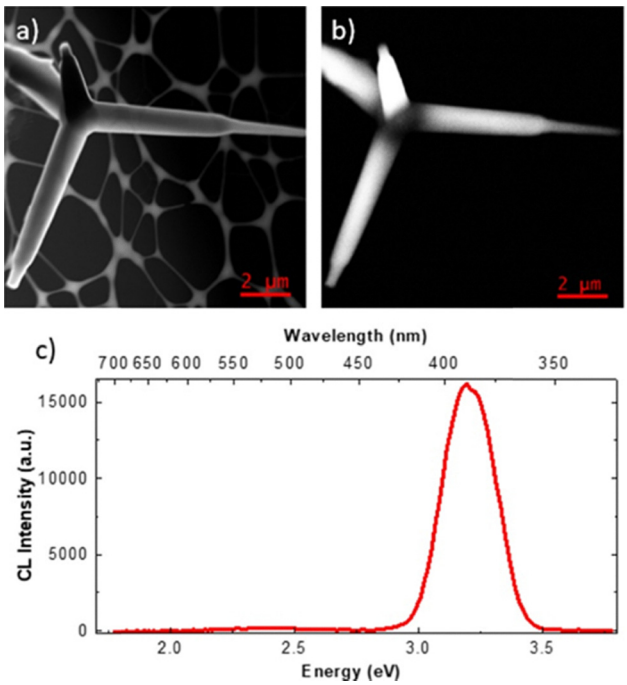

Fig. 14 Correlative analysis of the structural and optical properties of a single T-ZnO particle. (a) High-resolution scanning transmission electron microscopy (STEM) image. (b) Corresponding panchromatic cathodoluminescence (CL) map, showing highly luminescent arms contrasting with a non-luminescent (dark) central junction. (c) Overall CL spectrum from the tetrapod, displaying the dominant UV near-band-edge (NBE) peak (~3.20 eV).[97] (a)–(c) Reproduced from ref. 97 with permision from IOP Science,[97] Copyright 2021.

3.1.3.1 Primary intrinsic point defects. At the heart of T-ZnO's defect landscape are the primary point defects: vacancies, interstitials, and antisites. These defects and their roles will be discussed in the following sections and Table 4 provides a summary of the primary intrinsic point defects of T-ZnO.

Oxygen vacancy (V_O). An oxygen atom missing from its lattice site, is one of the most studied defects in ZnO.[36,92,100,102] While historically and empirically linked to n-type conductivity,[12,13] foundational DFT studies suggest it is a deep donor, making it an unlikely source for the high background carrier concentrations (Fig. 15).[105,106] Instead, it likely functions as a charge compensation center and a primary contributor to visible PL, specifically the green emission "g" band (Fig. 15b), though surface states remain a debated alternative origin.[87,97,107] V_O exists in multiple charge states (V_O^0, V_O^+, V_O^{2+}) contingent on the Fermi level.[29] Its paramagnetic state (V_O^+) is detectable *via* electron paramagnetic resonance (EPR) but is thermodynamically unstable (Fig. 15c).[47,85,105]

Zinc vacancy (V_{Zn}). A zinc atom absent from its lattice site,[36,85,87] the V_{Zn} is an acceptor-type defect,[88,103] which is more likely to form under oxygen-rich conditions. It acts to compensate n-type conductivity and is also linked to visible PL. While often associated with the green luminescence band, sometimes as part of a defect complex, theoretical and

Table 4 The intrinsic defect landscape of ZnO: functional roles and experimental signatures

Defect	Primary functional role	Electronic nature	Favored conditions	Key experimental signature(s)
Oxygen vacancy (V_O)	Charge compensation center; radiative & non-radiative recombination center.	Deep donor[105]	O-deficient (reducing)	Photoluminescence (PL) (green emission, debated); electron paramagnetic resonance (EPR) (for paramagnetic V_O^+); positron annihilation spectroscopy (PAS)
Zinc vacancy (V_{Zn})	Primary compensating acceptor in n-type ZnO.	Deep acceptor[88]	O-rich (oxidizing)	PAS
Zinc interstitial (Zn_i)	Potential source of temporary n-type conductivity; charge compensation center.	Shallow donor (high energy needed to form, limiting its amount)	Zn-rich	PL (violet/blue emission); difficult to detect directly
Oxygen interstitial (O_i)	Compensating deep acceptor.	Deep acceptor[88]	O-rich	PL (yellow/orange/red emission); Difficult to detect directly
Oxygen antisite (O_{Zn})	Likely insignificant due to very high energy needed to form.	Deep acceptor	Extreme lack of zinc or oxygen	No clear signature
Zinc antisite (Zn_O)		Donor		

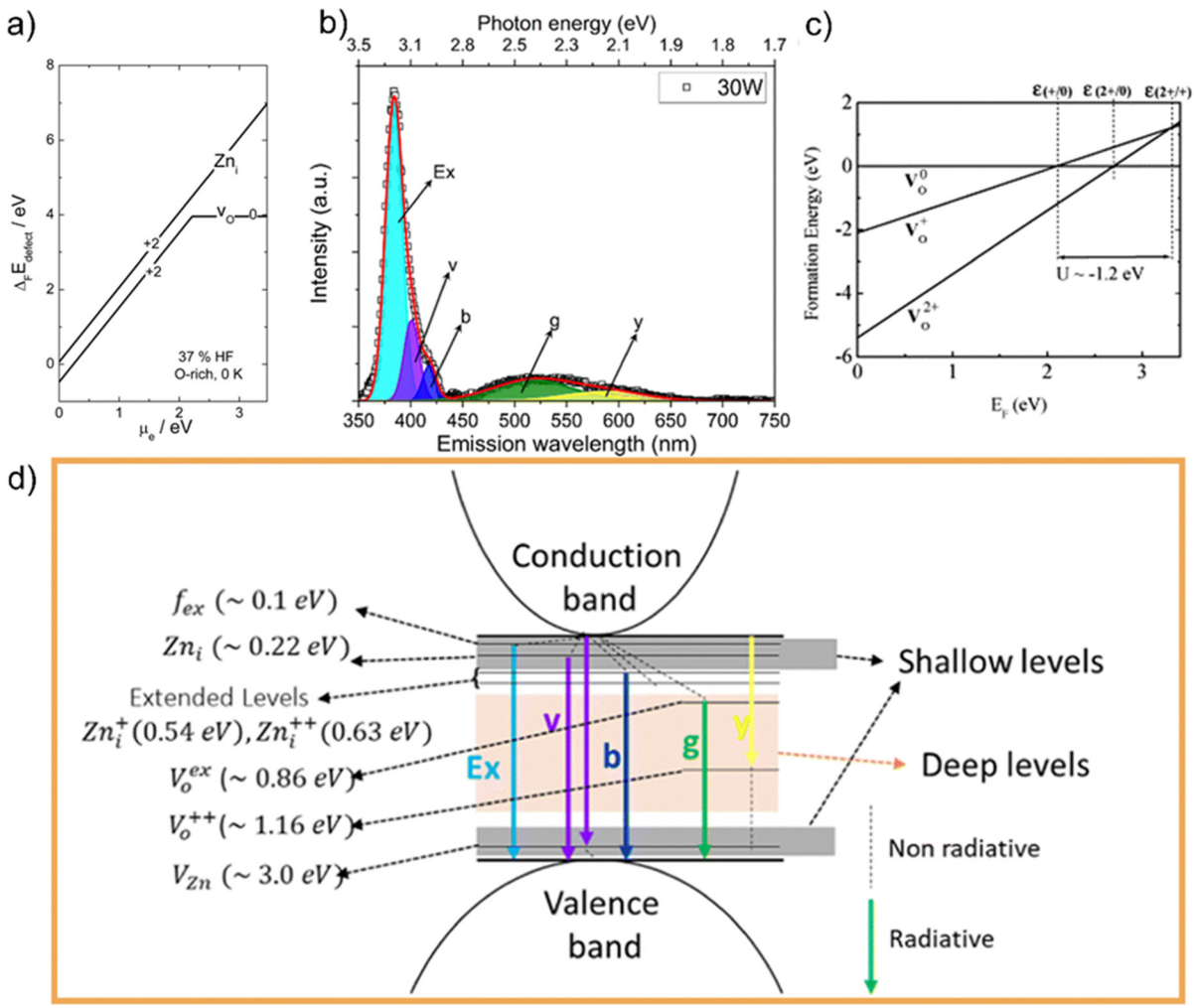

Fig. 15 First-principles calculations of intrinsic defect formation energies (ΔE_F) as a function of the Fermi level (E_F), with the valence band maximum set to 0.0 eV. (a) Comparative plot of the primary donor defects, the oxygen vacancy (V_O) and the zinc interstitial (Zn_i). (b) Representative PL spectrum of ZnO highlighting visible emission bands (green "g" and yellow "y") linked to intrinsic defects. (c) Detailed formation energies of the VO charge states, illustrating its "negative-U" property where the paramagnetic V_O^+ state is thermodynamically unstable. (d) Schematic energy band diagram of the ZnO intrinsic defect landscape, mapping the deep and shallow energy levels and their proposed radiative transitions for UV and visible emissions. (a) Reproduced from ref. 106 with permision from American Chemical Society,[106] Copyright 2014, (b) and (c) reproduced from ref. 105 with permision from Elsevier,[105] Copyright 2001, (d) reproduced from ref. 29 with permision from Royal Chemical Society,[29] Copyright 2024.

experimental studies have also linked it to emissions in the yellow or orange regions.[88]

Zinc interstitial (Zn_i). This occurs when a zinc atom occupies on an interstitial site in the crystal lattice. Zn_i is considered a mobile shallow donor (can donate an electron).[92,106] However, its high E^f limits its concentration under equilibrium, making it an improbable source for stable n-type conductivity.[105] Since neither V_O nor Zn_i are thermodynamically favorable as stable shallow donors, foundational DFT suggests that persistent n-type conductivity originates from extrinsic sources, most notably unintentional hydrogen (H) impurities.[105] Experimentally, Zn_i is often associated with violet/blue PL emissions (*e.g.*, ~420–450 nm).[36]

Oxygen interstitial (O_i). This is when an oxygen atom is in a space where it doesn't belong, often sharing a spot with another oxygen atom (split-interstitial configuration),[103] the O_i is a deep acceptor favored under O-rich conditions.[88,103] Although having a high E^f, it has been identified as a potentially dominant defect in certain electrochemical environments[103] and is linked to yellow, orange, or red PL bands (*e.g.*, a weak red emission around 705 nm).[87,108]

Antisite defects (O_{Zn}, Zn_O). These are defects where one type of atom is on the site of the other (*e.g.*, an oxygen atom on a zinc site). They are generally considered to have very high formation energies, E^f,[26] consequently, they are not expected to be present in significant concentrations under most conditions, and their direct contribution to properties is considered minor.[96]

A schematic of the energy levels for these primary defects and their corresponding radiative transitions is provided in Fig. 15d.

3.1.3.2 Defect complexes: the importance of interactions. Treating defects as isolated entities is an oversimplification; attractive electrostatic and strain-field interactions in the lattice often lead to the formation of defect complexes with electronic and optical signatures distinct from their constituents. Examples include donor–acceptor pairs (Zn_i and V_{Zn}) or vacancy pairs (V_{Zn} and V_O). Although potentially electrically neutral, these complexes function as significant scattering centers that impede carrier mobility and provide unique radiative or non-radiative pathways, such as the ~400 nm PL band, often attributed to Z_{ni}/V_{Zn} pairs.[29]

3.1.3.3 Spatial heterogeneity: a non-uniform defect landscape. Evidence indicates a spatially heterogeneous defect landscape where defects preferentially accumulate in specific regions.[37,47,102,109] The structurally disordered central core acts as a sink for point defects to relieve lattice strain, creating a high-density defect zone that hinders charge transport and initiates mechanical failure. Additionally, defects segregate toward the surfaces and arm tips. Energy dispersive X-ray (EDX) analysis confirms this non-uniformity, showing V_O enrichment at the arm tips and zinc deficiency near the bases (Fig. 16).[47] This thermodynamically driven segregation dictates that the most catalytically and sensorially active sites reside at the arm extremities, a critical factor for device design.

This more detailed picture of an interacting and unevenly distributed "defect landscape" (rather than a simple list of defects) is essential for moving toward a predictive understanding of T-ZnO's properties.

3.1.4 Defect engineering strategies: a thermodynamic approach. Defect engineering, the intentional manipulation of defect type, concentration, and spatial distribution is a primary tool for tailoring T-ZnO's functional properties.[37,91,102–104,109] This process is governed by applied thermodynamics, where the stability of a defect is dictated by its formation energy (E^f). By linking macroscopic processing parameters to these underlying thermodynamic principles, defect populations can be rationally tuned rather than empirically observed.

3.1.4.1 Foundational principles: defect formation energy. Defect concentration in a crystal scales exponentially with the Gibbs free energy of formation, which is dominated at a given temperature by the formation enthalpy, or formation energy (E^f).[106] For a defect D in charge state q, its E^f is not a fixed constant but a variable dependent on the atomic and electronic reservoirs in equilibrium with the host lattice:[103,105]

$$E^f(D^q) = E_{tot}(D^q{:}\text{host}) - E_{tot}(\text{host}) - \sum_i \Delta n_i \mu_i + qE_F \quad (1)$$

In this expression, $E_{tot}(D^q{:}\text{host})$ and $E_{tot}(\text{host})$ are the total energies of the supercell with and without the defect.[103] The

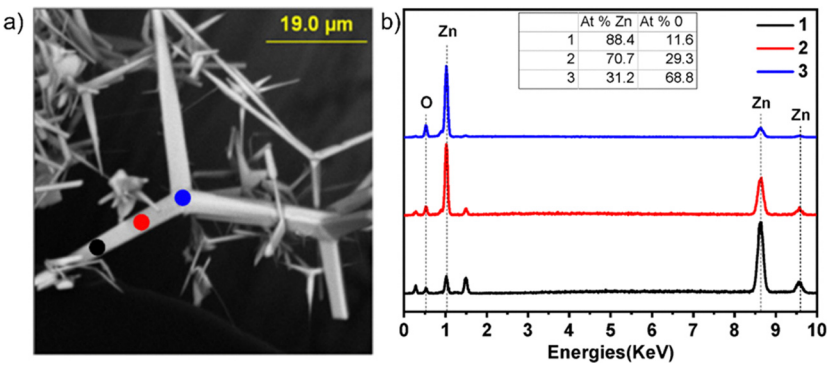

Fig. 16 Spatial defect heterogeneity in T-ZnO. (a) SEM image of a tetrapod indicating the points of EDX analysis: the arm tip (1, black), arm middle (2, red), and base/core (3, blue). (b) Corresponding EDX spectra and inset data table. The elemental quantification highlights an oxygen deficiency at the arm tip (point 1, 11.6% O) and a zinc deficiency near the base (point 3, 31.2% Zn). (a) and (b) Reproduced from ref. 47 with permision from MDPI,[47] Copyright 2023.

term n_i represents the number of atoms of type i added to ($n_i > 0$) or removed from ($n_i < 0$) the crystal to create the defect. Finally, μ_i is the chemical potential of that atomic species.[103] The final term accounts for the energy of exchanging q electrons with the electron reservoir, defined by the Fermi level (E_F), which is typically referenced relative to the valence band maximum.[103,105] For ZnO, the chemical potentials of zinc (μ_{Zn}) and oxygen (μ_O) are thermodynamically coupled by the stability of the ZnO lattice itself:[103]

$$\mu_{Zn} + \mu_O = \Delta H_f(ZnO) \quad (2)$$

This thermodynamic constraint defines the accessible processing window.[103] The chemical potentials μ_{Zn} and μ_O are inversely coupled: conditions that are rich in zinc (high μ_{Zn}) must be poor in oxygen (low μ_O), and *vice versa*. This equation provides a powerful predictive tool. The formation of an V_O serves as a clear example. Creating a V_O requires the removal of one oxygen atom from the lattice, for which $n_O = -1$. Due to the negative sign in front of the summation term in eqn (1), this action results in the μ_O making a positive contribution to the total formation energy. This leads to a direct thermodynamic consequence: lowering the E^f of a V_O requires lowering the μ_O. A low μ_O corresponds to an oxygen-poor environment. This provides the quantitative reason why reducing conditions (*i.e.*, oxygen-poor environments) make the formation of oxygen vacancies thermodynamically more favorable.[103,105]

3.1.4.2 Synthesis-level control of defect chemistry. The most fundamental strategy for defect engineering involves governing native defect chemistry during initial formation by modulating the thermodynamic parameters of the synthesis environment (Section 2).

Vapor-phase methods. In high-temperature routes such as CVD and thermal evaporation, gas-phase partial pressures directly establish the reactor's chemical potentials (μ_{Zn} and μ_O). Zn-rich conditions, achieved with a high Zn/O precursor ratio, establish a high μ_{Zn} and correspondingly low μ_O, thereby lowering $E^f(V_O)$ and $E^f(Z_{ni})$ and promoting the formation of n-type conductivity.[96] Conversely, O-rich conditions lower μ_{Zn} and increase the E^f of these donor defects, while making acceptor-like defects such as the V_{Zn} more stable.[103] The FTS presents a more complex scenario: rapid, localized combustion generates dynamic, non-equilibrium temperature and chemical potential gradients that uniquely shape the defect landscape.[21,37] Such synthesis-level control can yield counter-intuitive results; for example, adding an oxidizing agent (H_2O_2) during vapor-phase synthesis has been shown to paradoxically increase the final oxygen vacancy concentration.[38]

Solution-phase (wet) methods. In low-temperature solution-based synthesis, the chemical potentials are not set by gas pressures but by the concentrations of dissolved precursors, pH, and the stability of complex ions (*e.g.*, $[Zn(NH_3)_4]^{2+}$).[78] The controlled decomposition of these complexes ensures a steady-state flux of growth species, creating a chemical potential regime distinct from vapor-phase equilibrium.

It is crucial to note that while basic DFT studies have established these principle,[105] more recent work highlights the critical role of temperature.[37] High-temperature phonon contributions can significantly alter the Gibbs free energy of formation, particularly for V_O, thereby shifting the thermodynamic equilibrium and relative defect concentrations predicted by calculations at absolute zero (0 K) alone.[106]

3.1.4.3 Post-synthesis treatments: thermodynamic re-equilibration and surface modification. Post-synthesis treatments allow for the precise modification of T-ZnO defect populations through bulk thermodynamic re-equilibration or direct surface engineering.[47,110–113]

Atmosphere-controlled annealing. Thermal annealing is a primary method for re-equilibrating bulk defect populations under controlled thermodynamic conditions.[106] By exposing the material to specific atmospheres and temperatures, the external chemical potentials drive point defect diffusion and reaction toward a new equilibrium.[103] For example, annealing in O_2 or air raises the μ_O, which in turn increases the E^f of V_O and can facilitate their annihilation.[103,105] This is experimentally observed as a suppression of the defect-related green PL.[88] Li and Seebauer[104] validated this principle by demonstrating that the surface potential, a direct proxy for the near-surface defect population, could be precisely and reversibly tuned simply by controlling temperature and the external oxygen partial pressure. Their work confirms that the macroscopic environment dictates the microscopic defect thermodynamics.[103,106]

However, this equilibrium is governed by the competition between chemical enthalpy and thermal entropy. While moderate temperatures favor oxidation, annealing at extremes (*e.g.*, >1000C) can paradoxically increase oxygen vacancy concentrations, even in oxidizing atmospheres.[96,114] At these temperatures, the entropic driving force (ΔS) for lattice disorder overrides the chemical potential of the atmosphere; upon rapid cooling, these high-temperature vacancy populations are "frozen in," resulting in the oxygen-deficient surfaces characteristic of high-temperature processing.[96,114]

Energetic surface modification. Beyond thermal routes, post-synthesis UV irradiation provides a non-contact method to engineer surface defects. UV exposure can trigger a reversible switch from hydrophobic to hydrophilic wettability, which ESR and XPS correlate directly with an increased surface concentration of oxygen vacancies.[47]

Surface passivation and heterostructures. Surface engineering focuses on passivating active sites or constructing heterostructures to define functional properties. Surface passivation neutralizes electronic states that act as non-radiative recombination centers, often *via* conformal organic or inorganic coatings.[107] For instance, (3-aminopropyl)triethoxysilane (APTES) has been utilized to passivate surface traps, confirmed by shifts in defect-related PL (Fig. 17) and carrier dynamics evaluated through time-resolved PL (TRPL).[89,101,107]

Alternatively, the T-ZnO network can serve as a high-surface-area scaffold for core–shell heterostructure growth.[85,87,88,97,107,115] Sequential dipping procedures have been used to grow complex shells, such as ZnSe/CdSe/ZnSe, onto T-ZnO templates.[89] This

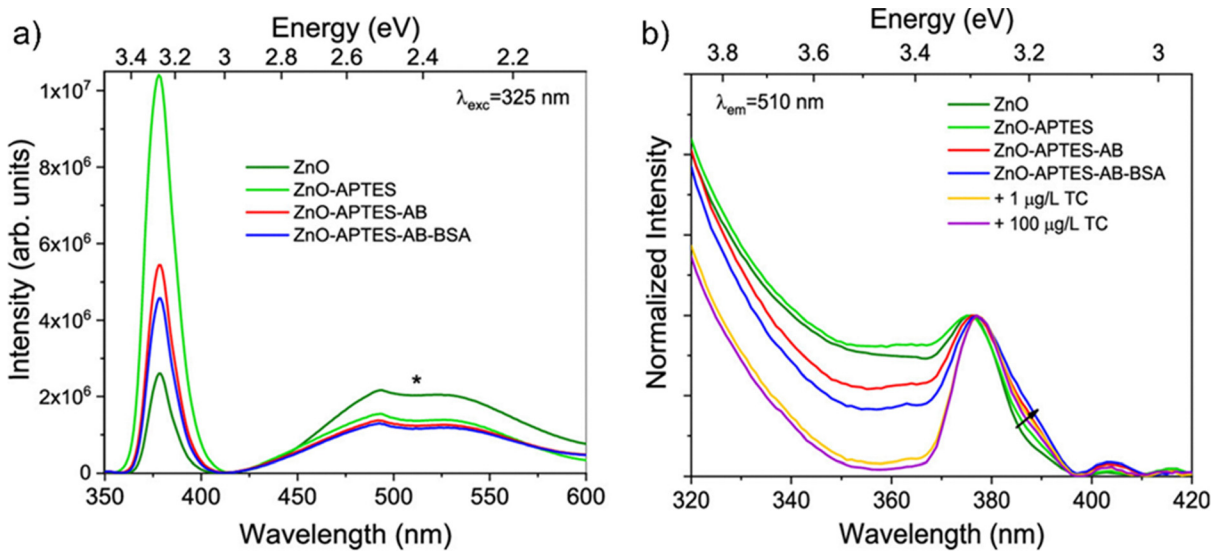

Fig. 17 Optical signatures of surface defect passivation. (a) PL spectra of bare ZnO (dark green) and APTES-passivated ZnO (light green), highlighting the relative intensities of the near-band-edge (NBE, ~378 nm) and defect-related deep-level emission (DLE, ~510 nm) bands. (b) Photoluminescence excitation (PLE) spectra showing a tail of states (arrow) associated with the surface defect landscape before and after functionalization. (a) and (b) Reproduced from ref. 107 with permision from American Chemical Society,[107] Copyright 2022.

enables the engineering of tailored band alignments to optimize charge separation for photovoltaics or to achieve wavelength-specific optical emissions by creating entirely new electronic interfaces.

3.1.4.4 Extrinsic doping. Extrinsic doping overrides native defect chemistry to precisely manipulate the thermodynamic landscape of T-ZnO by shifting the Fermi level (E_F) and modifying the local atomic environment.[91,100,109]

Fermi level and carrier control. Strategic shifting of E_F allows for precise conductivity control, though outcomes differ significantly between n-type and p-type regimes.[91]

• N-type doping: reliable n-type conductivity is achieved using group III elements (Ga, Al, In) as substitutional donors for Zn. These elements substitute for Zn and act as shallow donors, increasing the electron concentration and making the material suitable for applications like transparent conductive oxides (TCOs).[87,88]

• P-type doping: in contrast, achieving stable and reproducible p-type ZnO remains a major challenge.[88,116] Nitrogen is the most explored p-type dopant, aiming to substitute for oxygen and act as a shallow acceptor, pushing E_F towards the valence band.[13,90,105] However, as the E_F is reduced, the E^f of native donor defects like the V_O, decreases dramatically. This triggers the spontaneous formation of donors that counteract the intended acceptor levels, pinning E_F and hindering p-type stability.[105] Efforts to overcome this hurdle include nitrogen doping *via* urea solid-state reactions[109] or ammonia-flow nitridation,[90] alongside co-doping strategies with Fe, Cu, or Al to mitigate compensation effects.[87]

Modification of host energetics and reactivity. Beyond electronic control, dopants alter the host lattice's chemical reactivity by modifying local strain and bonding environments. Pala and Metiu[100] systematically demonstrated that substituting surface Zn with lower-valency cations (*e.g.*, Li^+, Ag^+) induces an "electron deficit," significantly reducing the Oxygen Vacancy Formation Energy (OVFE). This reduction increases lattice oxygen reactivity, enhancing oxidative catalytic power. Conversely, dopants that form stronger oxygen bonds (*e.g.*, Al^{3+}, Ti^{4+}) elevate the OVFE, rendering the oxide more stable and less reactive. This provides a predictive link between dopant chemistry and the thermodynamic stability of native surface defects.

These multifaceted strategies are consolidated in Table 5, which serves as a "control panel" linking functional goals to thermodynamic principles and experimental levers.

3.1.5 Characterization techniques for structure and defects. Resolving the interplay between T-ZnO's 3D morphology, crystal structure, and defect landscape necessitates a multi-modal characterization framework spanning the angstrom to micron scales.[87–89,97] While individual tools (summarized in Table 6) are powerful, they frequently lack the resolution to establish direct structure-function causality.

The contentious interpretation of PL spectroscopy illustrates this challenge. Although PL is a standard defect probe, attributing specific signals, particularly the ubiquitous green luminescence, exclusively to V_O remains highly debated.[87,88,107] Conflicting data exist, with some models linking V_O to red emission bands,[26] while others implicate surface states or adsorbed species.[36,104,107] Furthermore, photoluminescence excitation (PLE) spectroscopy reveals a complex near the band edge, providing electronic signatures of surface functionalization that PL alone cannot resolve.[107] Consequently, bulk PL measurements remain insufficient for definitive defect identification.[47,87,88] To achieve predictive control, the field must advance through two primary strategies:

(1) Correlative microscopy: future defect identification relies on multi-modal analysis performed on individual

Table 5 The defect engineering control panel for T-ZnO. Strategic overview, linking desired functional goals to thermodynamic principles, experimental actions, and essential verification methods for T-ZnO defect engineering

Desired functional goal	Thermodynamic lever	Experimental action	Verification method
Increase n-type conductivity	Decrease formation energy (E^f) of native donors (V_O, Zn_i)	Synthesis: use Zn-rich precursors. Post-synthesis: anneal in reducing atmosphere (*e.g.*, H_2/Ar).	Electrical: four-point probe. Spectroscopic: PL shows an increased NBE/DLE ratio.
Suppress defect-related PL (green luminescence)	Increase formation energy (E^f) of VO	Post-synthesis: anneal in oxidizing atmosphere (*e.g.*, O_2/air) at moderate temperatures (<800 °C).	Optical: PL spectroscopy shows a suppressed green emission peak.
Achieve p-type conductivity	Decrease E^f of acceptors (*e.g.*, N_O (N on O site)) while managing self-compensation	Doping: introduce nitrogen dopants (*e.g.*, *via* NH_3 anneal) potentially with co-dopants.	Electrical: hall effect measurement showing positive Hall coefficient.
Enhance oxidative catalytic activity	Decrease oxygen vacancy formation energy (OVFE) at the surface	Doping: introduce lower-valency dopants (*e.g.*, Li^+, Ag^+) to create an "electron deficit."	Chemical: catalytic performance testing (*e.g.*, CO oxidation). Surface: XPS analysis.
Passivate surface recombination centers	Neutralize electronically active surface states	Post-synthesis: apply a conformal surface coating (*e.g.*, APTES, Al_2O_3).	Optical: time-resolved PL shows an increased carrier lifetime.

Table 6 A strategic guide to characterizing the hierarchical structure and defects of T-ZnO

Technique	Scale of information	Primary application	Key limitations & things to note
Scanning electron microscopy (SEM)	Micro- to macro-scale	Visualizing overall morphology, network connectivity, and porosity.	Provides no information on crystal structure or atomic-scale defects.
Transmission electron microscopy (TEM)/high-resolution TEM (HRTEM)/selected area electron diffraction (SAED)	Nano- to atomic-scale	Confirming that arms are single crystals (SAED); Seeing the atomic lattice and planar defects (HRTEM).	Local probe: extremely small sampling volume; requires destructive preparation; difficult to obtain statistically relevant data.
X-ray diffraction (XRD)	Bulk/large area	Confirming the primary crystal phase (wurtzite) and phase purity; measuring average lattice strain.	Averaging: provides no information on local heterogeneity (*e.g.*, core *vs.* arm) or point defects.
Raman spectroscopy	Bulk/large area	Evaluating overall crystal quality and lattice vibrational modes; detecting local strain and disorder.	Interpretation of defect-induced modes can be complex; often requires low temperature for clear resolution.
Photoluminescence (PL) spectroscopy	Bulk/large area	Evaluating overall optical quality (near-band-edge/deep-level emission (NBE/DLE) ratio); investigating the presence of deep-level electronic states.	Highly debated interpretation: the origin of the visible deep-level emission (*e.g.*, green luminescence) is controversial. It is often attributed to V_O, but contributions from V_{Zn} and surface states are widely argued in literature. Cannot identify specific defects in isolation.
Electron paramagnetic resonance (EPR) spectroscopy	Bulk/large area	Clearly identifying specific paramagnetic defects, such as the singly-ionized oxygen vacancy (V_O^+).	Selective: only sensitive to defects with unpaired spins; "silent" to neutral or fully ionized defects V_O^{2+}
X-ray photoelectron spectroscopy (XPS)	Surface ($\sim$2–10 nm)	Quantifying surface elemental composition and chemical states (*e.g.*, distinguishing lattice O from hydroxyls).	Surface only: provides no information about the bulk crystal; requires ultra-high vacuum (UHV).
Conductive atomic force microscopy (c-AFM)	Nanoscale (surface)	Mapping local conductivity across surfaces and junctions; quantifying the electronic barrier height of individual T-ZnO-to-T-ZnO contacts.	Mainly a surface probe; does not provide simultaneous atomic-level structural information of the underlying junction.
In situ TEM with nano-probes	Nanoscale (single junction)	Directly correlating the atomic structure of a specific junction (*e.g.*, degree of sintering) with its measured current–voltage (*I–V*) characteristics.	Technically demanding: high risk of beam damage or contact resistance artifacts; represents the most advanced single-junction characterization.

nanostructures.[21,38,47,85,86,97,107] Applying HRTEM for atomic structure,[38,86] Electron energy loss spectroscopy (EELS) for local chemistry, and CL for emission mapping,[47,97] to the exact same tetrapod eliminates the ambiguity of ensemble averaging. This suite must incorporate spatially resolved spectroscopy; for example, EPR can distinguish V_O^+ populations at the T-ZnO core ($g = 1.962$) v from those at the surface ($g = 1.998$).[85] Additionally, ultraviolet photoemission spectroscopy (UPS) is essential for measuring Fermi levels and constructing precise band alignments in core–shell heterostructures.[89] This approach, combining high-resolution imaging like HRTEM and CL[38,47,86,97] with advanced electronic and chemical-state mapping (EELS, UPS, EPR), would create a clear connection between a directly observed atomic-scale feature (*e.g.*, a specific twin boundary or defect cluster) and its measured optical and electronic properties, eliminating the uncertainty found in measurements that average over a large sample.

(2) *In situ* and *operando* characterization: moving beyond static snapshots to real-time observation is critical for understanding T-ZnO dynamics. ETEM offers the potential to visualize

nucleation events during synthesis and track defect migration under controlled thermal or atmospheric loads.[12,104] Furthermore, operando measurements allow for monitoring structural changes within operating devices. These techniques are essential to resolve long-standing structural questions, such as the precise atomic arrangement of the central core, and to provide the experimental evidence required for the rational design of T-ZnO properties.

3.2 Electronic and transport properties

The intrinsic semiconducting nature of the WZ unit cell forms the foundation of T-ZnO's electronic behavior, yet the overall conductivity is shaped by a hierarchy of multi-scale effects. At the atomic level, point defects such as vacancies and interstitials introduce donor and trap states that modulate carrier concentration and mobility. At the nanoscale, surface defects and arm-tip states influence local charge distribution and depletion layers, affecting transport along individual arms. The central core, typically rich in defects, can act as a resistive bottleneck, limiting inter-arm conduction. Finally, at the macroscale, the connectivity and percolation of tetrapods within the network govern the global transport properties, as even well-conducting arms are constrained by junctions and network topology. Understanding this multi-level interplay is key to interpreting T-ZnO's electronic behavior and guiding the rational design of functional devices.

3.2.1 The semiconducting nature of ZnO. As a direct, wide-bandgap semiconductor crystallizing in the WZ structure (Section 3.1.1), ZnO possesses intrinsic electronic properties defined by two critical parameters. These parameters govern the material's performance in optoelectronics but simultaneously impose fundamental physical constraints.

1. The wide bandgap: at room temperature, ZnO's bandgap of approximately 3.37 eV[52] (which increases to ~3.44 eV at low temperatures[96]). This wide gap ensures high optical transparency and renders the material ideal for UV-regime applications, including photodetectors and light-emitting diodes (LEDs).[29,48,86,88,90,92,111,117–119] However, the wide bandgap is also the primary barrier to stable p-type doping; it favors the formation of deep rather than shallow acceptor levels and creates a thermodynamic drive for the spontaneous formation of compensating native donor defects (Section 3.2.2).

2. The exciton binding energy trade-off: ZnO possesses an exceptionally large exciton binding energy of 60 meV,[13,29,88,92,111,118,120–122] significantly exceeding the room-temperature thermal energy (~26 meV). While this stability facilitates efficient radiative recombination for light-emitting devices (Section 3.3.2), it complicates light-harvesting and detection mechanisms. Photogenerated electron–hole pairs tend to remain as bound, neutral excitons rather than free carriers. To generate a measurable photocurrent (Fig. 18), these excitons must be dissociated, a process requiring high internal or external electric fields to overcome the associated energy barrier.[37] Consequently, this requirement can limit the conversion efficiency of ZnO-based photodetectors and photovoltaic cells.

3.2.2 Origin of n-type conductivity. Undoped ZnO characteristically exhibits residual n-type conductivity, as confirmed by Seebeck measurements[123–125] and Mott–Schottky analysis.[90] For decades, this behavior was conventionally attributed to the spontaneous formation of native donor defects, primarily V_O and Zn_i, during growth under oxygen-deficient conditions.[85,96,126] However, this long-held view has been largely superseded by foundational first-principles calculations. Ground-breaking DFT studies demonstrated that these native defects are energetically unfavorable as sources of high carrier concentrations.[105] These calculations revealed that the V_O is a deep donor[123] (its energy level is too far from the conduction band to be an effective source of free electrons) while the Zn_i has a high E^f, making it unlikely to form in sufficient quantities to explain the observed conductivity.

The modern consensus, strongly supported by this computational work. It points to the unintentional incorporation of hydrogen impurities as the primary source of ZnO's intrinsic n-type behavior.[103,105] Ubiquitous in growth environments, hydrogen acts as a robust shallow donor in ZnO, occupying interstitial or substitutional sites (Fig. 19). Despite this shift, native defects remain critical as charge-compensating entities.[85] The thermodynamic framework established in Section 3.1.4

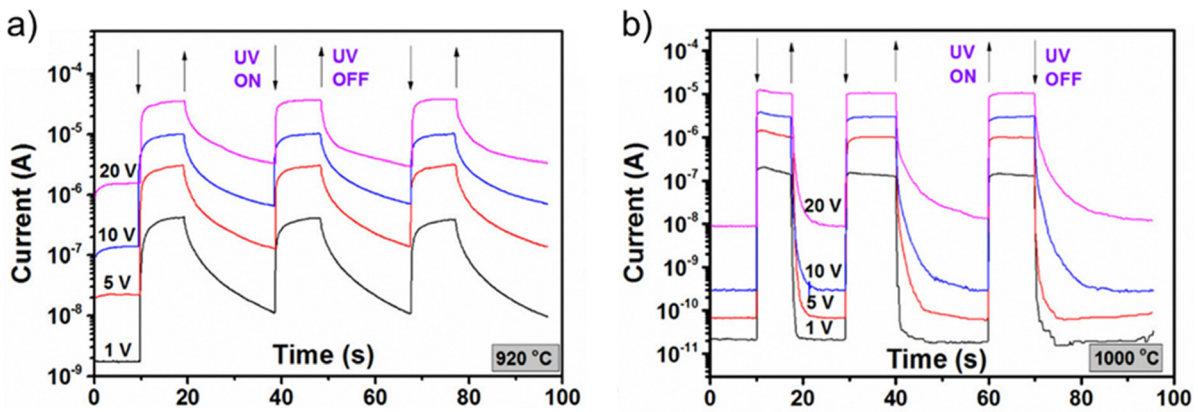

Fig. 18 Dynamic photocurrent response to UV light for T-ZnO networks synthesized at (a) 920 °C and (b) 1000 °C. The 920 °C sample exhibits a slow response with persistent photocurrent, whereas the 1000 °C sample demonstrates a fast, reversible on/off response. (a) and (b) Reproduced from ref. 37 with permision from American Chemical Society,[37] Copyright 2025.

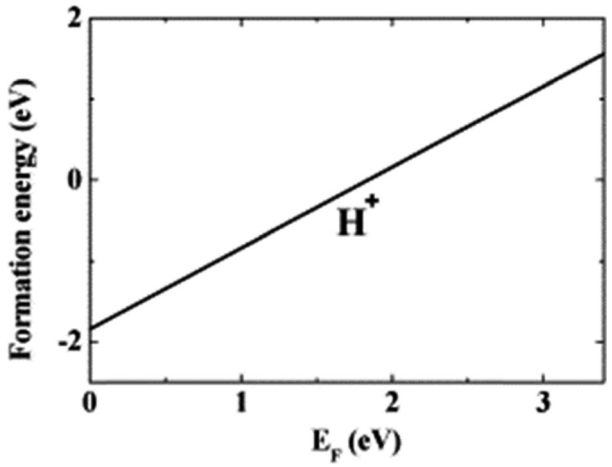

Fig. 19 Calculated formation energy (E^f) of hydrogen (H) in ZnO as a function of the Fermi level (E_F), with the valence band maximum (EV) set to 0.0 eV and the conduction band minimum (EC) at ~3.37 eV. The plot demonstrates that hydrogen exists exclusively in the positive charge state (H^+), as the neutral (H^0) and negative (H^-) charge states remain thermodynamically unstable across the entire bandgap. Reproduced from ref. 105 with permision from Elsevier,[105] Copyright 2001.

shows that their formation energies are strongly dependent on the E_F. Any attempt to make the material p-type (*e.g.*, by nitrogen doping) lowers the E_F, which in turn dramatically lowers the E^f of these native donors.[103] This triggers the spontaneous formation of donors that neutralize introduced acceptors, a self-compensation mechanism that remains the fundamental barrier to stable p-type ZnO.[88,96,116]

Ultimately, the carrier concentration in T-ZnO is a multifaceted function of its synthesis and processing history. Concentrations vary with intrinsic defect density, notably low in FTS T- products,[102] intentional doping, and post-treatment conditions.[87] Furthermore, secondary factors such as alloying,[87] which can widen the bandgap,[91] or the presence of extended defects like dislocations that can act as electron traps and scattering centers, thereby reducing carrier mobility, can also influence the overall electronic behavior.[47,125]

3.2.3 Charge transport dynamics. Efficient charge transport in T-ZnO is not governed by a single factor but emerges from a hierarchy of resistive bottlenecks across multiple length scales. Understanding these constraints is essential for the rational design of high-performance architecture-centric electronics.

3.2.3.1 Bottlenecks of the electronic pathway

The ideal single-crystalline arm. At the most fundamental level, each arm of a T-ZnO tetrapod is a single-crystalline WZ structure. In an ideal, bulk crystal of this quality, electron mobility would be high, naturally limited only by phonon scattering at room temperature.[125,127,128] This highly crystalline arm represents the intrinsic limit of conductivity, a low-resistance pathway relative to the network architecture. In practice, however, this ideal pathway is immediately compromised by a series of bottlenecks, which effectively degrade this performance long before the macroscopic scale is reached (Fig. 20).

Bottleneck I (nanoscale): surface scattering and pinch-off. The first major degradation to this ideal transport occurs at the nanoscale. In arms with small diameters (<100 nm), the high surface-to-volume ratio means that surface scattering from charged defect states[88,107] and physical surface roughness becomes a dominant limiting factor, significantly reducing the effective mobility compared to bulk ZnO.[104,107] This effect is physically governed by the Debye length (L_D), which defines the width of the surface depletion region caused by trapped charge at surface states.[52,86,104] This principle leads to a critical design constraint known as the "pinch-off" effect (Fig. 20a): as the arm diameter is reduced to twice the L_D ($d \sim 2L_D$), these depletion regions can merge and deplete the entire arm of free carriers, making it highly resistive.[37]

Bottleneck II (single tetrapod): the central core junction. The second bottleneck impedes transport within a single tetrapod. As detailed in Section 3.1.2, the structurally complex and often defect-rich central core, which contains a high density of defects and misfit stresses from its complex growth, acts as a potent scattering center (Fig. 20b). Direct impedance spectroscopy by Huh *et al.*[129] further demonstrate that this junction region contributes disproportionately to the overall electrical resistance of a ZnO tetrapod. Although its volume fraction is small, the junction exhibits a higher local resistance than the WZ arms, thereby dominating the total resistance pathway, shown by

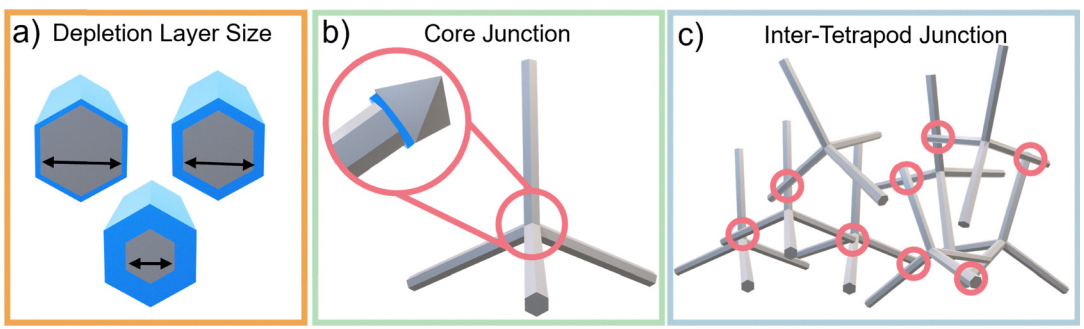

Fig. 20 Schematic of the hierarchical charge transport bottlenecks in T-ZnO. (a) The nanoscale bottleneck: surface depletion layers (blue) and the "pinch-off" effect in thinner arms. (b) The microscale bottleneck: the defect-rich central core junction impeding intra-tetrapod charge flow. (c) The macroscale bottleneck: inter-tetrapod junctions (red circles) acting as the dominant resistive barriers across the macroscopic network.

Fig. 21. This junction introduces significant potential energy barriers[52] that hinder the efficient flow of charge from one arm to another, directly impacting the measured I-V characteristics of individual tetrapods and manifesting in techniques like intensity modulated photocurrent spectroscopy (IMPS).[89]

Bottleneck III (the network): the dominant inter-tetrapod junction. While nanoscale effects and the core structure influence transport, experimental evidence indicates that the dominant bottleneck in any macroscopic T-ZnO assembly arises at the T-ZnO-to-T-ZnO junctions (Fig. 20c).[87,121] Conduction across the 3D network relies on these inter-tetrapod contacts, which provide multiple interconnected pathways.[13,88,95,121,124] This has shown to improve carrier collection in devices such as solar cells and sensors when compared to nanoparticle films.[13] However, for high-mobility electronics, transport is ultimately limited by the high resistance at these junctions.[87,121]

This bottleneck can be understood by modeling the junction as a nanoscale grain boundary.[96] irst, the cross-sectional area of the junction is typically much smaller than that of a single tetrapod arm, limiting the available conduction pathway. Second, electronic defect states at the interface trap charges, creating a plane of fixed negative charge that further hinders electron flow. This charge repels mobile electrons in the adjacent arms, resulting in two opposing depletion zones at the junction. The resulting potential profile is commonly described as a double Schottky barrier (DSB).[130] This explains the experimentally observed low effective mobility of T-ZnO networks, which remains far below the mobility of a single, defect-free arm.

3.2.3.2 Junction engineering: targeting the dominant bottleneck. The hierarchical analysis of transport dynamics dictates that while all bottlenecks influence performance, enhancing macroscopic conductivity necessitates targeting the dominant inter-tetrapod junction. This "junction engineering" *via* post-synthesis modification is established as a critical strategy for optimizing network-level transport properties.[87] Mitigation of the junction barrier is primarily pursued through two complementary paradigms:

1. Geometric modification *via* sintering: thermal annealing at high temperatures promotes stronger interconnections between tetrapods. This geometric solution increases the physical cross-sectional area for current flow, thereby directly reducing the junction resistance.

2. Electronic modification *via* passivation: surface passivation offers a chemical/electronic solution. By coating the T-ZnO network with a suitable passivating layer, it is possible to chemically neutralize the electronic trap states at the grain boundary facilitating more efficient charge transport.

The fundamental divergence in transport physics between an isolated, single-crystalline arm and the macroscopic assembly is central to T-ZnO electronics. These scale-dependent distinctions, which define the hierarchy of transport bottlenecks, are summarized in Fig. 22. Resolving the junction-limited nature of these networks remains the prerequisite for the full realization of T-ZnO-based electronic and optoelectronic architectures.

3.2.4 Band structure engineering: a thermodynamic perspective. The electronic band structure of T-ZnO can be precisely engineered through alloying and doping to modulate both the bandgap and carrier concentration. Modern strategies must be framed within the thermodynamic context established in Section 3.1.4, as any lattice modification intrinsically alters the formation energies of native defects. This principle underpins the two primary approaches to band structure engineering:

3.2.4.1 Alloying: tuning the bandgap at a thermodynamic cost. Alloying ZnO with isovalent elements provides a direct method for bandgap tuning. Introducing magnesium (forming $Mg_xZn_{1-x}O$) widens the bandgap towards the deep-UV, while alloying with cadmium (forming $Cd_xZn_{1-x}O$) narrows it towards the visible region.[96] This allows for precise tailoring of the material's spectral response for applications like wavelength-selective photodetectors or solar cells. However, this engineering comes at a thermodynamic cost. Alloying alters the host lattice parameters and chemical bond energies, which in turn modifies the E^f of native point defects. For instance, theoretical studies have shown that in MgZnO alloys, the E^f of key compensating donor defects, like the V_O, can be even lower than in pure ZnO under certain conditions.[103] This exacerbates the material's intrinsic tendency to self-compensate, making the already difficult challenge of achieving p-type conductivity even more challenging in these wide-bandgap alloys.

3.2.4.2 Doping: a thermodynamic competition. Doping with aliovalent elements is primarily used to control carrier concentration by shifting the E_f,[105] which leads to the following two scenarios:

- N-type doping: this is a thermodynamically straightforward process. Doping with group III elements like gallium (Ga) or aluminum (Al) introduces shallow donor states that readily

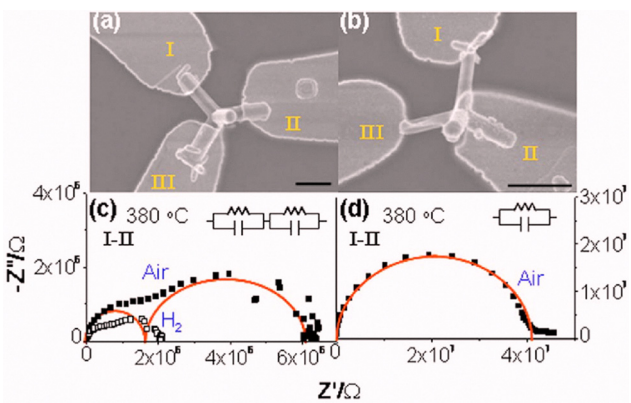

Fig. 21 The SEM images of (a) two T-ZnO arms measured in series with the T-ZnO core and (b) only one contacted T-ZnO arm. The impedance spectra measured from (c) of the setup shown in (a) and (d) of setup shown in (b), respectively, at 380 °C under air (solid squares). Also included in (c) is the impedance spectrum measured under hydrogen at 380 °C (open squares). The scale bars shown in (a) and (b) indicate 1 micrometer. (a)–(d) Reproduced from ref. 129 with permision from AIP Publishing,[129] Copyright 2008.

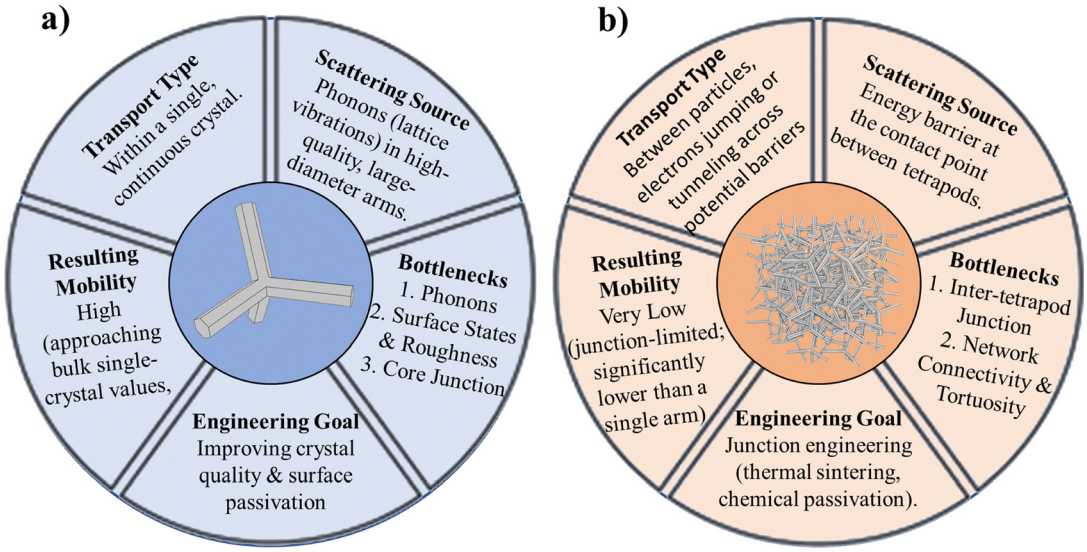

Fig. 22 A comparison of charge transport types and engineering targets in T-ZnO. (a) The single T-ZnO particle, (b) the interconnected T-ZnO network.

ionize, reliably increasing the n-type conductivity for applications like TCOs.[88]

• P-type doping: in contrast, p-type doping is a thermodynamic competition. The goal of introducing acceptors, such as nitrogen substituting for oxygen, is to lower the E_F towards the valence band.[96] However, as E_F moves lower, the E^f of native donor defects (like V_O) decreases dramatically, as determined by the qE^F term in the formation energy equation (eqn (1)). The material responds to the introduction of acceptors by spontaneously forming these low-energy donor defects to counteract them. This powerful self-compensation mechanism, predicted by first-principles thermodynamics,[105] is the fundamental reason why achieving stable p-type ZnO remains a major challenge (Fig. 23).[88,90,96,131] This illustrates that doping is not simply a matter of adding impurities but a battle against the intrinsic thermodynamic tendencies of the host crystal.

3.2.5 The critical link: bridging the junction gap. While T-ZnO's intrinsic electronic properties are defined by its WZ structure and defect chemistry (Section 3.1), macroscopic transport is ultimately dictated by morphological bottlenecks. The inter-tetrapod junction represents the primary constraint on network mobility; however, much of the current physical

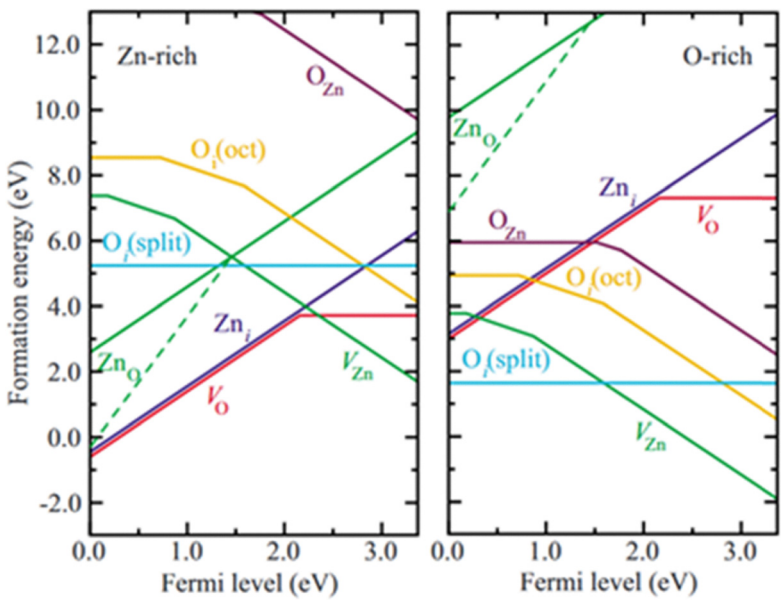

Fig. 23 Calculated formation energies (E^f) of native point defects in ZnO as a function of the Fermi level (E_F) under (left) Zn-rich and (right) O-rich conditions. The Fermi level is referenced to the valence band maximum, 0.0 eV. Solid lines represent the most thermodynamically stable charge state for a given defect, where the slope indicates the specific charge state and the kinks denote thermodynamic transition levels. Reproduced from ref. 131 with permision from American Physical Society,[131] Copyright 2007.

Table 7 T-ZnO electronic transport: from challenge to engineering target

Core electronic challenge	Conventional view (past)	Modern consensus (present)	Engineering imperative (future)	T-ZnO specific implication
Undoped n-type conductivity	Native defects (V_O, Zn_i) act as primary donors.	Hydrogen impurities: unintentional H-incorporation is the dominant shallow donor; native defects act as compensators.	Impurity control: mitigate H-incorporation for high-purity applications, or exploit it for robust n-type transparent conductors.	Doping baseline: defines the carrier concentration floor for T-ZnO networks; shifts focus from vacancy control to hydrogen management.
P-type doping difficulty	High formation energy of acceptors; low solubility.	Self-compensation: lowering the Fermi level (E_F) spontaneously lowers the formation energy of native donors, which neutralize acceptors.	Fermi level engineering: develop co-doping or non-equilibrium strategies to kinetically suppress compensating donor formation.	Device limitation: hinders T-ZnO p–n homojunctions; limits applications to unipolar (n-type) or heterojunction devices.
Wide bandgap/ exciton energy	Stable UV emission; optical transparency.	Recombination trade-off: high exciton binding energy ($\sim$60 meV) favors emission but reduces free carrier generation for photocurrents.	Field management: integrate strong internal fields to dissociate excitons (for PV/detectors) or enhance confinement (for LEDs).	Surface dominance: high surface-to-volume ratio of T-ZnO arms exacerbates surface recombination, competing with intrinsic bulk emission.
Macroscopic charge transport	Modeled as a simple resistor network.	Junction dominated: transport is limited by a hierarchy of bottlenecks: inter-tetrapod DSBs > core impedance > surface scattering.	Junction engineering: direct modification of the barrier (sintering, chemical passivation) and characterization *via* c-AFM/*in situ* TEM.	The critical bottleneck: network mobility is decoupled from crystal quality; high-performance requires solving the junction bottleneck.

understanding is derived from indirect bulk measurements. Resolving the discrepancy between single-particle potential and network-level performance is the ''grand challenge'' of the field. Transitioning from empirical optimization to rational design necessitates direct nanoscale characterization. Advanced techniques, including conductive atomic force microscopy (c-AFM) and *in situ* TEM, are critical for quantifying local barrier heights and the electronic structure of individual T-ZnO-to-T-ZnO contacts.

Table 7 consolidates this multi-scale perspective, contrasting historical paradigms with the modern consensus to identify critical engineering targets. This synthesis illustrates the interplay between intrinsic semiconducting behavior, the hierarchy of transport bottlenecks, and the thermodynamic boundaries of band engineering.

3.3 Optical properties

Building upon the understanding of T-ZnO's electronic structure, this section delves into its equally crucial optical properties. The unique functionality of T-ZnO arises from a complex, multi-scale interaction with light. This section deconstructs this hierarchy, beginning with the intrinsic absorption and emission processes dictated by the atomic-scale electronic structure. It then explores the primary strategies used to engineer these core properties, such as bandgap tuning and hybridization. From there, the discussion moves to the resonant cavity effects governed by the nano- to microscale arm geometry and finally explores the network-level light scattering that emerges at the macroscale. This framework provides a cohesive story of how T-ZnO's structure engineers its interaction with light from the quantum to the macroscopic level.

3.3.1 Intrinsic absorption and photoluminescence (PL). The core process of T-ZnO's optical response lies at the atomic scale, where its electronic structure and defect chemistry determine the fundamental processes of photon absorption and energy conversion. This section explores these two key processes in detail.

3.3.1.1 Absorption. The primary optical absorption feature of T-ZnO is a sharp UV absorption edge below 400 nm.[29,48,52,89,90,120,132–134] This is defined by a strong excitonic absorption peak often observed between 370–390 nm (Fig. 15b).[26,29,52,86,89,90,119,120,132] With absorption coefficients exceeding10^5 cm^{-1},[89] this peak corresponds to the fundamental, direct bandgap transition from the O_2p-derived valence band to the Zn_{4s}-derived conduction band.[88,93] This intrinsic UV sensitivity is critical for applications like photocatalysis, where absorbed photons generate the electron–hole pairs necessary for redox reactions,[86,90,110–113,133,135,136] and for UV photodetectors.[48,52,86,97,120,121]

While pristine ZnO primarily absorbs in the UV, defects (Section 3.1.3) introduce mid-gap electronic states that facilitate sub-bandgap absorption.[90,109] This allows limited, but functionally important photocatalytic activity under visible light,[13,47,87,90,109,135,137] although this is often insufficient for high-efficiency applications without further engineering.[88,90]

3.3.1.2 Photoluminescence (PL). PL serves as a critical diagnostic for evaluating T-ZnO quality and its defect landscape. T-ZnO typically exhibits two competing emission channels (representative spectrum in Fig. 24).

(I) UV near-band-edge (NBE) emission: this is a sharp, intense emission band observed near 380–390 nm at room temperature.[36,107,132,135] Driven by ZnO's high exciton binding energy (Section 3.2.1), it originates from the radiative recombination of excitons. The NBE is a composite of transitions involving free excitons and excitons bound to neutral donors

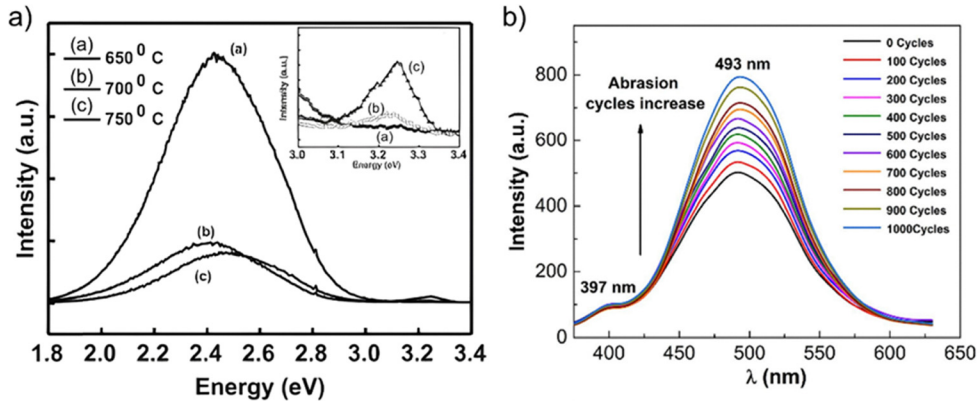

Fig. 24 PL spectra of T-ZnO illustrating the competition between the UV near-band-edge (NBE) and green deep-level emission (DLE) bands. (a) Spectra as a function of growth temperature, demonstrating the relative suppression of the green DLE and dominance of the NBE emission at higher temperatures. (b) Spectra as a function of mechanical abrasion, showing the proportional increase of the green DLE peak (~493 nm) alongside a stable UV NBE peak (~397 nm). (a) Reproduced from ref. 92 with permision from Elsevier,[92] Copyright 2015, (b) reproduced from ref. 135 with permision from Elsevier,[135] Copyright 2022.

(D^0X) or acceptors (A^0X).[29,87,88,105,137–139] A dominant NBE signal is the hallmark of high crystalline perfection and low defect density.[29,88,97,107,132,134,138–140] Under high excitation densities, this excitonic recombination can enable optically pumped UV lasing.[122]

(II) Deep-level emission (DLE): a broad emission band typically spanning the green-yellow-orange region (~500–650 nm) and frequently centered at ~510 nm.[107,132,135,137,141] This band represents an inefficient "energy leak," where energy is lost through light-producing transitions involving deep-level electronic states.[29,88,105,107,132,135,137,142] These include the point defects (V_O and Zn_i), and complexes described in Section 3.1.3, as well as extrinsic impurities (Cu, Li, N).[87,88,96,106,107,134,135,139,142]

The green luminescence debate: the origin of the prominent green luminescence (GL) band (~500–550 nm) is particularly widely debated.[87,88,134,137,143] The debate is polarized between two primary viewpoints: the intrinsic bulk defect model and the surface state model. A critical comparison of the evidence reveals why consensus remains elusive, and there are two viewpoints:

Viewpoint 1: the oxygen vacancy (V_O) model. This classic model attributes GL to the recombination of a photogenerated hole with an electron trapped at a singly ionized V_O (V_O^+) deep within the bulk lattice.[144] Experimentally, GL intensity often increases in samples synthesized under reducing (oxygen-poor) conditions, which thermodynamically favors V_O formation. EPR studies have frequently shown a correlation between GL intensity and the $g \sim 1.96$ signal attributed to paramagnetic defects.[145,146] Foundational DFT calculations indicate that the formation energy of VO is high in n-type ZnO[147] and that its thermodynamic transition levels do not perfectly align with the green spectral emission, casting doubt on it being the *sole* origin.

Viewpoint 2: the surface state model. This model suggests that GL originates from electron transitions involving surface-adsorbed species (*e.g.*, –OH groups) or surface vacancies/dangling bonds, rather than bulk defects. The high surface-to-volume ratio of T-ZnO makes surface effects dominant.[148] Strong evidence comes from size-dependent studies where GL intensity scales with surface area.[148] Crucially, surface passivation experiments (*e.g.*, coating with polymers)[149] often quench the GL band without altering the bulk crystal, directly implicating the surface as the emission source. This model struggles to explain why GL is observed in large, bulk-like single crystals where surface contributions should be negligible.[150]

While frequently associated with defects such as the V_O or surface imperfection,[92,97,107,132,135,140] compelling evidence from time-resolved PL and CL studies suggests that surface-adsorbed species or complex surface oxygen dynamics may also be responsible.[87,88,96,104] This ongoing uncertainty highlights the necessity of the advanced correlative microscopy techniques proposed in Section 3.1.5 to create a definite link between atomic structure and optical signature.

3.3.1.3 Photoluminescence as a diagnostic tool. The relative intensities, peak positions, and lifetimes of the NBE and DLE bands are highly sensitive to synthesis conditions (Fig. 24a), defect concentrations (Fig. 24b), and even spatial location on the tetrapod structure.[26,29,87,97,135,137–139,143,151] This makes PL a valuable diagnostic tool, allowing researchers to assess the properties of T-ZnO and its performance in several key ways:

Assessing quality: the ratio of the NBE to DLE intensity (NBE/DLE) serves as a key qualitative metric for material quality, where a higher ratio generally indicates a lower density of non-radiative defect pathways and often correlates with higher photocatalytic or photoelectrochemical efficiency.[36,92,152]

Probing charge transfer: TRPL is a powerful technique for studying charge transfer dynamics. In hybrid systems, the quenching of PL intensity is a direct indicator of efficient charge transfer from the ZnO to an attached molecule or nanoparticle (Fig. 25), signifying reduced recombination and improved device performance.[89,97,107,132,134]

Overall, the PL spectrum provides a rich fingerprint of T-ZnO's internal workings, revealing both its ideal performance (NBE) and its efficiency losses (DLE). While its use for identifying

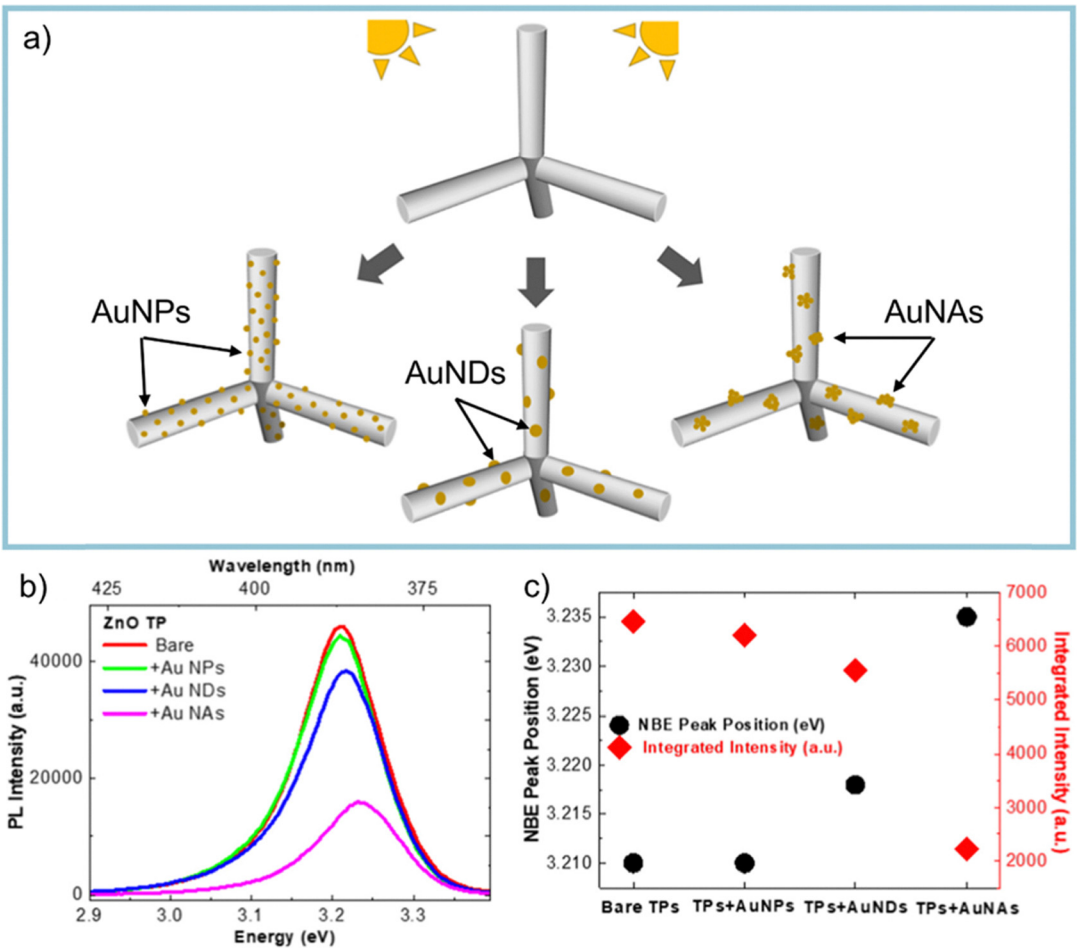

Fig. 25 PL quenching in T-ZnO/Au hybrid systems. (a) Schematic illustrating the *in situ* photochemical growth of various gold nanostructures, nanoparticles (AuNPs), nano-domes (AuNDs), and nanoparticle aggregates (AuNAs), onto the T-ZnO scaffold. (b) Comparative PL spectra demonstrating the progressive quenching of the near-band-edge (NBE) emission of bare T-ZnO upon hybridization. (c) Quantification of the integrated NBE intensity drop as a function of the Au nanostructure morphology. (a-c) Reproduced from ref. 97 with permision from IOP Science,[97] Copyright 2021.

specific defects is filled with uncertainty, its role as a comprehensive diagnostic for material quality and charge transfer dynamics is essential. To provide a detailed reference for these various emission bands and their debated origins, the key PL signatures are summarized and critically assessed in Table 8.

3.3.2 Engineering optical absorption: bandgap tuning and hybridization. Overcoming the intrinsic limitations of T-ZnO, specifically its negligible visible light absorption, requires targeted engineering through two primary paradigms: bandgap modulation and hybridization.

3.3.2.1 Bandgap and absorption tuning. The precise optical bandgap and absorption characteristics of T-ZnO can be intentionally modified through several routes. At the nanoscale, quantum confinement in smaller nanostructures can induce a blue-shift in the absorption edge, effectively widening the bandgap.[86,89,96] Variations in lattice strain (Section 3.1.1), controlled during synthesis, can also subtly tune the bandgap.[29] More powerfully, doping with elements like nitrogen can introduce mid-gap states that narrow the effective bandgap and extend the material's absorption response into the visible region (Fig. 26a),[88,90,109,154] a chemical and structural modification confirmed by XPS and Raman spectroscopy (Fig. 26b and c).[90] This is a key strategy for developing visible-light-driven photocatalysts and photodetectors. Conversely, surface engineering can be used to passivate the ZnO surface and intentionally suppress its intrinsic photo-activity. Applying conformal coatings like polydimethylsiloxane (PDMS) or diamond-like carbon has been shown to hinder ZnO's photocatalytic response or prevent UV-induced wettability changes, which is crucial for applications where long-term stability is required.[119,155]

3.3.2.2 Hybridization for visible light harvesting. Hybridization leverages the high surface-to-volume ratio and ultra-porous topology of the T-ZnO network (Section 3.6.1) to create intimate interfaces with sensitizing materials.[88,93,109] These heterostructures bypass intrinsic absorption limits through three main strategies:

- Quantum dots (QDs): to create type-II heterojunctions that facilitate efficient charge separation after light absorption in the QD.[89]
- Plasmonic nanoparticles: noble metals like Ag or Au[97,140] are used to leverage localized surface plasmon resonance (LSPR). The intense, localized electromagnetic fields generated

Table 8 An analytical guide to the competing radiative channels in T-ZnO

Radiative channel	Emission	Approx. wavelength (nm)	Proposed origin	Diagnostic significance & impact on efficiency
Primary excitonic channel (efficient pathway)	NBE (UV)	~375–385	Excitonic recombination (*e.g.*, FX, D^0X);[88,92,107,132,139] exciton–exciton collision[26,36,137]	A key metric of crystal quality; a high NBE/DLE ratio indicates low defect density.[92,151,152] Its intensity also measures energy transfer at interfaces in hybrid system.[140]
Secondary defect channels (loss pathways)	Violet/blue	~400–450	Zn_i-related transitions; possibly Zn_i–V_{Zn} pairs[29,36]	Indicates the presence of interstitial-type donor defects.
	Green	~490–550	Highly debated: V_O is the common proposal, but surface states and other defects are also candidate.[85,87,88,92,107,132,135,137,153]	Represents a primary "energy leak." While its origin is ambiguous, its presence signifies a high density of deep-level traps that reduce overall quantum efficiency.[105,107,135,137,151,153]
	Yellow/orange	~550–650	O_i; V_{Zn}-related complexes,[88] V_O[29]	Indicates the presence of deep acceptor-type defects or complexes, another energy-loss pathway.
	Red	~640–710	V_O or O_i states; N-doping.[26,88,137]	Can be a signature of specific processing conditions (*e.g.*, excess oxygen) or intentional doping.

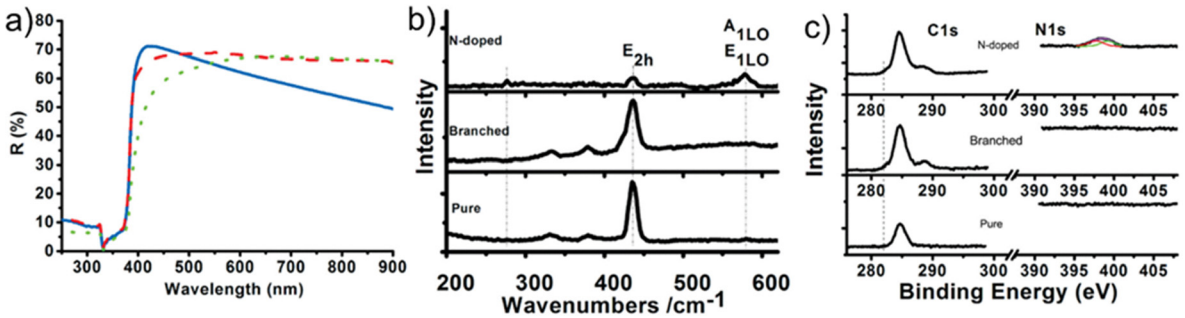

Fig. 26 Spectroscopic evidence for nitrogen doping in T-ZnO and its effect on optical absorption. (a) Diffuse reflectance spectra comparing pure T-ZnO (blue) and N-doped T-ZnO (green), highlighting a sub-bandgap absorption tail in the visible region (~400–650 nm) for the doped sample. (b) Raman spectra showing the emergence of a new defect-related peak (~275 cm^{-1}) and the suppression of the primary ZnO (E2h) mode in the N-doped sample. (c) XPS spectra displaying the N 1s peak (inset) in the N-doped sample, which is absent in pure T-ZnO. (a)–(c) Reproduced from ref. 90 with permision from American Chemical Society,[90] Copyright 2012.

by the LSPR dramatically enhance light absorption in the adjacent ZnO. The processes efficiency is highly sensitive to the size and morphology of the nanoparticles.[97,140]

• Carbon materials, dyes, and polymers: heterostructures with carbon-based materials like graphene oxid,[119,132,134,143] polymers[135] are formed to create junctions that promote charge separation and extend spectral absorption.

Hybrid systems, which increase the visible light harvesting of T-ZnO, utilize a diverse toolkit of physical mechanisms to overcome its intrinsic limitation.[47] These include LSPR-induced near-field enhancement[97,140] and better charge separation across Schottky barriers (for metal-ZnO hybrids[97]) or semiconductor heterojunctions.[87–89,97,133,134] The effectiveness of the charge separation processes can be seen for example *via* the quenching of CL (Fig. 27), which provides direct proof of energy transfer from the T-ZnO to the plasmonic sensitize.[140] This can also be studied in detail using TRPL.[89,137]

Such engineered absorption properties are pivotal for advancing applications in photocatalysis,[13,21,88,132–135,137] Surface-enhanced Raman spectroscopy (SERS),[133] and visible-light photodetectors.[86]

3.3.3 Nanoscale resonant cavity effects. At the nano- to microscale, the precise hexagonal transverse geometry of individual T-ZnO arms enables them to function as high-performance optical waveguides and resonant microcavities.[137,142,151] A primary consequence of this geometry is the emergence of whispering gallery modes (WGMs).[137–139] These modes occur when light, typically generated *via* internal PL, becomes trapped by sequential total internal reflection against the arm's optically smooth facets. This circular confinement induces constructive interference at specific resonant wavelengths, manifesting as sharp, periodic peaks that modulate the broad UV-NBE emission spectrum (Fig. 28I).[138,139,142] This phenomenon serves as a rigorous functional "quality check" for T-ZnO, as resonance is hypersensitive to structural integrity:

• Surface roughness: any significant roughness on the crystal facets will scatter light out of the resonant cavity, preventing mode formation or dramatically lowering the quality factor (*Q*-factor).[139,142,151]

• Crystalline defects: internal defects can act as non-radiative recombination or absorption centers, increasing optical losses and destroying the resonance.[142]

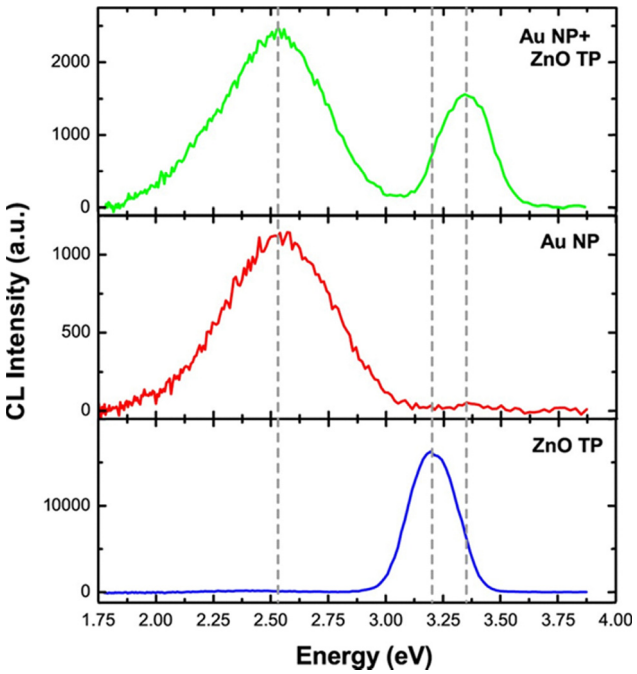

Fig. 27 Cathodoluminescence (CL) spectra of a T-ZnO/Au plasmonic hybrid. The spectrum of the bare T-ZnO (blue) shows a dominant UV near-band-edge (NBE) emission (~3.3 eV). In the Au NP/ZnO hybrid (green), this UV emission is quenched (~10×), while the Au localized surface plasmon resonance (LSPR) emission peak (~2.4 eV) is simultaneously enhanced. Reproduced from ref. 140 with permision from Springer Nature,[140] Copyright 2016.

Consequently, the experimental observation of high-finesse WGM peaks validates a synthesis process's ability to yield near-perfect, defect-minimized crystal facets, linking the advanced optics of T-ZnO directly to the precision growth methods detailed in Section 2.[142,151] In exceptionally high-purity arms, the strong coupling regime between confined WGM photons and intrinsic excitons facilitates the formation of hybrid light-matter quasiparticles known as exciton-polaritons.[138,139] This state is characterized by a distinctive anti-crossing in the polariton dispersion curve (Fig. 28II), signaling a structurally and electronically pristine system capable of supporting stable excitons. Beyond linear interactions, the non-centrosymmetric wurtzite lattice enables nonlinear phenomena, such as second-harmonic WGMs within the T-ZnO legs.[156] These advanced optical properties position T-ZnO-based resonators as promising candidates for polariton-based lasers, UV emitters with tunable decay dynamics,[138,139] and ultrasensitive optical biosensors,[142,151] all of which require a high degree of structural perfection.

3.3.4 Macroscale light scattering and trapping. While individual arms function as nanoscale waveguides, the assembly of interconnected tetrapods into a complex, porous framework gives rise to emergent macroscopic optical phenomena.[29,52,88–90,109,119,120,132,143] At this hierarchical level, light interaction shifts from intra-arm confinement to collective scattering and trapping within the 3D network topology. This macroscale light manipulation serves as a primary engineering lever for maximizing the efficiency of light-driven architectures.

3.3.4.1 The mechanism of light trapping. The physical origin of this behavior lies in the material's hierarchical architecture, where micron-scale tetrapods and high porosity create a spatially varying refractive index landscape. This network functions as a three-dimensional array of scattering centers where Mie scattering dominates photon dynamics.[119] This process randomizes photon trajectories, inducing a "light trapping" effect wherein incident photons are constrained to tortuous paths.[7,143] Consequently, the effective optical path length is dramatically increased, significantly boosting the probability of photon-material interaction and absorption.[7,13,143] This trapping effect significantly boosts the probability that the photon will be absorbed.[48] The functional implications include:

- Enhanced light harvesting: in devices like DSSCs, this light trapping leads to an increase in light harvesting efficiency.[90,154]
- Improved photocatalysis: for photocatalysis, the increased photon absorption probability directly leads to a higher rate of electron–hole pair generation, improving the overall reaction efficiency.[137,143]

3.3.4.2 Architectural synergy and signal amplification. The magnitude of this scattering can be so intense that the network's effective scattering cross-section exceeds the material's intrinsic absorption coefficient by an order of magnitude across broad spectral ranges.[47,143] Crucially, a synergy exists between macroscale scattering and the atomic-scale defect landscape.[90] While the porous architecture traps light to increase interaction frequency,[7] surface defects, specifically oxygen vacancies facilitate the absorption of lower-energy visible photons.[47] In this configuration, the scattering network acts as a geometric amplifier, enhancing the efficacy of defect-mediated absorption and substantially boosting the overall photoresponse of the system.

The preceding sections have described the multi-scale nature of T-ZnO's interaction with light, revealing a sophisticated hierarchy of optical phenomena. To consolidate these distinct levels, Table 9 provides a summary in the form of an optical engineering toolkit. This framework highlights how each structural scale (from the atomic to the macroscopic) offers a unique physical phenomenon that can be leveraged as a distinct tool for manipulating light, along with the key experimental strategies for tuning its performance.

3.3.5 Critical Link and the grand challenge for optical engineering. The optical performance of T-ZnO is a product of a multi-scale interaction hierarchy. Atomic-scale transitions dictate the fundamental rules of absorption and emission (Section 3.3.1), while the nano-to-microscale arm geometry enables resonant cavity effects (Section 3.3.3). At the macroscale, the porous network topology functions as a light-trapping architecture, utilizing multiple scattering events to maximize absorption probability (Section 3.3.4).

However, the field's understanding of the energy relaxation pathways following photon absorption remains fragmented. While individual radiative and non-radiative channels are qualitatively identified, a quantitative map of the competing energy decay pathways within the complex network topology is still missing. Consequently, the grand challenge for T-ZnO photonics is to

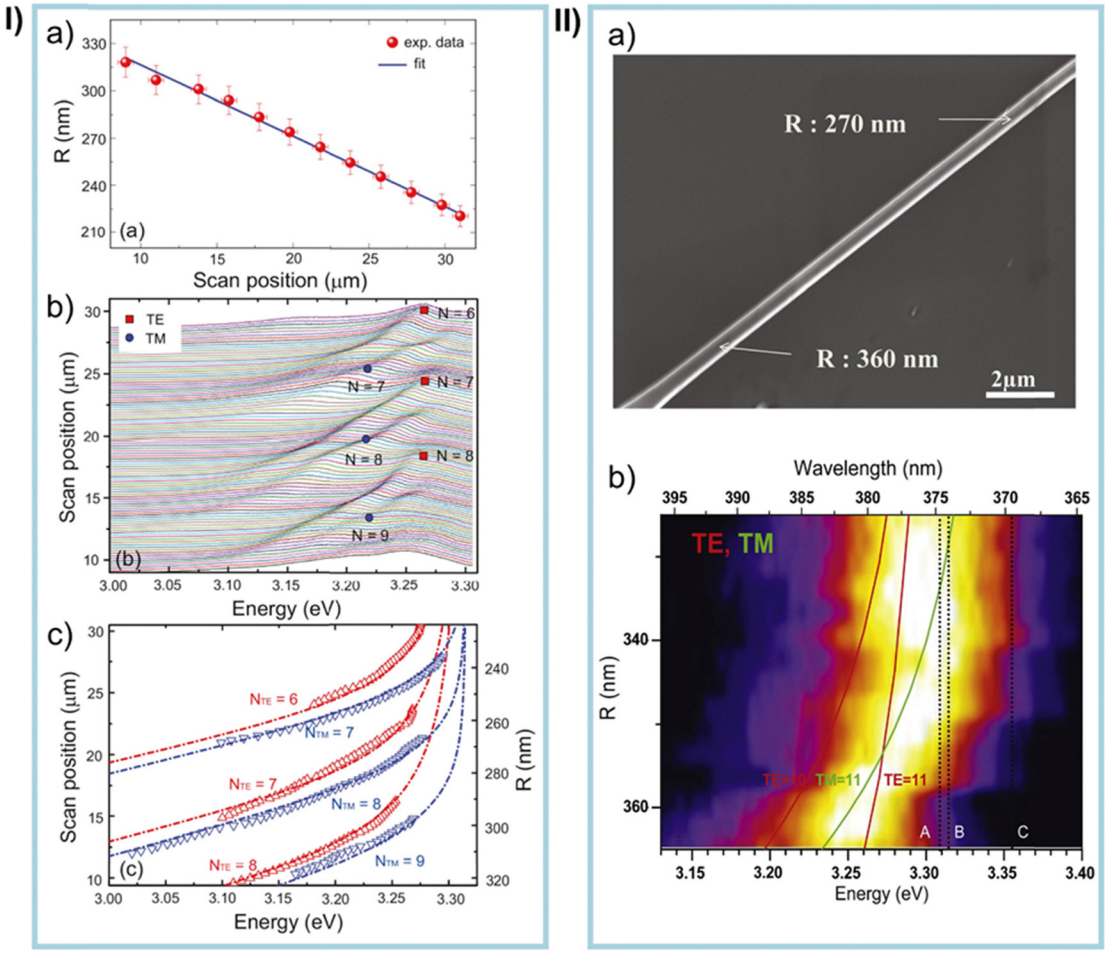

Fig. 28 Whispering gallery mode (WGM) formation and exciton-polariton coupling in T-ZnO arms. (I) WGM peak observation: (a) T-ZnO arm radius (*R*) profile along the scan position. (b) Waterfall plot of spatially resolved PL spectra showing broad UV near-band-edge (NBE) emission modulated by periodic WGM peaks. (c) WGM energy shift *versus* arm radius fitted with a WGM-polariton model (dashed lines). (II) WGM-polariton dispersion: (a) SEM image of a tapered arm. (b) Spatially resolved cathodoluminescence (CL) map showing the NBE emission splitting into discrete WGM modes, with solid lines representing theoretical fits for the characteristic anti-crossing dispersion curve. (I (a)–(c)) Reproduced from ref. 138 with permision from Elsevier,[138] Copyright 2018, (II (a) and (b)) reproduced from ref. 139 with permision from Elsevier,[139] Copyright 2013.

Table 9 The T-ZnO optical toolkit. This table summarizes how T-ZnO's hierarchical structure provides a multi-scale toolkit for engineering light, from atomic-level absorption to macro-scale light trapping

Scale of interaction	Dominant physical phenomenon	Primary engineering "Tool"	Key paramter (strategy)	Primary diagnostic method
Atomic scale (Section 3.3.1)	Bandgap absorption & PL	Control spectral sensitivity and diagnose material quality.	Bandgap tuning: doping, alloying. Hybridization: sensitizing with QDs, plasmonic nanoparticles, or dyes.	UV-Vis spectroscopy, PL, time-resolved PL.
Nano- to microscale (Section 3.3.3)	Waveguiding & WGMs	Create resonant microcavities for high-Q sensing, micro-lasers, and advanced emitters.	Synthesis perfection: growing arms with optically smooth facets and minimal crystalline defects.	High-resolution PL spectroscopy to resolve sharp, periodic WGM peaks.
Macroscale (Section 3.3.4)	Mie scattering & light trapping	Enhance overall light harvesting efficiency by increasing the effective optical path length.	Architectural control: tuning network porosity, tetrapod size, and density during synthesis.	Diffuse reflectance spectroscopy; measuring quantum efficiency in devices (*e.g.*, solar cells, photocatalysts).

transcend static characterization and elucidate the complete energy cascade. This requires resolving a fundamental question: How is excitation energy partitioned among competing channels?

Resolving this partition requires determining specific quantum yields for each pathway:

- Non-radiative losses: quantifying energy dissipation at spatially localized defect sinks (the disordered central core) *versus* dispersed surface states.
- Radiative branching: distinguishing the ratio of excitonic NBE UV emission to defect-mediated DLE.

Table 10 The optical energy cascade in T-ZnO: tracking photon fate from harvest to extraction

Stage of interaction	Dominant structural feature	Physical mechanism	Primary loss channel	Engineering target
1. Light harvesting (photon entry)	Macroscopic network: porosity and random arm orientation.	Multiple scattering (Mie): the 3D architecture extends the optical path length, increasing interaction probability.	Reflection/transmission: light escaping the network before absorption occurs.	"Black" ZnO: optimize packing density to maximize scattering events (light trapping).
2. Excitation (absorption)	Crystal lattice: wurtzite band structure ($E_g \sim 3.37$ eV).	Exciton generation: formation of stable electron–hole pairs with high binding energy (60 meV).	Thermalization: hot carrier cooling to the band edge (phonon emission).	Bandgap tuning: doping (Mg/Cd) to shift the absorption edge for solar spectrum overlap.
3. Recombination (carrier dynamics)	Surface & core: high surface-area-to-volume ratio; disordered core.	Radiative *vs.* non-radiative: competition between UV emission and trap-assisted decay.	Surface traps: non-radiative recombination at surface states or core defects.	Passivation: core–shell structures to eliminate surface traps and boost quantum yield.
4. Extraction (photon exit)	Microscopic geometry: hexagonal arm cross-section.	Resonance: arms act as Fabry–Pérot or WGM cavities.	Reabsorption: emitted photons being re-absorbed by the network before escaping.	Lasing cavities: exploit arm geometry to achieve coherent random lasing or WGM lasing.

• Charge separation: determining the efficiency of carrier extraction for photocatalytic redox reactions or photocurrent generation.

Overcoming this challenge necessitates a shift from steady-state, ensemble-averaged measurements to advanced, time-resolved, and spatially-resolved spectroscopies. Future research must utilize femtosecond transient absorption spectroscopy to track ultrafast carrier cooling and spatially-resolved time-correlated single photon counting (TCSPC) to map recombination lifetimes across the specific arm-core-arm architecture. Mapping these energetic processes is the prerequisite for transitioning from empirical optimization to predictive, efficiency-focused optical engineering.

Table 10 deconstructs this energy cascade, identifying the dominant structural features, loss mechanisms, and specific engineering imperatives for each stage of the light-material interaction.

3.4 Mechanical properties

The mechanical performance of T-ZnO is a critical enabler for its application in flexible electronics, structural composites, and functional supports. Unlike typically brittle bulk ceramics, T-ZnO exhibits counter-intuitive resilience and flexibility, emergent properties derived not from the material itself, but from its hierarchical architecture. This analysis deconstructs these properties from the single-arm scale to the interconnected network level.

3.4.1 Individual tetrapod arms. The individual arms of T-ZnO, comprising single-crystalline WZ (Section 3.1.1), maintain a high intrinsic stiffness with a Young's modulus of approximately140–150 GPa.[157,158] Despite the brittle nature of bulk ZnO, these nanoscale filaments demonstrate exceptional bending strength.[157] This resilience is governed by two physical mechanisms. First, the principle of flaw tolerance applies at the nanoscale.[159–161] Second, their high-aspect-ratio geometry results in a very low second moment of inertia. This geometric feature enables large bending radii under relatively low stresses.[162] According to Griffith's theory, the failure of brittle materials is initiated at pre-existing flaws (microcracks, voids, *etc.*).[159] The extremely small volume of a nanoscale arm has a statistically insignificant probability of containing a critical-sized flaw.[161] Lacking these failure initiation sites, the arm's strength can approach its theoretical limit, allowing it to bend to a high degree without fracturing.[161]

However, this ideal behavior is weakened by the arm's real-world structure. The practical mechanical response is significantly influenced by the landscape of defects,[161] particularly in the structurally complex and strained central core (Section 3.1.2), which can be considered the most susceptible region to stress concentration of the entire tetrapod. Extended defects like twin boundaries and stacking faults are concentrated in this region. These defects can act as stress concentrators and crack initiation sites. Detailed nanomechanical studies on individual carbon-based tetrapods derived from ZnO templates confirm this behavior. Specifically, they show that the structure's deformation is governed by a reversible localized buckling mechanism at the central joint (Fig. 29).[163] Although this model was developed for hollow carbon-based microtubes, Veys *et al.*[164] suggest that a similar buckling mechanism also occurs in solid ZnO tetrapods. The quantitative relationship between specific defect populations and key metrics like fracture toughness or fatigue resistance under cyclic loading remains a critical but under-investigated area. This lack of a predictive model means that the design of durable T-ZnO-based devices currently relies on empirical observation rather than rational engineering, highlighting a major challenge for the field.

3.4.2 Interconnected T-ZnO networks. When individual arms assemble into large-scale interconnected networks, T-ZnO transitions from a brittle ceramic to a resilient, flexible ceramic architecture.[8,115,120,154,165] In this regime, macroscopic properties, such as extreme compressibility and elastic recovery, are dictated by the geometric topology of the network rather than the intrinsic brittleness of the wurtzite lattice.[120,166] The fundamental physical principle behind this behavior is the

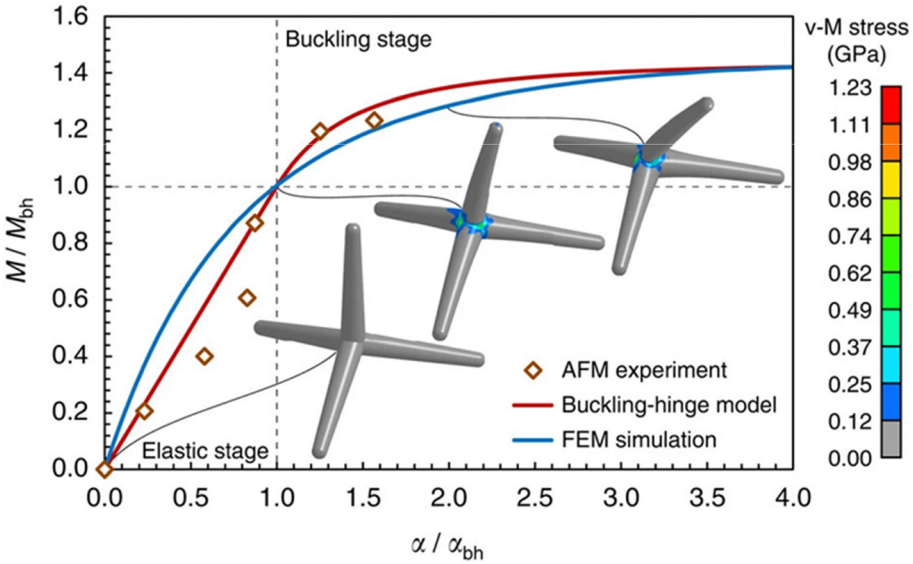

Fig. 29 Simulation and modeling of localized buckling in a single T-ZnO tetrapod. The main plot compares experimental bending data (dots) with an analytical model (red line) and a finite element method (FEM) simulation (blue line). The inset FEM contour plots visualize the concentration of von Mises stress at the central joint. Reproduced from ref. 163 with permision from Springer Nature,[163] Copyright 2017.

morpholgies ability to transform the dominant deformation mode. In a bulk ceramic, applied stress is concentrated in one area, leading to a crack forming and spreading quickly, resulting in catastrophic brittle fracture.[159] The open, interconnected 3D architecture of a T-ZnO network fundamentally frustrates this natural failure mode.[159,160] An advancing crack cannot find a continuous path and is effectively stopped at junctions between induvidual tetrapods. Instead, the applied strain is delocalized across the entire network.[160] It is converted into a series of collective, non-catastrophic deformation events. These primarily involve the bending (Fig. 30) of thousands of individual arms and rotation at inter-tetrapod junctions.[121,160,163,166] This transformation of a single, catastrophic fracture event into a distributed, gradual bending response[166] is the core reason why the network exhibits its characteristic flexibility and resilience.

This behavior creates a unique set of macroscopic properties. The networks are characterized by low density and high porosity (Fig. 31),[8,85,120,165–168] which can be tuned over a wide range. Specific porosity values of derived materials/composites are often reported to exceed 90%,[120,165–168] with the ability to be tuned between 50–98% *via* synthesis and post-processing.[120,165,168,169] This lightness and mechanical adaptability is clearly exemplified in architectures derived from T-ZnO networks, such as aero-boron nitride (Aero-BN),[167] three-dimensional carbon nanotube assemblies (t-CNTs),[166,168] stretchable aerographite hybrids,[8] hybrid T-ZnO foams,[87] or necklace-like N-doped tubular carbon structures.[85]

Critically, the effective Young's modulus (E_{eff}) of the network does not behave like a simple solid but follows a power-law relationship with network density (ρ) (Fig. 32): $E_{eff} \propto \rho^n$, where the exponent n (typically 2–3) depends on the network architecture and the nature of the junctions.[8] This relationship identifies density as the primary lever for tuning structural stiffness. However, global mechanical integrity remains contingent on the nature of inter-tetrapod contacts, which range from weak physical entanglement to robust, sintered necks[87] that provide the necessary support for structural loads.[8,121,167]

3.4.3 Composite reinforcement. Beyond its utility as a free-standing network, T-ZnO serves as a high-efficiency mechanical reinforcement filler in polymer composites, such as those based on PDMS.[36,94,170,171] Its hierarchical 3D architecture offers reinforcement capabilities that significantly surpass conventional 0D (spherical) or 1D (nanowire/fiber) fillers (Fig. 33).[48] The fundamental physical reason for this superiority is the ability of the tetrapods to achieve mechanical percolation at an extremely low volume fraction.[36] Mechanical percolation refers to the formation of a continuous, sample-spanning, stress-bearing network of filler particles within the polymer matrix.[48] The tetrapodal geometry is exceptionally efficient at creating this network.[171] Unlike 1D rods, which require high concentrations and specific alignments to connect, or 0D spheres, which only percolate at very high loadings, the four arms of the T-ZnO naturally branch out in 3D space.[48,171] This allows them to physically interlock with neighboring tetrapods,[135] forming a rigid, interconnected backbone throughout the composite with very little material.[48] The self-dispersing nature of tetrapods, which resist agglomeration, further aids in the formation of a homogeneous and effective networks.[48,171]

Under external loading, the percolated T-ZnO network provides a high-efficiency pathway for stress transfer. This mechanism is the mechanical analogue to the electrical percolation discussed in Section 3.2.3: whereas the network in Section 3.2.3 provides a continuous path for carriers, here it provides a continuous path for mechanical flux. Applied stress is effectively shunted from the compliant polymer matrix into the rigid, interconnected inorganic framework. This transition from matrix-dominated to

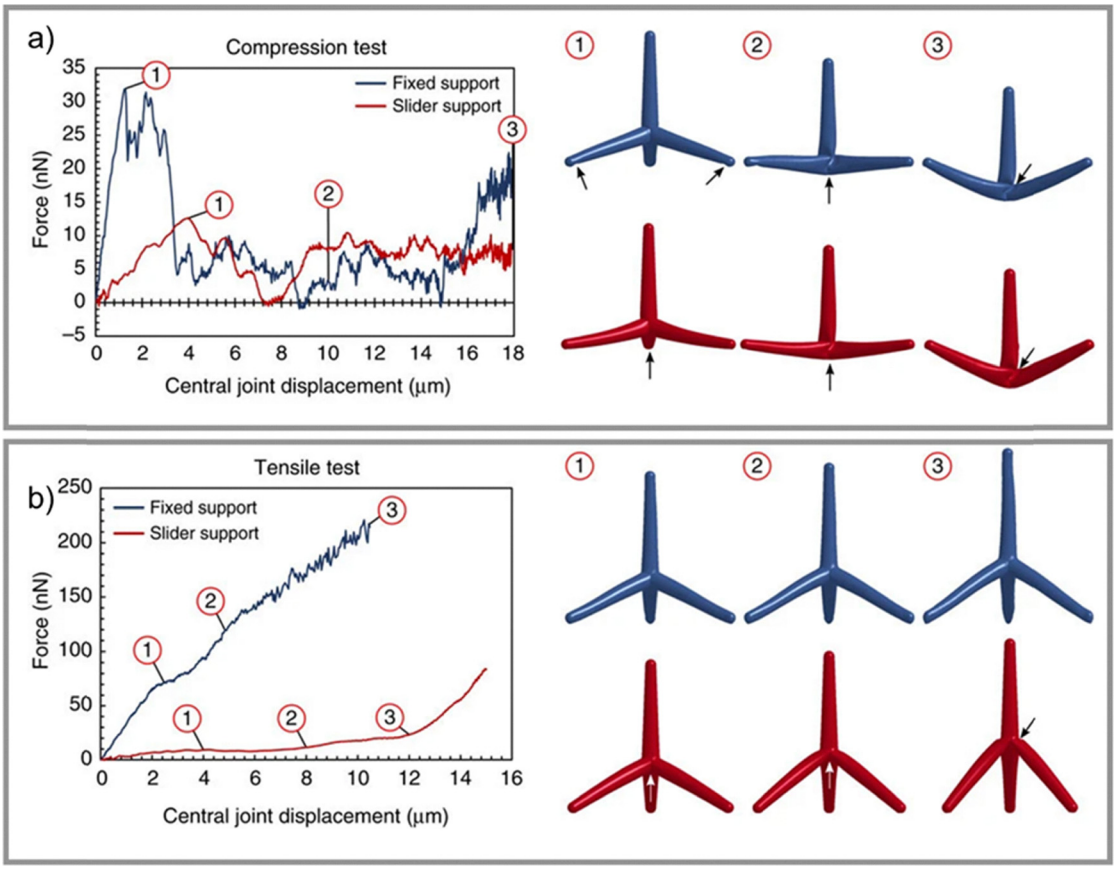

Fig. 30 Finite element method (FEM) simulations of a single T-ZnO tetrapod's mechanical response. (a) Compression test showing a localized buckling mechanism, with arrows indicating the formation of buckling hinges that lead to a non-linear snap-through instability. (b) Tensile test showing the structural response under tension, plotted on a 10 times higher force scale compared to compression. (a) and (b) Reproduced from ref. 163 with permision from Springer Nature,[163] Copyright 2017.

filler-dominated load-bearing results in dramatic enhancements to composite stiffness, tensile strength, and fatigue resistance (Fig. 34).[36,94,115,135,170,171]

3.3.4 Critical link and the grand challenge for mechanical design. The mechanical profile of T-ZnO exemplifies how structural hierarchy dictates macroscopic function. This transition from the nanoscale flaw tolerance of individual arms (Section 3.4.1) to the collective, non-catastrophic buckling of the 3D network (Section 3.4.2) and the mechanical percolation in composites (Section 3.4.3), is deconstructed in Table 11.

As Table 11 elucidates, the mechanical response is not governed by a single variable, but by the interplay between network density and junction connectivity. Stiffness is primarily governed by the relative density (porosity). T-ZnO networks behave as open-cell cellular solids where the effective Young's modulus (E_{eff}) follows a classic power-law relationship with the relative density (ρ):

$$\frac{E_{\text{eff}}}{E_{\text{s}}} \propto C\left(\frac{\rho}{\rho_{\text{s}}}\right)^{n}$$

In this expression, E_{s} and ρ_{s} are he modulus and density of the solid material, C is a geometric constant, and n is a scaling exponent (typically $2 < n < 3$ for bending-dominated structures). This fundamental law dictates that density acts as the dominant "volume knob" for tuning the material's load-bearing capacity.

Second, the inter-tetrapod junction acts as the specific determinant of the deformation mode. While density sets the magnitude of the stiffness, the junction determines the material's resilience and operational range. Creating strong covalent necks *via* high-temperature sintering maximizes connectivity, yielding a rigid, stiff foam ideal for static structural support, though this comes at the cost of reduced elastic recovery. In contrast, relying on weak physical contacts results in a highly compliant network capable of large-scale reversible deformation (spring-back behavior). This configuration is perfectly suited for flexible sensors, albeit with a lower overall stiffness.[121] Therefore, rational mechanical design requires simultaneously tuning the macroscopic density to set the modulus and the microscopic junction chemistry to define the failure mode.

This complexity points directly to the ultimate goal of the field: the development of a "digital twin" for T-ZnO. The grand challenge is to create a predictive, multi-scale computational model that can accurately forecast the macroscopic mechanical response based on the microscopic parameters of the network. Initial steps, such as combining finite element simulations with analytical models to capture the non-linear buckling

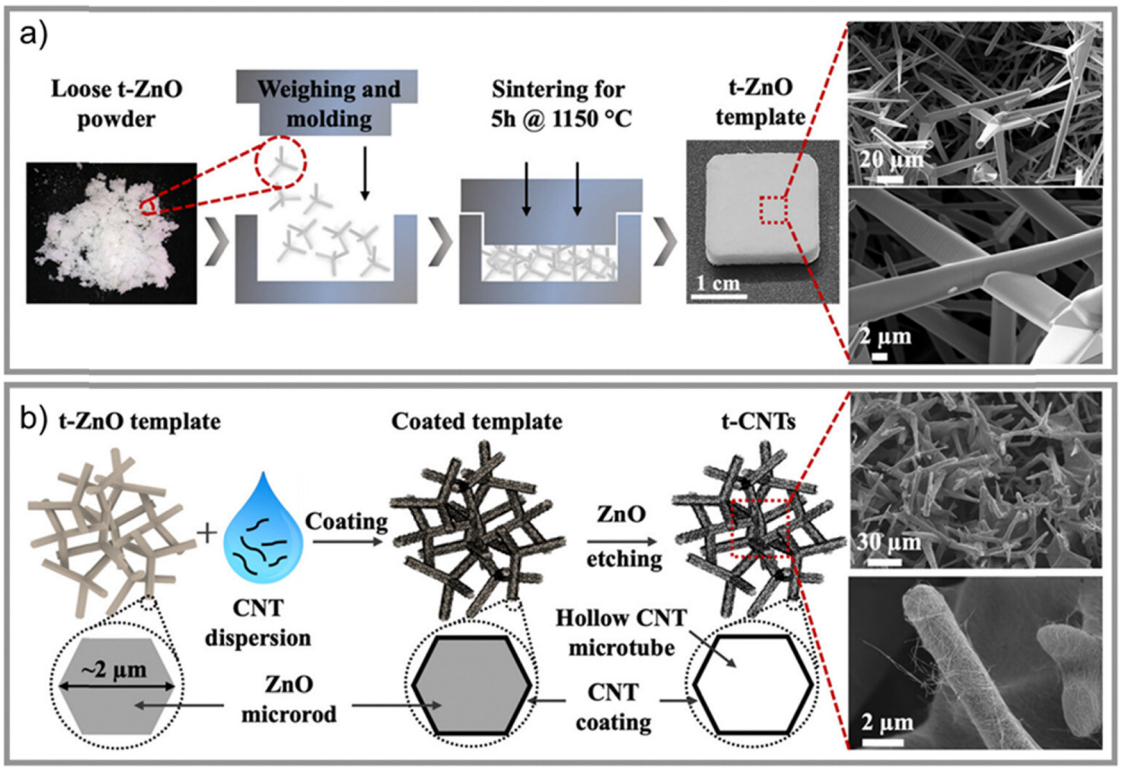

Fig. 31 Synthesis and hierarchical architecture of T-ZnO networks and derived three-dimensional carbon nanotube (t-CNT) assemblies. (a) Fabrication process of the T-ZnO template from loose powder to a sintered, interconnected network, alongside SEM images of the resulting porous 3D architecture. (b) Sacrificial templating process illustrating the coating of a CNT dispersion onto the T-ZnO scaffold followed by ZnO etching, yielding a freestanding, hollow t-CNT assembly. (a) and (b) Reproduced from ref. 166 with permision from American Chemical Society,[166] Copyright 2024.

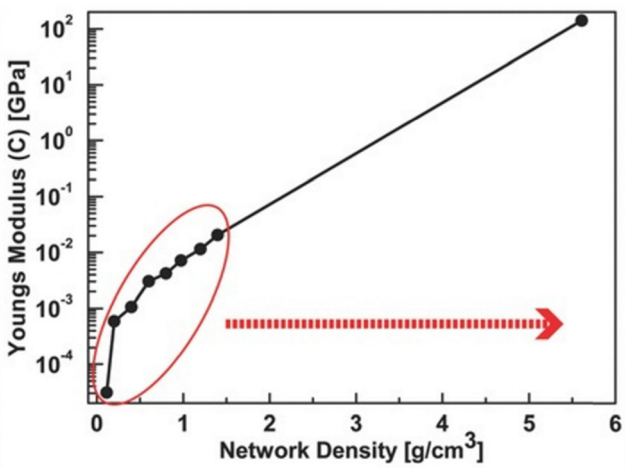

Fig. 32 Young's modulus *versus* density of the T-ZnO network. The log–log plot illustrates the power-law relationship ($E_{eff} \propto \rho^{n}$) between the effective stiffness of the network and its macroscopic density. Reproduced from ref. 59 with permision from John Wiley & Sons,[59] Copyright 2013.

mechanics of a single tetrapod, have been successfully demonstrated and serve as key validation for this approach (Fig. 29). However, extending this to a full network requires solving three difficult problems: capturing the non-linear mechanics of arm buckling,[163] modeling the complex friction/adhesion physics of the junctions, and representing the random topology of the network. Success necessitates hybrid approaches integrating physics-based finite element analysis (FEA) with ML to handle topological complexity. Solving this challenge will finalize the evolution of T-ZnO from a laboratory discovery to a predictably engineered ceramic metamaterial.

3.5 Piezoelectric properties

Beyond its role as a passive electronic and optical medium, the T-ZnO architecture functions as an active electromechanical transducer. It converts mechanical energy into a suite of functional outputs, serving as a platform where single-strain inputs are translated into tailored electronic, optical, or chemical work.[36,51,94] The operative mechanism is the intrinsic piezoelectricity of the WZ lattice (Section 3.1.1), which generates an internal electric field or piezopotential, under mechanical stress.[94,172,173] The 3D tetrapodal geometry amplifies this effect by routing and concentrating strain at critical junctions, creating complex potential landscapes.[95] This transducer functionality is deconstructed across three coupled domains:

- Piezotronics: how the piezopotential is used to directly control the flow of charge carriers, creating an electronic signal from a mechanical force.
- Piezo-phototronics: how the piezopotential is used to dynamically alter the band structure at interfaces, controlling the generation, separation, or recombination of photogenerated carriers and creating a strain-tunable optical response.

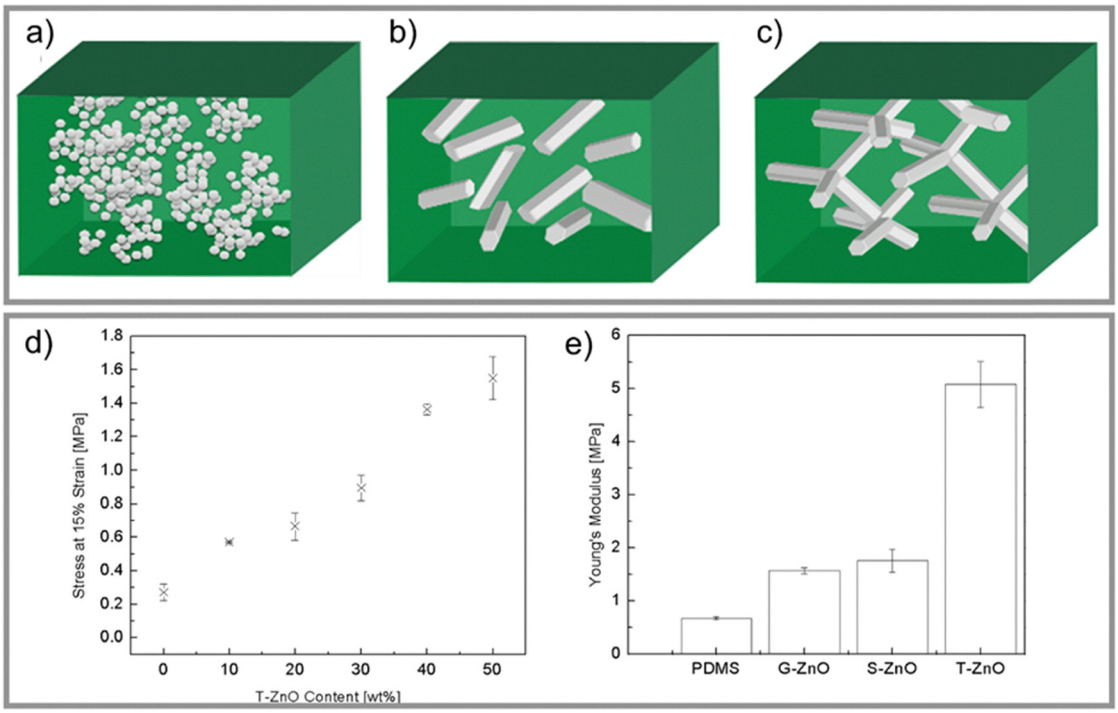

Fig. 33 Schematic illustrating different filler geometries in polymer composites and their mechanical performance. (a) 0D nanosized spherical particles (S-ZnO). (b) 1D microsized ground short fibers (G-ZnO). (c) 3D microsized tetrapodal particles (T-ZnO). (d) Stress at 15% strain *versus* T-ZnO filler fraction in a PDMS composite. (e) Comparison of the Young's modulus of pure PDMS and composites containing 50 wt% of S-ZnO, G-ZnO, and T-ZnO fillers. (a)–(e) Reproduced from ref. 171 with permision from PloS One,[171] Copyright 2014.

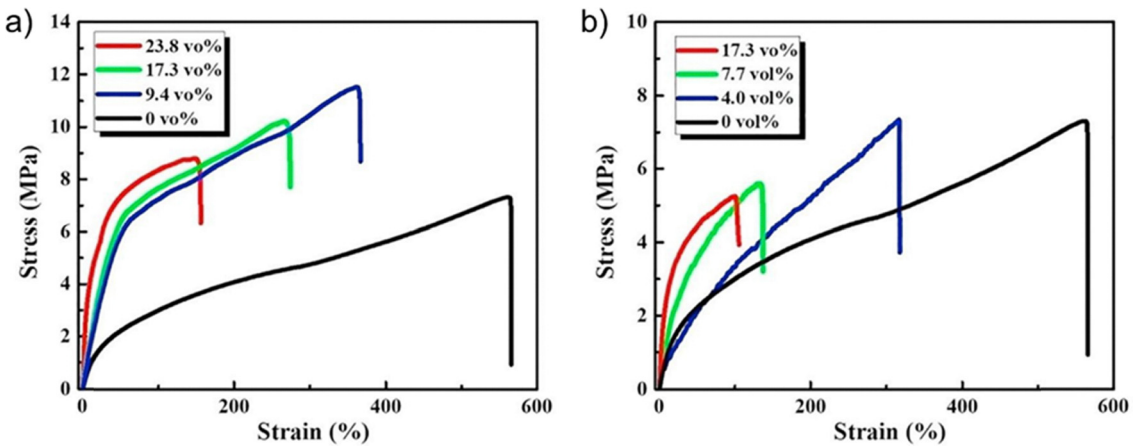

Fig. 34 Stress–strain curves for a T-ZnO/Ag/WPU composite film, illustrating the effect of the 3D T-ZnO filler network on the tensile strength and Young's modulus of the polymer matrix. (a) and (b) Reproduced from ref. 115 with permision from Elsevier,[115] Copyright 2019.

• Piezocatalysis: how the strain-induced electric fields are used to enhance the efficiency of chemical reactions at the material's surface.

By establishing the physical origins and inherent limitations of the piezopotential, this section demonstrates how T-ZnO's architecture transforms simple mechanical deformation into a versatile energy-conversion engine.[172]

3.5.1 The piezopotential. The operational foundation of the T-ZnO transducer is the intrinsic piezoelectricity of the non-centrosymmetric wurtzite lattice (Section 3.1.1).[36,95] Lacking a center of inversion, the WZ structure is characterized by a specific set of piezoelectric constants (Γ_{33}, Γ_{13}, Γ_{14}) and dielectric permittivity components (ε_{33}, ε_{13}), resulting in a net spontaneous polarization along the [0001] *c*-axis.[93,174]

3.5.1.1 The piezopotential mechanism. Mechanical stress induces a relative displacement between the Zn^{2+} cations and O^{2-} anions, creating an internal ionic dipole.[51,94,172,174] The resulting macroscopic electric field, the piezopotential, locally modulates the electronic band structure by shifting the

Table 11 A hierarchical view of T-ZnO's mechanical properties: from brittle component to flexible metamaterial

Scale/system	Key mechanical behavior	Basic physical principle	Primary engineering application	Critical limitation/design trade-off
Tetrapod arm	High stiffness & flexibility[157,158,161]	Intrinsic WZ crystal stiffness[157] combined with nanoscale flaw tolerance (low probability of critical-sized defects).[158,159,161]	The basic, stiff building block for the macroscopic network.	The defect-rich central core acts as a stress concentrator[158,163] and the final limit on the arm's ideal strength.
Macroscopic network	"Flexible ceramic" behavior (high compressibility & resilience)[8,120,166]	1. Transformation of deformation mode (fracture to bending).[163,166] 2. Stiffness scales with network density (power law: $E \propto \rho^n$).	Flexible sensor,[120] compressible catalyst supports, lightweight structural materials.[8,154,165,167]	A trade-off between stiffness (from strongly fused junctions) and flexibility/ability to spring back (from weak, physical junctions).[87,121,154]
Composite reinforcement	Efficient mechanical reinforcement[94,115,135,168,171]	The 3D shape forms a continuous, stress-bearing network at an extremely low volume fraction, enabling efficient stress transfer.[48,115,135,168,171]	High-performance polymer composites with enhanced strength and durability.[36,94,115,171]	Reinforcement is limited by the quality of the bonding at the filler-matrix interface. Poor bonding leads to early failure.

conduction and valence band edges.[88,95] This piezopotential serves as a dynamic "gate" to modulate carrier transport (piezotronic effect).[93,95,175] This coupling of ZnO's dual semiconducting (Section 3.2) and piezoelectric properties[36,88,93,172,175,176] also allows mechanical stress to profoundly influence optoelectronic processes. The piezopotential can modulate the generation, separation, transport, or recombination of photogenerated carrier,[174,176] thereby tuning light emission or detection efficiency in what is termed the piezo-phototronic effect.[172,176] Further discussion on the origin of piezoelectricity in WZ ZnO can be found in.[172]

3.5.1.2 The critical limitation. The primary bottleneck for T-ZnO piezoelectricity is free carrier screening.[93,172] Because ZnO is an n-type semiconductor[88] with a high background electron concentration (Section 3.2.2), mobile electrons[93] migrate in response to the strain-induced field. These electrons are attracted to positively polarized zones and repelled from negative ones, effectively neutralizing the ionic polarization and weakening the net electric field.[95,172] Consequently, the observable piezoelectric response is governed by a dynamic competition between the rate of piezopotential generation (strain-driven) and the rate of carrier screening (conductivity-driven).[95] Efficient device design requires not only a high piezoelectric coefficient but also precise engineering of the material's electronic properties to mitigate this screening effect (Fig. 35).[172]

3.5.2 Geometric amplification *via* strain concentration. While the WZ lattice provides the intrinsic piezoelectric "engine," the 3D tetrapodal architecture functions as a geometric amplifier, significantly elevating the functional output relative to 1D nanorods (NRs) (Fig. 36).[36,51,94,95] This architectural advantage is quantitatively confirmed by T-ZnO sensors reaching sensitivities of 182.5 mV N^{-1},[94] far exceeding the performance of sensors based on 1D ZnO nanowires (23.6 mV kPa^{-1}).[177]

3.5.2.1 The mechanism of strain concentration. The primary physical driver of this amplification is architected strain concentration at the arm roots.[95] Unlike 1D structures where stress is more uniformly distributed, the T-ZnO geometry "funnels" mechanical energy toward the base of the arms and the structurally complex central core (Section 3.1.2).[163] Since the piezopotential is directly proportional to local strain, this concentration locally amplifies the piezoelectric output (Fig. 36b–d), rendering the tetrapod a significantly more sensitive transducer than linear nanostructures. This geometric configuration offers two decisive operational advantages:

- Independent cantilever action: each arm can bend independently like a cantilever.[163,175] This enables a single tetrapod to resolve the magnitude and 3D direction of complex stress vectors simultaneously, a multi-axial sensing capability inherently absent in 1D rods.[95,175]
- Complex potential landscapes: the 3D architecture supports complex deformation modes, including concurrent bending and torsion across multiple arms. This generates a spatially varying piezopotential distribution, particularly near the core junction (Fig. 36a).[36,95] Such complex landscapes enable advanced functional devices,[95] such as three-terminal logic switches, where localized mechanical force on a single "gate" leg modulates carrier transport between the remaining arms.[175]

This geometrically amplified transduction allows for the precise mechanical tuning of conductance[175] and enhance the response of piezocapacitive sensors[51] establishing T-ZnO as a superior platform for active electromechanical devices.

3.5.3 Piezotronics. Following the generation of a strain-amplified piezopotential, piezotronics emerges as the primary electronic domain of the T-ZnO transducer. In this regime, the strain-induced field serves as a dynamic, localized gate voltage to directly modulate charge carrier transport.[95,172]

3.5.3.1 The mechanical gate mechanism. When a T-ZnO arm is bent, the resulting piezopotential locally raises or lowers the conduction and valence band edges. This band modulation can alter the height of a Schottky barrier at a metal contact or change the local carrier concentration within the semiconductor channel,[172] thereby controlling the flow of current.[95,175] This process is functionally analogous to a field-effect transistor (FET), but where the gating input is a mechanical force rather than an electrical voltage.[172]

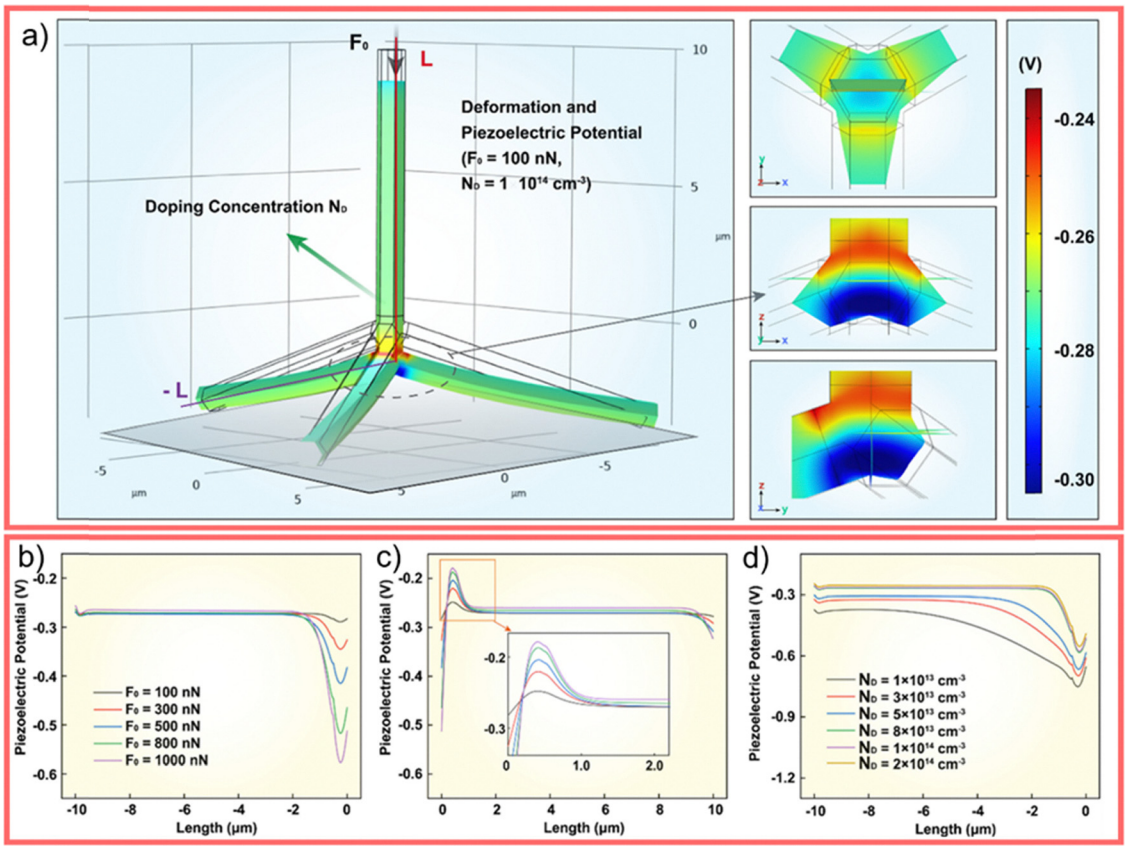

Fig. 35 Finite element method (FEM) simulations of the T-ZnO piezopotential and its governing factors. (a) 3D model of the T-ZnO structure displaying the piezopotential distribution generated by an applied force (F^0). Insets show the strain and potential concentrations at the core junctions. (b) and (c) Piezopotential profiles along the T-ZnO arms as a function of the applied force magnitude (F^0). (d) Calculated piezopotential under a constant force *versus* background donor concentration (N_D), illustrating the carrier screening effect. (a)–(d) Reproduced from ref. 95 with permision from Elsevier,[95] Copyright 2024.

3.5.3.2 Spatial localization and screening dynamics. The sensitivity of this gating effect is maximized at regions of peak strain, specifically the arm roots and the central core junction (Section 3.5.2).[163] These localized high-strain zones enable high-precision control over charge transport. However, as noted in Section 3.5.1, the operational efficiency remains governed by the carrier screening effect. The net modulation of current depends on the kinetic equilibrium between the strain-induced ionic field and its electrostatic neutralization by mobile background electrons.

3.5.3.3 The single-tetrapod logic switch. The pinnacle of this application is the single-tetrapod electromechanical switch (Fig. 37).[175] By applying a localized force to a single "gate" arm, a piezopotential is generated at the central junction. This potential acts to either enhance or deplete the conductive pathway between the remaining "source" and "drain" arms, facilitating discrete "ON" and "OFF" logic states. The output is hypersensitive to both force direction and source–drain bias, providing a level of control[175] that underpins the development of advanced flexible logic, multi-axial strain sensors, and integrated electromechanical circuits.[36,95]

3.5.4 Piezo-phototronics. The piezopotential used to gate electronic transport can also be leveraged to modulate optical interactions. Piezo-phototronics represents the optoelectronic domain of the T-ZnO transducer, where piezoelectricity dynamically tunes the generation, separation, and recombination of photogenerated carriers.[172,176] The core principle involves using the strain-induced piezopotential to change the local electronic band structure at a critical interface,[173,174] such as a metal–semiconductor Schottky contact[176] or a p–n junction.[172]

When a T-ZnO structure is strained, the resulting piezopotential can change the Schottky barrier height,[176] tilt the energy profile of a junction, or modify the width of a depletion region. This directly influences the key processes governing optoelectronic device performance: the generation, separation, transport, and/or recombination of photogenerated charge carriers (linking to concepts in Sections 3.2 and 3.3). For example, a strategically applied strain can create an electric field that assists in separating electron–hole pairs at a junction, reducing recombination and thereby enhancing the efficiency of a photodetector or photovoltaic cell.[172,176] As with piezotronics, the effectiveness of this modulation is subject to the fundamental limitation of carrier screening.[172,176] The ability of the piezopotential to sustainably alter the band structure is in constant competition with its neutralization by the material's mobile charge carriers.

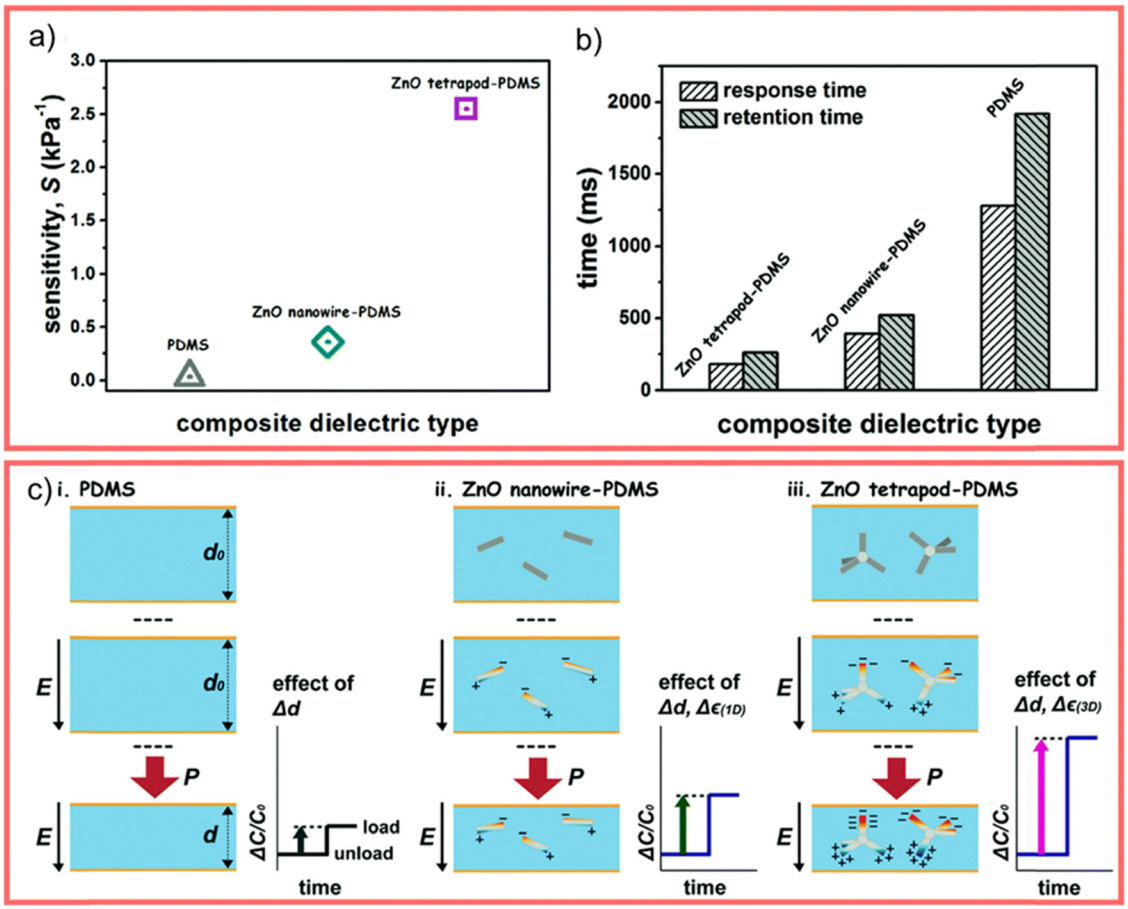

Fig. 36 Comparison of piezocapacitive sensor performance using 3D T-ZnO tetrapods, 1D ZnO nanowires (NWs), and pristine PDMS. (a) Pressure sensitivity curves for the T-ZnO composite (2.55 kPa^{-1}), 1D ZnO NW sensor (0.36 kPa^{-1}), and pristine PDMS device (0.034 kPa^{-1}). (b) Response and retention time profiles for the T-ZnO device. (c) Schematic illustrating the changes in polarization and permittivity ($\Delta\varepsilon_{(3D)}$) under applied pressure for 3D T-ZnO geometries compared to 1D nanowires under pressure. (a)–(c) Reproduced from ref. 51 with permision from Royal Chemical Society,[51] Copyright 2021.

A definitive demonstration of this principle is the strain-tunable UV sensor (Fig. 38).[176] Under UV illumination, the sensitivity of a T-ZnO-based sensor to mechanical force is dramatically amplified. This is driven by a synergy at the Schottky contact: the mechanically induced piezopotential and the accumulation of photogenerated holes work in tandem to lower the SBH. This combined stimulus produces a current response far exceeding the sum of individual force or light inputs, enabling high-performance, multi-modal sensing.[176]

The tetrapodal architecture expands these possibilities through independent arm control. The ability to strain one arm to modulate the photoresponse in another suggests a path toward integrated opto-electromechanical logic, a degree of spatial and functional complexity unattainable in simple 1D nanowire systems.[175,176]

3.5.5 Piezocatalysis and piezo-photocatalysis. Beyond electronic and optical domains, the T-ZnO transducer facilitates a potent "chemical channel," wherein mechanical energy is harvested to initiate or accelerate redox reactions at the crystal surface.[93] This phenomenon, known as piezocatalysis, can also be coupled with light to create piezo-photocatalysis, where mechanical and optical stimuli co-modulate reaction kinetics.[173,174]

3.5.5.1 The mechanism of piezochemical transduction. The central role of the strain-induced piezopotential is to mitigate the primary bottleneck in catalysis: the rapid recombination of charge carriers.[172–174] When T-ZnO is subjected to mechanical stress (*e.g.*, from ultrasound or vibration), the resulting piezopotential creates a strong internal electric field. This field tilts the band structure and drives the spatial separation of charge carriers,[172–174] in piezo-photocatalysis, these are photogenerated electron–hole pairs; in piezocatalysis, they are mobile surface charges or thermally generated carriers.[174] This improved charge separation is the key to enhanced catalytic activity. By extending carrier lifetimes, the piezopotential increases the availability of charges for critical redox reactions, facilitating the generation of reactive oxygen species (ROS).[173] These highly reactive radicals serve as the primary agents for the degradation of organic pollutants and the inactivation of bacteria.

The T-ZnO network is uniquely optimized for this "chemical work" compared to 1D structures.[88,120] The independent deformation of multiple arms across the 3D topology maximizes the generation of diverse piezopotential gradients throughout the network, significantly enhancing global catalytic efficiency

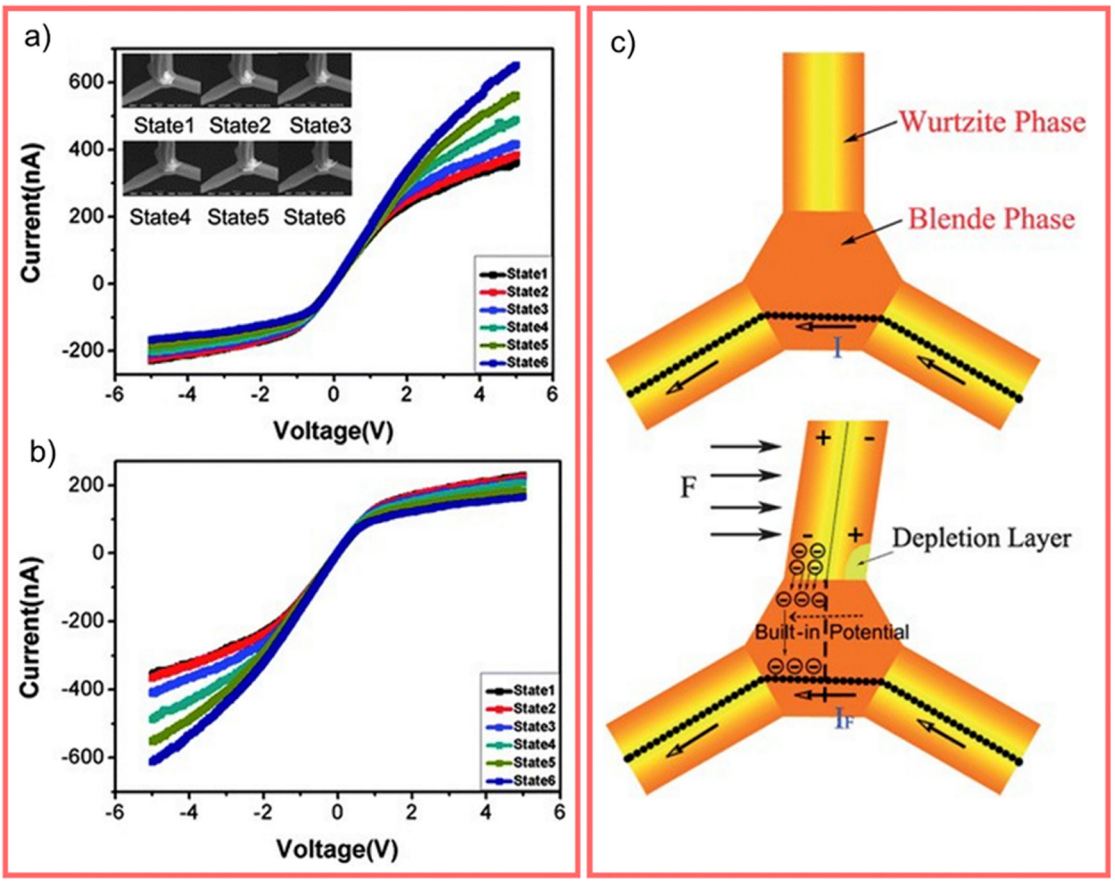

Fig. 37 Experimental data and theoretical modeling of a single-tetrapod T-ZnO piezotronic logic device. (a) and (b) Current–voltage (*I*–*V*) curves measured while applying a mechanical force to bend the "gate" leg towards the (a) source electrode and (b) drain electrode. (c) Theoretical model illustrating the generation of a localized piezopotential and depletion layer at the core junction under an applied force (F). (a)–(c) Reproduced from ref. 175 with permision from Royal Chemical Society,[175] Copyright 2011.

relative to simple nanorods.[137] This architectural advantage has been validated in environmental remediation and disinfection, providing a robust pathway for converting ambient vibrations into high-value chemical work.[173,174]

3.5.6 Critical link and the grand challenge for piezofunctional design. The piezoelectric properties of T-ZnO demonstrate how hierarchical structure facilitates a transition from passive material to active transducer. This functional journey, from the atomic origin of the piezopotential (Section 3.5.1) to its geometric amplification (Section 3.5.2) and subsequent application in electronic, optical, and chemical domains, is synthesized in Table 12.

As Table 12 elucidates, while the functional outputs are diverse, they are unified by a common physical bottleneck: the electrostatic screening of the piezopotential. The ultimate objective for the field is the evolution of T-ZnO into a "programmable piezotronic metamaterial." This paradigm envisions a macroscopic network that can be dynamically reconfigured to perform disparate functions on demand through the application of precisely tuned, anisotropic strain fields. The central scientific question is whether T-ZnO can be "programmed" *via* its stress state: could an *X*-axis strain maximize piezotronic sensitivity for force sensing, while a transition to *Z*-axis strain reconfigures surface band-bending to optimize the network for piezocatalytic disinfection?

Realizing this level of control is a formidable "grand challenge" requiring:

1. Multi-physics modeling capable of mapping complex strain vectors onto the 3D piezopotential landscape of an entire stochastic network.

2. Kinetic accounting for the competitive screening rates of mobile carriers in real-time.

Solving these problems would mark the transition of T-ZnO from a material with isolated properties to a fully integrated, programmable electromechanical device platform.

3.6 The tunable functional interface

Beyond its intrinsic electronic and mechanical properties, the functional efficacy of T-ZnO is determined by its interaction with the external environment. This interaction is mediated not by a static boundary, but by a programmable "tunable functional interface." This section frames the T-ZnO surface as the primary active zone, the locus for all heterogeneous processes including catalysis,[133] sensing,[102] and bio-integration occur.[88,166] The utility

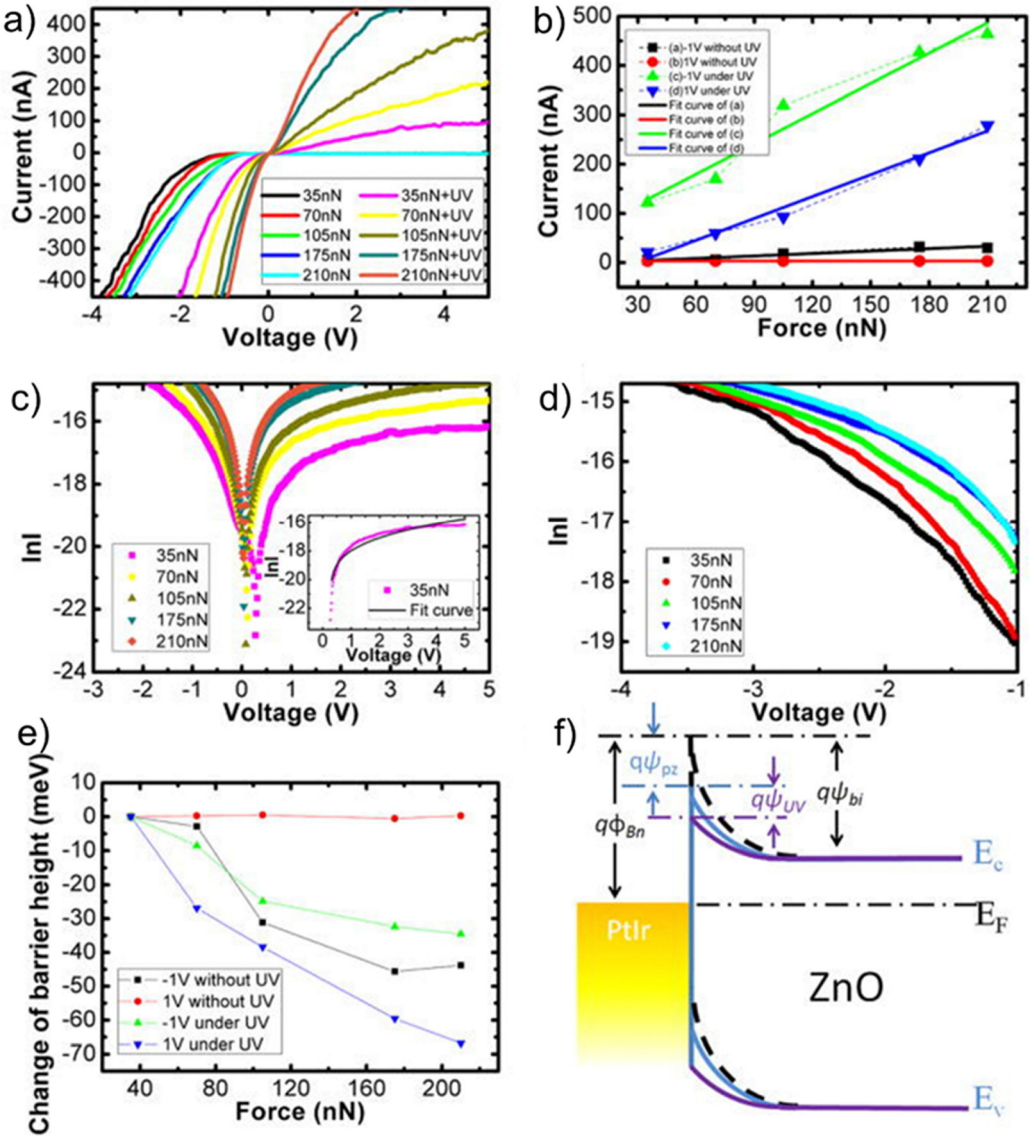

Fig. 38 The piezo-phototronic effect: experimental data and theoretical model for a strain-tunable force sensor, demonstrating the synergistic coupling of mechanical strain and UV illumination. (a) and (b) Experimental *I*–*V* curves and the resulting current–force (sensitivity) plot. The sensitivity (the slope of the line in b) is dramatically enhanced under UV illumination, increasing from 0.17 A N^{-1} (dark, red line) to 2.05 A N^{-1} (UV, green line). (e) Quantification of the mechanism, showing the change in Schottky barrier height as a function of force. The barrier is lowered significantly more under the combined effect of strain and UV light. (f) The theoretical energy band diagram explaining the synergy. Both the strain-induced piezopotential ($q\Psi_{bi}$) and the accumulation of photogenerated holes ($q\Psi_{UV}$) work together to lower the SBH, boosting the device's current and sensitivity. (a)–(f) Reproduced from ref. 176 with permision from AIP Publishing,[176] Copyright 2013.

Table 12 T-ZnO as a mechanical-to-multi-domain transducer: input, mechanism, and output

Device channel	Controlling principle	Basic physical mechanism	Key engineering application	Critical limiting factor
Electronic domain	Piezotronics	Piezopotential acts as a gate to control the flow of charge by changing energy barriers.	Strain/force sensors, electromechanical logic switches.	Free carrier screening: the neutralization of the piezopotential by background free electrons, reducing the gating effect
Optoelectronic domain	Piezo-phototronics	Strain-induced fields modify band alignment at interfaces, controlling the separation or recombination of electron–hole pairs.	Strain-tunable photodetectors, enhanced-efficiency solar cells.	Screening-induced quenching: high carrier concentration weakens the internal field necessary for assisting charge separation.
Chemical domain	Piezocatalysis	The surface piezopotential drives the spatial separation of charge carriers, prolonging their lifetime for redox reactions (*e.g.*, ROS formation)	Enhanced pollutant degradation; Vibration-assisted disinfection	Surface potential reduction: screening reduces the magnitude of the surface potential available to drive redox chemistry

of this interface is derived from four distinct engineering vectors that allow for the precise programming of interfacial behavior:

• Hierarchical porosity and scale: an architectural feature that defines the magnitude and accessibility of the active surface area.[48]

• Atomic-scale landscape: the intrinsic chemical reactivity governed by specific crystal facets and point defect distributions.

• Surface functionalization: the capacity for covalent or non-covalent modification to introduce exogenous chemical functionalities.

• Dynamic wettability: a switchable gating mechanism that regulates molecular access to the interface through stimulus-responsive surface energy changes.[47]

Synergistically optimizing these parameters transforms T-ZnO from a passive scaffold into a sophisticated, multi-functional platform for advanced interfacial engineering.

3.6.1 Hierarchical porosity and surface area. The primary structural lever for engineering the functional interface is the T-ZnO architecture itself, which serves as a scaffold to maximize the scale and accessibility of the active zone.[109,154] The synergy between nanoscale arm dimensions and the interconnected 3D topology results in an exceptionally high specific surface area.[12,13,86,178] Measured SSA values vary significantly depending on the specific morphology, ranging from $\sim$11 m^2 g^{-1} for individual particles[132] to over 754 m^2 g^{-1} for certain interconnected forms.[179] Critically, the functional advantage of T-ZnO lies not just in the magnitude of the SSA, but in its open porosity, ensuring nearly 100% environmental accessibility.[48] The network creates a multi-scale open-pore structure, which consists of the following:

• Large super-macropores between clusters of tetrapods act as highways for rapid, convective mass transport.

• Smaller macropores within the interlocked arms allow for diffusive access to the deeper regions of the network.

This system is paramount for any heterogeneous application, as it ensures that reactants can efficiently reach the high density of active sites on the internal surfaces.[13,179] Total network porosity is highly tunable, frequently exceeding 90%.[13,37,120,165]

This unique combination of high, accessible surface area and complex 3D shape also provides distinct advantages in composite materials.[48,135] The tetrapod geometry promotes homogeneous self-dispersion within a matrix and ensures that its nanoscopic features remain accessible, unlike simple nanoparticle agglomerates.[38,48] The branching structure can also increase the effective roughness factor of a surface,[90] a key parameter for tuning wettability. Furthermore, t his entire highly accessible architecture is a transferable property, when T-ZnO networks are used as sacrificial templates, the resulting aeromaterials inherit this high porosity, demonstrating the power of T-ZnO as an architectural design.[120,143,165]

3.6.2 The atomic landscape: facet-dependent reactivity and defect sites. While morphology defines the scale of interaction, the interface's ultimate functionality is dictated by its atomic-scale landscape, a synergistic combination of crystallographic orientation, point defects, and chemical adsorbates.[104,109] The WZ crystal structure of T-ZnO exposes various crystallographic

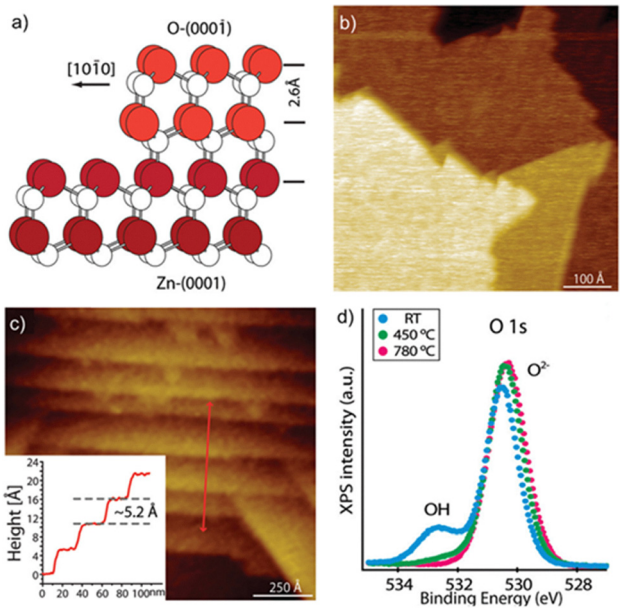

Fig. 39 Structural and chemical characterization of the polar O-terminated (000$\bar{1}$) facet. (a) Ball model of the wurtzite crystal structure illustrating the polar stacking of Zn and O atoms. (b) and (c) Scanning tunneling microscopy (STM) and AFM images displaying the step-terrace surface morphology, with the inset in (c) showing a height profile across the steps. (d) O 1s XPS spectra showing peaks corresponding to bulk lattice oxygen (O^{2-}) and surface hydroxyl (–OH) groups as a function of temperature. (a)–(d) Reproduced from ref. 180 with permision from American Chemical Society,[180] Copyright 2011.

facets, primarily the polar {0001} planes and the non-polar {1010} and {1120} facets.[93] Fig. 39 provides a detailed look at the polar O-terminated (000$\bar{1}$) facet.[180] The non-polar facets are charge-neutral and thermodynamically stable. In contrast, the polar (0001) and (000$\bar{1}$) facets are terminated exclusively by a single ion type (either Zn^{2+} or O^{2-}), creating a net surface charge and a diverging electrostatic potential.[93] This configuration is thermodynamically unstable, an effect known as the "polar catastrophe".[180]

To stabilize themselves, these polar surfaces must undergo significant atomic or electronic reconstructions. This can involve the formation of triangular surface pits, the adsorption of counter-ions (like hydroxyl groups), or the creation of a high density of surface vacancies.[38,180] This mandatory reconstruction is the physical origin of the polar facets' superior reactivity compared to non-polar planes.[87,173] These reconstructed surfaces present a high density of unique, low-coordination (atoms with fewer bonds than usual), and electronically active sites that are ideal for molecular adsorption and catalysis.[87,93,179]

3.6.2.1 The role of surface defects and adsorbates. The atomic landscape is further populated by intrinsic defects and ambient adsorbates that act as the primary engines for heterogeneous redox reactions.[87,105] The two main types are:

• Surface defects: intrinsic point defects, particularly V_O at or near the surface, act as critical sites for dissociative molecular adsorption and electron transfer.[38,47,87,107] Their concentration and chemical state, which can be measured by surface-sensitive

techniques like XPS,[38,88,115,179] directly correlate with photocatalytic activity.[137,181]

• Adsorbates: under ambient conditions, the T-ZnO surface is not pristine but is typically covered with a layer of adsorbed species, primarily hydroxyl groups (OH)[180] and molecular oxygen (O_2).[86,87,120,179] These adsorbates are not just contaminants; they are essential parts of the active interface.[103,179] Surface hydroxyls can act as proton donors/acceptors or as sites for generating highly reactive hydroxyl radicals ($^{\bullet}OH$) during photocatalysis,[47,109] while adsorbed oxygen is the primary electron acceptor for generating superoxide radicals ($O_2^{\bullet-}$). The presence and nature of these species can be readily identified using techniques like Fourier-transform infrared spectroscopy (FTIR).[86,135,179]

Mastering this atomic landscape, specifically the interplay between polar stabilization and defect distribution, is the prerequisite for engineering high-selectivity sensors and high-efficiency catalysts.[100]

3.6.3 Surface functionalization strategies. While the intrinsic properties of the ZnO surface are highly tunable, the surface can be further enhanced by functionalization. The T-ZnO morphology, with its high accessible surface area (Section 3.6.1) and an abundance of surface hydroxyl groups (^{-}OH) and defect sites,[12,13,86,87,135,179] serves as a uniquely flexible framework for these advanced modification techniques. This section deconstructs the three primary paradigms used to exploit this framework: robust covalent attachment, conformal coating for core–shell architectures, and targeted molecular immobilization.

3.6.3.1 Covalent attachment. The primary method for creating robust, permanent modifications is through covalent attachment, most commonly achieved *via* silanization. The high density of surface hydroxyls provides ideal reaction sites for silane coupling agents. For example, octadecyltrichlorosilane (OTS) can be used to create a low-surface-energy layer.[113] Alternatively, aminosilanes like APTES provide anchor points for further functionalization.[107,182] This creates a stable base-layer that can then be used to chemically bond a wide variety of functional molecules, including the following:

• Biomolecules: for creating highly specific bio-interfaces, such as immobilizing Deoxyribonucleic Acid (DNA) for gene delivery[182] or antibodies for biosensing applications.[88,107] Fig. 40 provides a complete model for this process, showing both the step-by-step chemical functionalization (Fig. 40a) and the resulting changes in the electronic band structure (Fig. 40b–e) that create the sensing mechanism.[107]

• Polymers or nanoparticles: for improving filler-matrix adhesion in composites or creating hybrid materials.[48,135,140,171,179]

3.6.3.2 Conformal coating and shell accretion. The open, 3D topology of the T-ZnO network serves as a superior template for the accretion of uniform, continuous coatings or shells,[102,133] effectively generating a new functional interface atop the ZnO core. A broad spectrum of materials can be deposited to form core–shell heterostructures with synergistic properties:

• Plasmonic nanoparticles: decorating the surface with Ag[12,13,88] or Au[97,140] nanoparticles is a primary strategy for inducing LSPR. This effect enhances photocatalytic efficiency and enables SERS (Fig. 41).[140]

• Other semiconductors: depositing shells of materials like TiO_2,[12,13,133] or ZnSe/CdSe (*via* dipping procedures[89]) creates

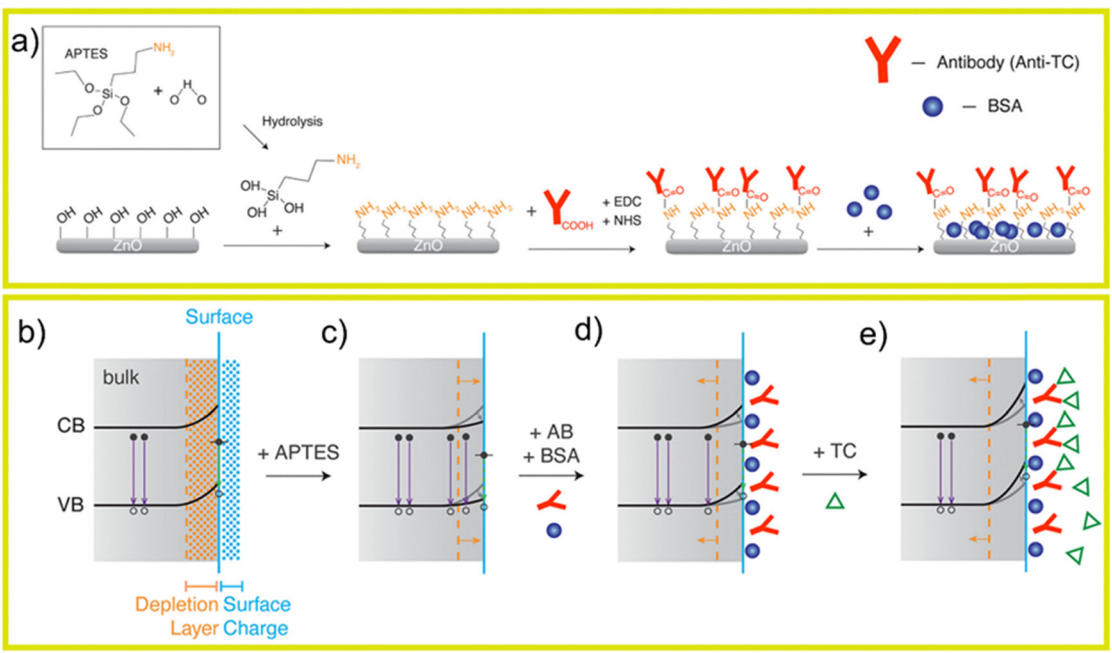

Fig. 40 Schematic model of T-ZnO biosensor functionalization and interfacial band bending. (a) Chemical procedure for covalent attachment (silanization), detailing the functionalization of the native ZnO surface with APTES to provide amine ($-NH_2$) anchors for antibody binding. (b)–(e) Energy band diagrams illustrating the progressive modification of surface band bending following each functionalization step. (a)–(e) Reproduced from ref. 107 with permision from American Chemical Society,[107] Copyright 2022.

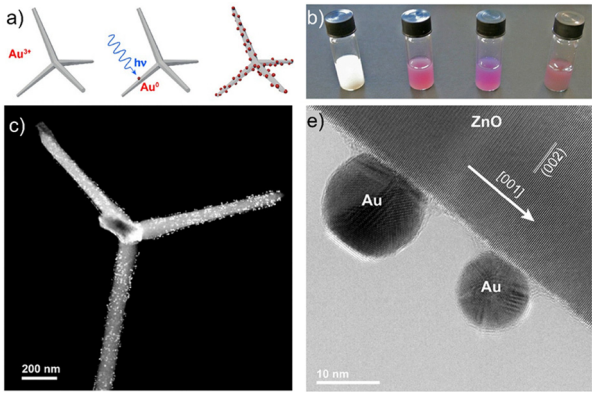

Fig. 41 Surface functionalization of T-ZnO with plasmonic gold (Au) nanoparticles. (a) Schematic of the photochemical synthesis for decorating a T-ZnO scaffold with Au nanoparticles. (b) Photographs of the T-ZnO dispersion displaying color changes during progressive Au nanoparticle formation. (c) HAADF-STEM image of a T-ZnO arm uniformly decorated with Au nanoparticles. (e) High-resolution TEM image showing the interface between the crystalline Au nanoparticles and the T-ZnO surface. (a)–(e) Reproduced from ref. 140 with permision from Springer Nature,[140] Copyright 2016.

heterojunctions with staggered band alignments. These configurations are engineered to maximize charge separation and minimize recombination losses.[87,88,97]

- Protective layers: ultrathin protective layers of materials such as Al_2O_3,[88] TiO_2,[90] amorphous silica derived from TEOS,[178] or diamond-like carbon nanocomposites[119] are utilized to passivate electronic surface states. These coatings serve as a critical defense against photocorrosion, ensuring long-term device stability in harsh environments.
- Polymers and metal–organic framework (MOFs) and 2D-nanomaterials: the network can be coated with polymers like PDMS,[155] polymethacrylates[135,136] or poly(*N*-isopropylacrylamide) (PNIPAM) hydrogels,[165] or with MOFs like zeolitic imidazolate framework, ZIF-8,[12,102] or 2D-nanomaterials like two-dimensional transition metal carbides/nitrides (MXenes),[183] to create hybrid materials for specialized applications.

3.6.3.2 Molecular immobilization. Finally, the extensive and accessible surface, combined with its chemically active sites (Section 3.6.2), allows for the efficient adsorption and immobilization of specific molecules. Fig. 42 presents a definitive case study of this mechanism, detailing both the synthesis of a T-ZnO hybrid (Fig. 42a) and the precise electrostatic mechanism (Fig. 42b) by which surface sites adsorb target analytes.[179] This is a key strategy for creating interfaces with highly targeted functions, for instance:

- Dye sensitization: adsorbing dye molecules to enhance visible light absorption for photocatalysis.[12,135]
- Selective sensing: creating surfaces tailored for the specific adsorption of gas molecules[12,13,37,102] or other chemical analytes[88,179] for high-sensitivity sensor devices.[86,120]
- biomolecular immobilization: attaching specific biomolecules for biosensing[12,88,107,120] or advanced biomedical applications. A notable example involves amino-modified tetrapods used to electrostatically bind plasmid DNA. The unique tetrapodal geometry allows the structures to 'stand' on cell membranes, facilitating gene delivery while minimizing cytotoxicity by preventing full cellular uptake.[182]

Through these diverse strategies, the T-ZnO surface can be transformed from its native state into a highly programmed, multifunctional interface, precisely tailored for a wide variety of advanced applications.

3.6.4 Wettability as an active gating mechanism. Beyond static chemical functionalization, the dynamic modulation of surface wettability serves as an active functional gate, regulating molecular access to the T-ZnO interface.[178] Pristine, flat ZnO surfaces are intrinsically hydrophilic due to the presence of surface hydroxyl groups.[111] However, the hierarchical roughness of a T-ZnO network, with its micro- and nanoscale features, can trap air pockets between the arms, rendering the surface hydrophobic or even superhydrophobic in what is known as a Cassie–Baxter state.[110,112,178]

Crucially, this wettability is not static and can be reversibly switched using various external stimuli, including UV irradiation, thermal annealing, and applied electric fields.[110–113,184] The most widely studied method is photoswitching. Under UV irradiation with photon energy greater than ZnO's bandgap, electron–hole pairs are generated. The holes migrate to the surface and react with lattice oxygen ions (O^{2-}) to create surface oxygen vacancies. These defect sites are kinetically favorable for the dissociative adsorption of water molecules from the ambient air. This leads to a high density of surface hydroxyl groups and a transition to a hydrophilic or superhydrophilic state.[110,112,113] Conversely, this process can be reversed and the hydrophobic state restored through thermal annealing[135] or by extended storage in the dark, which removes the adsorbed hydroxyl groups.[110,112] While this intrinsic photoswitching is a property of the ZnO material itself, hybrid systems can also be designed where the switching is governed by organic photochromic molecules (like azobenzene derivatives) integrated into the T-ZnO composite network.[155]

This switchable behavior has profound functional consequences, allowing the surface to be actively "gated" on or off for specific applications. A hydrophilic surface promotes intimate contact between the T-ZnO lattice and the surrounding aqueous medium. This maximizes the interaction between reactants and active sites, which can accelerate interfacial processes such as photocatalysis by over 2.5 times compared to the hydrophobic state (Fig. 43).[47] Conversely, a superhydrophobic state, by trapping a layer of air, can effectively shut down the same reaction by preventing aqueous reactants from reaching the catalytic surface; experiments on ZnO nanorods confirm that achieving a superhydrophobic state leads to minimal photocatalytic activity.[111]

This inherent photosensitivity, however, is not always desirable, as uncontrolled changes in wettability can compromise the long-term stability of a device. This effect can be intentionally suppressed through surface engineering. For instance, applying a thin, conformal passivating layer, such as a diamond-like carbon nanocomposite film, can physically block the UV-induced mechanism and stabilize the surface wettability over time, even under UV

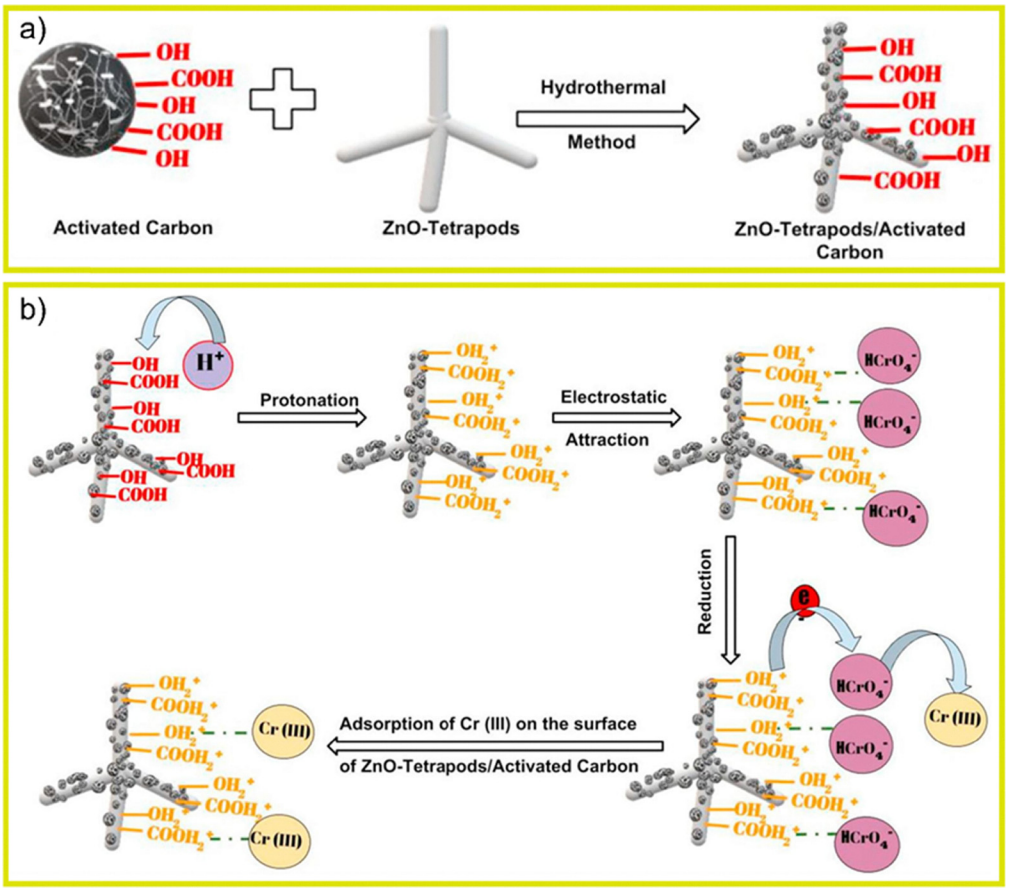

Fig. 42 A case study of T-ZnO functionalization for molecular adsorption. (a) A schematic showing the synthesis of a T-ZnO/Activated Carbon hybrid material. (b) The detailed mechanism for molecular immobilization, demonstrating how surface hydroxyls ($^{-}$OH) act as essential active sites that are protonated to electrostatically attract and adsorb a target chemical analyte (Cr(VI)). (a) and (b) Reproduced from ref. 179 with permision from Elsevier,[179] Copyright 2019.

exposure.[119] Thus, the wettability of a T-ZnO interface is a highly tunable property that can be used as a functional gate or protected for stability, depending on the specific application requirements.

3.6.5 Critical link and the grand challenge for interfacial design. The interfacial properties of T-ZnO represent the ultimate expression of its hierarchical design. Rather than a static boundary, the T-ZnO surface functions as a highly programmable functional interface, the material's primary active zone for all heterogeneous interactions. The power of this platform lies in the synergistic deployment of four distinct engineering parameters: a vast, accessible surface area (Section 3.6.1), an intrinsically reactive atomic landscape (Section 3.6.2), a versatile capacity for exogenous functionalization (Section 3.6.3), and a dynamically switchable wettability gate (Section 3.6.4). Table 13 serves as a strategic roadmap for this engineering process, linking specific functional goals to the chemical modifications and physical mechanisms that drive them.

As Table 13 illustrates, mastering these individual parameters to create single-function interfaces represents the current state-of-the-art. The next frontier lies in multi-functional integration. Therefore, the grand challenge for the field is the development of a "spatially-addressable, multi-functional bio-interface."

This vision entails using the T-ZnO network not just as a uniform scaffold, but as an integrated device with distinct, spatially defined functional zones. The central scientific objective is to achieve a level of regional control that allows different functions to be programmed onto specific segments of the same tetrapod network, the "lab-on-a-tetrapod" concept. Future research must establish the feasibility of compartmentalizing the 3D architecture such that:

- Zone A is functionalized with enzymes for specific biodetection.
- Zone B is decorated with plasmonic nanoparticles to serve as a SERS hotspot.
- Zone C features dynamically switchable wettability to function as a microfluidic gate or valve.

Achieving this requires the development of spatially selective functionalization techniques and a predictive understanding of how these distinct engineered zones interact within a continuous 3D architecture. Solving this challenge will transform T-ZnO from a passive scaffold into a truly programmable

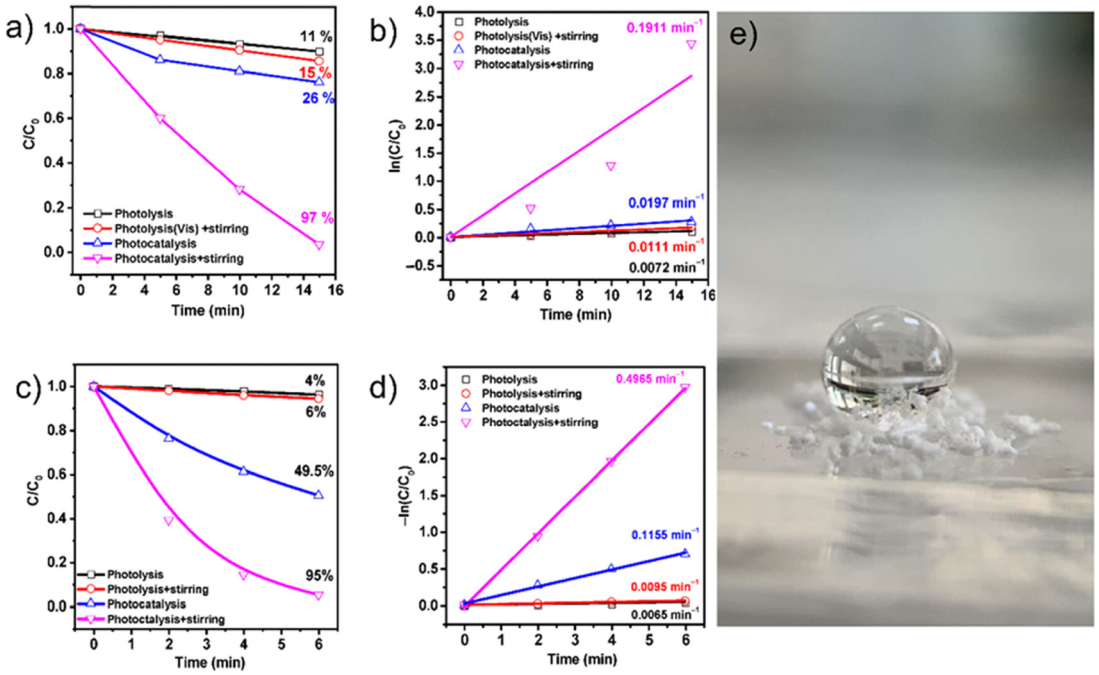

Fig. 43 (a) and (b) Changes in the concentration of MB and kinetic curves for hydrophobic ZnO-Ts. (c) and (d) Changes in the concentration of MB and kinetic curves for hydrophilic ZnO-Ts. (e) A photograph of a water droplet on the surface of the hydrophobic ZnO-T powder. (a)–(e) Reproduced from ref. 47 with permision from MDPI,[47] Copyright 2023.

Table 13 A guide to programming the T-ZnO functional interface

Primary engineering goal	Functionalization strategy & physical mechanism	Resulting interfacial property	Target application
Enhance visible light absorption	Hybridization with sensitizers: LSPR from plasmonic NPs (Ag, Au)[97,140] Heterojunctions with QDs or dyes[89]	Increased optical cross-section in the visible range; improved charge separation.	Visible-light photocatalysis, solar cells, photodetectors.
Engineer surface reactivity	Catalytic decoration: attachment of noble metal NPs (*e.g.*, Au, Pt); creation of heterojunctions with co-catalysts (*e.g.*, TiO_2)[133]	Creation of new active sites; modified adsorption energies; enhanced charge separation at interfaces.	Heterogeneous catalysis, surface-enhanced Raman spectroscopy.[140]
Create bio-specific interfaces	Biomolecular attachment: covalent anchoring of enzymes, antibodies, or DNA *via* silanization[13,107,182]	Specific molecular recognition capability; tailored biocompatibility.	Biosensing, targeted drug/gene delivery, bio-scaffolds.
Tune surface wetting & adhesion	Surface energy engineering: modification with low-surface-energy molecules (*e.g.*, PFO,[178] OTS[113]) or uniform coating with polymers (*e.g.*, PDMS[155]) to engineer hierarchical roughness and control surface energy.	Tailored surface energy, leading to superhydrophobicity or superhydrophilicity	Self-cleaning surfaces, anti-fouling coatings, water-oil separation membranes
Improve stability & passivation	Dielectric coating: conformal deposition of chemically stable, wide-bandgap oxides (*e.g.*, Al_2O_3, TiO_2)[87,88,90]	Passivation of electronic surface states; creation of a protective barrier against photocorrosion.	Stable photoanodes for water splitting, durable optoelectronic devices.

platform for the most complex, integrated interfacial systems in modern materials science.

3.7 Integrated structure–property nexus: from coupled physics to core design principles

The true structure–property nexus in T-ZnO demonstrates how a shared, hierarchical morphology forces distinct physical domains into a simultaneous, tightly coupled state. Rather than acting as a passive scaffold, the tetrapodal architecture dictates an instantaneous transduction of energy across multiple physical regimes. For instance, the application of a macroscopic mechanical force to the network does not yield a simple, isolated structural deformation. Instead, the force is geometrically concentrated as localized strain at the arm roots, which instantaneously generates a highly localized piezopotential. This strain-induced field simultaneously redefines the electronic landscape by shifting charge carrier transport pathways, alters the optical recombination rates of excitons, and induces surface band-bending that immediately modifies the rates of solid–liquid interfacial catalysis. Consequently, engineering T-ZnO requires acknowledging that any single input will invariably trigger a tightly coupled, multi-physics response.

3.7.1 The T-ZnO design blueprint. As illustrated in the multiscale blueprint (Fig. 44–46), T-ZnO's functionality emerges across three distinct tiers: the atomic foundation, the nanoscale geometry, and the macroscale network.

3.7.1.1 Atomic scale (Fig. 44). The fundamental characteristics of T-ZnO are dictated by WZ thermodynamics. At this level, the crystal lattice provides the intrinsic high mechanical stiffness, the wide bandgap necessary for UV optics, and the non-centrosymmetry required for piezoelectricity. Furthermore, the defect landscape, primarily governed by unintentional hydrogen impurities and intrinsic thermodynamic limits, serves as the baseline tuning layer for conductivity and visible-range emission. However, this scale also introduces absolute thermodynamic constraints, most notably the spontaneous formation of native donor defects (self-compensation) that severely limits the feasibility of stable p-type doping.

3.7.1.2 Nano/micro scale (Fig. 45). The geometry of the individual tetrapod arms translates these atomic properties into localized functionalities. The high aspect ratio and single-crystalline nature of the arms enable nanoscale flaw tolerance and permit them to function as optical microcavities supporting WGMs. Simultaneously, this scale introduces the system's primary structural bottlenecks: nanoscale surface depletion layers that can pinch off charge transport, and the highly defective central core, which acts as a mechanical stress concentrator and a primary scattering center for electrons.

3.7.1.3 Macroscale (Fig. 46). The collective behavior of the interconnected 3D network yields macroscopic properties that differ fundamentally from the bulk material. The tetrapodal geometry transforms the intrinsically brittle ceramic into a flexible, compressible macroscopic foam and converts a pristine UV absorber into a highly efficient, broad-spectrum light scatterer *via* Mie scattering. The ultimate performance limitation at this scale is defined by the inter-tetrapod junctions, where the formation of double Schottky barriers dictates the macroscopic electrical and thermal transport efficiency of the entire network.

3.7.2 The three design axioms. The complex interplay across these hierarchical scales indicates that engineering T-ZnO is strictly a multi-objective optimization problem governed by three fundamental design axioms:

3.7.2.1 Axiom 1: morphological translation of intrinsic properties. The 3D architecture dictates how bulk material properties manifest at the macroscale. The tetrapodal structure acts as a geometric translator, enabling the emergence of properties, such as macroscopic mechanical flexibility and extreme porosity, that the intrinsic ceramic constituents cannot achieve in thin-film or bulk forms.

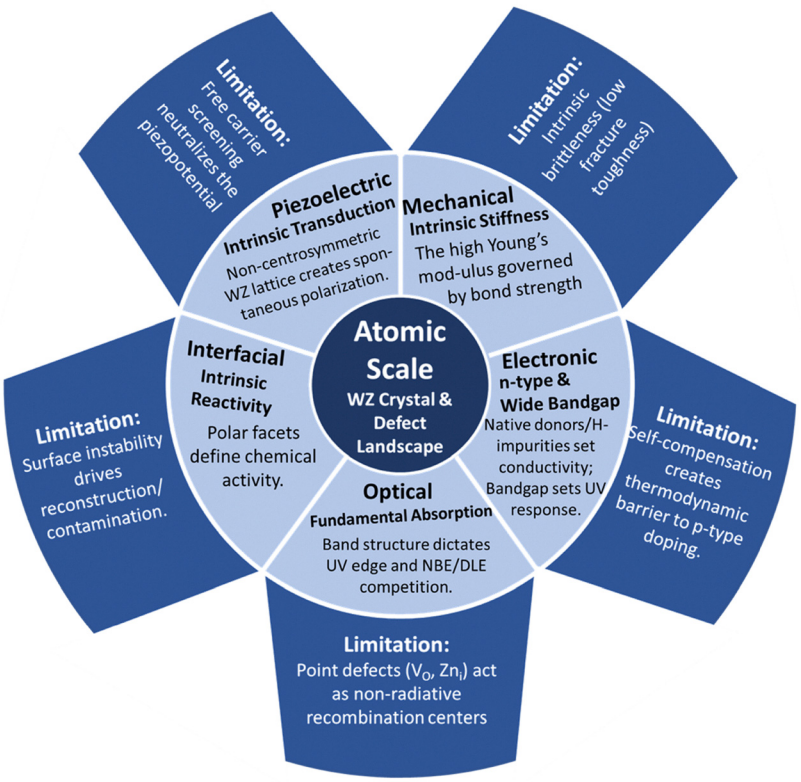

Fig. 44 Atomic scale properties of T-ZnO. This diagram illustrates the intrinsic material characteristics of the crystal lattice and defect landscape, highlighting the fundamental mechanical stiffness, wide-bandgap electronic behavior, and polar-facet reactivity alongside their inherent physical limitations.

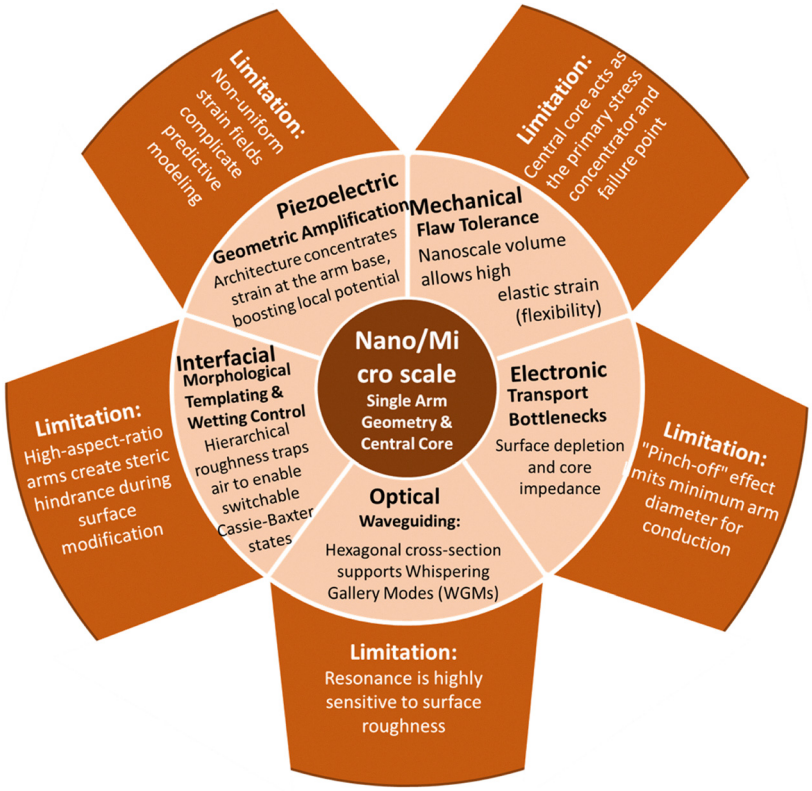

Fig. 45 Nano/micro scale geometric effects in T-ZnO. This figure details how the single-arm geometry and central core architecture influence properties such as flaw tolerance and optical waveguiding, while introducing bottlenecks like surface depletion and strain concentration at the arm base.

3.7.2.2 Axiom 2: the inevitability of multi-physics trade-offs. Because the physical domains in T-ZnO are inherently coupled, optimizing one parameter frequently degrades another. For example, heavily doping the network to maximize electrical conductivity inherently increases the concentration of free charge carriers, which subsequently screen and dampen the strain-induced piezoelectric response. Similarly, enhancing the mechanical strength of the macroscopic network *via* high-temperature sintering creates rigid covalent bonds that destroy its structural flexibility. Engineering T-ZnO, therefore, requires managing these compromises rather than attempting to eliminate them.

3.7.2.3 Axiom 3: dynamic evolution of the functional interface. The structure–property relationships within T-ZnO are not static. Under operational conditions, the material undergoes continuous evolution: the surface defect landscape interacts with environmental adsorbates, the central cores accumulate mechanical fatigue, and the functional interface degrades. This dynamic behavior highlights a critical ''synthesis-stability nexus'', wherein the initial synthesis parameters dictate not only the as-grown properties but also the evolutionary degradation and ultimate operational lifetime of the material.

3.7.3 The unified challenge: bridging scales *via* computational modeling. Overcoming the empirical, trial-and-error limitations of current T-ZnO engineering requires moving beyond isolated material characterizations. The unifying challenge for the field is the development of a predictive, multi-physics computational framework for T-ZnO. Achieving this requires bridging distinct computational methodologies across all relevant length scales. It necessitates linking fluid dynamics models (governed by the second Damköhler and Péclet numbers) from the initial synthesis phase to atomistic DFT calculations of defect and surface energetics. These atomic insights must then be upscaled into continuum mechanics models, utilizing FEM or phase-field modeling to predict macroscopic stress distribution, network percolation, and carrier transport. Ultimately, because of the inescapable compromises defined by Axiom 2, the successful deployment of T-ZnO is an exercise in precision engineering. The following section (Section 4) will explore how researchers navigate this highly coupled multi-physics matrix, identifying and exploiting the optimal operational regimes to drive current and emerging applications.

4 T-ZnO applications

The true promise of T-ZnO lies not only in enhancing existing technologies but also in enabling entirely new approaches, ranging from innovative microstructured actuators to wearable sensors that monitor health in real-time and ultralightweight materials with the potential to revolutionize aerospace, medicine and soft robotics. This section highlights the applications that are beginning to translate T-ZnO's potential into reality. The unique combination of properties detailed in Section 3, from its semiconducting (Section 3.2) and piezoelectric nature

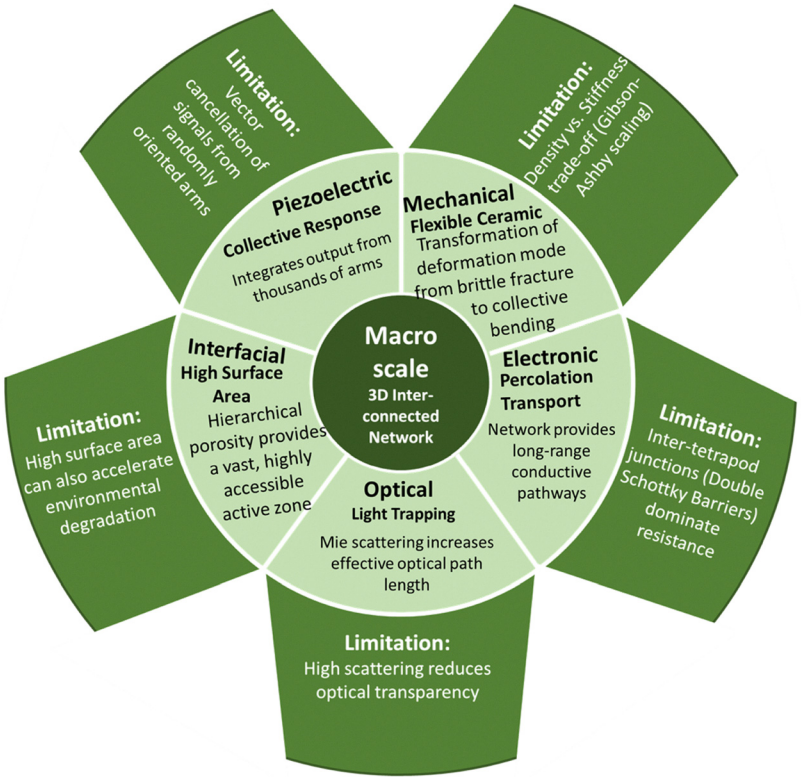

Fig. 46 Macro scale performance of 3D interconnected networks. This model describes the collective behavior of tetrapod-based networks, focusing on the transformation into a flexible ceramic, long-range percolation transport, and high surface area accessibility, while noting trade-offs in optical transparency and signal cancellation.

(Section 3.5) to its remarkable mechanical resilience (Section 3.4) and high specific surface area (Section 3.6.1), establishes T-ZnO as a uniquely versatile platform for a wide range of advanced applications. The utility of T-ZnO is not just a sum of these individual characteristics. Instead, it is a result of their synergistic interplay, as summarized in the integrated structure–property nexus (Section 3.7). The applications that stem from this versatility can be broadly categorized based on the primary role the material plays. On one hand, many applications exploit the intrinsic properties of ZnO, where the material itself is the active component in sensing, catalysis, or optoelectronics. On the other hand, a ground-breaking class of applications leverages its unique 3D morphology. Here, the tetrapod network acts purely as a structural backbone for mechanical reinforcement or, more innovatively, as a sacrificial template. This templating capability allows researchers to architect entirely new materials with unprecedented properties, literally sculpting other materials from the micro to the macro scale using the T-ZnO network as a removable template. A visual overview of these distinct application pathways, from active sensors to templated aeromaterials, is presented in Fig. 47. This section will explore these diverse applications, highlighting how T-ZnO's hierarchical structure is leveraged to achieve novel functionalities.

4.1 T-ZnO as an active functional material

Applications in this category exploit the intrinsic electronic (Section 3.2), optical (Section 3.3), piezoelectric (Section 3.5), or chemical properties (Section 3.6) of ZnO itself. Here, the material's high surface area and unique morphology serve to enhance its inherent performance. In its role as an active functional material, T-ZnO directly employs its fundamental material characteristics to interact with and respond to its environment. This includes leveraging its intrinsic semiconducting nature (Section 3.2), where electrical conductivity can be precisely modulated by external stimuli like UV light or gas adsorption. As well as its distinct optical properties, governed by a wide bandgap (Section 3.3.1) and characteristic PL (Section 3.3.2) and its piezoelectric effect, which originates from its non-centrosymmetric crystal structure (Section 3.5.1) and allows for the conversion of mechanical stress into electrical energy.

Crucially, performance in these applications is not merely a function of bulk ZnO properties but is dramatically amplified by the tetrapod architecture. The high surface-to-volume ratio of the nanoscale arms (Section 3.6.1) creates a vast interface for interaction, making the material exceptionally sensitive. Furthermore, the interconnected 3D network ensures this surface is highly accessible and provides robust pathways for efficient charge transport (Section 3.2.3). This prevents the performance losses often seen in simple nanoparticle or nanowire agglomerates. In essence, the unique morphology acts as a structural amplifier. This makes T-ZnO a superior platform for devices like highly sensitive sensors and materials for advanced surface engineering and environmental control.

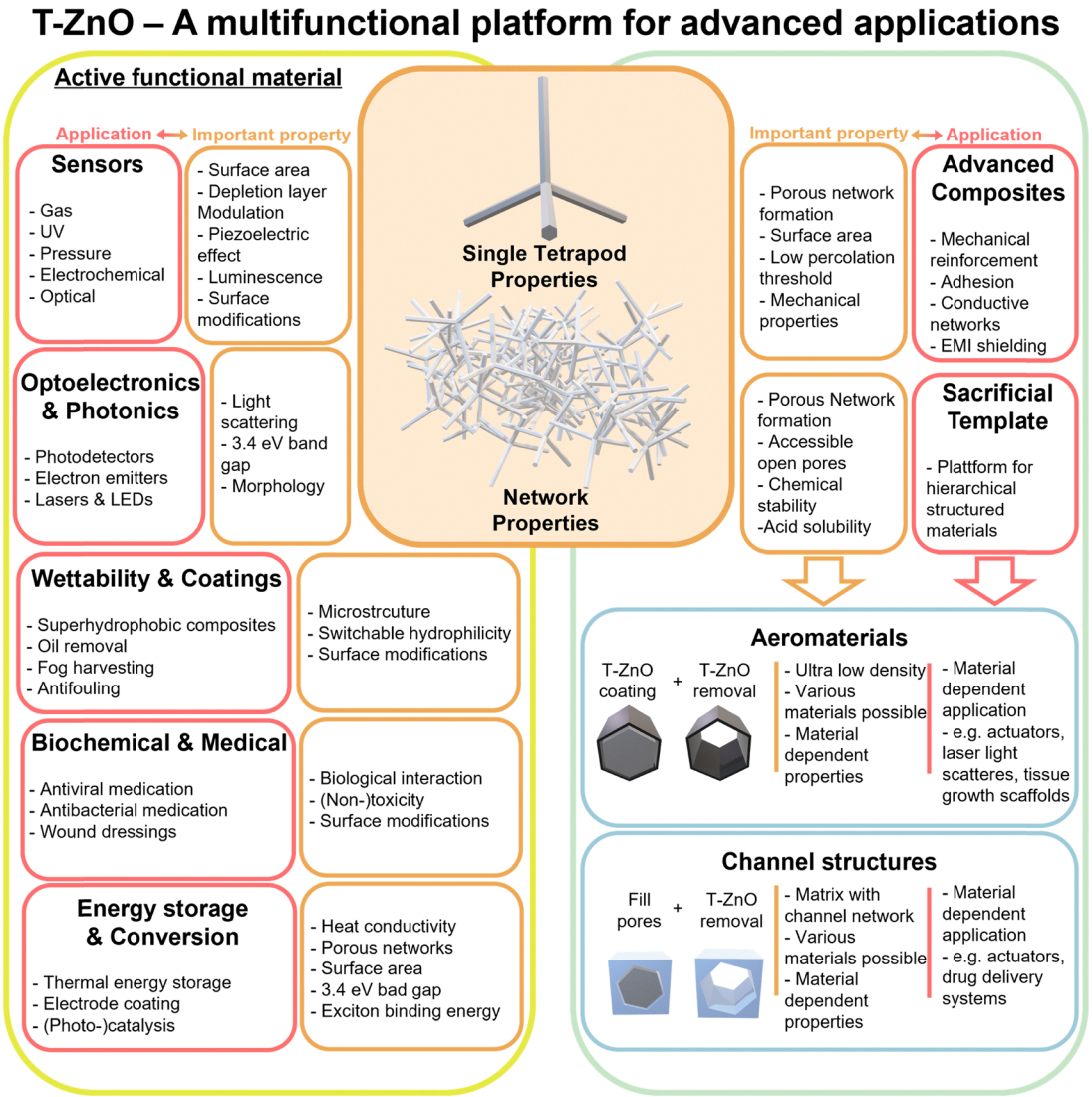

Fig. 47 T-ZnO as a multifunctional application platform. The unique interplay between the properties of individual T-ZnO tetrapods and extended T-ZnO networks (orange boxes) unlocks a wide range of applications (red boxes). These can be broadly divided into two categories: (i) T-ZnO as an active functional material, where its intrinsic properties are directly utilized, and (ii) T-ZnO as a structural element, where it either enhances composite performance or serves as a sacrificial template to transfer its unique 3D network architecture into aeromaterials and channel structures (blue boxes).

4.1.1 Sensing applications

4.1.1.1 Chemiresistive sensors (gas). The high specific surface area (Section 3.6.1) and semiconducting nature (Section 3.2) of T-ZnO make it well suited for chemiresistive sensing, where changes in electrical resistance are induced by interactions with the chemical environment or radiation. In gas and UV sensors, the tetrapodal morphology offers a clear advantage over simpler particle shapes. It suppresses dense agglomeration and preserves a high accessible surface area.

Gas sensing with T-ZnO has been extensively studied. The sensing mechanism is based on resistance changes caused by the interaction of target gas molecules with chemisorbed oxygen ions on the ZnO surface. These interactions modulate the electron depletion layer and alter conductive pathways (Fig. 48a). This field was comprehensively reviewed in 2018[12] and significant progress has since been made, particularly in improving sensitivity and selectivity (Section 3.6.4). For example, Poschmann *et al.*[102] coated T-ZnO with a thin ZIF-8 layer. This formed a molecular sieve that enabled highly selective hydrogen sensing even in the presence of methane. Their device achieved fast response times (1–2 s), low operating temperature (100 °C), and a reported 60-fold sensitivity enhancement. While promising, such approaches raise concerns regarding long-term stability in humid environments and the scalability of multi-step fabrication processes.

In a similar vein, the combination of T-ZnO with graphene oxide[185] and CuO[186,187] have been reported as materials for selective hydrogen gas sensors. A further effective method involves surface modification of T-ZnO with $ZnFe_2O_4$. This has also demonstrated promising results in enhancing selectivity in gas sensing applications. For example, Mei *et al.*[188] coated the surface of T-ZnO *via* a hydrothermal approach and tested the material as a gas sensor for different volatile organic

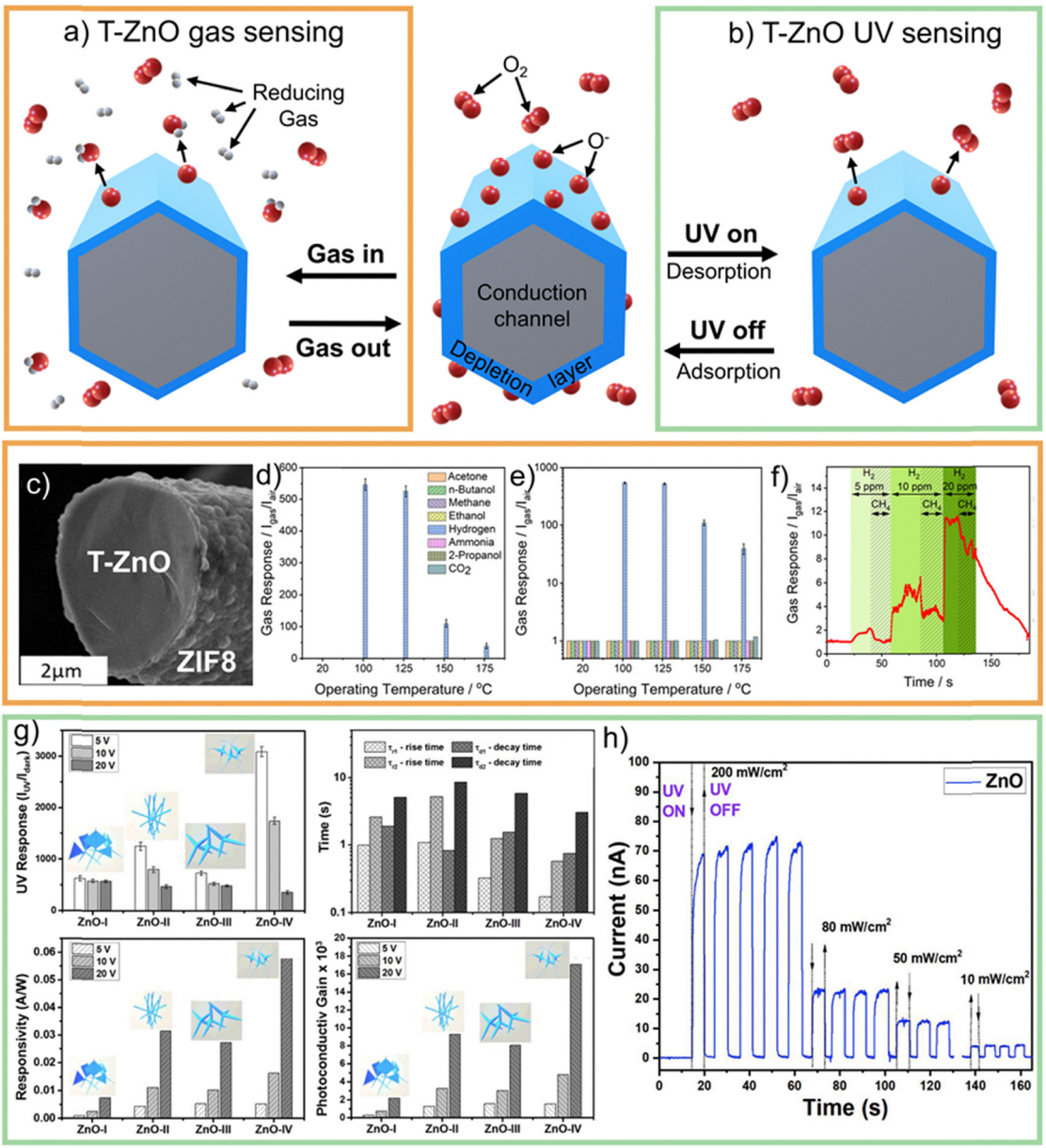

Fig. 48 Chemoresistive sensing mechanism in T-ZnO. A cross-section of a T-ZnO arm illustrates surface depletion layer modulation. In the dark or with oxidizing gases, adsorbed oxygen ions (O_2^-) capture electrons, narrowing the conductive channel and increasing resistance. Conversely, (a) reducing gases or (b) UV irradiation release trapped electrons, widening the channel and lowering resistance.[37,86] (c)–(f) Surface modification of T-ZnO with ZIF-8, detailing gas sensing responses to various gases across different temperatures on (d) linear and (e) logarithmic scales, alongside response curves for H_2/CH_4 mixtures, collectively highlighting enhanced H_2 sensitivity.[102] (g) UV sensitivity of gas sensor measurements for different T-ZnO morphologies and (h) dynamic response under varying UV light intensities.[202] (c)–(f) Reproduced from ref. 102 with permision from American Chemical Society,[102] Copyright 2023, (g)–(h) reproduced from ref. 202 with permision from Elsevier,[202] Copyright 2019.

compounds (VOCs) and reported a high selectivity for ethanol. Li *et al.*[189] coated the surface of T-ZnO with a $ZnFe_2O_4$ as well, using a wet-chemical approach followed by a calcination step. Their material shows satisfactory results as a H_2S sensor with a detection limit of 2 ppm at 250 °C. Next to the detection of hydrogen,[102,185,186,190,191] ethanol[188,192] and H_2S,[189] T-ZnO based gas sensors have been discussed for the detection of O_2,[193] NO,[194] methane[195,196] and different VOCs.[197,198]

Interestingly, these results are obtained even though the most chemically active sites, the polar {0001} facets at the tetrapod tips (Section 3.6.2), contribute only weakly to the electrical percolation pathways. These pathways are dominated by less reactive non-polar side-facet junctions. Moreover, most studies employ tetrapods with micrometer-scale arm diameters. However, Gupta *et al.*[196] showed that significantly higher sensitivities are achieved when the arm diameter approaches the nanometer-scale depletion layer thickness, where charge transport becomes strongly surface-controlled.

Despite promising laboratory-scale results, several challenges remain critical for real-world implementation. Humidity

cross-sensitivity, the frequent need for elevated operating temperatures (100–250 °C),[199,200] and insufficient long-term stability testing remain recurring issues. From an outlook perspective, future research should focus less on demonstrating new analytes. Instead, it should prioritize systematic optimization of morphology, defect concentration, and network architecture, as well as strategies enabling room-temperature operation and robust signal compensation.

4.1.1.2 Chemiresistive sensors (UV). Complementing its utility in gas detection, T-ZnO is also highly effective for UV sensing. UV light below ~375 nm excites electrons from the valence to the conduction band (Section 3.3.1), generating charge carriers that decrease resistance. Simultaneously, holes migrate to the ZnO surface, react with adsorbed oxygen, and release electrons back into the conduction band (Fig. 48b). This combines photogeneration with surface chemistry (Section 3.6.2). The high exciton binding energy of ZnO (60 meV, Section 3.2.1) enables room-temperature UV detection. Compared to spherical ZnO particles, T-ZnO exhibits superior sensitivity, response, and recovery times. This is primarily due to its highly porous, three-dimensional network, which increases accessible surface area and enhances interactions with oxygen and UV radiation.[52,86,120,197,201–203] Although T-ZnO generally exhibits superior UV-sensing properties compared to spherical ZnO particles, further optimization of its morphology and size holds the potential to enhance sensor device performance. Ilickas *et al.*[86] compared different T-ZnO sizes regarding UV sensitivity. T-ZnO arm diameters of approximately twice the L_D showed the best sensing performance. This is a key parameter whose influence on charge transport was introduced in Section 3.2.3. These results agree with the findings by Postica *et al.*,[202] who discussed the influence of different T-ZnO morphologies on UV sensitivity. They demonstrated that T-ZnO with thin and long tips and diameters close to the L_D shows the best UV sensitivity (Fig. 48g and h). *Via* a functionalization of T-ZnO with CNTs further improvement of the UV sensing performances is possible due to an improved carrier separation at the T-ZnO/CNT interface. The superior UV-detection capabilities of T-ZnO are increasingly being validated in real-world applications (*e.g.*, monitoring UV exposure in ruminant animals[201]). This demonstrates that the reliability and robustness of T-ZnO-based UV sensors have already reached a high level.

Collectively, these findings for both gas and UV sensing highlight a key design principle. The unique, high-surface-area network of T-ZnO amplifies its intrinsic semiconducting properties, making it an excellent platform for next-generation chemiresistive sensors. An additional critical design consideration, often overlooked, is the tetrapod arm diameter. Ideally, this should match the depletion layer thickness to maximize sensitivity.[86,196,202]

4.1.1.3 Electromechanical sensors (pressure & strain). The piezoelectric properties (Section 3.5) and mechanical robustness (Section 3.4) of T-ZnO enable its use in pressure sensors. These devices either generate a voltage proportional to applied force *via* the piezoelectric effect or show a change in capacitance *via* the capacitive effect (Fig. 49a). Although T-ZnO is intrinsically piezoelectric, the random orientation of tetrapods in a composite matrix causes the piezoelectric potentials of individual arms to largely cancel, limiting the macroscopic response. Consequently, capacitive sensors are often more effective. Here, T-ZnO is embedded in a polymer matrix (*e.g.*, PDMS or polyvinylidene fluoride, PVDF) to form dielectric structures whose capacitance changes under mechanical force. The interlocking tetrapod network provides high compressibility and resilience for enhanced sensitivity (Fig. 49b). These T-ZnO/polymer composite sensors[204] yield mechanically robust devices while maintaining high sensitivity, with detection limits as low as 1 Pa.[36,51,94,205–208] These sensors have been tested for advanced technologies especially in biomedical applications. For example, Wang *et al.*[94] presented a pressure sensor based on a T-ZnO/PDMS composite with a sensitivity of 182.5 mV N^{-1}. This demonstrated distinct responses to objects of varying stiffness and highlighted its potential use as an end-effector component in surgical robots (Fig. 49c–f). This technology is further developed in several studies enabling detection of body movements by athletes[206] or the flexion and detection of fingers, which is usable to directly translate sign language.[205]

The practical application of these sensors, however, requires addressing several challenges. One key issue is mechanical hysteresis in the polymer matrix, where the material does not immediately return to its initial state, potentially causing signal drift. The long-term durability and fatigue resistance under thousands of compression cycles are also critical for wearable or robotic applications. These factors are highly dependent on the interfacial adhesion between the T-ZnO filler and the polymer matrix. Moreover, as noted by Liu *et al.*[206] these composites can exhibit cross-sensitivity to temperature and humidity, which can interfere with the pressure signal. Future work must focus on developing materials with reduced hysteresis and implementing compensation algorithms to deconvolve pressure signals from these environmental variables.

Such signal disentanglement can even enable multifunctional sensing, as demonstrated by Wang *et al.*,[209] who reported a sensor capable of independently detecting multiple stimuli, including strain, temperature, and the contacted material. This was achieved by minimizing signal interference *via* machine-learning-based separation of the underlying physical effects. Furthermore, functionalization of T-ZnO (*e.g.*, with laccase-like oxidase) enables additional sensing modalities, such as lactate concentration.[207] This establishes T-ZnO as a versatile platform for pressure sensors with advanced signal-processing capabilities.

To proceed in the field of T-ZnO based pressure sensors, systematic investigations of tetrapod size, network concentration, and defect density are needed. Understanding their effects on sensor sensitivity would be highly valuable for identifying optimal T-ZnO design parameters. At present, existing studies vary widely in these and other parameters. Tetrapod sizes, for example, range from a few micrometers[205,209] to several hundred micrometers.[207,208] This variability makes it difficult to draw clear conclusions about their influence on performance.

4.1.1.4 Optical & electrochemical biosensors. Beyond chemiresistive and mechanical sensing, T-ZnO's unique combination

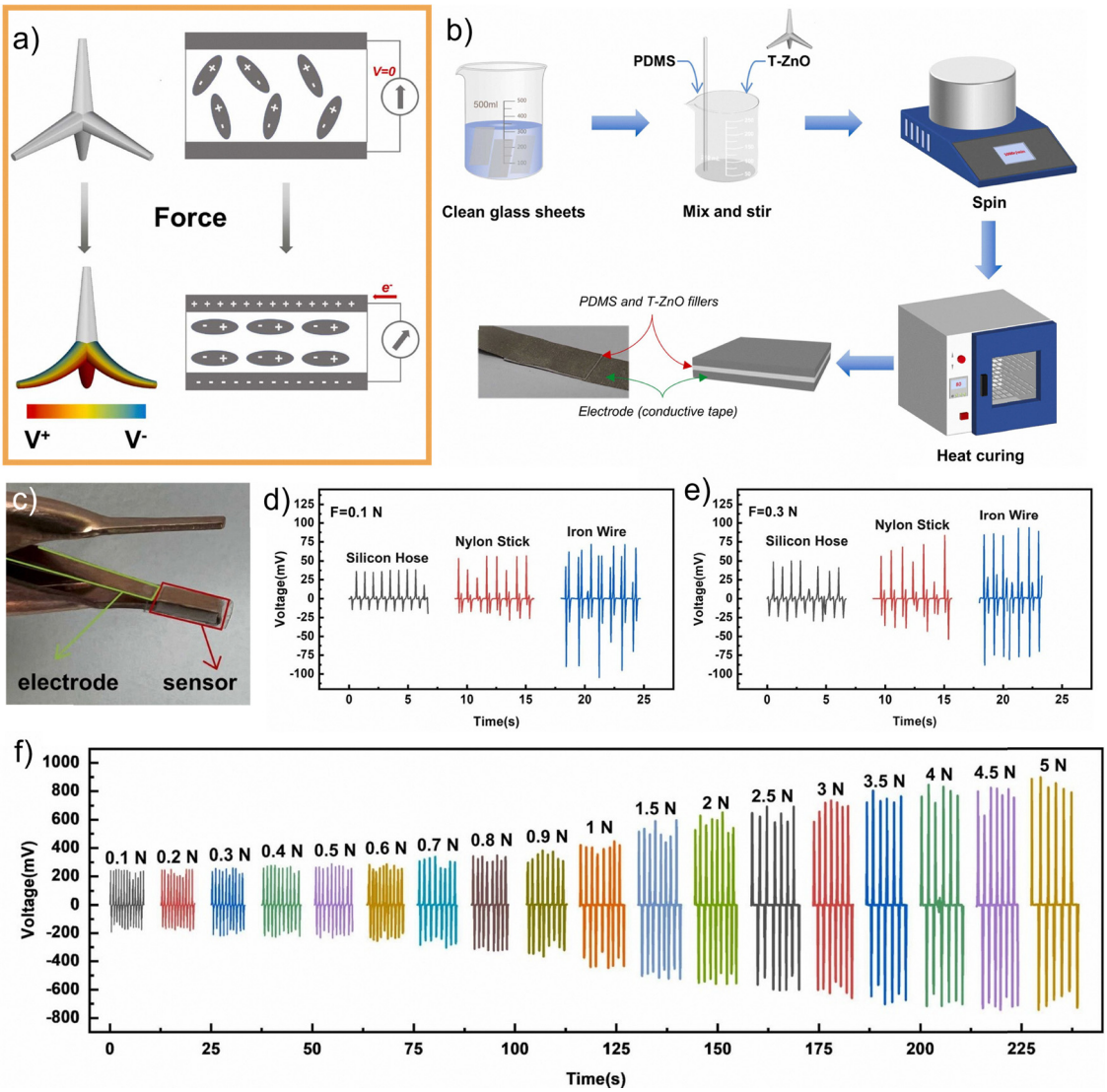

Fig. 49 Piezocapacitive sensing mechanism in T-ZnO. (a) Schematic illustration of the piezocapacitive effect. (b) Fabrication process of a T-ZnO/PDMS thin film sensor. (c) Photograph of the T-ZnO/PDMS-based piezocapacitive device. (d) and (e) Output voltage signals when gripping different materials under applied forces of 0.1 N and 0.3 N, respectively. (f) Voltage response of the sensor to varying gripping forces from 0.1 N to 5 N. (a)–(f) Reproduced from ref. 94 with permision from Elsevier,[94] Copyright 2024.

of high surface area, strong optical response, and good electrical conductivity makes it an ideal scaffold for advanced biosensors. Its 3D architecture provides a stable and accessible platform for immobilizing biological recognition elements (like enzymes or antibodies), whose activity can then be read out using various signal transduction methods, primarily optical and electrochemical (Fig. 50a).

The optical properties of T-ZnO (Section 3.3) expand the materials sensing capabilities to further sensing applications under wet conditions. In such sensing devices, detection often relies on the quenching effect (decreasing effect on the PL intensity) of target molecules on the PL of T-ZnO under UV irradiation. The high crystal quality of T-ZnO arms provides a strong and stable baseline PL signal, while their high surface area allows for a dense functionalization with bioreceptors, amplifying the quenching effect and boosting sensitivity. Fundamentally, the efficiency of this quenching process depends on the precise energy level alignment between the T-ZnO band edges and the analyte's molecular orbitals. This factor can be significantly influenced by surface defects (Section 3.1.3), which act as competing recombination pathways. For example, Li *et al.*[210] used this mechanism to detect dopamine in a 3D-printed hydrogel containing neurons, opening avenues for creating self-monitoring, 3D-printed tissues as *in-vitro* models for neurological diseases. The self-monitoring 3D tissue might also become an alternative for animal testing regarding its higher degree of conformity with real human tissue compared to 2D cultures (Fig. 50b and c). The PL modifiying sensing mechanism has also shown its usability for tetracycline,[107] streptavidine[211] and SARS-CoV-2[212] sensors. However, regarding real-world applicability, several challenges remain. In particular, small variations in synthesis conditions, defect concentration,

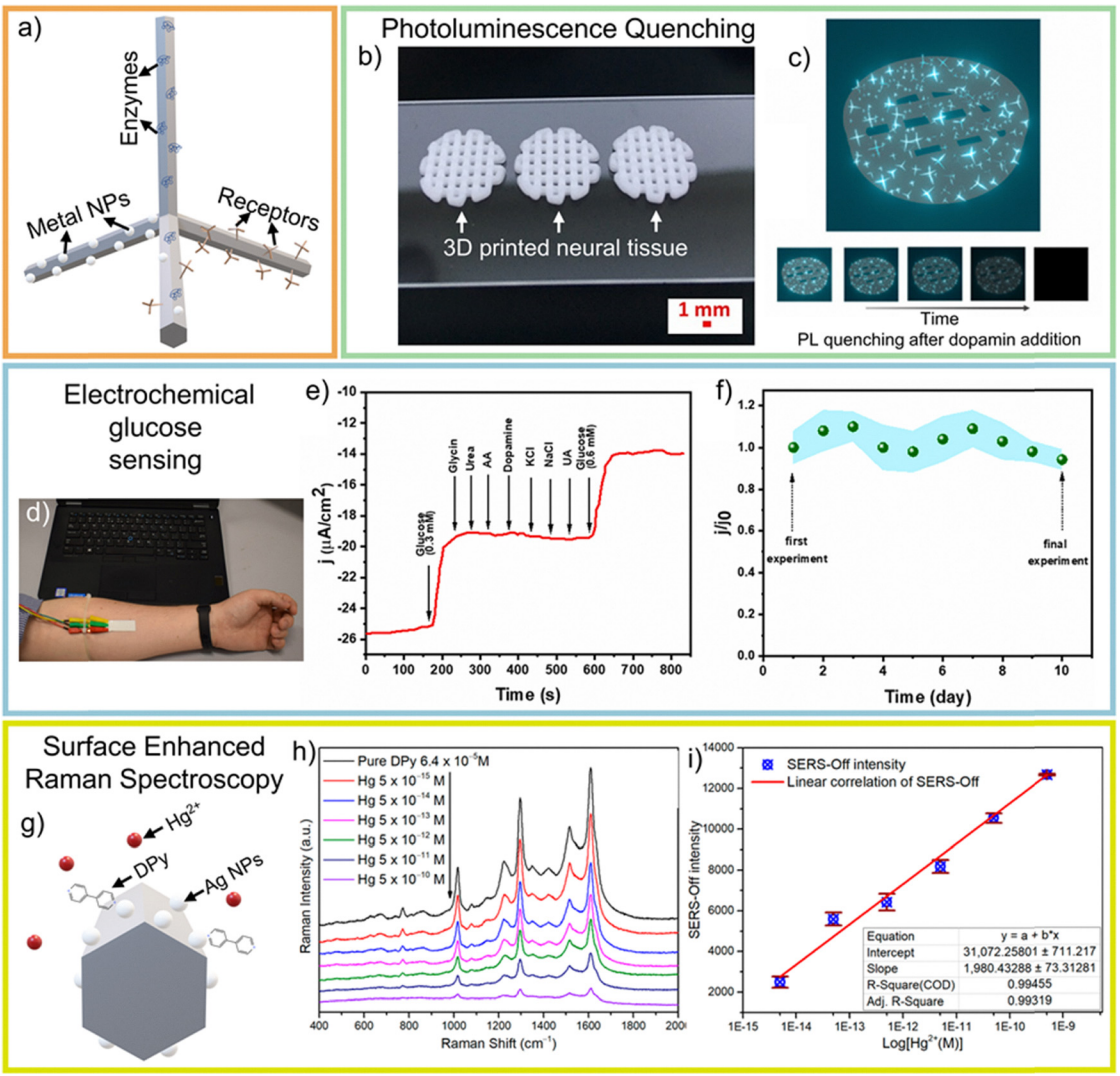

Fig. 50 Optical & electrochemical biosensors. (a) For biosensing, T-ZnO can be surface-functionalized with various materials such as metal nanoparticles, enzymes, or other bioactive molecules. (b) Photograph of a T-ZnO-containing bioprinted scaffold. (c) PL quenching observed after dopamine addition to the scaffold.[210] (d) Photograph of an electrochemical glucose sensor incorporating T-ZnO. (e) High selectivity of the sensor toward glucose. (f) Stable performance for sweat-based glucose detection over several days.[213] (g) Schematic of a T-ZnO arm functionalized with Ag nanoparticles and DPy in a mercury ion environment. (h) Detection of Hg^{2+} ions using this composite *via* SERS (i) Sensitivity reaching the femtomolar range.[219] (a)–(c) Reproduced from ref. 210 with permision from Elsevier,[210] Copyright 2023, (d)–(f) reproduced from ref. 213 with permision from Elsevier,[213] Copyright 2022, (h)–(i) reproduced from ref. 219 with permision from MDPI,[219] Copyright 2021.

and the degree of broken tetrapods can significantly affect luminescence properties (*e.g.*, intensity; Section 3.3), posing challenges for the reproducible production of sensors with consistent performance.

Moreover, T-ZnO has been explored as a sensing material for glucose detection, where its interconnected network provides efficient pathways for electrochemical signal transduction.[213–215] For example, Myndrul *et al.*[213] coated a flexible electrode with MXene coated T-ZnO, which was modified with glucose oxidase and coated with a Nafion layer to fix the enzyme. The resulting sensor is flexible and can be attached to the skin (Fig. 50d–f). There it can selectively determine the glucose concentration of the sweat, showing good correlation to the glucose concentration in the blood and with a detection limit of 17 μM. This non-invasive approach could be a relief for diabetes patients. While promising, it is important to note that the physiological correlation between sweat and blood glucose is complex and remains a subject of clinical debate, representing a significant challenge for the real-world application of any sweat-based glucose sensor.[216] Such electrochemical sensing mechanisms for biomarker molecules are not limited to sugars but can also be extended to other analytes such as uric acid[217] or epidermal growth factor receptor 2 (HER-2),[218] a key biomarker for breast cancer. Despite these initial promising results on electrochemical sensing with T-ZnO-based sensors, further studies are needed to evaluate long-term stability. Early reports indicate changes in sensor performance[218] and many studies do not assess long-term effects.[214,217] With improved understanding in this direction, electrochemical

T-ZnO-based sensors could become a cost-effective and minimally invasive option for clinical biomarker monitoring.

Furthermore, The unique geometry of T-ZnO can be leveraged to create plasmonic ''hot spots'' for SERS biosensor,[219–221] enabling ultra-low detection limits. Tangsuwanjinda *et al.*[219] demonstrated this by decorating T-ZnO with Ag nanoparticles and 4,4′-dipyridyl (DPy), which allowed the system to detect Hg^{2+} ions in the femtomolar range (Fig. 50g–i). However, the use of this sensor is tied to the possession of a typically expensive Raman spectrometer, which may be a barrier to the widespread adoption of this technique.

Overall, T-ZnO-based biosensors represent a promising branch of T-ZnO-based sensing technologies, but they typically face challenges common to the field.[222] A primary challenge is non-specific binding, where unwanted molecules from complex biological fluids (like blood) adhere to the surface, causing false signals.[223] The long-term stability of the immobilized bioreceptors and the potential for Zn^{2+} ion leaching, which could affect both the sensor's function and local cell viability, also require careful consideration.[224] Finally, developing robust methods for calibrating these sensors, especially for wearable and *in-vivo* applications, remains a critical step for their translation from the lab to clinical use.

4.1.2 Optoelectronics & photonics. The optical properties of T-ZnO (Section 3.3) are not exclusively interesting for sensing applications but also for different optoelectronic devices and photonics. Here, the unique architecture of T-ZnO provides distinct advantages, from enhanced light-trapping in photodetectors to forming natural resonant cavities for microlasers. On the one hand the direct optical properties of T-ZnO are useful to create innovative devices and on the other hand aeromaterials created by a sacrificial template approach using T-ZnO networks (Section 4.3) show advanced optical properties, interesting for manifold applications (*e.g.* laser light scattering). The latter are covered in Section 4.3.2.2.

T-ZnO has been explored as an active component in various optical and electronic devices.[225–228] For instance, Giubileo *et al.*[225] investigated the application of T-ZnO tips as electron-emitting elements. Their study demonstrated that T-ZnO exhibits stable electron emission with a low turn-on voltage of just 7 V. This combination of stability and low operating voltage suggests its potential utility in applications where energy efficiency and compact device design are critical. However, for practical field emission devices, the crucial next step is to evaluate the long-term operational lifetime under continuous operation, as high-field emission can lead to tip degradation.

Karthick *et al.*[226] demonstrated that the integration of T-ZnO with a p-type silicon wafer results in a robust photodetector, where the 3D network can improve performance through enhanced light scattering and efficient charge collection pathways. This benefit, however, comes with a critical trade-off: the numerous inter-tetrapod junctions that form the network can also act as potential barriers or trap states, which may limit the device's response speed. Furthermore, PL,[88,97,229,230] WGMs[231] (which make individual arms ideal micro-resonators for lasing), and second harmonic oscillation[232] of T-ZnO are discussed in the literature,[88,97,229–232] regarding their use in different optoelectronic devices.

Realizing high-quality WGM lasing, however, is critically dependent on synthesizing T-ZnO with exceptionally smooth crystallographic facets, as surface roughness can dramatically suppress the resonant modes (Section 3.3.3). While these phenomena are promising for different optoelectronic devices, the long-standing difficulty in achieving stable p-type ZnO remains a significant hurdle for developing efficient T-ZnO-based LEDs. Ultimately, a key challenge for the field is bridging the gap from demonstrating these powerful optical phenomena in single, isolated tetrapods to developing scalable fabrication methods for creating reliable, large-area devices.

4.1.3 Surface engineering & environmental control

4.1.3.1 Advanced wettability and coatings. The development of superhydrophobic and superhydrophilic surfaces plays a major role in materials science due to their broad applicability, including water harvesting and antifouling. T-ZnO is a versatile material for tuning surface wettability, as it can exhibit both hydrophilic and hydrophobic behavior. This switchable wettability arises from changes in the surface concentration of oxygen vacancies, which can be induced, for example, by UV irridiation or thermal treatment (Fig. 51a). T-ZnO can also increase surface roughness, reducing solid–liquid contact and thereby increasing the contact angle, which enables superhydrophobic surfaces, especially when combined with hydrophobic polymers (Section 3.6.3). The combination of tunable surface chemistry and inherent 3D microtexturing makes T-ZnO a highly effective component for advanced functional coatings.

Superhydrophobicity has been achieved in several studies utilizing T-ZnO. Typically, a polymer precursor is mixed with T-ZnO and applied to a surface, for example by spray coating. Yamauchi *et al.*[233] presented such an approach, combining T-ZnO with PDMS to either cast a monolith or spray-coat a thin film onto a target substrate. The authors describe the resulting composite structure as analogous to a porcupine fish, where the flexible PDMS matrix mimics the skin and the rigid T-ZnO tetrapods resemble scales that create surface roughness. The resulting composite exhibits superhydrophobic behavior, with a water contact angle of 150°, which remains stable even after mechanical abrasion and bending (Fig. 51b).

Through adapting the microstructure in to a gecko-, petal- or lotus-like surface structure of a PDMS/T-ZnO composite *via* different coating approaches, the water contact angle is modifiable as shown by Weng *et al.*[234] (Fig. 51c). Furthermore, the quality of T-ZnO-based superhydrophobic coatings can be monitored *via* their PL response after abrasion. Increased abrasion cycles cause more cracking of the T-ZnO particles, generating new surfaces and defects, which in turn increase the overall PL. This effect provides a non-destructive method for quality control, as demonstrated *via* T-ZnO-methacrylate copolymer composites by Liu *et al.*[135] Additional composites exhibiting similarly pronounced superhydrophobic properties have been reported, further demonstrating the versatility and applicability of T-ZnO-based materials for the fabrication of superhydrophobic surfaces.[119,235–242]

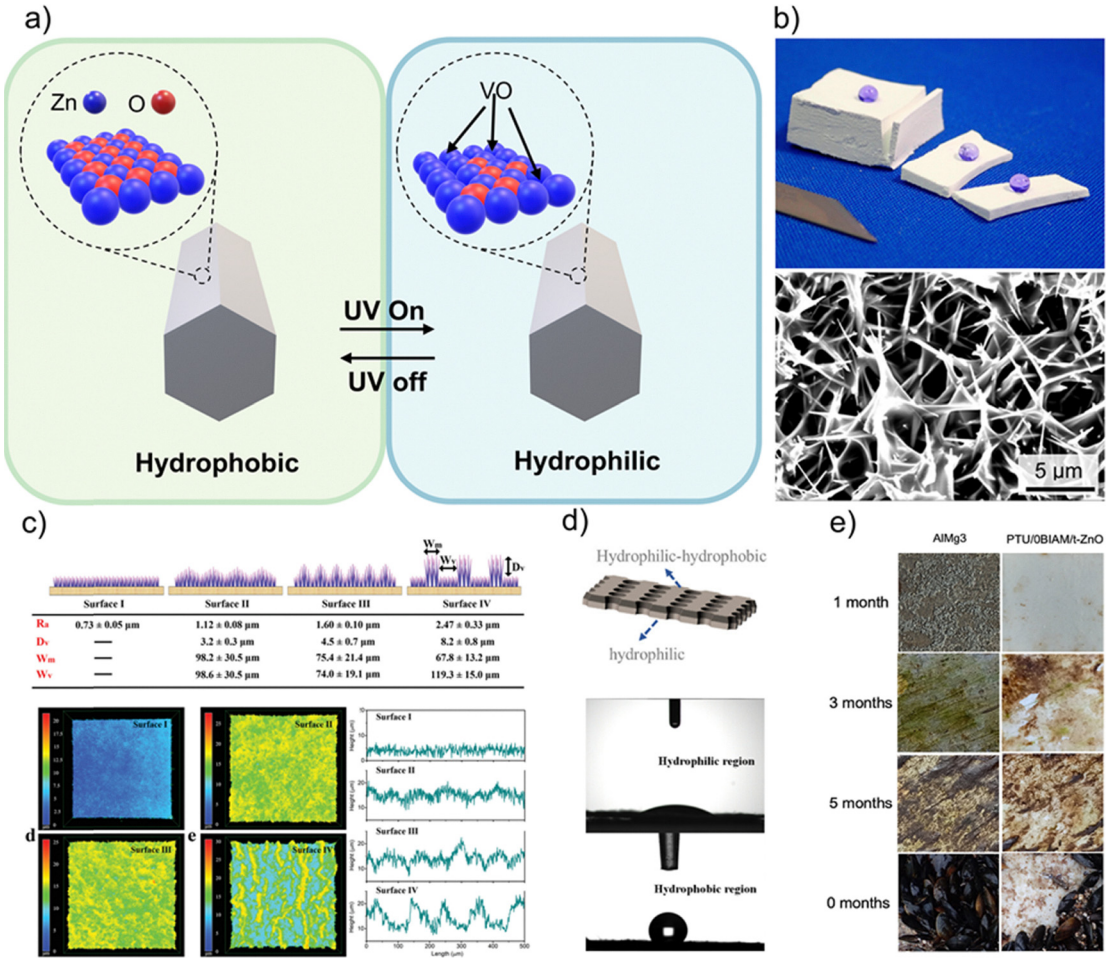

Fig. 51 T-ZnO wettability and coatings. (a) UV irradiation enhances T-ZnO water wettability by increasing the concentration of surface oxygen vacancies (VO). (b) Superhydrophobic T-ZnO/PDMS composite and its corresponding SEM microstructure.[233] (c) Tailoring of the T-ZnO/PDMS microstructure enables precise control over hydrophilicity.[234] (d) Schematic of T-ZnO-incorporated Janus membranes exhibiting distinct dual-sided wettability for fog-harvesting applications.[249] (e) Antifouling effects of T-ZnO-based coatings against marine biofouling.[253] (b) Reproduced from ref. 233 with permision from American Chemical Society,[233] Copyright 2019, (c) Reproduced from ref. 234 with permision from Wiley,[234] Copyright 2022, (d) Reproduced from ref. 249 with permision from American Chemical Society,[249] Copyright 2023, (e) Reproduced from ref. 253 with permision from Elsevier,[253] Copyright 2023.

Wettability is not only relevant in water-based systems. Bajpayee *et al.*[243] developed a superhydrophobic composite coating comprising T-ZnO, amorphous silica, and fluorinated polyhedral oligomeric silsesquioxane (F-POSS). The combination of multiscale surface texturing, enabled by the T-ZnO and chemical surface functionalization with F-POSS not only renders the surface non-wettable by low surface tension liquids such as alcohols and *n*-hexadecane. The resulting minimization of the contact area between the liquid and the surface further effectively suppresses ice nucleation by inhibiting heterogeneous nucleation at the solid–liquid interface. Furthermore, anti-icing surfaces based on T-ZnO/PDMS composites have been reported by Weng *et al.*[244,245]

Although most studies on T-ZnO composite coatings focus on superhydrophobicity, T-ZnO can also be employed to create superhydrophilic surfaces. This has been demonstrated for a T-ZnO coating functionalized with perfluorooctanesulfonate, achieving a water contact angle of 0° and a contact angle of 160° for viscous oil. When applied to a stainless-steel mesh with micrometer-scale pores, the coating functions as an effective separation membrane, enabling the removal of residual oil from water-oil mixtures, with purified water containing less than 300 ppm of oil.[178]

In conclusion, T-ZnO is a versatile material for creating both superhydrophobic and superhydrophilic surfaces. Tetrapod sizes in the micrometer range from a few micrometers[233,237,240] up to hundred micrometers[235,236] appear sufficient for these applications. Surface homogeneity does not seem critical, as both uniform[233] and non-uniform tetrapods[236,238] can achieve superhydrophobicity. However, tetrapod density appears to influence hydrophilicity.[236] To confirm these trends, further studies with more systematically comparable parameters are desirable. Furthermore, several challenges remain to be addressed. Although abrasion stability has been tested with promising results,[233] the long-term stability of T-ZnO-based coatings is still uncertain, since the switchable hydrophilicity may become

problematic if oxygen vacancy concentrations change over time, requiring repeated treatments such as UV irradiation. Yet, UV exposure could also activate the photocatalytic properties of T-ZnO, potentially degrading both the coating itself and commonly used polymer matrices. In particular, polymers such as PDMS are prone to UV-induced decomposition.[246] Furthermore, many reported composites combine T-ZnO with fluorinated polymer matrices.[178,235,243] While such systems demonstrate excellent performance, fluorinated polymers pose significant health and environmental risks and are subject to increasing regulatory restrictions.[247] Their use should therefore be avoided. T-ZnO, however, may enable the development of coatings with comparable performance without relying on fluorinated polymers.[233,234]

In addition to superhydrophobic and superhydrophilic surfaces, advanced T-ZnO-based composites with switchable, heterogeneous, or patterned wettability have been investigated in several studies, enabling their use in applications such as oil–water separation and fog harvesting.

Switchable wettability can be achieved, for example, by functionalizing a T-ZnO/PDMS composite with azobenzene molecules. Upon UV irradiation, the azobenzene moieties undergo a trans-to-cis isomerization, rendering the surface hydrophilic. Subsequent exposure to visible light reverses this process, restoring the *trans* configuration and thus hydrophobic surface properties. The switching occurs within several minutes, with the water contact angle shifting from approximately 140° (hydrophobic) to 40° (hydrophilic) and back. This dynamic behavior enables the material to be used for selective separation processes, such as oil removal from water-oil mixtures or water removal from oil–water mixtures, depending on the desired wettability state.[155,248]

Furthermore, the design of surfaces with spatially heterogeneous wettability has attracted considerable interest for enabling multifunctional membranes with directionally controlled fluid transport. In this context, Janus membranes, characterized by distinctly different surface properties on each side, offer unique opportunities for applications such as fog harvesting (Fig. 51d). Liu *et al.*[135] proposed an approach for fog harvesting using T-ZnO coatings, in which a cotton fabric was coated with a T-ZnO/poly(methyl methacrylate) (PMMA) composite. Patterned wettability was achieved through selective UV illumination. During fog harvesting experiments, water droplets nucleated and accumulated on the hydrophilic regions, while droplets on the hydrophobic areas rolled off, enabling efficient water transport. These patterned wettability fog harvesters demonstrated a water collection rate of 3.4 mg min^{-1} cm^{-2}. Following a similar concept, Chenxi *et al.*[249] synthesized Janus membranes for fog harvesting, showing high stability against UV exposure and abrasion by sand, conditions typical of dry environments such as deserts. Their membranes exhibited fog harvesting efficiencies of 28.3 mg min^{-1} cm^{-2}. Li *et al.*[250] developed a Janus membrane by spray-coating one side of a copper mesh with a T-ZnO/PDMS composite while growing $Cu(OH)_2$ nanoneedles on both sides. The T-ZnO/PDMS-coated side exhibited hydrophobicity with a water contact angle of 153°, whereas the opposite side, composed solely of $Cu(OH)_2$ nanoneedle arrays, was hydrophilic. This asymmetric wettability facilitated condensation on the hydrophobic side, and the resulting surface energy gradient induced a Laplace pressure-driven transport of water to the hydrophilic side, where it could be efficiently harvested at rates up to 30.8 mg min^{-1} cm^{-2}. These fog-harvesting efficiencies are comparable to those of the latest high-performance fog-harvesting devices.[251]

Overall, T-ZnO demonstrates significant potential for applications requiring switchable, heterogeneous, or patterned wettability. While preliminary studies have shown promising performance in abrasion tests[155,248] and repeated cycle,[250] the long-term stability and effectiveness of the necessary complex composites remain untested. With further investigation into their durability, both intrinsic properties and microscale structural features of T-ZnO-based materials could be leveraged to address challenging wettability application requirements. These technologies may find broader applications in areas such as fog harvesting.[135,249,250]

Applied research on T-ZnO composite coatings is also highly relevant in the field of antifouling. Fouling presents substantial challenges, particularly in the shipping industry, where surface deterioration and increased roughness lead to higher fuel consumption and thus to elevated CO_2 emissions. The surface structure and wettability of T-ZnO-based antifouling coatings reduce the adhesion of fouling organisms, resulting in decreased growth of marine organisms at the surfaces and surfaces that are easier to clean (Fig. 51e).[252–254] Additionally, some antifouling coatings have demonstrated a reduction in $CaCO_3$ crystal deposition, which commonly occurs in water pipes and can cause serious issues such as blockages and corrosion.[255] These findings demonstrate that T-ZnO enables coatings capable of significantly extending duty cycles for surfaces exposed to aqueous media, from marine structures such as ship hulls[252,253] and fishing nets[254] to water distribution system,[255] by controlling surface structure and wettability. Moreover, T-ZnO-based coatings have been shown to be biocompatible and could therefore represent an eco-friendly alternative to the copper-based biocidal coatings commonly employed in marine environments. Nonetheless, the material quantities required for large-scale applications, such as ship hulls, are considerable, and industrial synthesis capacity is only beginning to reach the necessary scale.

Aside from T-ZnO-based coatings designed to engineer surface wettability, leveraging the intrinsic wettability of T-ZnO and its unique structural features, several studies have introduced advanced coatings and composites that further exploit further properties of T-ZnO, such as its chemical reactivity and interlocking structures.[256–258]

For instance, Liu *et al.*[256] developed an aluminum phosphate coating for Ti-6Al-4V alloys incorporating Al_2O_3-coated T-ZnO particles. The T-ZnO releases Zn^{2+} ions, which facilitate crosslinking within the aluminum phosphate matrix. The Al_2O_3 coating on T-ZnO controls the ion release rate, enabling smooth and homogeneous crosslinking. This coating process occurs at a low temperature of 70 °C, resulting in good adhesion, increased hardness, and crack-free coatings. The low

processing temperature is energy-efficient and prevents phase transformations in the alloy that could lead to increased brittleness. Another strategy, presented by Brindha *et al.*[258] used the unique tetrapodal structure of T-ZnO to develop polymer composite coatings with enhanced adhesion to Mg alloys. These coatings form effective barriers against aqueous electrolytes such as KOH, making them promising candidates for anode protection in primary Mg batteries. These findings demonstrate that coatings containing T-ZnO can exploit not only the interplay between wettability and microstructure but also other intrinsic properties, enabling the design of advanced high-performance coatings.

4.1.3.2 Particle-based systems for decontaminant adsorption. As discussed in the theoretical section (Section 3.6), T-ZnO exhibits noteworthy surface properties. In particular, individual tetrapods and T-ZnO networks possess a high and readily accessible specific surface area, which can be easily modified. These characteristics make T-ZnO highly suitable for decontamination applications, where contaminants are removed from a medium *via* adsorption. To enhance selectivity or maximize adsorption capacity, T-ZnO is frequently incorporated into composite materials.

In the literature, the main focus is on the development of T-ZnO-based adsorbents for the removal of heavy metal ions[179,259,260] or oil.[261] For example Sharma *et al.*[179] synthesized a composite containing T-ZnO and activated carbon, which demonstrated removal rates of Cr(VI) ions of up to 97%. In another approach, T-ZnO was coated with Fe_2O_3 nanorods and PDMS to form a nanocomposite capable of efficiently removing oil from wastewater. For instance, diesel removal rate is up to 96% and adsorption capacity 1135 mg g^{-1}. Through the magnetic Fe_2O_3 nanorods the composite can easily be removed from the cleaned water after adsorption of the oil.[261]

Although T-ZnO shows promising potential for wastewater decontamination, primarily due to its large and tunable surface area that enables efficient adsorption of contaminants, several drawbacks must be considered. ZnO itself is toxic to aquatic organisms, and if T-ZnO particles are not fully recovered after treatment, they may increase rather than reduce water toxicity. In acidic media, zinc ions can leach into the water, further contributing to ecotoxicity.[262,263] In addition, compared to established adsorbents such as activated carbon or zeolites,[264] T-ZnO remains relatively costly, which currently limits its broader applicability.

4.1.4 Biochemical & medical. Zinc oxide has a long history of use in medical applications, with therapeutic uses documented as far back as two millennia ago.[12,265] Despite this long-standing recognition of ZnO's healing properties, the fundamental biological mechanisms underlying its effects are only now being elucidated, largely due to interdisciplinary research bridging nanomaterial science and biomedicine. Numerous nanomaterials have been explored for therapeutic applications and often exhibit promising effects. However, many also display cytotoxic properties, which can diminish or even negate their therapeutic potential. ZnO nanomaterials, while offering attractive properties such as antibacterial activity, are not exempt from these issues and have been shown to exhibit cytotoxicity, for instance toward human colon carcinoma cells.[266] The toxicity of nano-ZnO is primarily attributed to the release of Zn^{2+} ions, which are chemically active and can induce oxidative stress and dam age in biological systems.[266,267]

In contrast, T-ZnO microparticles hold significant promise for biomedical applications. Due to their size, being larger than typical cells, they are typically not internalized *via* endocytosis, yet they still retain key nanoscale properties for medical applications. Moreover, compared to conventional ZnO nanoparticles with diameters of just a few nanometers, T-ZnO microparticles have a substantial, yet much lower, surface-to-volume ratio, which may reduce the release of Zn^{2+} ions. This characteristic may contribute to a lower cytotoxicity, making them a safer alternative for biomedical use.[58,182,268,269] Moreover, T-ZnO structures circumvent common drawbacks associated with conventional nanomaterial morphologies, such as nanoparticles or nanorods, including the tendency to agglomerate.[12]

As a result, research into the biomedical applications of T-ZnO has expanded significantly, culminating in the establishment of Phi-Stone AG, a company that produces good manufacturing practice (GMP)-certified, pharmaceutical-grade T-ZnO microparticles for medical applications. A notable commercial product is Afinovir, a wound protection gel that incorporates T-ZnO.[270]

4.1.4.1 Antibacterial and antiviral applicationsv. Several studies have reported the antibacterial and antiviral properties of T-ZnO. Among these, its antibacterial activity is the most extensively documented. Nevertheless, the underlying mechanism remains a subject of ongoing investigation. It is commonly proposed that the antibacterial effect arises either from the release of Zn^{2+} ions and/or the generation of ROS.[268,271] T-ZnO has been evaluated against a variety of bacterial strains, consistently demonstrating superior antibacterial performance (Fig. 52a). For instance, Collares *et al.*[272] incorporated T-ZnO as a filler in dental resin sealers and observed effective antibacterial activity against *Enterococcus faecalis*. Furthermore, the combination of T-ZnO with thin film based surface acoustic waves showed increased antibacterial properties.[273] Additional studies have further substantiated the antibacterial potential of T-ZnO.[271,274–281]

In addition to its antibacterial properties, T-ZnO also exhibits promising antiviral activity. Beyond the commonly discussed mechanisms, such as the release of Zn^{2+} ions and the generation of ROS, further antiviral mechanisms have been proposed. For instance, studies have shown that infections caused by Hepatitis E and Hepatitis C viruses can be inhibited by ZnO nanoparticles and T-ZnO structures.[282] This occurs through a dual mechanism. First, physical binding and entrapment of the viruses at the material surface prevents viral entry into host cells. Second, the material inhibits viral replication. However, compared to conventional ZnO nanoparticles, T-ZnO has demonstrated superior antiviral efficacy, which may be attributed to its unique morphology and the distinct crystal structures and surface facets.[282] The virus-trapping capability is

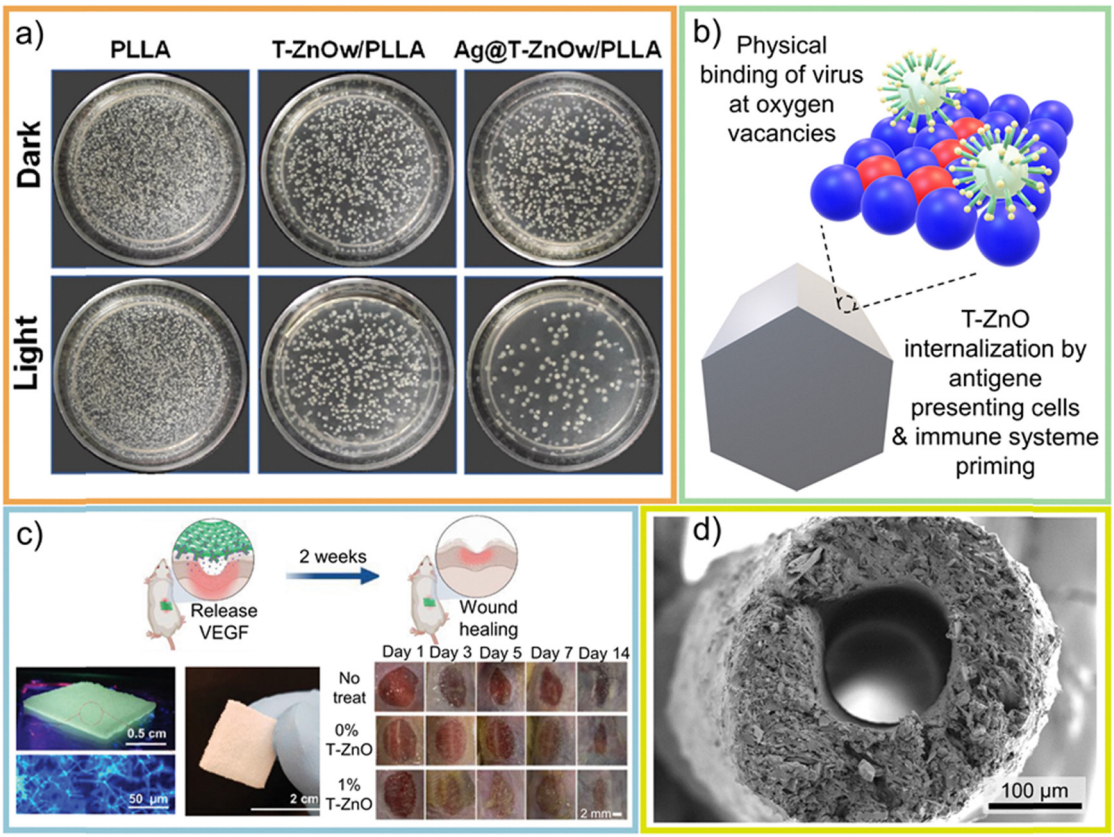

Fig. 52 (a) Antibacterial activity of T-ZnO/Ag NP/poly-L-lactic acid composites against *E. coli* on agar plates.[276] (b) Schematic of the proposed virus-trapping mechanism at oxygen vacancies on the T-ZnO surface, followed by internalization by antigen-presenting cells and subsequent immune system priming.[284] (c) Smart wound scaffold composed of T-ZnO, VEGF, and a hydrogel matrix, with *in vivo* testing on mouse wounds.[268] (d) SEM image of a glaucoma stent containing T-ZnO.[170] (a) Reproduced from ref. 276 with permision from Elsevier,[276] Copyright 2022, (c) Reproduced from ref. 268 with permision from Wiley,[268] Copyright 2021, (d) Reproduced from ref. 170 with permision from American Chemical Society,[170] Copyright 2023.

believed to be driven by oxygen vacancies at the surface of T-ZnO.[283] Additionally, viruses bound to T-ZnO can be internalized by antigen-presenting cells, thereby priming the immune system for a more effective response (Fig. 52b).[284] This antiviral activity makes T-ZnO a promising candidate not only for direct therapeutic applications but also for the development of antiviral surface coatings. Such coatings have been successfully demonstrated, for example, to reduce the infectivity of SARS-CoV-2.[285]

Antibacterial and antiviral applications represent one of the most advanced research areas for T-ZnO. Particularly noteworthy is its ability to entrap viruses at the T-ZnO particle surface[283] and promote their exposure to antigen-presenting cells, thereby priming the immune system.[284] These properties make T-ZnO highly attractive for tackling of viral diseases like Hepatitis E and C.[282] Intensive research in this field has already led to the development of first market-ready pharmaceutical products. Further long-term studies evaluating T-ZnO's effectiveness against additional diseases could further enhance the medical relevance of T-ZnO.

4.1.4.2 T-ZnO containing composites for biomedical applications. Not only the direct antibacterial, antiviral, or antifungal effects of T-ZnO are relevant for biomedical applications. Other properties, such as its mechanical stability and PL, are also of great interest. In many cases, it is the combination of multiple T-ZnO properties within composites that leads to highly effective biomedical products.

For example, Siebert *et al.*[268] developed a smart wound dressing platform by incorporating H_2O_2-modified and vascular endothelial growth factor (VEGF)-decorated T-ZnO into 3D-printed gelatin methacryloyl (GelMA) hydrogel wound patches. In this multifunctional system, T-ZnO plays several crucial roles. First, its intrinsic antibacterial properties reduce bacterial load at the wound site. Second, due to its large and accessible surface area, T-ZnO offers binding sites for bioactive molecules such as VEGF, which, in this design, can be released in a light-triggered manner within the optical spectrum (Fig. 52c). Additionally, the incorporation of T-ZnO as a filler material enhances the mechanical integrity of the hydrogel scaffold, contributing to the structural robustness of the wound patch. T-ZnO has also demonstrated its potential in other advanced wound dressing platforms, *e.g.* in a composite with alginate.[274] Furthermore, T-ZnO has been integrated with PDMS for the manufacturing of stents used in minimally invasive glaucoma surgery to effectively reduce intraocular pressure. Compared to stents

composed solely of PDMS, the composite stents exhibit an increased elastic modulus while maintaining sufficient flexibility to conform to the curvature of the eye (Fig. 52d). Moreover, the incorporation of T-ZnO reduces fibroblast viability, leading to antifibrotic properties upon implantation, likely due to the combined effects of surface roughness and the release of Zn^{2+} ions.[170,286,287]

Altogether, the combination of T-ZnO with other materials for biomedical applications has been explored through a variety of approaches. In these studies, multiple intrinsic properties of T-ZnO are often leveraged simultaneously. Most commonly, its inherent antibacterial activity is coupled with either its surface modifiability or its favorable mechanical properties.[170,268,274,288] Given the commercial availability of pharmaceutical-grade T-ZnO, the reported findings hold significant promise and are of considerable interest for further research and development.

4.1.5 Energy storage & conversion. The mechanical properties of T-ZnO, particularly its ability to form interconnected, open-porous networks (see Section 3.4.2), make it highly attractive for applications in energy storage and conversion. In the context of energy storage, the low percolation threshold of T-ZnO networks is of particular interest, as it allows control over thermal and electrical conductivity. For energy conversion, such as in (photo)catalytic processes, the open-porous architecture provides a large accessible surface area (Section 3.6.1), while the material's functionalization capabilities (Section 3.6.4) further enhance its utility in catalytic applications.

4.1.5.1 Thermal energy storage and batteries. Energy storage is one of the central challenges in the global transition from a fossil-based economy to one relying on renewable energy sources such as wind, solar, and hydropower. Unlike conventional fossil-fuel power plants that provide a stable and continuous energy output, renewable energy systems are inherently intermittent, with their output fluctuating according to diurnal cycles, weather conditions, and seasonal variations. As a result, robust and scalable energy storage solutions are essential to bridge the gap between energy supply and demand, both in the short and long term. These solutions range from widely adopted technologies like batteries to less conventional approaches such as thermal energy storage. T-ZnO has been investigated in several of these systems and has demonstrated the potential to enhance their performance at the laboratory scale.

One promising strategy to enhance the performance of energy storage systems is the integration of T-ZnO networks into phase change material (PCM) matrices.[48,289–291] For example, Balasubramanian *et al.*[48] utilized paraffin wax as an organic PCM. This material is capable of storing substantial amounts of thermal energy during its phase transition from solid to liquid and releasing it upon solidification. However, the practical application of paraffin wax is limited by its inherently low thermal conductivity. By incorporating T-ZnO structures into the paraffin matrix, the thermal conductivity was improved by up to 94% without compromising the material's latent heat capacity. This significant enhancement enables more efficient solar thermal energy harvesting and improved thermal management.

Moreover, T-ZnO structures have shown utility beyond organic PCMs. Zhu *et al.*[289] demonstrated that also in inorganic systems, such as $CaCO_3$-based PCMs, the addition of T-ZnO (at a mole ratio of just 5%) can increase thermal conductivity by 17.8%. This improvement is particularly beneficial at high heating rates, where enhanced thermal transport directly accelerates reaction kinetics. These findings highlight the potential of T-ZnO templated networks to improve both organic and inorganic PCM systems, broadening their applicability in thermal energy storage technologies.

In addition to its role in thermal energy storage, T-ZnO has also demonstrated potential in the field of electrochemical energy storage. Chang *et al.*[292] investigated the use of T-ZnO as a coating for graphite anodes in lithium-ion batteries. Safety remains a critical issue in lithium-ion battery technology, with internal short circuits posing a major risk. These can initiate localized heating, triggering a chain of exothermic reactions that lead to a phenomenon known as thermal runaway. By applying a T-ZnO coating to the graphite electrode, direct contact between the anode and cathode can be mitigated, thereby reducing the likelihood of internal short circuits. The unique open-porous architecture of the T-ZnO network provides thermal stability while maintaining efficient ion diffusion pathways. Unlike dense nanoscale ZnO coatings such as short rods, the tetrapodal structure minimizes obstruction to lithium-ion transport. This approach substantially improves the safety of lithium-ion batteries, without compromising ion transport due to the open porous architecture of the T-ZnO network.

To conclude, in energy storage, thermal systems as well as batteries, T-ZnO is not typically employed as a direct storage material. Instead, its incorporation into existing systems can significantly enhance performance or safety. This improvement arises mainly from the combination of its high thermal conductivity and its ability to form highly porous networks, which facilitate or enable efficient transfer processes such as heat and ion transport.[48,292] However, for thermal energy storage, the transition of T-ZnO into real-life applications would require large amounts of low-cost material, with industrial production just starting to scale up. In batteries, by contrast, the potential benefits must be carefully balanced with the complex electrochemistry of these systems, where ZnO may introduce additional effects that still need systematic investigation. However, another major potential in the field of electrochemical energy storage lies in the use of T-ZnO as a sacrificial template to fabricate hierarchically structured electrodes. Such architectures can significantly improve electrode performance by combining large accessible surface areas with efficient transport pathways, as discussed in Section 4.3.2.4.

4.1.5.2 (Photo-)catalysis. ZnO absorbs light in the UV region due to its band gap of approximately 3.2 eV (see Section 3.3.1). It also exhibits a large exciton binding energy of 60 meV (see Section 3.2.1) and is known for its photocatalytic activity. Combined with its chemical stability, radiation resistance, relative abundance, and low toxicity, ZnO has become one of the most extensively studied photocatalysts, with a wide range

of nano- and microstructured morphologies explored. Among these, the tetrapod morphology has demonstrated superior photocatalytic performance in various studies.[13,293–296] This is attributed to a lower concentration of nonradiative defects, minimizing energy losses, a high accessible specific surface area and reduced electron–hole recombination facilitated by abundant surface states. As the photocatalytic properties of T-ZnO have been comprehensively reviewed in a recent publication by Pujara *et al.*,[13] they will not be discussed in further detail here.

An aspect of T-ZnO not addressed in the review by Pujara *et al.*[13] is its unique capability to form interconnected networks that serve as sacrificial templates for the synthesis of novel materials. This templating strategy enables the fabrication of photocatalytically active materials with complex, hierarchically porous architectures. Such structures can enhance photocatalytic efficiency by providing a high surface area, improved mass transport, and better light-harvesting capabilities, features particularly advantageous for gas-phase and high-throughput catalytic applications (see Section 4.3.2.4).

Beyond photocatalysis, T-ZnO has also been investigated in several direct catalytic applications. In these contexts, T-ZnO typically serves as a support material, for instance for metallic nanoparticles. Compared to other ZnO-based substrates, T-ZnO often demonstrates enhanced catalytic performance, likely due to specific interactions between the catalyst and the unique surface properties of the T-ZnO structure.[297–299]

4.2 T-ZnO as active structural material

Beyond applications that leverage its intrinsic properties, a ground-breaking class of technologies utilizes T-ZnO primarily for its unique 3D shape. The tetrapods ability to form robust, mechanically interlocked networks (achieving three-dimensional percolation with a low filling factor) makes the architecture itself the key functional feature (Section 3.4.2). This structure is exploited in two main ways. First, it can serve as a permanent structural backbone within a composite material. Second, it acts as a removable, sacrificial template to architect entirely new classes of materials from the micro to the macro scale. The latter will be discussed in a Section 4.3.

4.2.1 Advanced composite materials. The unique, complex geometry of T-ZnO makes it an exceptional structural filler for advanced composites, where it provides benefits far beyond simple volume filling.[300–308] One key application is in mechanical reinforcement and adhesion.[300,302,303,305,307] As detailed in the discussion on composite reinforcement (Section 3.4.3), the 3D shape of the tetrapods is ideal for creating a strong mechanical interlock within a matrix. For example, Meinderink *et al.*[303] took advantage of the tetrapodal structure by spray coating a mixture of poly(acrylic acid) and T-ZnO onto poly(propylene) to interconnect two poly(propylene) foils. This was used to interconnect two poly(propylene) foils, which are typically hard to glue due to their low surface energy. The T-ZnO mechanically interlocks the polymer foils, which significantly increases the shear strength of the laminate layers. Moreover, T-ZnO can be incorporated into polymers and improve their mechanical properties.[302] By using epoxy as the polymer matrix, the incorporation CNTs not only facilitates the formation of a conductive network but also reinforces the mechanical properties of the composite. It has been suggested that the presence of T-ZnO improves the dispersion of CNTs and promotes the development of well-connected conductive pathways within the epoxy matrix.[300]

To summarize T-ZnO acts as more than a simple filler: its tetrapodal geometry enables strong mechanical interlocking, improves adhesion and enhances matrix reinforcement. In addition, it supports the dispersion of other nanofillers like CNTs, fostering well-connected networks and thus enabling multifunctional, high-performance composites.[300–305] Nevertheless, the limited lab- and small-scale industrial production of T-ZnO composites still hinders real-world applications. This is mainly due to the large T-ZnO loadings required in composites and the currently high, non-competitive cost of T-ZnO for fillers.

4.2.2 Advanced T-ZnO composites for EMI shielding. T-ZnO's as a structural backbone is also expertly exploited in composites designed for electromagnetic interference (EMI) shielding. As modern electronics proliferate, the increase in the usage of wireless communication poses a huge risk for precise electronic equipment. Therefore, the search for advanced materials which can block Electromagnetic radiation effectively is of high importance. Especially materials, which absorb lots of the incoming electromagnetic radiation are interesting, because they do not contaminate their environment with reflected radiation. However, it is not simple to achieve high shielding effectiveness combined with high absorption of electromagnetic waves because materials that provide strong reflection, which is typically required for high shielding, often prevent electromagnetic waves from penetrating the material, which is necessary for absorption to occur.[309]

To overcome this obstacle several approaches using T-ZnO in composite shielding materials are proposed.[115,310–314] These methods leverage the high surface area (Section 3.6.1) and amenability to surface functionalization (Section 3.6.4) of the T-ZnO network. For example, Xu *et al.*[115] mixed electroless silver plated T-ZnO with Fe_3O_4 coated rGO in a water based polyurethane emulsion, which forms a gradient thin film during evaporation of the water, because the Ag coated T-ZnO is denser then the Fe_3O_4 coated reduced Graphene Oxide. This gradient is responsible for the material's excellent microwave shielding performance, which works as follows: the microwaves enter the material through the Fe_3O_4@rGO-rich side, which has low reflectivity. There, the microwaves are attenuated through magnetic and dielectric losses. The conductive Ag@T-ZnO-rich side has high reflectivity and reflects the microwaves back into the Fe_3O_4@rGO-rich side, where they are attenuated again. With this approach the authors achieve a shielding effectiveness of up to 87 dB in the X-band with the shielding effectiveness contributing mainly from absorptive mechanisms and just 2.4 dB contributing from reflection.[115] Further developments involve composites of T-ZnO with carbon cloth as a broadband absorbers,[310] or the use of T-ZnO as a sacrificial template to synthesize a lightweight and absorbing aeromaterial based on a

carbon backbone decorated with MnO_2 and poly aniline[311] or a combination of PNIPAM hydrogel with MXenes and silver nanowires, which allows switchable shielding performance due to stimuli responsive behaviour of the hydrogel.[312]

In conclusion, T-ZnO serves as a versatile structural backbone in EMI shielding composites, enabling high absorption and efficient reflection management through its 3D network architecture, large surface area, and functionalizability. The published composites surpass shielding effectiveness above 40 dB, which is suitable for most applications.[315] Although recently reported porous materials with similarly complex synthesis achieve shielding effectiveness up to 109 dB,[316] T-ZnO-based composites exhibit lower absolute shielding. However, their tunable surface properties open opportunities for designing complex, lightweight shielding materials with enhanced or even switchable capabilities, representing promising directions for future research.

4.3 T-ZnO as sacrificial template for novel architectures

The most innovative application of T-ZnO's structure, is its use as a sacrificial template. This approach does not leverage the intrinsic properties of ZnO, but its unique morphology to architect entirely new materials. A template is a material that prescribes the shape of (nano-)material growth or agglomeration. A template-based synthesis approach consists of three steps: (i) template preparation, (ii) template-guided synthesis/agglomeration of the target molecule/material in the desired shape and (iii) removal of the template structure. There is a huge variety of different template synthesis approaches.[317] T-ZnO is particularly well-suited as a template to prescribe the structure for a multitude of different advanced materials, because of its unusual shape, its ability to form highly porous and accessible networks as described in Section 3.6.1, its insolubility in many environments (except acidic environments with pH < 6), which makes it easily removable *via* acids, its rather low production costs and its low toxicity.[12,318]

4.3.1 Fabrication strategies: aeromaterials and channel networks. In general, there are two different approaches to use T-ZnO particles as a template (Fig. 53). The first approach involves coating the T-ZnO network with a thin film of target material (*via* methods related to surface functionalization, Section 3.6.4) followed by the removal of T-ZnO, resulting in ultralightweight structures known as ''aeromaterials'', which consist of interconnected tubes in the shape of the hexagonal T-ZnO arms. Conversely, the second approach entails filling the voids of a T-ZnO network with a target material completely followed by removing the T-ZnO, yielding a ''interconnected microchannel network'' within the target material with channels in the shape of the removed T-ZnO particles.

The seminal example of aeromaterials is ''aerographite'', the first structure described in the literature, which is synthesized *via* a T-ZnO templating approach. Aerographite is synthesized following a dry-chemical CVD approach, in which a thin layer of graphite is deposited at the surface of a T-ZnO network. The hydrogen present in the reaction atmosphere is capable of reducing the ZnO to Zn, which evaporates at elevated temperatures and allows a simultaneous template removal. At its publication date in 2012 aerographite was the most lightweight material on earth with a density of 0.2 mg cm^{-3}, illustrating that extreme material properties are possible by using an inherently low-density, high-porosity T-ZnO network (Section 3.6.1) as a template structure.[8] Since the discovery of aerographite, numerous CVD-based approaches for synthesizing diverse aeromaterials have been reported. Building on this, a related technique known as hybrid vapor phase epitaxy (HVPE)[319] has been employed to grow a wide range of thin films directly on T-ZnO templates. This method also enables subsequent aerofication, expanding the versatility and material diversity of aeromaterial fabrication Table 14. A review article focusing on the gas-phase synthesis of aeromaterials, particularly semiconducting aeromaterials, was published in 2025.[320]

The synthesis of ultralightweight aeromaterials is not limited to gas phase processes, which can generate different homogeneous thin films at the T-ZnO template, but are technically rather complex setups. It is also possible to wet-chemically coat T-ZnO with a thin film of a target material. This can be done either by infiltrating nanomaterial dispersions into a T-ZnO network or by growing a thin film from solution at the surface of the T-ZnO. The infiltration approach was first published in 2017 by Schütt *et al.*[321] A comprehensive explanation of the infiltration method is provided by Rasch *et al.*[18] Usually a 1D or 2D nanomaterial dispersion containing *e.g.* exfoliated graphene, graphene oxide, MXenes, MoS_2 or CNTs is infiltrated into the highly accessible pores of a T-ZnO network (Section 3.6.1). Through evaporating the solvent, a thin layer of nanomaterial deposits at the surface of the T-ZnO. This simple infiltration procedure can be repeated to increase the layer thickness of the nanomaterial. The direct wet-chemical growth of a material at the surface of T-ZnO was first published in 2023.[19] Especially the growth of SiO_x films at the surface of T-ZnO has been investigated in several publications, because it is simple to achieve compared to other transparent and light scattering aeromaterials *e.g.* Aero-hBN.[19,322] The wet-chemical approach (infiltration; direct growth) allows to synthesize samples with several centimetre side length, which enables use cases with a demand for large volumes, *e.g.* air filters.[323]

A key advantage of the T-ZnO template approach, compared to the synthesis of other ultralightweight structures like aerogels, is the ease with which composite aeromaterials can be created. This is due to the fact that different nanomaterials can be introduced or synthesized step by step on the mechanically robust (Section 3.4) and chemically amenable surface of the T-ZnO network.[19,20] In conventional aerogel synthesis, all nanomaterials are typically introduced simultaneously, which frequently complicates or even precludes the process, as their incorporation may require incompatible reaction conditions.

To summarize the synthesis of aeromaterials is methodologically diverse. The thin-film formation on the T-ZnO scaffold has been realized through three primary routes: gas-phase deposition techniques like CVD or HVPE, the infiltration of pre-synthesized nanomaterial dispersions (*e.g.*, graphene oxide, MXenes, CNTs, *etc.*), or direct wet-chemical growth from precursor solutions. Gas-phase methods were the first to be

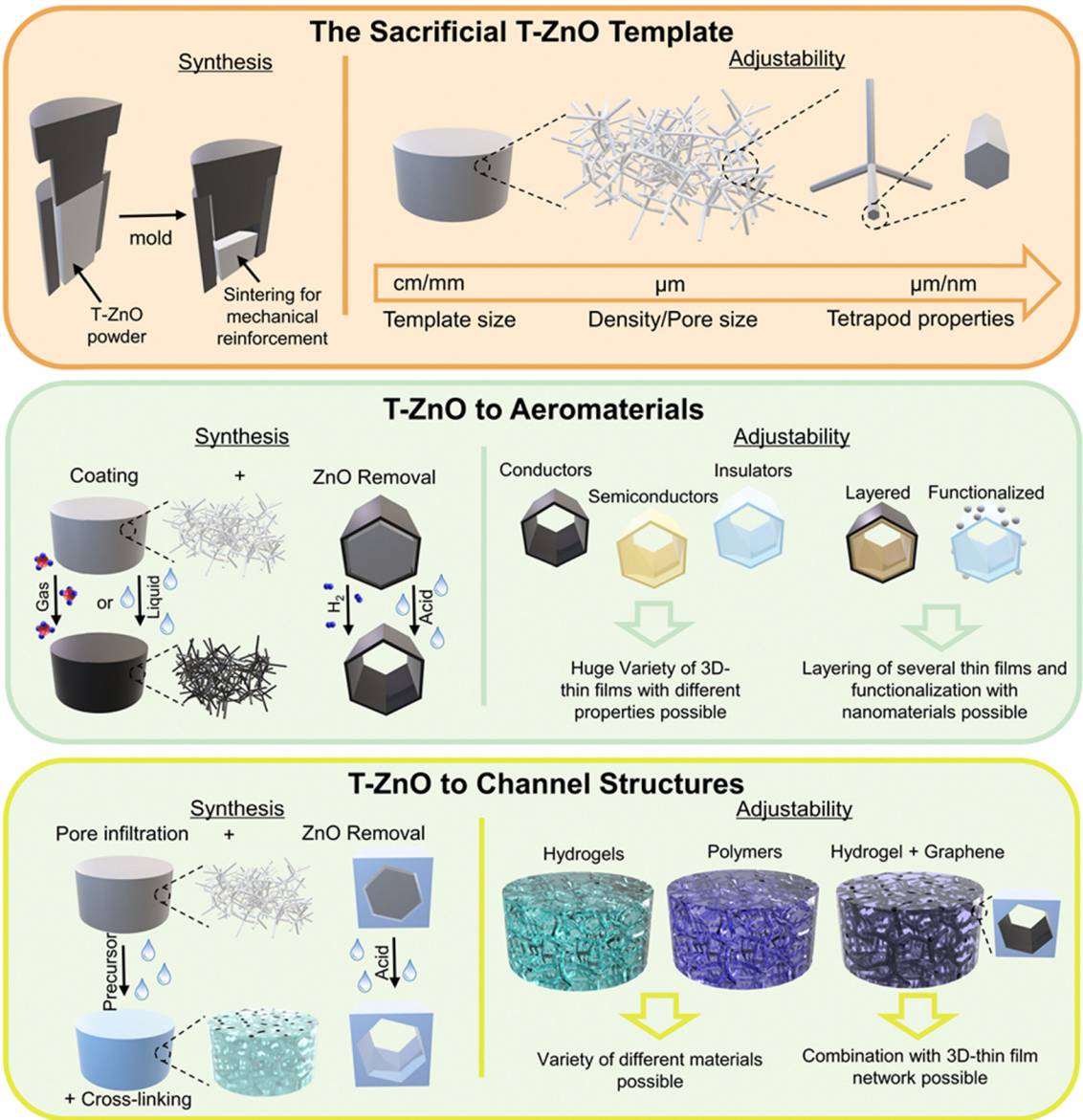

Fig. 53 Schematic illustration of the synthesis and properties of sacrificial T-ZnO templates, their use in the fabrication of aeromaterials and channel structures *via* different coating and template removal strategies, and the resulting diversity and tunability of both aeromaterials and channel structures.

reported and remain a powerful tool for discovering novel aeromaterials with high-quality, homogeneous coatings.[8,319,324,325] However, their high synthetic complexity (often requiring vacuum systems and high temperatures) limits scalability in terms of both sample size and production quantity. In contrast, wet-chemical approaches are generally less demanding and more amenable to upscaling, making them promising for applications requiring larger material volumes.[323,326]

In addition to the template-guided synthesis of aeromaterials based on T-ZnO network structures, another important class of materials can be structurally defined using these templates, so-called channel structures. In this approach, the interconnected pores of the T-ZnO network are fully infiltrated with a matrix material, such as a polymer (*e.g.*, PDMS)[327] or a hydrogel (*e.g.*, PNIPAM).[165] After complete infiltration, the T-ZnO template is selectively removed, leaving behind a continuous matrix embedded with a network of interconnected microchannels that mirror the original T-ZnO architecture.[165,327–330]

Moreover, it is also possible to synthesize an aeromaterial and subsequently infiltrate its entire pore structure with a matrix material, such as epoxy. This process results in a continuous matrix embedded with a three-dimensional thin-film network replicating the geometry of the aeromaterial. In this way, percolating networks with ultra-low filler loadings can be achieved. This combines mechanical integrity with functional properties such as electrical conductivity or thermal management.[331–333]

An additional approach involves coating the T-ZnO network with a thin film of another material prior to infiltrating its pores with a matrix material. After infiltration, the T-ZnO

Table 14 Overview of published materials synthesized *via* a T-ZnO template approach

Material	type	Synthesis approach	Application (scenarios)	Author (pulication date)
Graphite	Aeromaterial	CVD	Supercondensator	Mecklenburg *et al.* (2012)[8]
Graphite + GaN	Aeromaterial	CVD + HVPE	Sensors	Schuchardt *et al.* (2015)[319]
Graphite + epoxy	Channel	CVD + infiltration	Conductive composite	Chandrasekaran *et al.* (2016)[331]
Graphite + peptides + PEG	Aeromaterials	CVD + infiltration	Cell growth	Lamprecht *et al.* (2016)[367]
Graphite	Aeromaterial	CVD	Gas sensor	Lupan *et al.* (2016)[362]
Silicon	Aeromaterial	Plasma-enhanced CVD	Gas sensor	Hölken *et al.* (2016)[365]
Graphite + nano T-ZnO	Aeromaterial	CVD + sputtering	Optoelectronics	Tiginyanu *et al.* (2016)[143]
Graphite + epoxy	Channel	CVD + infiltration	Pressure sensor	Garlof *et al.* (2016)[332]
Graphite + epoxy	Aeromaterial + Channel	CVD + infiltration	Electronics	Garlof *et al.* (2017)[333]
Graphite	Aeromaterial	CVD	Supercapacitor	Parlak *et al.* (2017)[368]
Graphite	Aeromaterial	CVD	Theoretical	Meija *et al.* (2017)[163]
Carbon + diamond + SnO_2	Aeromaterial	Hot-filament chemical vapor deposition (HFCVD)	Electro wettability	Silva *et al.* (2017)[369]
Graphite	Aeromaterial	CVD	Gas sensing	Lupan *et al.* (2017)[364]
MWCNT	Aeromaterial + Channel	Infiltration	Electronics	Schütt *et al.* (2017)[321]
Graphite + Si/SiO_x NP	Aeromaterial	CVD + plasma jet	Biomedical	Daria *et al.* (2018)[370]
Graphite + InP	Aeromaterial	CVD + HVPE	Strain sensors	Plesco *et al.* (2018)[363]
MWCNT + hydroxyapatite + SiO2	Aeromaterial	Infiltration	Cell growth	Taale *et al.* (2018)[346]
GaN	Aeromaterials	HVPE	Electronics	Tiginyanu *et al.* (2019)[371]
Graphite + CdTe	Aeromaterial	CVD	Gas sensing	Strobel *et al.* (2019)[372]
MWCNT, graphite, graphene	Aeromaterial	Infiltration, CVD	Cell growth	Taale *et al.* (2019)[347]
Carbon	Aeromaterial	CVD	Lithium-sulfur batteries	Yang *et al.* (2019)[354]
GaN	Aeromaterial	HVPE	Pressure sensor	Dragoman *et al.* (2019)[360]
Graphite	Aeromaterial	CVD	Theoretical	Marx *et al.* (2019)[373]
MWCNT	Aeromaterial	Infiltration	Electronics	Pöhls *et al.* (2019)[168]
Graphite + hydroxyapatite	Aeromaterial	CVD + electrophoresis	Cell growth	Taale *et al.* (2019)[345]
Graphene, graphene oxide, reduced graphene oxide	Aeromaterial	Infiltration	Electronics	Rasch *et al.* (2019)[18]
Carbon + ZIF-8	Aeromaterial	Wet-chemical growth + pyrolysis	Supercapacitors	Yuksel *et al.* (2020)[85]
Carbon + polyaniline	Aeromaterial	Carbonization + polymerization	EMI	Li *et al.* (2020)[311]
Hexagonal BN	Aeromaterial	CVD	Laser light scattering	Schütt *et al.* (2020)[167]
PDMS	Channel	Infiltration	Drug delivery	Rasch *et al.* (2020)[327]
Ga_2O_3	Aeromaterial	HVPE	EM transparency	Braniste *et al.* (2020)[374]
ZnS	Aeromaterial	HVPE	Switchable hydrophilicity	Plesco *et al.* (2020)[343]
MWCNT + sulfur	Aeromaterial	Infiltration + vapor infiltration	Lithium sulfur batteries	Cavers *et al.* (2020)[355]
Graphene	Aeromaterial	Infiltration	Theoretical	Rezvani *et al.* (2021)[375]
Ga_2O_3 + Pt/Au	Aeromaterial	HVPE	Photocatalysis	Plesco *et al.* (2021)[376]
Hydrogel + graphene	Channel	Infiltration + crosslinking	Conductive hydrogel	Arndt *et al.* (2021)[334]
GaN	Aeromaterial	HVPE	Actuation	Braniste (2021)[324]
Graphene, reduced graphene oxide	Aeromaterial	Infiltration	Electrically powered repeatable air explosions (EPRAE) (actuation)	Schütt *et al.* (2021)[336]
Hydrogel	Channel	Infiltration + crosslinking	Cell migration	Siemsen *et al.* (2021)[328]
Hydrogel (PNIPAM)	Channel	Infiltration + crosslinking	Actuation	Spratte *et al.* (2022)[165]
Graphene oxide	Aeromaterial	Infiltration	Cell growth	Wang *et al.* (2022)[349]
PDMS	Channel	Infiltration	Drug delivery	Hauck *et al.* (2022)[330]
MoS_2	Aeromaterial	Hydrothermal	Potassium batteries	Ma *et al.* (2022)[377]
TiO_2	Aeromaterial	HVPE	Photocatalysis	Ciobanu *et al.* (2022)[358]
Partially reduced graphene oxide	Channel (Membrane)	Vacuum filtration	Pressure sensor	Ren *et al.* (2023)[361]
Ga_2O_3/$ZnGa_2O_4$	Aeromaterial	HVPE	Lithium batteries	Wolff *et al.* (2023)[357]
(Poly(3,4-ethylenedioxythiophene): poly(styrenesulfonate) + polytetrafluoroethylene (PTFE))	Aeromaterial	Infiltration + initiated CVD	Strain invariant conductor	Barg *et al.* (2023)[344]
Hydrogel (PNIPAM) + graphene	Channel	Infiltration + crosslinking	Soft actuation	Hauck *et al.* (2023)[335]
Graphene	Aeromaterial	Infiltration	Air filtration	Reimers *et al.* (2023)[323]
SiO_2 + reduced graphene oxide	Aeromaterial	Wet chemical growth + infiltration	Light driven actuators	Saure *et al.* (2023)[19]
MXene	Aeromaterial	Infiltration	Supercapacitors	Spurling *et al.* (2024)[353]
CNT	Aeromaterial	Infiltration	Underwater thermoacoustic	Liu *et al.* (2024)[166]
$Ce_{1-x}Zn_xO_{2-\delta}$	Aeromaterial	Wet-chemical growth	Photocatalysis	Lumma *et al.* (2024)[20]
SiO_2 + $CsPbBr_3$	Aeromaterial	Wet-chemical growth	Laser light scattering + light conversion	Saure *et al.* (2024)[322]
Alginate	Channel	Infiltration + crosslinking	Tissue engineering	Li *et al.* (2024)[329]
ZnS	Aeromaterial	HVPE	Physical vapor transport	Ursaki *et al.* (2024)[378]
GaN	Aeromaterial	HVPE	Photocatalysis	Ciobanu *et al.* (2024)[379]
TiO_2	Aeromaterial	HVPE	Photocatalysis	Ciobanu *et al.* (2024)[325]
Graphene	Aeromaterial	Infiltration	Actuation	Reimers *et al.* (2025)[326]
TiO_2	Aeromaterial	ALD	UV Photodetector	Nicolaescu *et al.* (2025)[366]

template can be removed, resulting in a three-dimensional channel system with functionalized or coated channel walls. This method enables the fabrication of complex hierarchical structures, where the coating imparts additional chemical, electrical, or mechanical functionality to the internal surfaces of the channel network.[321,334,335]

4.3.2 T-ZnO templated materials: material class overarching characteristics. Given the structural diversity of aeromaterials (distinguished by their base material, tetrapod morphology, film thickness, and synthesis method), it is challenging to define universal properties for the entire class. Nevertheless, several distinguishing features characterize these materials. The following parts detail the typical structural, mechanical, and economic characteristics that define this material class.

4.3.2.1 Structural porosity and transport. First, the structure of aeromaterials is highly open-porous, characterized by a network of macropores that is typically interconnected throughout the entire structure. This unique open porosity allows for the rapid transport of gases or liquids between the internal pore volume of the aeromaterial and the surrounding environment. Compared to other low-density structures, such as aerogels which often contain closed or rather closed pore architectures, this degree of openness is untypical. This structural openness is a key element for many specific applications, such as actuation and tissue growth scaffolds, where mass transport is critical.[336]

Only a few materials exhibit structures comparable to T-ZnO-derived aeromaterials. The closest analogues are materials derived from open-porous melamine foams (*e.g.*, Basotect). These melamine foams are inexpensive and industrially mass-produced. However, their use as templates for lightweight structures has several significant drawbacks. In particular, the removal of the melamine backbone is challenging; unlike T-ZnO, it is not soluble under mild conditions and tends to melt before decomposing, which typically destroys the fragile three-dimensional thin films deposited on the structure. A commonly employed alternative is to first carbonize the melamine foam, deposit the thin film, and subsequently remove the carbonized backbone by oxidation.[337] The harsh conditions required for this backbone removal limit the use of melamine foams as templates to only a few aeromaterial classes, such as SiO_2-based systems, and hinder their applicability to others, including carbon-based aeromaterials which would burn away alongside the template.

4.3.2.2 Mechanical properties and stability. Beyond their structural similarities, aeromaterials typically exhibit low absolute mechanical strength. However, when normalized to their extremely low density, their mechanical performance is often remarkable and has been rigorously tested in several studies.[8,18,321] This behavior can likely be attributed to a specific buckling-hinge mechanism observed in the nodes of the hollow tetrapods.[163] Mechanical stress remains a serious threat to the structural integrity of these materials, as most aeromaterials can be destroyed under direct compression. Nevertheless, they are sufficiently stable to be carefully integrated into devices and can withstand notable pneumatic pressures, such as those generated by gas streams. This robustness makes them attractive for applications including air filtration,[323] gas-phase photocatalysis,[20] and actuators.[326,336] Furthermore, the shelf life of typical aeromaterials (whether carbon-based, semiconducting, or SiO_2-based) under standard conditions is long, extending over years to decades. In addition, exceptional application-related cycle stability against temperature and heat has been demonstrated over thousands of cycles.[336]

4.3.2.3 Environmental impact and safety. The environmental impact of degraded or destroyed aeromaterials has not yet been investigated in detail. However, this impact is expected to depend strongly on both the constituent materials and the distinct microstructure of the aeromaterials. With respect to material composition: (i) aeromaterials are extremely lightweight, resulting in a very low total material mass released into the environment, which reduces potential impact particularly when toxic components are present; and (ii) a large proportion of investigated aeromaterials are carbon-based and, in principle, biodegradable. Regarding the microstructure, aeromaterials are typically readily destroyed by (i) mechanical stress or (ii) heat. Nevertheless, the environmental and biological impact of aeromaterial fragments, which retain microrod-like structures, has not yet been assessed. We therefore strongly recommend further scientific investigation, particularly concerning the potential risks and consequences of the inhalation of aeromaterial fragments.

4.3.2.4 Scalability and commercialization. To date, most aeromaterials have been synthesized only in laboratory-scale quantities. Nevertheless, initial studies have demonstrated the fabrication of large area aeromaterial plates, indicating the feasibility of upscaling. This upscalability is closely linked to increasing supplies from T-ZnO manufacturers, such as the Phi-Stone AG company.[270] An important advantage is that the most extensively studied carbon-based aeromaterials do not depend on critical or costly resources such as rare earth elements or noble metals. Despite this, the overall production process, including T-ZnO synthesis, template construction, template coating, and template removal, remains highly specialized and complex. Consequently, aeromaterials are likely to remain relatively expensive. This makes them most suitable for applications where: (i) only small amounts are required, (ii) long-term use is feasible, and (iii) the aeromaterial enables significantly superior performance compared with conventional approaches. Despite these challenges, a company named Aero Materials GmbH initiated the commercialization of aeromaterials this year.[338]

4.3.2.5 Channel networks. Compared to aeromaterials, channel networks derived from T-ZnO exhibit a relatively dense, matrix-dominated structure. They consist of a matrix material permeated by interconnected, tube-shaped pores, with the pore volume typically accounting for only 5–10% of the total volume. Nevertheless, even this volumetrically small pore fraction can

significantly alter material properties, for example by strongly affecting flow behavior in hydrogels.[335] Generating such a well-percolating pore network within a dense matrix while maintaining such a high solid volume fraction is challenging, and only a few comparable manufacturing approaches exist to achieve this topology. A widely known technique to fabricate microchannels is using standard lithographic methods. However, these methods limit channel density and depth, making it difficult to realize true three-dimensional microchannel architectures. To date, only a few methods exist that successfully enable true 3D microfluidics.[339] The serial nature of many 3D printing processes creates practical difficulties in realizing dense structures over large areas, and inherent resolution limits often prevent the routine construction of channels with inner diameters smaller than 50 μm.[340] Unlike tetrapodal T-ZnO templates, a 3D-printed interconnected backbone is not self-assembled and requires precise, active fabrication. However, to advance the application of T-ZnO-derived microchannel networks to microfluidic applications, the microchannels must be maniuplated individually. Furthermore, other templates than T-ZnO can be used to achive channel structures (*e.g.*, sugar crystals). While these are typically more cost-effective than T-ZnO, they lack the highly anisotropic tetrapodal morphology necessary to achieve sufficient percolation at low filler concentrations.

Because channel structures predominantly consist of the matrix material (*e.g.*, polymers such as PDMS), their mechanical properties are typically close to those of the matrix itself. These properties can be modified by introducing fillers into the pore network. Owing to their similarity to bulk materials, the environmental impact and durability of T-ZnO-derived channel networks are likewise largely determined by the matrix material used to form the pore network. To date, channel networks have only been produced at the laboratory scale. In principle, upscaling of this class of materials is feasible, but as with aeromaterials, it strongly depends on the availability of scalable T-ZnO production. However, compared to aeromaterials, far fewer applications currently justify the production costs of channel structures. Consequently, no industrial approaches toward their commercialization are known so far.

4.3.3 Functional applications of templated architectures. The templating approach using T-ZnO networks as a prescribing structural element enables three-dimensional material design from the microscale to the macroscale. This is applicable to a multitude of different materials (*e.g.*, 2D-nanomaterials, 1D-nanomaterials, polymers, silica, *etc.*). While all of these structures originate from the unique geometry of the T-ZnO network, the resulting materials exhibit fundamentally different properties. For instance, aerographene is highly electrically conductive and strongly absorbs light in the optical range,[336] whereas aero-hBN is electrically insulating and transparent in the visible spectrum.[167] Consequently, each material derived from a T-ZnO template offers distinct functional characteristics and can be tailored for entirely different application scenarios (Fig. 54). The three-dimensional structuring introduced by the T-ZnO template plays a key role in imparting additional functionalities to the resulting materials. This significantly enhances

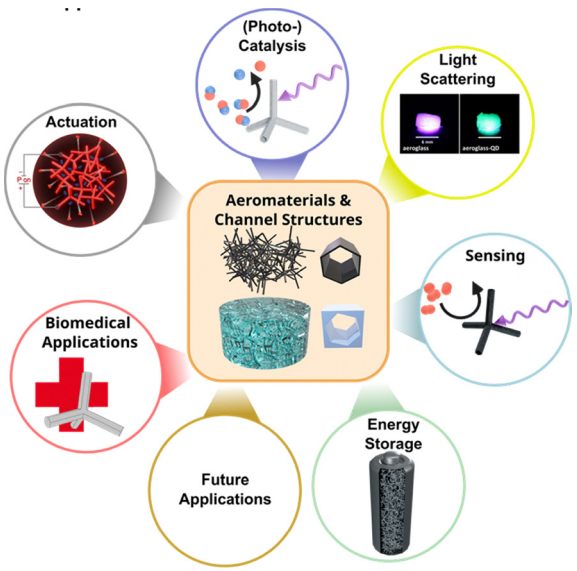

Fig. 54 Applications of aeromaterials and channel structures. Materials derived from T-ZnO templates enable a wide range of applications.

their suitability for various applications or even enables entirely new fields of use. This opens up a vast research space for the development, characterization, and application-driven evaluation of novel materials. A comprehensive discussion of all possible application scenarios lies beyond the scope of this review. An overview of the various materials synthesized *via* a T-ZnO templating approach is provided in Table 14. However, a selection of particularly innovative examples will be highlighted in the following sections. We specifically focus on actuators and optical materials for laser light illumination, biomedical applications, energy storage and conversion, and sensors.

4.3.3.1 Actuation and smart materials. The unique structure of T-ZnO is particularly advantageous for the development of actuators and smart materials. These are materials that can significantly change their properties in a controlled manner in response to external stimuli such as temperature or pressure. T-ZnO enables precise three-dimensional microstructuring within macroscopic samples, unlocking novel functionalities or significantly enhancing performance.

An innovative actuation concept introduced by Schütt *et al.*[336] is based on low-density aeromaterials composed of conductive, two-dimensional carbon materials arranged in a three-dimensional architecture defined by a T-ZnO template. Upon Joule heating, these structures can be rapidly heated by several hundred Kelvin within just a few milliseconds. The high specific surface area of the aeromaterial facilitates efficient heat transfer to the surrounding gas molecules. This results in a rapid and significant expansion of gas volume. Due to the aeromaterial's low heat capacity, it quickly returns to its initial temperature. This process, referred to as electrically powered repeatable air explosion (EPRAE), can be repeated up to six times per second. It shows great promise for a large variety of applications, including lightweight electrically driven pneumatic systems, catalysis, sensing, sorption, propulsion,

thermoacoustics, and microfluidics (Fig. 55I). This actuation method has been extensively investigated in the context of onboard pressure supply systems for soft robotics.[326] Furthermore, Saure *et al.*[19] developed an alternative aeromaterial based on SiO_2, which is both transparent and highly scattering in the visible spectrum. By incorporating small amounts of homogeneously distributed rGO flakes, a three-dimensional light-absorbing structure was synthesized. Due to the material's low heat capacity, exposure to high-intensity light, such as from a powerful lamp, can rapidly increase its temperature by several hundred degrees Celsius throughout the entire volume. This results in a gas expansion effect comparable to that observed in the EPRAE process. Further publications have demonstrated the rapid heating capabilities of ultralight aeromaterials for applications such as underwater acoustic wave generation[166] and self-cleaning air filtration system.[323]

Actuators based on the EPRAE mechanism, represent an aeromaterial technology with the potential to significantly impact industrial production. In such environments, compressed air systems are among the largest electricity consumers, accounting for up to 10% of industrial energy use.[341] However, these systems are typically inefficient, with leakage and poor maintenance

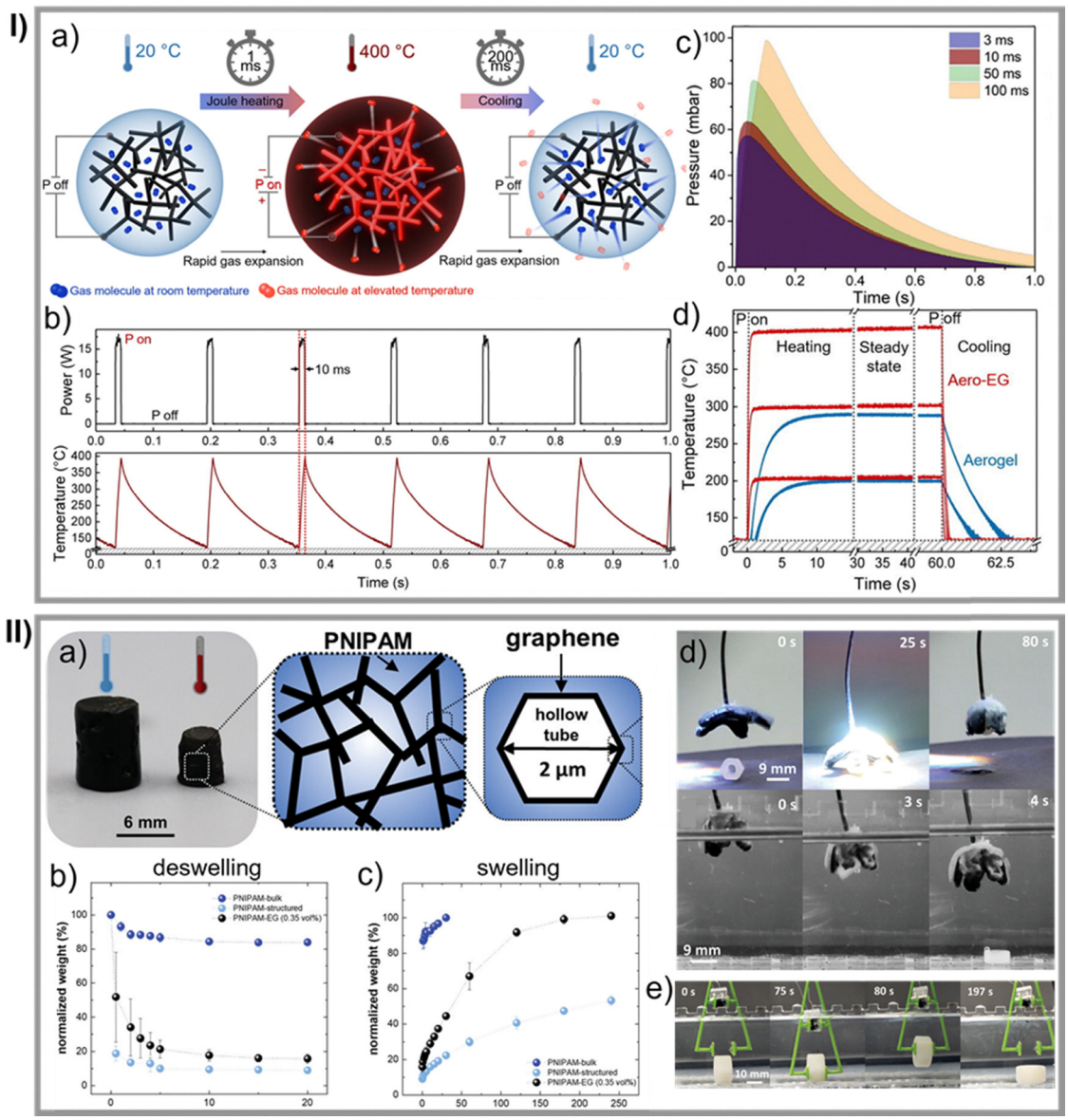

Fig. 55 Actuation concepts based on T-ZnO-templated materials. (I) EPRAE concept:[336] (a) Schematic of EPRAE, where Joule heating of a conductive aeromaterial causes instantaneous heat transfer and rapid air expansion. (b) Typical temperature-time profile. (c) Pressure generated across various power-pulse widths. (d) EPRAE effect comparison between conductive aeromaterials and aerogels. (II) Microstructured hydrogels:[335] (a) image and schematic of T-ZnO-templated PNIPAM hydrogels with graphene channel walls. (b) Temperature-induced deswelling. (c) Swelling behavior comparison of unstructured bulk, structured, and graphene-walled structured PNIPAM. (d) and (e) Gripper concepts utilizing the swelling/deswelling mechanics of these hydrogels as artificial muscles. (I (a)–(d)) Reproduced from ref. 336 with permision from Elsevier,[336] Copyright 2021, (I (a)–(e)) reproduced from ref. 335 with permision from Wiley,[335] Copyright 2023.

leading to energy losses of 30% or more.[342] The EPRAE mechanism enables localized, on-demand pressure generation, thereby eliminating the need for complex and leak-prone compressed-air distribution networks. Moreover, the EPRAE process generates pressure without relying on moving parts, in contrast to conventional mechanical compressors. As a result, EPRAE technology has the potential to substantially reduce both maintenance requirements and the overall energy demand associated with compressed-air systems. Recent studies have demonstrated that carbon-based conductive aeromaterials show promising cycling stability,[336] scalability,[323] and effective pressure generation[326,336] *via* EPRAE. Future research should aim at improving power-to-pressure conversion efficiency, increasing maximum pressure output, and identifying specific industrial applications where localized pressure supply would provide the greatest benefit. Even at its present stage of development, the EPRAE process may already provide valuable solutions for specific industrial applications.

Other aeromaterials, such as Aero-ZnS and Aero-GaN, exhibit distinct properties that enable self-propelling behavior at water surfaces, making them promising candidates for actuation-driven applications.[324,343] Moreover, Barg *et al.*[344] developed a multilayered aeromaterial composed of a conductive poly(3,4-ethylenedioxythiophene) polystyrene sulfonate (PEDOT:PSS) core coated with an insulating polytetrafluoroethylene (PTFE) layer, resulting in a strain-invariant conductor. This material shows promise for a range of applications, including soft electronics and energy storage systems. However, due to the complexity of its synthesis and the limited scalability of the approaches discussed, these concepts are currently more likely to remain of primarily scientific interest rather than being readily transferable to large-scale applications.

Another approach to designing advanced actuators involves channel structures templated by a porous T-ZnO network. Spratte *et al.*[165] filled the pores of such networks with a stimuli-responsive hydrogel, namely PNIPAM, which exhibits a volume change at a specific temperature. However, the swelling and deswelling capacity of bulk hydrogels is typically limited; the authors measured only a 12% volume reduction for unstructured hydrogels. By introducing microchannel structuring within the hydrogel network, a volume reduction of up to 90% was achieved, while the stiffness of the swollen hydrogel remained unchanged. Additionally, the response rate was significantly enhanced. This microchannel-structured hydrogel was successfully demonstrated as an artificial muscle to power a gripper (Fig. 55II).[165] By coating the T-ZnO network with a thin layer of conductive material, such as exfoliated graphene flakes, conductive hydrogels with exceptional conductivity and extremely low filler loading can be synthesized[334] Hauck *et al.*[335] further investigated composites combining the high conductivity of microchannel-structured hydrogels with the thermo-responsive behavior of PNIPAM. This composite material exhibited a 400% enhancement in actuation dynamics and a 4000% increase in actuation stress by effectively overcoming water transport limitations inherent to hydrogels. The volume change of the hydrogel can be triggered electrically or optically, enabling advanced actuation concepts for soft actuators. Channel-network-based actuators have demonstrated impressive performance. However, their synthesis and handling remain challenging. Consequently, alternative actuation technologies based on T-ZnO-templated materials, such as the EPRAE process, appear more promising for industrial applications. With further progress toward simplified synthesis routes and improved usability, this approach could become highly attractive for soft robotics.

4.3.3.2 Photonics and laser light scattering. T-ZnO networks exhibit unique optical properties, as discussed in Section 3.3. Many of these properties are directly transferred to aeromaterials structurally derived from T-ZnO and are further enhanced by the characteristics of the materials composing the new aeromaterial. Such materials are promising for a range of optical applications. For instance, an aeromaterial consisting of interconnected hollow h-BN microtubes and investigated by Schütt *et al.*[167] might be useful as a laser light diffuser. Due to the wide band gap of hBN ($\sim$6.5 eV), these aeromaterials exhibit extremely low absorption in the optical range. The interconnected h-BN microtubes act as individual Rayleigh scattering centers for incident laser light, diffusely scattering it in all directions with low speckle contrast. By simultaneously scattering blue, green, and red laser beams within the Aero-hBN, white light generation is achieved, which is conceptualized in Fig. 56a. This approach holds promise for high-brightness lighting applications with light outputs surpassing those of conventional LEDs, which are typically limited to about 5 kW cm^{-2}. However, the efficiency of laser diodes, especially in the green spectral region, remains a bottleneck. Saure *et al.*[322] have proposed an approach to address this challenge. Their work combines an aeromaterial based on SiO_2 (Fig. 56b), which exhibits optical properties in the visible spectrum comparable to boron nitride, with halide perovskite QDs (Fig. 56c), known for their high quantum yield. The $CsPbBr_3$ QDs used efficiently convert UV light into green emission at 505 nm, as demonstrated in Fig. 56d. While halide perovskite QDs are typically prone to degradation under environmental stressors, the authors present initial strategies to improve stability, including encapsulation with poly(ethylene glycol)dimethacrylate (pEGDMA).

These findings highlight the potential to incorporate QDs with different emission wavelengths into a laser-scattering aeromaterial. This enables a single, efficient laser diode to generate light that is both scattered and spectrally converted into the desired color output. For the transfer of this technology into real-world applications, emphasis should be placed on avoiding lead-based materials such as the QDs reported by Saure *et al.*,[322] as well as other highly toxic components. Ensuring the long-term stability of the laser light transformer and scatterer is also paramount. Furthermore, lasers can pose a serious health risk, particularly to the eyes, if the beam escapes a lighting device before being scattered by an aeromaterial. Therefore, developing safety mechanisms to ensure proper scattering and spatial distribution of the laser light is essential before this technology can be considered for real-world applications.

4.3.3.3 Biomedical applications. The hierarchical design capabilities enabled by the T-ZnO templating method also hold great potential for biomedical applications such as cell culture

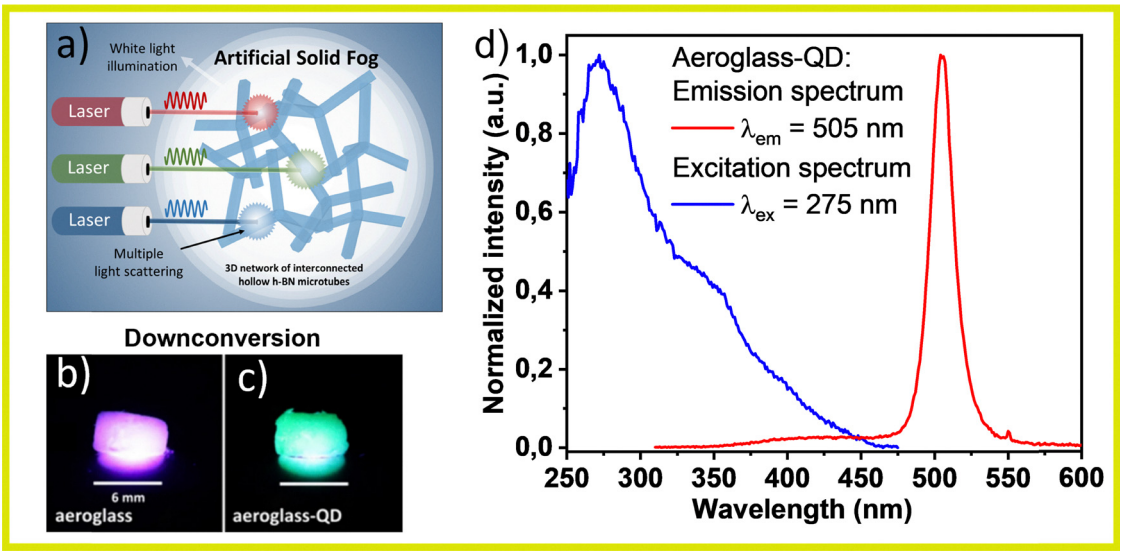

Fig. 56 (a) White-light generation *via* "artificial solid fog" using a 3D network of interconnected hollow h-BN microtubes (>99.99% porosity). Multiple light scattering within the foam converts directional RGB laser inputs into an isotropic, high-brightness white-light source.[167] (b) and (c) Photographs of pristine aeroglass and aeroglass-QD, respectively, under 275 nm excitation.[322] (d) Emission (λ_{ex} = 275 nm) and excitation (λ_{em} = 505 nm) spectra of the aeroglass-QD sample, demonstrating the down-conversion behavior of embedded QDs.[322] (a) Reproduced from ref. 167 with permision from Springer Nature,[167] Copyright 2020, (b)–(d) reproduced from ref. 322 with permision from Springer Nature,[322] Copyright 2024.

and drug delivery. In particular, aeromaterials are highly attractive as scaffolds for tissue engineering. This is due to their combination of a large, adaptable surface area for cell colonization and an open porous structure that facilitates effective nutrient transport (Fig. 57a).[329,345–349] This concept was demonstrated for instance by Taale *et al.*[346] who developed a multi-walled carbon nanotube (MWCNT)-based aeromaterial as a scaffold for osteoblast and fibroblast growth. The MWCNT scaffold was readily functionalized with biomineralizing agents, such as hydroxyapatite and bioactive glass nanoparticles, resulting in high cell viability and promising biocompatibility. When assessing aeromaterials for cell scaffolds, a particularly advantageous aspect is their hierarchical architecture, which closely mimics the multiscale structural complexity of natural biological systems. The open porosity of aeromaterial networks provides space for tissue growth while their interconnected pores facilitate nutrient transport.[329,345–349] Both of which are key challenges in designing functional tissue scaffolds.[350] Future research should focus on further enhancing this multiscale porosity to more closely replicate the extreme hierarchical architecture of biological systems. Increasing template

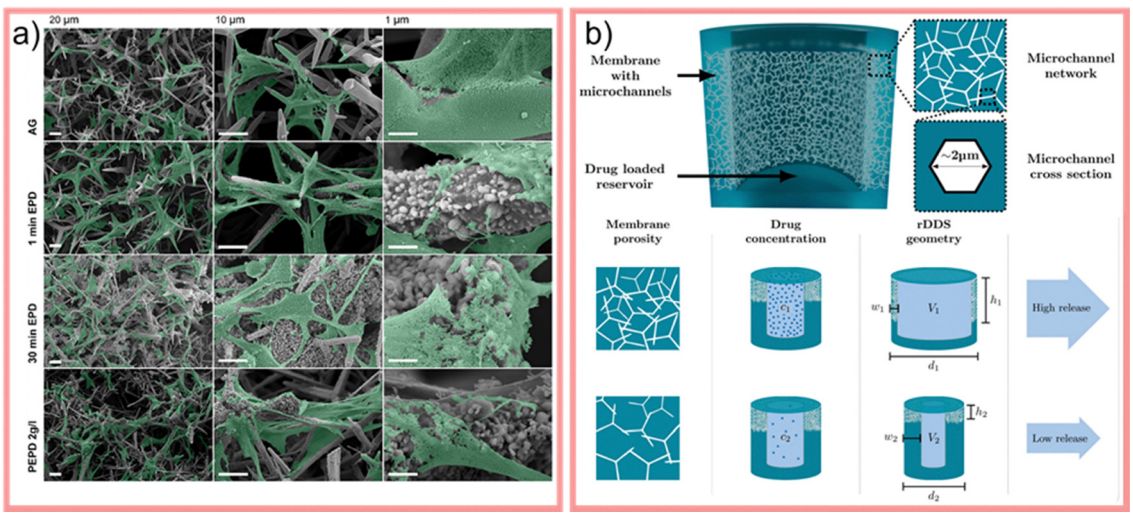

Fig. 57 Biomedical applications based on T-ZnO-templated materials. (a) SEM images of aerographite scaffolds for cell growth. The aerographite was decorated with hydroxyapatite nanoparticles *via* periodic electrophoretic deposition and cultivated with pre-osteoblast cells (green).[345] (b) Drug-reservoir concept using a T-ZnO-templated PDMS microchannel network. Release occurs *via* diffusion, with rates tunable by adjusting channel density (membrane porosity) and membrane thickness.[330] (a) Reproduced from ref. 345 with permision from American Chemical Society,[345] Copyright 2019, (b) reproduced from ref. 330 with permision from MDPI.,[330] Copyright 2022.

complexity through methods such as laser cutting or additive manufacturing may enable the development of biomimetic scaffolds. These could support the simultaneous growth of multiple biological structures, including cells and blood vessels, marking an important step toward the artificial fabrication of functional organs.[351]

In addition to aeromaterials, channel structures templated *via* T-ZnO networks offer significant potential for biomedical applications, particularly in the field of controlled drug delivery. One notable example is the work by Rasch *et al.*[327] who developed a PDMS-based microchannel network that functions as a drug reservoir and enables diffusion-controlled release. By adjusting the density and distribution of the drug-releasing channels, they achieved a highly tunable drug release profile (Fig. 57b). This simple yet effective system shows promise for applications such as glioblastoma therapy. Building on this concept, Hauck *et al.*[330] expanded the approach through detailed computational modeling of T-ZnO-templated channel networks, enhancing understanding and design optimization of such drug-delivery systems. Using T-ZnO-templated channel networks as drug delivery systems is a highly promising approach, as demonstrated in the literature. The commonly used PDMS matrix is easy to incorporate, and with further clinical evaluation, this straightforward technology could become a viable real-world application.

Hydrogel-based channel structures created *via* a T-ZnO templating approach can further serve as biomimetic models for human tissue. Siemsen *et al.*[328] investigated the migration behavior of cancer cells within these structures. They demonstrated that large-scale scaffolds can be infiltrated by cancer cells within just a few days. Their study also revealed that both the stiffness and the microarchitecture of the hydrogel significantly influence cellular invasion and nuclear dynamics. This underscores the importance of mechanical and structural cues in tumor progression. This study further highlights the potential of T-ZnO-templated materials for applications where diverse and complex biological architectures need to be mimicked.

4.3.3.4 Energy storage and conversion. The ability to fabricate hierarchically structured materials with large surface areas, tunable surfaces, and interconnected open porosity is highly attractive for applications in energy storage and conversion.

In the context of energy storage, T-ZnO-templated structures are particularly promising for the development of advanced supercapacitor electrodes.[352] High-performance supercapacitors require thick electrodes that combine high areal mass loading with efficient ion and electron transport, which can be achieved through a carefully engineered pore architecture. The T-ZnO templating approach has demonstrated impressive capabilities in this regard, as shown by Spurling *et al.*[353] who developed an MXene-based aeromaterial for supercapacitor applications (Fig. 58). Their design achieved a high areal loading of 7.2 mg cm^{-2}, a material density of 1.44 g cm^{-3}, and an excellent specific capacitance of 240 F g^{-1} (140 F cm^{-3}). Remarkably, even at high scan rates of 200 mV s^{-1}, the electrodes maintained an areal capacitance of 1.4 F cm^{-2}, outperforming state-of-the-art MXene-based supercapacitor electrodes. In a different approach, Yuksel *et al.*[85] developed an aerocomposite composed of nitrogen-doped tubular carbon and ZIF-8 particles, which was evaluated as an electrode material for zinc-ion supercapacitors. The resulting device exhibited an ultrahigh rate capability of up to 2000 mV s^{-1} and achieved a specific capacitance of 341.2 F g^{-1} at a current density of 0.1 A g^{-1}.

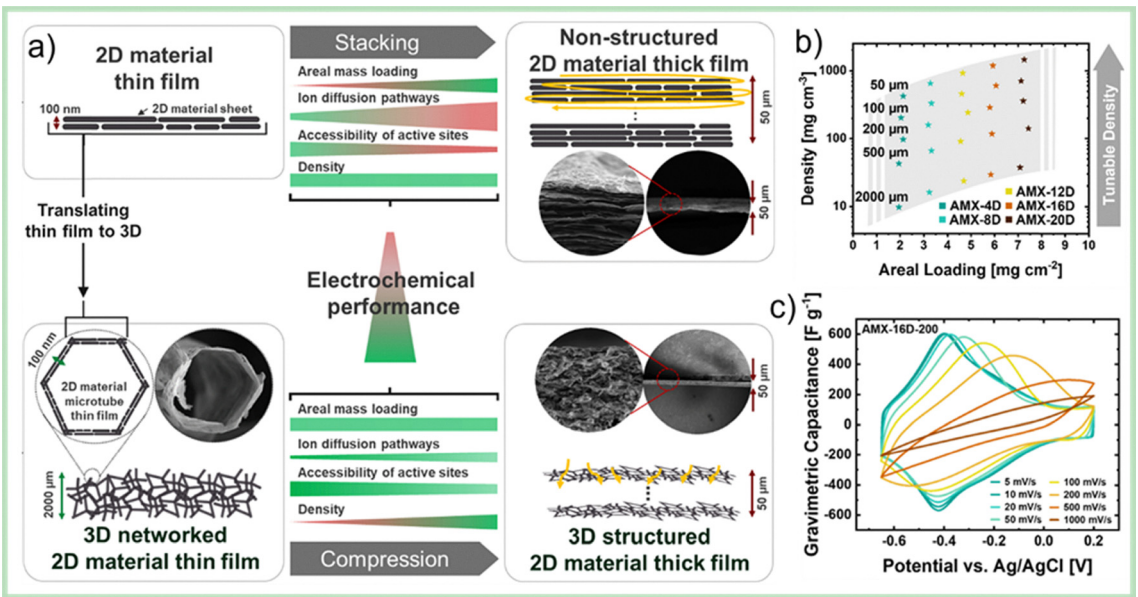

Fig. 58 Supercapacitors based on aero-MXenes. (a) Comparison between a conventional 2D nanomaterial thick film and a thick film produced by compressing an MXene-based aeromaterial, resulting in a 3D-structured thick film with a pronounced influence on electrochemical performance. (b) Density and areal loading of 3D-structured MXene (the grey area indicates the feasible electrode region; stars indicate the prepared and tested samples). (c) Cyclic voltammogram of a 3D-structured MXene film with a mass loading of 5.8 mg cm^{-2} in 0.5 M H_2SO_4 at scan rates from 5 mV s^{-1} to 1000 mV s^{-1}. (a) Reproduced from ref. 353 with permision from Elsevier,[353] Copyright 2024.

In addition to supercapacitors, hierarchically porous materials derived from T-ZnO have also been investigated for battery applications, particularly in lithium–sulfur (Li–S) batteries. In this context, the primary function of the T-ZnO-derived frameworks is to immobilize polysulfides. This mitigates the shuttle effect, thereby significantly enhancing the cycling stability and overall lifespan of the battery.[354–356] Furthermore, an atypical material for battery applications, composed of β-Ga_2O_3/$ZnGa_2O_4$, has been investigated in this context. It demonstrated promising initial capacities of 714 mAh g^{-1} and, beyond its electrochemical applicability, exhibited narrow-band PL emission at 504 nm under UV irradiation, thereby highlighting the multifunctional versatility of aeromaterials derived from T-ZnO templates.[357]

Despite promising lab-scale results, particularly for T-ZnO-templated supercapacitor electrodes, this technology remains far from real-world application. The high costs associated with T-ZnO, nanomaterials and aerofication make energy storage devices economically unfeasible. This is especially true when compared to other T-ZnO-templated technologies, such as EPRAE-based actuation, which offer unique functionalities and thus greater commercial potential despite high production costs.

Regarding energy conversion, materials synthesized *via* a T-ZnO templating approach have not yet been extensively studied. However, they hold significant potential, particularly in (photo)catalysis. This is due to their open porous architecture, which facilitates high flow conditions in gas-phase reactions while maintaining a large surface area and, consequently, a high density of catalytically active sites. This has been explored in several publications, with typically photocatalytic materials such as zinc-doped cerium oxide[20] (Fig. 59a) and titanium dioxide[325,358] (Fig. 59b). The structural benefits of these aeromaterials extend beyond morphology, as their mechanical robustness under gas flow[20] (Fig. 59c) enables stable operation in continuous-flow reactions. Their photocatalytic activity has also been demonstrated through the degradation of tetracycline using Aero-TiO_2 under visible and UV irradiation, including continuous-flow UV conditions (Fig. 59d).[325] Furthermore, among the many strategies aimed at enhancing photocatalytic performance, most of which focus on modifications at the nano- and microscale, the use of sacrificial T-ZnO templates presents a unique opportunity. It allows for structural control across multiple length scales, from the nanoscale to the macroscale. Notably, the macroscale is often overlooked in photocatalyst design. Yet, the ability to tailor features across all relevant scales, including the macroscale, may significantly improve photocatalytic efficiency.[20,359]

4.3.3.5 Sensing. T-ZnO itself is a versatile and promising material for various sensing applications (see Section 4.1.1). Its primary advantages in this field stem from its unique three-dimensional architecture. This provides, for example, a high surface area, excellent accessibility of active sites, and enhanced interaction with analytes. By employing T-ZnO as a structural template for the fabrication of three-dimensionally structured materials, these benefits can be transferred to other functional materials. This significantly improves their sensing performance. For example, Dragoman *et al.*[360] employed T-ZnO networks as sacrificial templates to synthesize an aeromaterial composed of GaN, which exhibits a high piezoelectric coefficient and demonstrates excellent sensitivity to pressures ranging from 5 to 40 atm. Due to its low density and mechanical robustness, this material holds significant promise for aerospace applications. In another innovative approach, Ren *et al.*[361] utilized the unique geometry of T-ZnO to fabricate a bio-inspired pressure sensor. By combining T-ZnO and graphene oxide *via* vacuum filtration, followed by T-ZnO etching and partial reduction, they created a selective membrane for cations. When placed between NaCl solution reservoirs, pressure applied to one reservoir induces the migration of cations through the membrane, generating a measurable signal as a result of net charge flow. This sensor demonstrated a sensitivity of 0.282 nA Pa^{-1} and response and recovery times of 90 ms and 110 ms, respectively. Further studies have highlighted the gas-

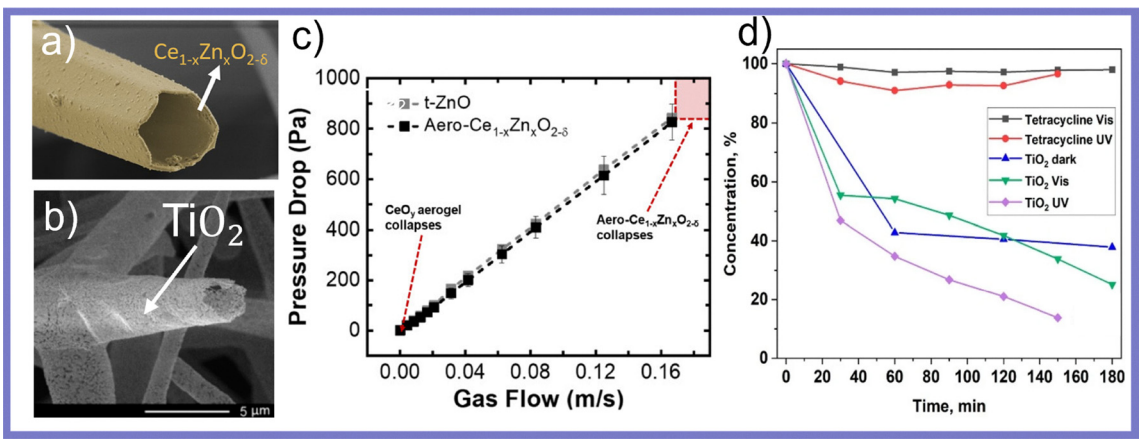

Fig. 59 Applications of aeromaterials as photocatalysts: (a) SEM image of Aero-$Ce_{1-x}Zn_xO_{2-\delta}$ showing the hollow, architecture. (b) SEM image of Aero-TiO_2 highlighting the open porous framework. (c) Pressure-drop curves of Aero-$Ce_{1-x}Zn_xO_{2-\delta}$ compared with pristine T-ZnO, illustrating the mechanical stability and gas-flow characteristics of the aeromaterial structure. (d) Photocatalytic degradation of tetracycline using Aero-TiO_2 under visible and UV irradiation. (a) and (c) Reproduced from ref. 20 with permision from American Chemical Society,[20] Copyright 2024, (b) reproduced from ref. 358 with permision from MDPI,[358] Copyright 2022, (d) reproduced from ref. 325 with permision from Springer Nature,[325] Copyright 2024.

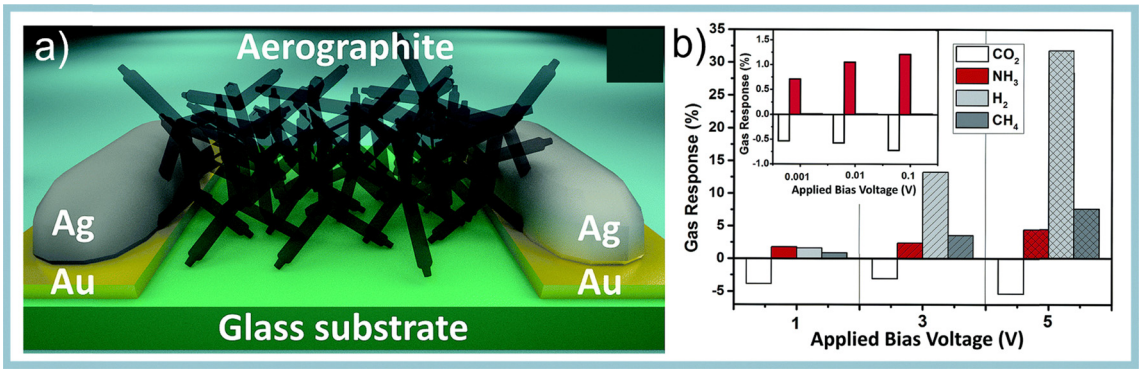

Fig. 60 (a) Schematic representation of the aerographite-based gas sensor structure, showing the interconnected aerographite network bridging Ag/Au contacts on a glass substrate. (b) Gas response of the aerographite sensor at room temperature as a function of applied bias voltage for CO_2 (500 ppm), NH_3 (100 ppm), H_2 (10 000 ppm), and CH_4 (10 000 ppm). (a) and (b) Reproduced from ref. 362 with permision from Royal Chemical Society,[362] Copyright 2016.

sensing capabilities.[362–365] and UV-Photodetection capabilities[366] of T-ZnO-templated materials. (Fig. 60a) shows a schematic gas sensor based on aerographite by Lupan *et al.*[362] (Fig. 60b) shows the response of the sensor after exposition to various gases and concentrations as a function of the applied bias voltage.[362] These examples demonstrate how the distinctive architecture of T-ZnO can be exploited as a microstructural template for designing advanced and highly responsive sensing devices at the lab scale. However, mass production of aeromaterial-based sensors remains challenging due to the need for highly reproducible control of film thickness, conduction pathways, and contacts. Such precision is less critical in other applications (*e.g.*, cell scaffolds or EPRAE-based systems), suggesting that the commercialization of T-ZnO-templated sensors will likely lag behind other T-ZnO-templated material technologies.

4.3.4 Current landscape and future perspectives for T-ZnO templated materials. The following section summarizes all published materials synthesized *via* a T-ZnO templating approach, shown in Table 14. The table lists their composition, the type (aeromaterial or channel structure), the synthesis approach, the tested application or suggested application scenario and the publication date.

The extensive list of materials and applications catalogued in Table 14 illustrates a dynamic and rapidly expanding field of research. To better synthesize these developments and identify future opportunities, we have distilled this information into a strategic "opportunity matrix" (Fig. 61). This matrix maps the primary material classes against their application domains, with the research maturity of each area color-coded according to its chronological emergence. The matrix reveals a clear

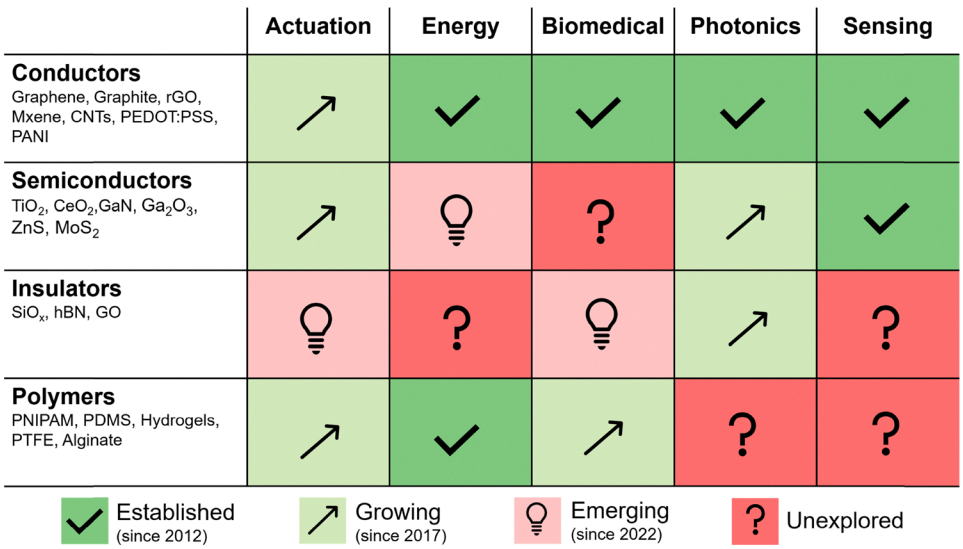

Fig. 61 The T-ZnO templating landscape, an opportunity matrix. This matrix provides a strategic overview of the research field, mapping material classes against key application domains. The color-coding indicates the research maturity for each intersection, based on the chronology of publications in Table 14: established (green, foundational work, since 2012), growing (light green, active diversification, since 2017), emerging (light red, recent breakthroughs, since 2022), and unexplored (red, potential future research avenues). The matrix highlights the field's evolution from foundational carbon-based materials towards a diverse and functionally driven frontier.

three-phase evolutionary trajectory. The field was founded on established (green) research into carbon and semiconductor materials mainly for sensing applications, which served as the initial proof-of-concept. A second wave of growing (light green) research, beginning around 2017, saw a diversification into new applications like actuation, largely driven by the adoption of more scalable synthesis methods. From 2022 until 2025 (light red) the field of T-ZnO templated materials made further progress in refining existing materials and synthesis approaches to tackle larger scale applications like air filters. Furthermore, more complex materials were synthesized like rGO flake loaded SiO_2 aeromaterials, which can be used for actuation *via* a volumetric photothermal response. In addition, the opportunity matrix shows material class application combinations, which have not been explored yet (red), but may represent significant opportunities for future investigation.

4.4 Key learnings from T-ZnO applications

The application landscape of T-ZnO is defined by a powerful duality. This is a direct consequence of the unique structure–property nexus described in Section 3. The material can be leveraged either as a functionally active component, where its intrinsic properties are paramount, or as a structurally transformative sacrificial template. To provide a critical overview, the diverse application areas discussed in this section are systematically summarized and evaluated in Table 15. This table offers a comparative analysis of each domain's technological maturity and the key challenges hindering its translation from the laboratory to industrial scale.

4.4.1 Key takeaway. As an active material, the interconnected tetrapod network acts as a structural amplifier. It takes the intrinsic electronic and piezoelectric properties of the ZnO WZ crystal (Sections 3.2 and 3.5) and magnifies their effect through its high surface area and robust percolation pathways (Sections 3.4 and 3.6). Conversely, the templating paradigm leverages solely a T-ZnO network's mechanical integrity and hierarchical porosity as a sacrificial blueprint. This approach allows for a paradigm shift from material-centric to architecture-centric, creating novel materials that inherit the form but not the function of ZnO.

4.4.2 Critical learning. The most profound insight is T-ZnO's role as a universal architectural platform that enables the decoupling of chemistry from architecture. The ability to meticulously control T-ZnO synthesis (Section 2) allows us to perfect a complex, hierarchical structure in one material system. This ''solved'' architecture can then be imprinted onto a vast library of other functional materials (*e.g.*, conductive carbons, catalytic oxides, soft hydrogels). These materials possess superior intrinsic properties but lack a natural pathway to form such intricate networks. This transfer of spatial information is the single most powerful capability offered by the T-ZnO platform.

4.4.3 Critical link. Across this diverse application space, two fundamental barriers consistently impede the transition from laboratory potential to real-world impact. First, ensuring long-term operational stability. Second, bridging the enormous scalability gap rooted in the synthesis methods discussed in Section 2. These are not merely material-level problems; they are systemic hurdles. They prevent T-ZnO-based structures from becoming reliable components in functional, integrated systems. Addressing these challenges requires a conceptual leap beyond material optimization. It demands the systems-level thinking embodied by the challenges that will define the future perspectives of this field in the final section.

5. A practical outlook for T-ZnO architected materials

This review has outlined the key structure–property relationships of T-ZnO. Its utility does not arise from ideal crystallinity,

Table 15 A critical comparison of the primary application domains for T-ZnO. The table evaluates each area based on the core scientific principles being exploited, its estimated technology readiness level (TRL), and the most significant barriers that must be overcome for widespread, real-world impact

Application area	Primary T-ZnO property leveraged	Current TRL (estimated)	Primary bottleneck for scale-up
Sensing applications (gas, UV, pressure, bio)	Chemiresistive effect, piezoelectricity, high surface area, and functionalizable surface	3–6 (lab-scale to pilot-scale; prototypes in real-world scenarios)	Long-term stability & drift, cross-sensitivity (to humidity/temp), and reproducibility in complex biological media.
Surface engineering & environmental (coatings, decontamination, catalysis)	Switchable wettability, hierarchical porosity/high surface area, and photocatalytic activity	2–6 (proof-of-concept to early industrial trials)	Long-term durability (especially under UV), cost-competitiveness with existing solutions (*e.g.*, activated carbon), and environmental concerns of some components (*e.g.*, fluorinated polymers).
Biomedical & healthcare (antibacterial, wound dressings, stents)	Biocompatibility, antibacterial/ antiviral activity, and mechanical reinforcement in composites.	5–10 (advanced development to early commercialization)	Ensuring long-term biocompatibility, navigating complex regulatory approval pathways, scaling-up pharma grade T-ZnO production
Energy storage & conversion (batteries, thermal storage)	Thermal conductivity, hierarchical porosity (for ion transport), and photocatalytic properties.	2–4 (lab-scale/proof-of-concept)	Scalable, low-cost synthesis for bulk applications; improving overall energy conversion/storage efficiency; ensuring long-term cycling stability.
Composite reinforcement & EMI shielding (structural fillers, shielding materials)	Mechanical percolation and 3D interlocking network to create a functional backbone.	2–4 (advanced research with promising laboratory results)	Optimizing filler-matrix interfacial adhesion for mechanical strength; balancing absorption *vs.* reflection for EMI shielding; cost.
Sacrificial templating (aeromaterials & channel structures)	Unique 3D morphology, hierarchical porosity, and chemical removability (*via* etching).	2–s6 (advanced research/ prototypes in real-world scenarios/emerging field)	Complexity of multi-step processing; scalability of high-quality coating methods (gas-phase *vs.* wet-chemical); cost of template production coating and template removal at industrial scale.

but from a complex, defect-rich architecture that is arrested far from its thermodynamic ground state. The same atomic defects that enable n-type conductivity can also quench luminescence or initiate mechanical fatigue. This trade-off is intrinsic and defines the performance envelope of T-ZnO-based systems. Rather than viewing defect-dependency as a liability, we propose treating it as a programmable feature. T-ZnO is a material in which defects, junctions, and network topology are not accidents, but control knobs. These effects are supported by experimental observations reported in the literature. Charge trapping at defect sites can record prior exposure to stress, light, or electrical bias. Meanwhile, junctions govern how electrical or mechanical signals propagate through the network.

5.1 Templating as a manufacturing approach

T-ZnO-based materials are best understood through the concept of architectural templating, which occupies a distinct position within advanced manufacturing. Additive manufacturing enables precise macroscopic shape control but provides limited access to complex nano- and microscale networks. Conversely, self-ordered assembly produces nanoscale features but offers little control over macroscopic form. T-ZnO templating bridges this critical gap. T-ZnO solves the "scalability gap" in nanotechnology by using self-assembly to create macroscopic, manipulatable parts. It allows for the transfer of a pre-formed, self-assembled nano-micro architecture into bulk materials with high fidelity. This effectively scales the benefits of the nanoscale to the human hand. T-ZnO performs best when function arises from the tetrapodal network itself. Examples include high porosity, rapid mass transport, low density, and large accessible surface area. Comparable benefits can also be achieved when these network properties are transferred into new material classes. In this way, T-ZnO enables functional systems that remain difficult to achieve using conventional fillers or fabrication strategies.

5.2 From laboratory studies to practical systems

Looking ahead, future progress in T-ZnO design depends on controlling morphology together with the type, density, and spatial distribution of imperfections. This is necessary to achieve defined and testable functions. This requires correlating synthesis parameters with measurable outputs such as junction density, percolation threshold, carrier mobility, and mechanical compliance. Two complementary strategies can be distinguished. First, T-ZnO can act as an active framework in which sensing, memory-related effects, and signal routing arise directly from the network architecture. Second, it can serve as a sacrificial template to transfer this architecture into polymers, carbons, or oxides. This separates structural function from ZnO chemistry. Achieving either strategy depends on predictive synthesis and scalable processing. From a development perspective, bringing T-ZnO from laboratory studies to practical use requires a clear and structured development path. Recent advances in synthesis, structural control, and integration indicate that T-ZnO can act as more than a passive functional filler. It can function as a connected network whose macroscopic response is governed by interactions between many junctions. This, in turn, requires control over individual tetrapods, their connections, and the integration of resulting networks into stable and scalable material systems.

5.2.1 Predictive synthesis. The first step is the transition from empirical synthesis to predictive design of T-ZnO. This requires quantitatively linking reactor conditions to tetrapod geometry, defect density, and network topology. This data is the foundational input required to build the "digital twin" envisioned in Section 3.7. A concrete research direction is the development of predictive growth models for a defined target, such as a T-ZnO network with a specified junction density and percolation threshold. In such a scenario, reactor temperature profiles, precursor concentration, and residence time must be systematically varied and correlated with three-dimensional network descriptors. These datasets will not only guide synthesis but serve as the ground-truth calibration for the digital twin. This allows researchers to virtually simulate and optimize application-relevant architectures before physical fabrication begins.

5.2.2 Network integration and interfaces. Once predictive synthesis is established, the focus shifts to network integration. Here, performance is governed primarily by junction behavior, including contact resistance, adhesion, and strain transfer. A critical milestone will be the fabrication of thin, percolated T-ZnO layers embedded in elastomeric matrices to serve as pressure- or deformation-sensitive coatings. In this case, junction engineering through surface functionalization or partial coating directly controls signal stability and sensitivity under cyclic loading. This provides a clear link between interface design and macroscopic response.

5.2.3 Scalability and manufacturing. For practical use, T-ZnO systems must transition from batch to continuous processing to address the ultimate barrier: Cost. If high-purity T-ZnO remains prohibitively expensive, it cannot compete with conventional fillers like carbon black. Future success depends on techno-economic breakthroughs, not just scientific ones. This includes moving from energy-intensive batch furnaces to continuous flow reactors and investigating the use of recycled zinc sources to lower feedstock costs. These economic constraints will play a decisive role in defining which architectures are viable beyond the laboratory scale.

5.2.4 Interdisciplinary integration. Progress across all development directions depends on interdisciplinary research that links synthesis, characterization, data analysis, and system integration. Without this integration, relationships between processing conditions, structure, and performance remain fragmented. This slows reproducibility and scale-up.

Together, the technical directions described above form a single, connected development path. Predictive synthesis, network integration, and scalable manufacturing inform and constrain each other through continuous feedback.

5.3 Development roadmap and application perspectives

Table 16 summarizes a development roadmap for T-ZnO network materials, highlighting current practice, key limitations, and concrete steps required for progress.

If these challenges can be addressed, the T-ZnO platform could enable several application directions that rely on

Table 16 Outlook and roadmap for T-ZnO-based technologies

Area	Current practice	Main limitation	Required advance	TRL	Outcome	Feedback
Predictive synthesis	Trial-and-error synthesis	Weak process-structure link	Link reactor conditions to tetrapod geometry and junction density	2 → 4	Controlled network topology	Enables integration and scale-up
Network integration	Single-function composites	Poor interface control	Control contact resistance, adhesion, and strain transfer	1 → 3	Predictable electrical and mechanical response	Defines failure modes that dictate synthesis targets.
Manufacturing scale-up	Lab-scale batch synthesis	Low throughput, high energy cost	Develop continuous, energy-efficient reactors	2 → 5	Scalable production of T-ZnO networks	Sets hard cost limits that eliminate non-viable precursors.
Interdisciplinary expertise	Disciplinary separation	Fragmented workflows	Integrate synthesis, characterization, and system design	N/A	Faster iteration and reproducibility	Closes the loop between atomistic simulation and reactor engineering.

controlled network architecture rather than material composition alone. In catalysis and energy-related systems, the well-defined geometry of tetrapod junctions can be used to create microstructured catalysts and battery or supercapacitor electrodes. These would feature high accessible surface area, efficient mass transport, and improved mechanical stability. T-ZnO-derived networks can also be used as physical systems in which charge transport is distributed across many junctions. Their electrical response is governed by network topology and junction properties. This leads to history-dependent behavior without relying on conventional circuit design. This nonlinear, memory-driven response suggests that T-ZnO networks could serve as physical substrates for reservoir computing and neuromorphic hardware. For example, an elastomeric patch embedded with a T-ZnO network could be utilized as an adaptive tactile sensor (a smart skin), where the network inherently processes and filters complex mechanical stimuli, such as human touch or robotic grasping forces, without the need for external analog-to-digital microprocessors. The same open, multiscale architectures make T-ZnO templates suitable as scaffolds for biological systems or hybrid bio-inorganic materials. Here, surface chemistry can be tailored to control interactions with organic matter. Beyond static structures, these networks further enable materials whose properties evolve over time. Examples include actuators with tunable porosity or conductive pathways that change under electrical or mechanical loading. Together, these examples illustrate how control over network architecture can translate into additional, application-specific functionality.

Ultimately, T-ZnO represents a paradigm shift from Material-Centric to Architecture-Centric design. It is a versatile building block for architected materials in which function is encoded in network structure rather than added through composition alone. Continued progress will depend on closing feedback loops between synthesis, structure, and performance. This must be supported by coordinated experimental, analytical, and processing expertise. With these elements in place, T-ZnO-based systems provide a well-defined platform for exploring structure-driven functionality across a range of material applications.

Conflicts of interest

The authors declare that they have no conflicts of interest.

Glossary of abbreviations

0D/1D/2D/3D	Zero-/one-/two-/three-dimensional
Aero-BN	Aero-boron nitride
APMP	Atmospheric-pressure microwave plasma
APTES	(3-Aminopropyl)triethoxysilane
c-AFM	Conductive atomic force microscopy
CDF	Counterflow diffusion flame
CFD	Computational fluid dynamics
CL	Cathodoluminescence
CNT	Carbon nanotube
CVD	Chemical vapor deposition
Da	Damköhler number (Da_I, Da_{II})
DFT	Density functional theory
DLE	Deep-level emission
DNA	Deoxyribonucleic acid
DPy	4,4′-Dipyridyl
DSSC	Dye-sensitized solar cell
E-FTS	Ethanol-assisted flame transport synthesis
ED	Electron diffraction
EDX	Energy dispersive X-ray (analysis)
EELS	Electron energy loss spectroscopy
EMI	Electromagnetic interference
EPRAE	Electrically powered repeatable air explosion
EPR	Electron paramagnetic resonance
ETEM	Environmental transmission electron microscopy
F-POSS	Fluorinated polyhedral oligomeric silsesquioxane
FEA	Finite element analysis
FEM	Finite element method
FET	Field-effect transistor
FTIR	Fourier-transform infrared spectroscopy
FTS	Flame transport synthesis
GelMA	Gelatin methacryloyl
GMP	Good manufacturing practice
HER-2	Epidermal growth factor receptor 2
HFCVD	Hot-filament chemical vapor deposition
HRTEM	High-resolution transmission electron microscopy
HVPE	Hybrid vapor phase epitaxy
IMPS	Intensity modulated photocurrent spectroscopy
L_D	Debye length
LED	Light-emitting diode
LSPR	Localized surface plasmon resonance
MCM	Melting-combustion method

MEMS	Micro-electro-mechanical systems
ML	Machine learning
MOF	Metal–organic framework
MWCNT	Multi-walled carbon nanotube
NBE	Near-band-edge (Emission)
OTS	Octadecyltrichlorosilane
OVFE	Oxygen vacancy formation energy
PCM	Phase change material
PDMS	Polydimethylsiloxane
Pe	Péclet number
PEDOT:PSS	Poly(3,4-ethylenedioxythiophene)polystyrene sulfonate
pEGDMA	Poly(ethylene glycol)dimethacrylate
PL	Photoluminescence
PLE	Photoluminescence excitation
PMMA	Poly(methyl methacrylate)
PNIPAM	Poly(*N*-isopropylacrylamide)
PTFE	Polytetrafluoroethylene
PVB	Polyvinyl butyral
PVDF	Polyvinylidene fluoride
QD	Quantum dot
ROS	Reactive oxygen species
SAED	Selected area electron diffraction
SAXS	Small-angle X-ray scattering
SEM	Scanning electron microscopy
SERS	Surface-enhanced Raman spectroscopy
SHS	Self-propagating high-temperature synthesis
STEM	Scanning transmission electron microscopy
STM	Scanning tunneling microscopy
TCO	Transparent conductive oxide
TEM	Transmission electron microscopy
TRPL	Time-resolved photoluminescence
T-ZnO	Tetrapodal zinc oxide
UPS	Ultraviolet photoemission spectroscopy
VEGF	Vascular endothelial growth factor
VOCs	Volatile organic compounds
WAXS	Wide-angle X-ray scattering
WGM	Whispering gallery mode
WZ	Wurtzite (crystal structure)
XPS	X-ray photoelectron spectroscopy
XRD	X-ray diffraction
ZB	Zinc-blende (crystal structure)
ZIF	Zeolitic imidazolate framework

Master glossary

Term	Definition
Active functional material	A design paradigm where the T-ZnO tetrapod itself performs the primary task (*e.g.*, sensing, catalysis) by leveraging its intrinsic electronic, optical, or piezoelectric properties.
Active structural material	A design paradigm where the T-ZnO network serves as a physical backbone. Its function relies on the 3D geometry and mechanical connectivity (*e.g.*, for reinforcement or EMI shielding) rather than chemical activity.
Aeromaterial	An ultra-lightweight, highly porous material synthesized by coating a sacrificial T-ZnO template with a target material (*e.g.*, Carbon, GaN) and subsequently etching away the ZnO, leaving a hollow, interconnected tubular network.
Antifouling	The capability of a surface coating to inhibit the attachment and growth of bio-organisms (*e.g.*, marine biofouling). In T-ZnO coatings, this is achieved through tunable wettability and surface micro-texture.
Architectural templating	The strategic manufacturing niche of T-ZnO. It involves using the self-assembled tetrapod network to transfer complex, high-fidelity micro-architectures to macroscopic materials, effectively bridging the scale gap between bottom-up synthesis and top-down fabrication.
Atom economy	A green chemistry metric that evaluates the efficiency of a chemical reaction by calculating how many atoms from the reactants are incorporated into the final product *versus* how many are lost as waste.
Band structure engineering	The modification of a material's electronic structure (specifically the bandgap and band edges) through alloying (*e.g.*, MgZnO) or doping to tailor its optical absorption or electrical properties.
Carbothermal reduction	A high-temperature synthesis mechanism used in CVD where carbon acts as a reducing agent to strip oxygen from a metal oxide (*e.g.*, ZnO) to generate metal vapor.
Cassie–Baxter state	A wetting regime where a liquid droplet sits on top of surface microstructures with trapped air pockets underneath, resulting in superhydrophobicity and high contact angles.
Channel structure	An inverse-opal-like material created by infiltrating the void space of a T-ZnO network with a matrix (*e.g.*, polymer, hydrogel) and removing the template, resulting in a solid block permeated by interconnected micro-channels.
Chemiresistive sensor	A sensor device that detects analytes (gases) or radiation (UV) by measuring changes in electrical resistance caused by the modulation of the surface depletion layer width.
Correlative microscopy	An analytical approach that applies multiple characterization techniques (*e.g.*, CL, SEM, EELS) to the *exact same* single nanostructure to directly link atomic-scale features to functional performance.
Damköhler number, second (Da_{II})	A dimensionless number representing the ratio of the chemical reaction rate to the diffusive mass transfer rate. In T-ZnO synthesis, a high Da_{II} indicates the system is reaction-dominated, favoring gas-phase nucleation of tetrapods.
Depletion layer	A space-charge region at the semiconductor surface depleted of mobile carriers. Its modulation by adsorbed oxygen or target gases is the fundamental transduction mechanism for T-ZnO gas sensors.
Digital twin	A comprehensive, multi-physics computational model capable of simulating the material's entire lifecycle. It connects macroscopic reactor parameters (T,P,Flow) directly to the resulting atomic structure and final functional performance.
Double Schottky barrier (DSB)	The potential energy barrier formed at the grain boundary between two contacting tetrapod arms. It creates back-to-back depletion regions, acting as the dominant resistive bottleneck for charge transport in the network.
Endocytosis	The cellular uptake mechanism for small particles. T-ZnO microparticles are typically larger than the threshold for endocytosis, which prevents cellular internalization and significantly reduces cytotoxicity compared to nanoparticles.
Exciton	A quasiparticle consisting of an electron and a hole bound together by electrostatic attraction. ZnO has a high exciton binding energy (60 meV), enabling stable room-temperature light emission.

Table (*continued*)

Term	Definition
Exciton-polariton	A hybrid light-matter quasiparticle resulting from the strong coupling of photons and excitons, typically observed in high-quality T-ZnO optical cavities.
Flaw tolerance	A nanomechanical principle based on Griffith's theory: as material volume decreases (to the nanoscale), the probability of containing a critical failure-inducing flaw drops, allowing ceramic T-ZnO arms to bend elastically without fracturing.
Fog harvesting	The collection of water from the atmosphere using functionalized surfaces. T-ZnO composites, particularly those with patterned wettability (Janus membranes), optimize the nucleation and transport of water droplets.
Formation energy (E_f)	The thermodynamic energy cost required to create a specific defect. It is not fixed but varies with the Fermi level and chemical potential (*e.g.*, Zn-rich *vs.* O-rich conditions).
Free carrier screening	The phenomenon where mobile charge carriers (electrons) redistribute to neutralize the strain-induced piezopotential, fundamentally limiting the efficiency of piezoelectric sensing in semiconducting ZnO.
Geometric amplification	The structural mechanism where the tetrapod geometry concentrates applied macroscopic force at the arm roots (junctions), generating a local piezopotential significantly higher than in simple nanowires.
Janus membrane	A membrane engineered with asymmetric wettability (*e.g.*, one side hydrophobic, the other hydrophilic) to drive directional water transport, utilized in fog harvesting and separation applications.
Kinetic control	A growth regime dominated by high energy and rapid flux. Atoms adhere to the crystal surface faster than they can diffuse to equilibrium positions, leading to anisotropic, high-energy shapes like tetrapods.
Localized buckling	The specific deformation mode of T-ZnO under compression, where the central core acts as a compliant hinge, allowing the network to deform reversibly rather than fracturing.
Materials-by-design	A paradigm shifting from empirical trial-and-error to the predictive, rational engineering of materials with specific target properties using computational modeling and fundamental physical laws.
Metastable	A state that is energetically higher than the ground state but kinetically stable over long periods. The cubic zinc blende (ZB) phase is hypothesized to be the metastable nucleus for T-ZnO.
Mie scattering	The elastic scattering of light by particles comparable in size to the light's wavelength. This is the dominant mechanism driving the strong ''light trapping'' and path-length enhancement in T-ZnO networks.
Molecular sieve	A porous coating (*e.g.*, ZIF-8) applied to T-ZnO sensors that filters gas molecules based on kinetic diameter, thereby enhancing selectivity (*e.g.*, allowing H_2 to pass while blocking larger molecules).
Monodispersity	The state of a collection of particles having uniform size and shape.
Near-band-edge (NBE) emission	Sharp, UV photoluminescence resulting from the direct recombination of excitons. A high NBE/DLE ratio is the primary metric for high crystal quality.
Non-centrosymmetric	A crystal lattice lacking a center of inversion (symmetry). This structural asymmetry in wurtzite ZnO leads to charge polarization under strain, the origin of the piezoelectric effect.
Nucleation	The initial symmetry-breaking event in crystal growth where a small cluster of atoms rearranges into a stable thermodynamic phase, providing the template for subsequent growth.
Passivation	The application of a coating or chemical treatment to neutralize surface defect states, thereby reducing non-radiative recombination and improving carrier mobility.
Piezo-phototronics	A field of coupled physics using the strain-induced piezopotential to modulate the band structure at an interface, thereby controlling the generation, separation, and transport of photo-excited carriers.
Piezotronics	A field using the piezoelectric potential as a ''gate'' voltage to tune the charge carrier transport in a semiconductor device (effectively a mechanical field-effect transistor).
Pinch-off effect	A transport condition in nanowires where the surface depletion regions overlap, causing the entire cross-section to become insulating.
Polar catastrophe	The thermodynamic instability of crystal facets terminated by a single ionic species (*e.g.*, the polar {0001} face). The surface reconstructs or adsorbs species (like $^-$OH) to neutralize this diverging potential, driving high chemical reactivity.
Predictive synthesis	The transition from empirical material discovery to data-driven manufacturing. It relies on establishing quantitative scaling laws (like Da_{II} and Pe) to accurately forecast morphological outcomes before physical synthesis begins.
Rational design	An engineering approach based on the predictive understanding of fundamental chemical and physical principles to create materials with specific, pre-determined functionalities.
Sacrificial templating	A manufacturing strategy where the T-ZnO network defines the architecture of a new material. The ''transcription'' of the tetrapodal geometry allows the fabrication of complex 3D structures from materials that cannot self-assemble into such shapes.
Self-compensation	A thermodynamic feedback loop where shifting the Fermi level (*e.g.*, to achieve p-type doping) lowers the formation energy of opposing native defects (*e.g.*, donors), which spontaneously form to neutralize the intended doping.
Supersaturation	A non-equilibrium state where a vapor or solution contains a concentration of solute exceeding the thermodynamic solubility limit. It is the primary thermodynamic driving force for nucleation.
Switchable wettability	The ability of T-ZnO surfaces to reversibly transition between hydrophobic and hydrophilic states under external stimuli (UV light, heat), acting as a gate for molecular access in sensors and coatings.
Synthesis-stability nexus	The principle that a material's ultimate lifecycle and failure modes are inextricably pre-determined by the thermodynamic path taken during its initial synthesis.
Synthesis-structure–property nexus	The foundational concept of materials science, describing the causal link where processing conditions determine atomic/micro-structure, which in turn dictates macroscopic material performance.
Thermal runaway	An uncontrolled exothermic chain reaction in batteries. T-ZnO coatings on separators or electrodes help prevent this by providing thermal stability and preventing internal short circuits.
Thermodynamic control	A growth regime dominated by stability and slow rates. Atoms have sufficient time to diffuse to low-energy sites, resulting in compact, faceted shapes like spheres or prisms to minimize surface energy.
Whispering gallery mode (WGM)	An optical resonance effect where light propagates around the hexagonal circumference of a T-ZnO arm *via* total internal reflection, acting as a high-quality optical cavity.
Wurtzite (WZ)	The thermodynamically stable, hexagonal crystal polymorph of ZnO. It is non-centrosymmetric and forms the arms of the tetrapod.
Zinc-blende (ZB)	The metastable, cubic crystal polymorph of ZnO. Several growth models propose that a ZB seed is required to initiate the tetrahedral symmetry of the tetrapod.

Data availability

No primary research results, software or code have been included and no new data were generated or analysed as part of this review.

Acknowledgements

The authors acknowledge the German Aerospace Centre (DLR – FKZ: 50RP2300A) and the German Research Foundation (DFG – 501386727) for the financial support of this work. Furthermore, this project received support from the German Research Foundation (DFG) through the German-Taiwan Collaborative Project (AD 183/35-1).

References

1 M. L. Fuller, Twinning in Zinc Oxide, *J. Appl. Phys.*, 1944, **15**, 164–170.
2 K. Nishio, T. Isshiki, M. Kitano and M. Shiojiri, Structure and growth mechanism of tetrapod-like ZnO particles, *Philos. Mag. A*, 1997, **76**, 889–904.
3 H. Iwanaga, M. Fujii and S. Takeuchi, Growth model of tetrapod zinc oxide particles, *J. Cryst. Grow.*, 1993, **134**, 275–280.
4 C. Ronning, N. G. Shang, I. Gerhards, H. Hofsäss and M. Seibt, Nucleation mechanism of the seed of tetrapod ZnO nanostructures, *J. Appl. Phys.*, 2005, **98**, 34307.
5 Q. Zhang, W. Fan and L. Gao, Anatase TiO_2 nanoparticles immobilized on ZnO tetrapods as a highly efficient and easily recyclable photocatalyst, *Appl. Catal., B*, 2007, **76**, 168–173.
6 O. Lupan, L. Chow and G. Chai, A single ZnO tetrapod-based sensor, *Sens. Actuators, B*, 2009, **141**, 511–517.
7 W. Chen and S. Yang, Dye-sensitized solar cells based on ZnO nanotetrapods, *Front. Optoelectron.*, 2011, **4**, 24–44.
8 M. Mecklenburg, A. Schuchardt, Y. K. Mishra, S. Kaps, R. Adelung, A. Lotnyk, L. Kienle and K. Schulte, Aerographite: ultra lightweight, flexible nanowall, carbon microtube material with outstanding mechanical performance, *Adv. Mater.*, 2012, **24**, 3486–3490.
9 F. Rasch, F. Schütt, L. M. Saure, S. Kaps, J. Strobel, O. Polonskyi, A. S. Nia, M. R. Lohe, Y. K. Mishra, F. Faupel, L. Kienle, X. Feng and R. Adelung, Wet-Chemical Assembly of 2D Nanomaterials into Lightweight, Microtube-Shaped, and Macroscopic 3D Networks, *ACS Appl. Mater. Interfaces*, 2019, **11**, 44652–44663.
10 Y. Ding, Z. L. Wang, T. Sun and J. Qiu, Zinc-blende ZnO and its role in nucleating wurtzite tetrapods and twinned nanowires, *Appl. Phys. Lett.*, 2007, **90**, 153510.
11 M. Shiojiri and C. Kaito, Structure and growth of ZnO smoke particles prepared by gas evaporation technique, *J. Cryst. Grow.*, 1981, **52**, 173–177.
12 Y. K. Mishra and R. Adelung, ZnO tetrapod materials for functional applications, *Mater. Today*, 2018, **21**, 631–651.
13 A. Pujara, R. Sharma, S. Sharma, M. Bechelany, Y. K. Mishra and J. Prakash, Novel zinc oxide 3D tetrapod nano-microstructures: recent progress in synthesis, modification and tailoring of optical properties for photocatalytic applications, *Mater. Adv.*, 2025, **6**(7), 2123–2153.
14 J. S. Tawale, K. K. Dey, R. Pasricha, K. N. Sood and A. K. Srivastava, Synthesis and characterization of ZnO tetrapods for optical and antibacterial applications, *Thin Solid Films*, 2010, **519**, 1244–1247.
15 M. C. Newton and P. A. Warburton, ZnO tetrapod nanocrystals, *Mater. Today*, 2007, **10**, 50–54.
16 M. Y. Guo, A. M. C. Ng, F. Liu, A. B. Djurisic, W. K. Chan, H. Su and K. S. Wong, Effect of native defects on photocatalytic properties of ZnO, *J. Phys. Chem. C*, 2011, **115**, 11095–11101.
17 B. Yin, Y. Qiu, H. Zhang, J. Lei, Y. Chang, J. Ji, Y. Luo, Y. Zhao and L. Hu, Piezoelectric effect of 3-D ZnO nanotetrapods, *RSC Adv.*, 2015, **5**, 11469–11474.
18 F. Rasch, F. Schütt, L. M. Saure, S. Kaps, J. Strobel, O. Polonskyi, A. S. Nia, M. R. Lohe, Y. K. Mishra, F. Faupel, L. Kienle, X. Feng and R. Adelung, Wet-Chemical Assembly of 2D Nanomaterials into Lightweight, Microtube-Shaped, and Macroscopic 3D Networks, *ACS Appl. Mater. Interfaces*, 2019, **11**, 44652–44663.
19 L. M. Saure, N. Kohlmann, H. Qiu, S. Shetty, A. Shaygan Nia, N. Ravishankar, X. Feng, A. Szameit, L. Kienle, R. Adelung and F. Schütt, Hybrid Aeromaterials for Enhanced and Rapid Volumetric Photothermal Response, *ACS Nano*, 2023, **17**, 22444–22455.
20 J. Lumma, T. Tjardts, E. Greve, L. M. Saure, S. Veziroglu, R. Adelung, L. Kienle, N. Wolff and F. Schütt, Synthesis of Highly Porous 3D Cerium Oxide Networks Designed for Catalytic Applications, *Cryst. Growth Des.*, 2024, **24**, 4914–4923.
21 Y. K. Mishra, G. Modi, V. Cretu, V. Postica, O. Lupan, T. Reimer, I. Paulowicz, V. Hrkac, W. Benecke, L. Kienle and R. Adelung, Direct Growth of Freestanding ZnO Tetrapod Networks for Multifunctional Applications in Photocatalysis, UV Photodetection, and Gas Sensing, *ACS Appl. Mater. Interfaces*, 2015, **7**, 14303–14316.
22 N. Hongsith, T. Chairuangsri, T. Phaechamud and S. Choopun, Growth kinetic and characterization of tetrapod ZnO nanostructures, *Solid State Commun.*, 2009, **149**, 1184–1187.
23 G. Modi, Zinc oxide tetrapod: a morphology with multifunctional applications, *Adv. Nat. Sci.: Nanosci. Nanotechnol.*, 2015, **6**, 33002.
24 H. Iwanaga, M. Fujii and S. Takeuchi, Inter-leg angles in tetrapod ZnO particles, *J. Cryst. Grow.*, 1998, **183**, 190–195.
25 H. Iwanaga, M. Fujii, M. Ichihara and S. Takeuchi, Some evidence for the octa-twin model of tetrapod ZnO particles, *J. Cryst. Grow.*, 1994, **141**, 234–238.
26 M. S. Riahimadvar and M. Tajaldini, Fast and one-step synthesis of small ZnO nano-tetrapods Using CO 2 laser in ambient air: physical properties, *Phys. Scr.*, 2022, **97**, 105811.
27 S. Rackauskas, K. Mustonen, T. Järvinen, M. Mattila, O. Klimova, H. Jiang, O. Tolochko, H. Lipsanen, E. I. Kauppinen and A. G. Nasibulin, Synthesis of ZnO tetrapods

for flexible and transparent UV sensors, *Nanotechnology*, 2012, **23**, 95502.
28 B.-B. Wang, J.-J. Xie, Q. Yuan and Y.-P. Zhao, Growth mechanism and joint structure of ZnO tetrapods, *J. Phys. D: Appl. Phys.*, 2008, **41**, 102005.
29 D. B. Padmanaban, P. Maguire and D. Mariotti, Non-equilibrium defect chemistry in oxygen-rich zinc oxide nano-tetrapods synthesized using atmospheric pressure microplasma, *J. Mater. Chem. A*, 2024, **12**, 9212–9231.
30 Y. Qiu and S. Yang, ZnO Nanotetrapods: Controlled Vapor-Phase Synthesis and Application for Humidity Sensing, *Adv. Funct. Mater.*, 2007, **17**, 1345–1352.
31 R. B. Saunders, E. McGlynn and M. O. Henry, Theoretical Analysis of Nucleation and Growth of ZnO Nanostructures in Vapor Phase Transport Growth, *Cryst. Growth Des.*, 2011, **11**, 4581–4587.
32 A. F. Gouveia, S. C. S. Lemos, E. R. Leite, E. Longo and J. Andrés, Back to the Basics: Probing the Role of Surfaces in the Experimentally Observed Morphological Evolution of ZnO, *Nanomaterials*, 2023, **13**(6), 978.
33 K. Zheng, C. X. Xu, G. P. Zhu, X. Li, J. P. Liu, Y. Yang and X. W. Sun, Formation of tetrapod and multipod ZnO whiskers, *Phys. E*, 2008, **40**, 2677–2681.
34 S. Rackauskas, O. Klimova, H. Jiang, A. Nikitenko, K. A. Chernenko, S. D. Shandakov, E. I. Kauppinen, O. V. Tolochko and A. G. Nasibulin, A Novel Method for Continuous Synthesis of ZnO Tetrapods, *J. Phys. Chem. C*, 2015, **119**, 16366–16373.
35 E. M. Wong, J. E. Bonevich and P. C. Searson, Growth kinetics of nanocrystalline ZnO particles from colloidal suspensions, *J. Phys. Chem. B*, 1998, **102**, 7770–7775.
36 Y. Liu, G. Lu, L. Guo, Y. Zhang and M. Chen, Flexible Pressure Sensor Based on Tetrapod-Shaped ZnO-PDMS Piezoelectric Nanocomposites, *IEEE Sens. J.*, 2023, **23**, 3532–3540.
37 S. Shree, V. Postica, L. Voß, C. Lupan, Y. K. Mishra, L. Kienle, R. Adelung and O. Lupan, Optimization of T-ZnO Process for Gas and UV Sensors, *ACS Appl. Electron. Mater.*, 2025, **7**, 3848–3863.
38 D. Yang, R. A. Gopal, T. Lkhagvaa and D. Choi, Oxidizing agent impacting on growth of ZnO tetrapod nanostructures and its characterization, *Environ. Res.*, 2021, **197**, 111032.
39 H. Yamamoto, Y. Otani, T. Seto, P. Nartpochananon and T. Charinpanitkul, Generation of uniform tetrapod-shaped zincoxide nanoparticles by gas-phase reaction with using flow restrictor, *Adv. Powder Technol.*, 2012, **23**, 71–79.
40 A. Krost, J. Christen, N. Oleynik, A. Dadgar, S. Deiter, J. Bläsing, A. Krtschil, D. Forster, F. Bertram and A. Diez, Ostwald ripening and flattening of epitaxial ZnO layers during in situ annealing in metalorganic vapor phase epitaxy, *Appl. Phys. Lett.*, 2004, **85**, 1496–1498.
41 Z. Zhou, J. Liu and S. Hu, Studies on the kinetics process of tetra-needle-like ZnO whisker growth, *J. Cryst. Grow.*, 2005, **276**, 317–320.
42 M. Ali and M. Winterer, Influence of nucleation rate on the yield of ZnO nanocrystals prepared by chemical vapor synthesis, *J. Phys. Chem. C*, 2010, **114**, 5721–5726.
43 E. S. Babu, S. Kim, J.-H. Song and S.-K. Hong, Effects of growth pressure on morphology of ZnO nanostructures by chemical vapor transport, *Chem. Phys. Lett.*, 2016, **658**, 182–187.
44 R. P. Sugavaneshwar and K. K. Nanda, Uninterrupted and reusable source for the controlled growth of nanowires, *Sci. Rep.*, 2013, **3**, 1172.
45 N. Martin, V. Lacour, C. M.-T. Perrault, E. Roy and Y. Leprince-Wang, High flow rate microreactors integrating in situ grown ZnO nanowires for photocatalytic degradation, *React. Chem. Eng.*, 2022, **7**, 750–757.
46 S. L. Yang, R. S. Gao, B. Yang, P. L. Niu and R. H. Yu, Morphology-controlled growth of tetrapod ZnO nanostructures by direct arc discharge, *Appl. Phys. A: Mater. Sci. Process.*, 2010, **99**, 9–13.
47 F. Orudzhev, A. Muslimov, D. Selimov, R. R. Gulakhmedov, A. Lavrikov, V. Kanevsky, R. Gasimov, V. Krasnova and D. Sobola, Oxygen vacancies and surface wettability: key factors in activating and enhancing the solar photocatalytic activity of ZnO tetrapods, *Int. J. Mol. Sci.*, 2023, **24**, 16338.
48 K. Balasubramanian, A. K. Pandey, R. Abolhassani, H.-G. Rubahn, S. Rahman and Y. K. Mishra, Tetrapods based engineering of organic phase change material for thermal energy storage, *Chem. Eng. J.*, 2023, **462**, 141984.
49 Q. Wan, K. Yu, T. H. Wang and C. L. Lin, Low-field electron emission from tetrapod-like ZnO nanostructures synthesized by rapid evaporation, *Appl. Phys. Lett.*, 2003, **83**, 2253–2255.
50 N. Babayevska, Ł. Przysiecka, I. Iatsunskyi, G. Nowaczyk, M. Jarek, E. Janiszewska and S. Jurga, ZnO size and shape effect on antibacterial activity and cytotoxicity profile, *Sci. Rep.*, 2022, **12**, 8148.
51 G.-W. Hsieh, S.-R. Ling, F.-T. Hung, P.-H. Kao and J.-B. Liu, Enhanced piezocapacitive response in zinc oxide tetrapod-poly(dimethylsiloxane) composite dielectric layer for flexible and ultrasensitive pressure sensor, *Nanoscale*, 2021, **13**, 6076–6086.
52 M. Ilickas, M. Marčinskas, D. Peckus, R. Mardosaitė, B. Abakevičienė, T. Tamulevičius and S. Račkauskas, ZnO UV sensor photoresponse enhancement by coating method optimization, *J. Photochem. Photobiol.*, 2023, **14**, 100171.
53 L. Lazzarini, G. Salviati, F. Fabbri, M. Zha, D. Calestani, A. Zappettini, T. Sekiguchi and B. Dierre, Unpredicted nucleation of extended zinc blende phases in wurtzite ZnO nanotetrapod arms, *ACS Nano*, 2009, **3**, 3158–3164.
54 F. Z. Wang, Z. Z. Ye, D. W. Ma, L. P. Zhu and F. Zhuge, Novel morphologies of ZnO nanotetrapods, *Mater. Lett.*, 2005, **59**, 560–563.
55 G.-H. Lee, Effect of annealing temperature on the morphology and optical properties of ZnO tetrapods grown by a thermal evaporation technique, *Ceram. Int.*, 2016, **42**, 14452–14455.
56 F. Liu, P. J. Cao, H. R. Zhang, J. Q. Li and H. J. Gao, Controlled self-assembled nanoaeroplanes, nanocombs, and tetrapod-like networks of zinc oxide, *Nanotechnology*, 2004, **15**, 949–952.

57 G. Zhao, L. Xia, S. Wu, L. Song, A. Wei and G. Wen, Ultrafast and mass production of ZnO nanotetrapods by induction-heating under air ambient, *Mater. Lett.*, 2014, **118**, 126–129.
58 H. Papavlassopoulos, Y. K. Mishra, S. Kaps, I. Paulowicz, R. Abdelaziz, M. Elbahri, E. Maser, R. Adelung and C. Röhl, Toxicity of functional nano-micro zinc oxide tetrapods: impact of cell culture conditions, cellular age and material properties, *PLoS One*, 2014, **9**, e84983.
59 Y. K. Mishra, S. Kaps, A. Schuchardt, I. Paulowicz, X. Jin, D. Gedamu, S. Freitag, M. Claus, S. Wille, A. Kovalev, S. N. Gorb and R. Adelung, Fabrication of Macroscopically Flexible and Highly Porous 3D Semiconductor Networks from Interpenetrating Nanostructures by a Simple Flame Transport Approach, *Part. Part. Syst. Charact.*, 2013, **30**, 775–783.
60 L. I. Istomina, K. A. Sakharov, E. I. Anosova, S. G. Protasova, A. M. Ionov, A. S. Starikova, A. V. Ilyakova, Y. A. Zakharova and S. V. Andreev, New method of synthesizing ZnO/ZnO2 particles of different morphologies in hydrogen peroxide vapor, *Mater. Chem. Phys.*, 2025, 131810.
61 J. Gröttrup, I. Paulowicz, A. Schuchardt, V. Kaidas, S. Kaps, O. Lupan, R. Adelung and Y. K. Mishra, Three-dimensional flexible ceramics based on interconnected network of highly porous pure and metal alloyed ZnO tetrapods, *Ceram. Int.*, 2016, **42**, 8664–8676.
62 F. Xu and S. Tse, Flame Synthesis of Zinc Oxide Nanostructures, 2012, DOI: 10.2514/6.2008-1454.
63 L. Chen, W. Song, C. Xie, L. Lin and J. Wang, A novel combustion method to prepare tetrapod nano-ZnO, *Mater. Lett.*, 2007, **61**, 4603–4605.
64 C.-C. Hwang, C.-S. Lin, G.-P. Wang, C.-H. Peng and S.-L. Chung, A self-propagating high-temperature synthesis method for synthesis of zinc oxide powder, *J. Alloys Compd.*, 2009, **467**, 514–523.
65 T.-L. Phan, V. Le Cuong, V. D. Lam and N. T. Dang, Various CVD-grown ZnO nanostructures for nanodevices and interdisciplinary applications, *Beilstein J. Nanotechnol.*, 2024, **15**, 1390–1399.
66 F. H. Alsultany, Z. Hassan and N. M. Ahmed, Large-scale uniform ZnO tetrapods on catalyst free glass substrate by thermal evaporation method, *Mater. Res. Bull.*, 2016, **79**, 63–68.
67 S. A. Al Rifai and E. P. Domashevskaya, The synthesis and optical properties of different zinc oxide nanostructures, *Russ. J. Phys. Chem.*, 2013, **87**, 2246–2252.
68 Y. Qiu, L. Hu, H. Zhang, L. Wang, J. Ma and B. Wang, Changing the Shape of ZnO Nanostructures by Controlling Oxygen Concentration: From Tetrapod-Like to Dandelion-Like Nanostructures, *Integr. Ferroelectr.*, 2011, **127**, 134–140.
69 K.-S. Yun, K.-I. Ri, Y.-G. Choe, K.-U. Kim and C.-H. Jang, Novel hierarchical structure of ZnO: Growth of spiny tetrapod *via* vapor phase synthesis, *Funct. Mater. Lett.*, 2025, **18**(7), 2551067.
70 W. Yu, X. Li and X. Gao, Catalytic Synthesis and Structural Characteristics of High-Quality Tetrapod-Like ZnO Nanocrystals by a Modified Vapor Transport Process, *Cryst. Growth Des.*, 2005, **5**, 151–155.
71 H. Li, Y. Huang, Y. Zhang, J. Qi, X. Yan, Q. Zhang and J. Wang, Self-catalytic Synthesis, Structures, and Properties of High-Quality Tetrapod-Shaped ZnO Nanostructures, *Cryst. Growth Des.*, 2009, **9**, 1863–1868.
72 S. L. More, M. Kovochich, T. Lyons-Darden, M. Taylor, A. M. Schulte and A. K. Madl, Review and Evaluation of the Potential Health Effects of Oxidic Nickel Nanoparticles, *Nanomaterials*, 2021, **11**(3), 642.
73 X.-H. Zhang, S.-Y. Xie, Z.-Y. Jiang, Z.-X. Xie, R.-B. Huang, L.-S. Zheng, J.-Y. Kang and T. Sekiguchi, Microwave plasma growth and high spatial resolution cathodoluminescent spectrum of tetrapod ZnO nanostructures, *J. Solid State Chem.*, 2003, **173**, 109–113.
74 H.-F. Lin, S.-C. Liao and C.-T. Hu, A new approach to synthesize ZnO tetrapod-like nanoparticles with DC thermal plasma technique, *J. Cryst. Grow.*, 2009, **311**, 1378–1384.
75 B.-J. Lee, S.-I. Jo and G.-H. Jeong, Synthesis of ZnO Nanomaterials Using Low-Cost Compressed Air as Microwave Plasma Gas at Atmospheric Pressure, *Nanomaterials*, 2019, **9**(7), 942.
76 J.-Y. Yang and G.-H. Jeong, Synthesis of ZnO Tetrapods Using Atmospheric Plasma Jet and Their Size-Dependent Photosensing Properties, *Appl. Sci. Converg. Technol.*, 2022, **31**, 149–152.
77 A. M. Schwan, S. Chwatal, C. Hendler, D. Kopp, J. M. Lackner, R. Kaindl, M. Tscherner, M. Zirkl, P. Angerer, B. Friessnegger, S. Augl, D. Heim, A. Hinterer, M. Stummer and W. Waldhauser, Morphology-controlled atmospheric pressure plasma synthesis of zinc oxide nanoparticles for piezoelectric sensors, *Appl. Nanosci.*, 2023, **13**, 6421–6432.
78 O. Lupan, L. Chow, G. Chai, B. Roldan, A. Naitabdi, A. Schulte and H. Heinrich, Nanofabrication and characterization of ZnO nanorod arrays and branched microrods by aqueous solution route and rapid thermal processing, *Mater. Sci. Eng., B*, 2007, **145**, 57–66.
79 O. Lupan, G. Chai and L. Chow, Novel hydrogen gas sensor based on single ZnO nanorod, *Microelectron. Eng.*, 2008, **85**, 2220–2225.
80 H. Zhang, D. Yang, D. Li, X. Ma, S. Li and D. Que, Controllable Growth of ZnO Microcrystals by a Capping-Molecule-Assisted Hydrothermal Process, *Cryst. Growth Des.*, 2005, **5**, 547–550.
81 J. Jiang, Y. Li, S. Tan and Z. Huang, Synthesis of zinc oxide nanotetrapods by a novel fast microemulsion-based hydrothermal method, *Mater. Lett.*, 2010, **64**, 2191–2193.
82 Y. Yang, Y. Jin, H. He, Q. Wang, Y. Tu, H. Lu and Z. Ye, Dopant-induced shape evolution of colloidal nanocrystals: the case of zinc oxide, *J. Am. Chem. Soc.*, 2010, **132**, 13381–13394.
83 M. Chen and D. A. Dixon, Machine-Learning Approach for the Development of Structure–Energy Relationships of ZnO Nanoparticles, *J. Phys. Chem. C*, 2018, **122**, 18621–18639.
84 A. Dmytruk, I. Dmitruk, Y. Shynkarenko, R. Belosludov and A. Kasuya, ZnO nested shell magic clusters as tetrapod nuclei, *RSC Adv.*, 2017, **7**, 21933–21942.

85 R. Yuksel, O. Buyukcakir, P. K. Panda, S. H. Lee, Y. Jiang, D. Singh, S. Hansen, R. Adelung, Y. K. Mishra, R. Ahuja and R. S. Ruoff, Necklace-like Nitrogen-Doped Tubular Carbon 3D Frameworks for Electrochemical Energy Storage, *Adv. Funct. Mater.*, 2020, **30**, 1909725.
86 M. Ilickas, R. Mardosaite, F. Cesano, S. Cravanzola, C. Barolo, D. Scarano, G. Viscardi and S. Rackauskas, ZnO tetrapod morphology influence on UV sensing properties, *Nanotechnology*, 2023, **35**, 15502.
87 O. Lupan, V. Postica, J. Gröttrup, A. K. Mishra, N. H. de Leeuw, J. F. C. Carreira, J. Rodrigues, N. Ben Sedrine, M. R. Correia and T. Monteiro, Hybridization of zinc oxide tetrapods for selective gas sensing applications, *ACS Appl. Mater. Interfaces*, 2017, **9**, 4084–4099.
88 J. Rodrigues, N. Ben Sedrine, M. R. Correia and T. Monteiro, Photoluminescence investigations of ZnO micro/nanostructures, *Mater. Today Chem.*, 2020, **16**, 100243.
89 K. Yan, L. Zhang, J. Qiu, Y. Qiu, Z. Zhu, J. Wang and S. Yang, A quasi-quantum well sensitized solar cell with accelerated charge separation and collection, *J. Am. Chem. Soc.*, 2013, **135**, 9531–9539.
90 Y. Qiu, K. Yan, H. Deng and S. Yang, Secondary branching and nitrogen doping of ZnO nanotetrapods: building a highly active network for photoelectrochemical water splitting, *Nano Lett.*, 2012, **12**, 407–413.
91 T. Santhaveesuk, D. Wongratanaphisan and S. Choopun, Enhancement of sensor response by TiO2 mixing and Au coating on ZnO tetrapod sensor, *Sens. Actuators, B*, 2010, **147**, 502–507.
92 N. Roy and A. Roy, Growth and temperature dependent photoluminescence characteristics of ZnO tetrapods, *Ceram. Int.*, 2015, **41**, 4154–4160.
93 D. Debnath, D. Sen, T. T. Neog, B. Saha and S. K. Ghosh, Growth of ZnO Polytypes: Multiple Facets of Diverse Applications, *Cryst. Growth Des.*, 2024, **24**, 871–885.
94 K. Wang, J.-N. Ma, C.-Y. Zhang, Z. Pei, W.-T. Tang and Q. Zhang, Self-powered high-sensitivity piezoelectric sensors for end-fixture force sensing in surgical robots based on T-ZnO, *Colloids Surf., A*, 2024, **697**, 134424.
95 Z. Zhang, M. Willatzen, Y. K. Mishra and Z. L. Wang, Transport studies in piezo-semiconductive ZnO nanotetrapod based electronic devices, *Mater. Today Electron.*, 2024, **8**, 100102.
96 A. Janotti and C. G. van de Walle, Fundamentals of zinc oxide as a semiconductor, *Rep. Prog. Phys.*, 2009, **72**, 126501.
97 M. Villani, F. Rossi, D. Calestani, G. Salviati and F. Fabbri, Evaluating the plasmon-exciton interaction in ZnO tetrapods coupled with gold nanostructures by nanoscale cathodoluminescence, *Nano Express*, 2021, **2**, 14004.
98 W. D. Yu, X. M. Li and X. D. Gao, Homogeneous-catalytic synthesis of tetrapodlike ZnO nanocrystals and their photoluminescence properties, *Chem. Phys. Lett.*, 2004, **390**, 296–300.
99 L. Manna, D. J. Milliron, A. Meisel, E. C. Scher and A. P. Alivisatos, Controlled growth of tetrapod-branched inorganic nanocrystals, *Nat. Mater.*, 2003, **2**, 382–385.
100 R. G. S. Pala and H. Metiu, Modification of the Oxidative Power of ZnO(10$\bar{1}$0) Surface by Substituting Some Surface Zn Atoms with Other Metals, *J. Phys. Chem. C*, 2007, **111**, 8617–8622.
101 C. Klingshirn, ZnO: From basics towards applications, *Phys. Status Solidi B*, 2007, **244**, 3027–3073.
102 M. P. M. Poschmann, L. Siebert, C. Lupan, O. Lupan, F. Schütt, R. Adelung and N. Stock, Surface Conversion of ZnO Tetrapods Produces Pinhole-Free ZIF-8 Layers for Selective and Sensitive H2 Sensing Even in Pure Methane, *ACS Appl. Mater. Interfaces*, 2023, **15**, 38674–38681.
103 M. Todorova and J. Neugebauer, Identification of bulk oxide defects in an electrochemical environment, *Faraday Discuss.*, 2015, **180**, 97–112.
104 M. Li and E. G. Seebauer, Defect engineering in semiconducting oxides: Control of ZnO surface potential via temperature and oxygen pressure, *AIChE J.*, 2016, **62**, 500–507.
105 C. G. van de Walle, Defect analysis and engineering in ZnO, *Phys. B*, 2001, **308–310**, 899–903.
106 T. S. Bjørheim and E. Kotomin, Ab Initio Thermodynamics of Oxygen Vacancies and Zinc Interstitials in ZnO, *J. Phys. Chem. Lett.*, 2014, **5**, 4238–4242.
107 M. Brás, J. Zanoni, B. P. Falcão, J. P. Leitão, F. M. Costa, T. Monteiro, S. O. Pereira and J. Rodrigues, Label-Free Nanoscale ZnO Tetrapod-Based Transducers for Tetracycline Detection, *ACS Appl. Nano Mater.*, 2022, **5**, 1232–1243.
108 M. S. Riahimadvar and M. Tajaldini, Fast and one-step synthesis of small ZnO nano-tetrapods Using CO2 laser in ambient air: physical properties, *Phys. Scr.*, 2022, **97**, 105811.
109 Y. Qiu, M. Yang, H. Fan, Y. Xu, Y. Shao, X. Yang and S. Yang, Synthesis and characterization of nitrogen doped ZnO tetrapods and application in photocatalytic degradation of organic pollutants under visible light, *Mater. Lett.*, 2013, **99**, 105–107.
110 R. Mardosaitė, A. Jurkevičiūtė and S. Račkauskas, Superhydrophobic ZnO Nanowires: Wettability Mechanisms and Functional Applications, *Cryst. Growth Des.*, 2021, **21**, 4765–4779.
111 H. Ennaceri, L. Wang, D. Erfurt, W. Riedel, G. Mangalgiri, A. Khaldoun, A. El Kenz, A. Benyoussef and A. Ennaoui, Water-resistant surfaces using zinc oxide structured nanorod arrays with switchable wetting property, *Surf. Coat. Technol.*, 2016, **299**, 169–176.
112 M. T. Z. Myint, N. S. Kumar, G. L. Hornyak and J. Dutta, Hydrophobic/hydrophilic switching on zinc oxide microtextured surface, *Appl. Surf. Sci.*, 2013, **264**, 344–348.
113 J. Li, Q. Sun, S. Han, J. Wang, Z. Wang and C. Jin, Reversibly light-switchable wettability between superhydrophobicity and superhydrophilicity of hybrid ZnO/bamboo surfaces *via* alternation of UV irradiation and dark storage, *Prog. Org. Coat.*, 2015, **87**, 155–160.
114 F. Oba, S. R. Nishitani, S. Isotani, H. Adachi and I. Tanaka, Energetics of native defects in ZnO, *J. Appl. Phys.*, 2001, **90**, 824–828.
115 Y. Xu, Y. Yang, D.-X. Yan, H. Duan, G. Zhao and Y. Liu, Flexible and conductive polyurethane composites for

electromagnetic shielding and printable circuit, *Chem. Eng. J.*, 2019, **360**, 1427–1436.
116 C. Klingshirn, ZnO: material, physics and applications, *Chem. Phys. Chem.*, 2007, **8**, 782–803.
117 S. Xu, Y. Qin, C. Xu, Y. Wei, R. Yang and Z. L. Wang, Self-powered nanowire devices, *Nat. Nanotechnol.*, 2010, **5**, 366–373.
118 R. K. Mishra, V. Kumar, G. Le Trung, G. J. Choi, J. W. Ryu, R. Bhardwaj, P. Kumar, J. Singh, S. H. Lee and J. S. Gwag, Recent advances in ZnO nanostructure as a gas-sensing element for an acetone sensor: a short review, *Luminescence*, 2023, **38**, 1087–1101.
119 A. Tamulevičienė, R. Mardosaitė, M. Ilickas, B. Abakevičienė, T. Tamulevičius, Š. Meškinis and S. Račkauskas, Highly-hydrophobic, transparent, and durable coatings based on ZnO tetrapods with diamond-like carbon nanocomposite, *Surf. Coat. Technol.*, 2023, **470**, 129863.
120 X. Tao, H. Jin, M. Mintken, N. Wolff, Y. Wang, R. Tao, Y. Li, H. Torun, J. Xie, J. Luo, J. Zhou, Q. Wu, S. Dong, J. Luo, L. Kienle, R. Adelung, Y. K. Mishra and Y. Q. Fu, Three-Dimensional Tetrapodal ZnO Microstructured Network Based Flexible Surface Acoustic Wave Device for Ultraviolet and Respiration Monitoring Applications, *ACS Appl. Nano Mater.*, 2020, **3**, 1468–1478.
121 D. Gedamu, I. Paulowicz, S. Kaps, O. Lupan, S. Wille, G. Haidarschin, Y. K. Mishra and R. Adelung, Rapid fabrication technique for interpenetrated ZnO nanotetrapod networks for fast UV sensors, *Adv. Mater.*, 2014, **26**, 1541–1550.
122 R. Chen, B. Ling, X. W. Sun and H. D. Sun, Room temperature excitonic whispering gallery mode lasing from high-quality hexagonal ZnO microdisks, *Adv. Mater.*, 2011, **23**, 2199–2204.
123 R. Rathnasekara, G. Mayberry and P. Hari, Thermoelectric, electrochemical, & dielectric properties of four ZnO nanostructures, *Materials*, 2022, **15**, 8816.
124 H. Zhao, B. Ouyang, L. Han, Y. K. Mishra, Z. Zhang and Y. Yang, Conjuncted photo-thermoelectric effect in ZnO–graphene nanocomposite foam for self-powered simultaneous temperature and light sensing, *Sci. Rep.*, 2020, **10**, 11864.
125 X. Liang and C. Wang, Electron and phonon transport anisotropy of ZnO at and above room temperature, *Appl. Phys. Lett.*, 2020, **116**(4), 043903.
126 M. Ahmad, C. Pan, J. Zhao, J. Iqbal and J. Zhu, Electron irradiation effect and photoluminescence properties of ZnO-tetrapod nanostructures, *Mater. Chem. Phys.*, 2010, **120**, 319–322.
127 A. R. Hutson, Electronic properties of ZnO, *J. Phys. Chem. Solids*, 1959, **8**, 467–472.
128 T. Makino, Y. Segawa, A. Tsukazaki, A. Ohtomo and M. Kawasaki, Electron transport in ZnO thin films, *Appl. Phys. Lett.*, 2005, **87**(2), 022101.
129 J. Huh, G.-T. Kim, J. S. Lee and S. Kim, A direct measurement of the local resistances in a ZnO tetrapod by means of impedance spectroscopy: The role of the junction in the overall resistance, *Appl. Phys. Lett.*, 2008, **93**(4), 042111.
130 G. Blatter and F. Greuter, Carrier transport through grain boundaries in semiconductors, *Phys. Rev. B: Condens. Matter Mater. Phys.*, 1986, **33**, 3952.
131 A. Janotti and C. G. van de Walle, Native point defects in ZnO, *Phys. Rev. B: Condens. Matter Mater. Phys.*, 2007, **76**, 165202.
132 R. A. Fernandes, M. J. Sampaio, E. S. Da Silva, P. Serp, J. L. Faria and C. G. Silva, Synthesis of selected aromatic aldehydes under UV-LED irradiation over a hybrid photocatalyst of carbon nanofibers and zinc oxide, *Catal. Today*, 2019, **328**, 286–292.
133 Q. Zhang, W. Fan and L. Gao, Anatase TiO2 nanoparticles immobilized on ZnO tetrapods as a highly efficient and easily recyclable photocatalyst, *Appl. Catal., B*, 2007, **76**, 168–173.
134 J. Chebwogen, F. W. Nyongesa, J. M. Mwabora, G. M. Ntshani and P. G. Ndungu, A Comparative Study of Sol–Gel Synthesized ZnO/GO and ZnO/g-C_3N_4 Nanocomposites in the Photocatalytic Degradation of Acetaminophen, *Int. J. Photoenergy*, 2025, **2025**, 9216858.
135 J. Liu, M. Li, C. Luo, S. Zhou and W. Chen, Eco-friendly synthesis of self-reporting robust superhydrophobic coatings with damage sensitive photoluminescence, *Chem. Eng. J.*, 2022, **431**, 134162.
136 C. Li, B. Lee, C. Wang, A. Bajpayee, L. D. Douglas, B. K. Phillips, G. Yu, N. Rivera-Gonzalez, B.-J. Peng, Z. Jiang, H.-J. Sue, S. Banerjee and L. Fang, Photopolymerized superhydrophobic hybrid coating enabled by dual-purpose tetrapodal ZnO for liquid/liquid separation, *Mater. Horiz.*, 2022, **9**, 452–461.
137 T. Reimer, I. Paulowicz, R. Röder, S. Kaps, O. Lupan, S. Chemnitz, W. Benecke, C. Ronning, R. Adelung and Y. K. Mishra, Single step integration of ZnO nano- and microneedles in Si trenches by novel flame transport approach: whispering gallery modes and photocatalytic properties, *ACS Appl. Mater. Interfaces*, 2014, **6**, 7806–7815.
138 F. Sun, L. Sun, B. Zhang and H. Wang, Spatially resolved surface-related exciton polariton dynamics in a single ZnO tetrapod, *Solid State Commun.*, 2018, **270**, 107–110.
139 S.-K. Lee, W. M. Chen, D. Hongxing, Z. Chen and I. A. Buyanova, Cathodoluminescence characterization of ZnO tetrapod structures, *Thin Solid Films*, 2013, **543**, 114–117.
140 G. Bertoni, F. Fabbri, M. Villani, L. Lazzarini, S. Turner, G. van Tendeloo, D. Calestani, S. Gradečak, A. Zappettini and G. Salviati, Nanoscale mapping of plasmon and exciton in ZnO tetrapods coupled with Au nanoparticles, *Sci. Rep.*, 2016, **6**, 19168.
141 A. E. Muslimov, V. V. Krasnova, L. Zadorozhnaya and V. M. Kanevsky, Influence of Morphological and Dimensional Parameters on Cathodoluminescent Properties of ZNO Microstructure Ensemble, *J. Surf. Investig.*, 2024, **18**, 1640–1644.
142 L. A. Zadorozhnaya, A. P. Tarasov and V. M. Kanevsky, The Growth Mechanism, Luminescence, and Lasing of Polyhedral ZnO Microcrystals with Whispering-Gallery Modes, *Photonics*, 2023, **10**(12), 1328.
143 I. Tiginyanu, L. Ghimpu, J. Gröttrup, V. Postolache, M. Mecklenburg, M. A. Stevens-Kalceff, V. Ursaki, N. Payami,

R. Feidenhansl, K. Schulte, R. Adelung and Y. K. Mishra, Strong light scattering and broadband (UV to IR) photoabsorption in stretchable 3D hybrid architectures based on Aerographite decorated by ZnO nanocrystallites, *Sci. Rep.*, 2016, **6**, 32913.

144 K. Vanheusden, C. H. Seager, W. T. Warren and J. A. Voigt, Correlation between photoluminescence and oxygen vacancies in ZnO phosphors, *Appl. Phys. Lett.*, 1996, **68**, 403–405.

145 K. Vanheusden, W. L. Warren, C. H. Seager, J. A. Voigt and B. E. Gnade, Mechanisms behind green photoluminescence in ZnO phosphor powders, *J. Appl. Phys.*, 1996, **79**, 7983–7990.

146 F. A. La Porta, J. Andres, M. V. Vismara, C. Frederico de Oliveira, J. R. Sambrano, M. S. Li, J. A. Varela and E. Longo, Correlation between structural and electronic order–disorder effects and optical properties in ZnO nanocrystals, *J. Mater. Chem. C*, 2014, **2**, 10164–10174.

147 Z. G. Yu, P. Wu and H. Gong, Theoretical and experimental studies on oxygen vacancy in p-type ZnO, *Phys. B*, 2007, **401**, 417–420.

148 I. Shalish, H. Temkin and V. Narayanamurti, Size-dependent surface luminescence in ZnO nanowires, *Phys. Rev. B: Condens. Matter Mater. Phys.*, 2004, **69**, 245401.

149 J.-P. Richters, T. Voss, L. Wischmeier, I. Rückmann and J. Gutowski, Influence of polymer coating on the low-temperature photoluminescence properties of ZnO nanowires, *Appl. Phys. Lett.*, 2008, **92**(1), 011103.

150 F. Leiter, H. Zhou, F. Henecker, A. Hofstaetter, D. M. Hofmann and B. K. Meyer, Magnetic resonance experiments on the green emission in undoped ZnO crystals, *Phys. B*, 2001, **308**, 908–911.

151 M. R. C. Sytu and J.-I. Hahm, Principles and Applications of ZnO Nanomaterials in Optical Biosensors and ZnO Nanomaterial-Enhanced Biodetection, *Biosensors*, 2024, **14**(10), 480.

152 N. K. Hassan, M. R. Hashim and N. K. Allam, ZnO nanotetrapod photoanodes for enhanced solar-driven water splitting, *Chem. Phys. Lett.*, 2012, **549**, 62–66.

153 M. Villani, F. Rossi, D. Calestani, G. Salviati and F. Fabbri, Evaluating the plasmon-exciton interaction in ZnO tetrapods coupled with gold nanostructures by nanoscale cathodoluminescence, *Nano Ex.*, 2021, **2**, 14004.

154 W. Chen, Y. Qiu and S. Yang, Branched ZnO nanostructures as building blocks of photoelectrodes for efficient solar energy conversion, *Phys. Chem. Chem. Phys.*, 2012, **14**, 10872–10881.

155 L. Juan, Y. Chenxi, N. Ziru, Y. Shenglan and H. Dongwen, Fabrication of flexible photo-responsive mesh with reversible wettability and enhanced mechanical damage resistance for efficient oil/water separation, *J. Environ. Chem. Eng.*, 2024, **12**, 114857.

156 Y. Zhang, H. Zhou, S. W. Liu, Z. R. Tian and M. Xiao, Second-harmonic whispering-gallery modes in ZnO nanotetrapod, *Nano Lett.*, 2009, **9**, 2109–2112.

157 D. Jiang, C. Tian, Q. Liu, M. Zhao, J. Qin, J. Hou, S. Gao, Q. Liang and J. Zhao, Young's modulus of individual ZnO nanowires, *Mater. Sci. Eng., A*, 2014, **610**, 1–4.

158 F. Muktepavela, L. Grigorjeva, K. Kundzins, E. Gorokhova and P. Rodnyi, Structure, nanohardness and photoluminescence of ZnO ceramics based on nanopowders, *Phys. Scr.*, 2015, **90**, 94018.

159 N. Zhang and M. Asle Zaeem, Nanoscale flaw tolerance behaviour of polycrystalline tetragonal zirconia nanopillars, *Int. J. Mech. Sci.*, 2020, **173**, 105405.

160 Z. Qin and M. J. Buehler, Flaw Tolerance of Nuclear Intermediate Filament Lamina under Extreme Mechanical Deformation, *ACS Nano*, 2011, **5**, 3034–3042.

161 M.-R. He, P. Xiao, J. Zhao, S. Dai, F. Ke and J. Zhu, Quantifying the defect-dominated size effect of fracture strain in single crystalline ZnO nanowires, *J. Appl. Phys.*, 2011, **109**(12), 123504.

162 C. Q. Chen and J. Zhu, Bending strength and flexibility of ZnO nanowires, *Appl. Phys. Lett.*, 2007, **90**(4), 043105.

163 R. Meija, S. Signetti, A. Schuchardt, K. Meurisch, D. Smazna, M. Mecklenburg, K. Schulte, D. Erts, O. Lupan, B. Fiedler, Y. K. Mishra, R. Adelung and N. M. Pugno, Nanomechanics of individual aerographite tetrapods, *Nat. Commun.*, 2017, **8**, 14982.

164 E. Veys, L. Makower, M. Williamson, L. M. Saure, R. Adelung, F. Schütt, N. M. Pugno and T. J. Marrow, In situ observation of compressive deformation of an interconnected network of zinc oxide tetrapods, *Scr. Mater.*, 2023, **224**, 115153.

165 T. Spratte, C. Arndt, I. Wacker, M. Hauck, R. Adelung, R. R. Schröder, F. Schütt and C. Selhuber-Unkel, Thermoresponsive Hydrogels with Improved Actuation Function by Interconnected Microchannels, *Adv. Intell. Syst.*, 2022, **4**(3), 2100081.

166 N. Liu, L. M. Saure, R. Sriramdas, F. Schütt, K. Wang, A. Nozariasbmarz, Y. Zhang, R. Adelung, R. H. Baughman, S. Priya, W. Li and B. Poudel, Underwater Thermoacoustic Generation by a Hierarchical Tetrapodal Carbon Nanotube Network, *ACS Nano*, 2024, **18**, 8988–8995.

167 F. Schütt, M. Zapf, S. Signetti, J. Strobel, H. Krüger, R. Röder, J. Carstensen, N. Wolff, J. Marx, T. Carey, M. Schweichel, M.-I. Terasa, L. Siebert, H.-K. Hong, S. Kaps, B. Fiedler, Y. K. Mishra, Z. Lee, N. M. Pugno, L. Kienle, A. C. Ferrari, F. Torrisi, C. Ronning and R. Adelung, Conversionless efficient and broadband laser light diffusers for high brightness illumination applications, *Nat. Commun.*, 2020, **11**, 1437.

168 J.-H. Pöhls, F. Schütt, C. O'Neill, S. Shree, M. B. Johnson, Y. K. Mishra, R. Adelung and M. A. White, Thermal and electrical transport properties in multi-walled carbon nanotube-coated ZnO tetrapods and self-entangled multi-walled carbon nanotube tubes, *Carbon*, 2019, **144**, 423–432.

169 E. Veys, L. Makower, M. Williamson, L. M. Saure, R. Adelung, F. Schütt, N. M. Pugno and T. J. Marrow, In situ observation of compressive deformation of an interconnected network of zinc oxide tetrapods, *Scr. Mater.*, 2023, **224**, 115153.

170 A. Gapeeva, H. Qiu, A. Cojocaru, C. Arndt, T. Riaz, F. Schütt, C. Selhuber-Unkel, Y. K. Mishra, A. Tura, S. Sonntag, S. Gniesmer, S. Grisanti, S. Kaps and R. Adelung, Tetrapodal

ZnO-Based Composite Stents for Minimally Invasive Glaucoma Surgery, *ACS Biomater. Sci. Eng.*, 2023, **9**, 1352–1361.

171 X. Jin, M. Deng, S. Kaps, X. Zhu, I. Hölken, K. Mess, R. Adelung and Y. K. Mishra, Study of tetrapodal ZnO-PDMS composites: A comparison of fillers shapes in stiffness and hydrophobicity improvements, *PLoS One*, 2014, **9**, e106991.

172 R. K. Pandey, J. Dutta, S. Brahma, B. Rao and C.-P. Liu, Review on ZnO-based piezotronics and piezoelectric nanogenerators: aspects of piezopotential and screening effect, *J. Phys. Mater.*, 2021, **4**, 44011.

173 J. He, C. Dong, X. Chen, H. Cai, X. Chen, X. Jiang, Y. Zhang, A. Peng and M. A. H. Badsha, Review of piezocatalysis and piezo-assisted photocatalysis in environmental engineering, *Crystals*, 2023, **13**, 1382.

174 P. Jia, J. Li and H. Huang, Piezocatalysts and Piezo-Photocatalysts: From Material Design to Diverse Applications, *Adv. Funct. Mater.*, 2024, **34**, 2407309.

175 K. Sun, J. Qi, Q. Zhang, Y. Yang and Y. Zhang, A novel logic switch based on individual ZnO nanotetrapods, *Nanoscale*, 2011, **3**, 2166–2168.

176 Z. Wang, J. Qi, S. Lu, P. Li, X. Li and Y. Zhang, Enhancing sensitivity of force sensor based on a ZnO tetrapod by piezo-phototronic effect, *Appl. Phys. Lett.*, 2013, **103**(14), 143125.

177 G. S. Wood, K. Jeronimo, C. Mahzan, M. Ammar Bin, R. Cheung and E. Mastropaolo, Zinc oxide nanowires-based flexible pressure sensor, *Micro Nano Lett.*, 2021, **16**, 432–435.

178 A. Bajpayee, T. E. G. Alivio, P. McKay and S. Banerjee, Functionalized Tetrapodal ZnO Membranes Exhibiting Superoleophobic and Superhydrophilic Character for Water/Oil Separation Based on Differential Wettability, *Energy Fuels*, 2019, **33**, 5024–5034.

179 M. Sharma, M. Joshi, S. Nigam, S. Shree, D. K. Avasthi, R. Adelung, S. K. Srivastava and Y. Kumar Mishra, ZnO tetrapods and activated carbon based hybrid composite: Adsorbents for enhanced decontamination of hexavalent chromium from aqueous solution, *Chem. Eng. J.*, 2019, **358**, 540–551.

180 J. V. Lauritsen, S. Porsgaard, M. K. Rasmussen, M. C. R. Jensen, R. Bechstein, K. Meinander, B. S. Clausen, S. Helveg, R. Wahl, G. Kresse and F. Besenbacher, Stabilization Principles for Polar Surfaces of ZnO, *ACS Nano*, 2011, **5**, 5987–5994.

181 S.-G. Heo, S.-I. Jo and G.-H. Jeong, Revealing the enhanced photocatalytic properties of ZnO tetrapods produced by atmospheric-pressure microwave plasma jet system, *Curr. Appl. Phys.*, 2023, **46**, 46–54.

182 L. Nie, L. Gao, P. Feng, J. Zhang, X. Fu, Y. Liu, X. Yan and T. Wang, Three-dimensional functionalized tetrapod-like ZnO nanostructures for plasmid DNA delivery, *Small*, 2006, **2**, 621–625.

183 S. Jangra, A. Raza, B. Kumar, J. Sharma, S. Das, K. Pandey, Y. K. Mishra and M. S. Goyat, MXene decorated ZnO-tetrapod for efficient degradation of Methyl Orange, Methylene Blue, and Rhodamine B dyes, *Mater. Sci. Eng., B*, 2025, **311**, 117832.

184 Q. Gao, J. Zhao, J. Hu and M. Wang, Applying a switchable superhydrophobic and hydrophilic ZnO nanorod array-coated stainless-steel mesh to electrically-induced oil/water separation, *Colloids Surf., A*, 2021, **628**, 127231.

185 F. Rasch, V. Postica, F. Schütt, Y. K. Mishra, A. S. Nia, M. R. Lohe, X. Feng, R. Adelung and O. Lupan, Highly selective and ultra-low power consumption metal oxide based hydrogen gas sensor employing graphene oxide as molecular sieve, *Sens. Actuators, B*, 2020, **320**, 128363.

186 B. Chakraborty, D. Litra, A. K. Mishra, C. Lupan, R. Nagpal, S. Mishra, H. Qiu, S. Railean, O. Lupan, N. H. de Leeuw, R. Adelung and L. Siebert, Ultra-selective hydrogen sensors based on CuO - ZnO hetero-structures grown by surface conversion, *J. Alloys Compd.*, 2024, **1002**, 175385.

187 B. Chakraborty, D. Litra, A. K. Mishra, C. Lupan, R. Nagpal, S. Mishra, H. Qiu, S. Railean, O. Lupan and N. H. de Leeuw, Ultra-selective hydrogen sensors based on CuO-ZnO hetero-structures grown by surface conversion, *J. Alloys Compd.*, 2024, **1002**, 175385.

188 H. Mei, S. Zhou, M. Lu and L. Cheng, Tetrapod-like ZnO/ZnFe2O4 based heterostructure for enhanced ethanol detection, *J. Alloys Compd.*, 2020, **840**, 155583.

189 D. Li, J. Ma and K. Chen, 2-D zinc ferrite ''moss'' furred on 3-D zinc oxide tetrapods to boost detection sensitivity of hydrogen sulfide, *J. Phys. Chem. Solids*, 2021, **148**, 109656.

190 C. Lupan, In-Depth Properties Analysis Of Znal2o4/Zno Micro-Nanostructures, *J. Eng. Sci.*, 2025, **32**, 35–45.

191 F. Rezaei, P. Kameli, S. Hakimpour, S. Salari, M. Ranjbar, T. Sarkar and B. Aslibeiki, Hydrogen Gas Sensing Properties of Pd-decorated ZnO Tetrapod Nanostructures, *Ceram. Int.*, 2025, **51**(27), 54582–54590.

192 J. Hu, H. Ma, Y. Zhou, L. Ma, S. Zhao, S. Shi, J. Li and Y. Chang, Gas-Sensing Properties and Mechanisms of 3D Networks Composed of ZnO Tetrapod Micro-Nano Structures at Room Temperature, *Materials*, 2024, **17**(1), 203.

193 Y. Lin, Z. Long, S. Liang, T. Zhong and L. Xing, A wearable exhaling-oxygen-sensing mask based on piezoelectric/gas-sensing coupling effect for real-time monitoring and uploading lung disease information, *J. Phys. D: Appl. Phys.*, 2022, **55**, 224001.

194 K. Lee, M. Sahu, S. Hajra, R. Abolhassani, K. Mistewicz, B. Toroń, H.-G. Rubahn, Y. K. Mishra and H. J. Kim, Zinc oxide tetrapod sponges for environmental pollutant monitoring and degradation, *J. Mater. Res. Technol.*, 2023, **22**, 811–824.

195 A. Knoepfel, B. Poudel and S. Gupta, Surface-Catalyzed Zinc Oxide Nanorods and Interconnected Tetrapods as Efficient Methane Gas Sensing Platforms, *Chemosensors*, 2023, **11**, 506.

196 S. Gupta and H. Zou, Implementing an Analytical Model to Elucidate the Impacts of Nanostructure Size and Topology of Morphologically Diverse Zinc Oxide on Gas Sensing, *Chemosensors*, 2025, **13**, 38.

197 R. Nagpal, C. Lupan, A. Bîrnaz, A. Sereacov, E. Greve, M. Gronenberg, L. Siebert, R. Adelung and O. Lupan, Multifunctional three-in-one sensor on t-ZnO for ultraviolet

and VOC sensing for bioengineering applications, *Biosensors*, 2024, **14**, 293.

198 F. Xu, W. Li, S. Sun, A. Zhong, X. Cheng, J. Shi, Z. Li, J. Li, W. Zhang and X. Wang, Expanding selectivity functionality of a ZnO nanotetrapod-based volatile organic compound sensor using Au nanoparticle decoration, *ACS Appl. Nano Mater.*, 2023, **6**, 8335–8345.

199 M. Waqas Alam, A. Sharma, A. Sharma, S. Kumar, P. Mohammad Junaid and M. Awad, VOC Detection with Zinc Oxide Gas Sensors: A Review of Fabrication, Performance, and Emerging Applications, *Electroanalysis*, 2025, **37**(1), e202400246.

200 H. Chen, L. Lv, K. Xue, P. Zhang, L. Du and G. Cui, Oral Exhalation H2S Sensor Based on Cu2O/ZnO Heterostructures, *ACS Sens.*, 2025, **10**, 2579–2588.

201 A. Knoepfel, N. Liu, Y. Hou, S. Sujani, B. R. Dos Reis, R. White, K. Wang, B. Poudel, S. Gupta and S. Priya, Development of Tetrapod Zinc Oxide-Based UV Sensor for Precision Livestock Farming and Productivity, *Biosensors*, 2022, **12**(10), 837.

202 V. Postica, I. Paulowicz, O. Lupan, F. Schütt, N. Wolff, A. Cojocaru, Y. K. Mishra, L. Kienle and R. Adelung, The effect of morphology and functionalization on UV detection properties of ZnO networked tetrapods and single nanowires, *Vacuum*, 2019, **166**, 393–398.

203 P. Schadte, R. Madurawala, M.-I. Terasa, M. Tienken, L. Joswig, J. Bahr, S. Kaps, L. Siebert and R. Adelung, Flexible, fast and freestanding UV sensors by printing of networked materials, *Appl. Mater. Today*, 2025, **45**, 102846.

204 Y. Liu, X. Zeng, L. Zhu, C. Wang, K. Geng and R. Yao, Effect of nanostructure morphology and concentration on the piezoelectric performance of flexible pressure sensor based on PVDFTRFE/nano-ZNO composite thin film, *Curr. Nanosci.*, 2024, **20**, 543–553.

205 C. Gao, Z. Long, T. Zhong, S. Liang and L. Xing, A self-powered intelligent glove for real-time human-machine gesture interaction based on piezoelectric effect of T-ZnO/PVDF film, *J. Phys. D: Appl. Phys.*, 2022, **55**, 194004.

206 B. Liu, M. Shen, L. Mao, Y. Mao and H. Ma, Self-powered Biosensor Big Data Intelligent Information Processing System for Real-time Motion Monitoring, *Z. Anorg. Allg. Chem.*, 2020, **646**, 500–506.

207 Y. Mao, M. Shen, B. Liu, L. Xing, S. Chen and X. Xue, Self-Powered Piezoelectric-Biosensing Textiles for the Physiological Monitoring and Time-Motion Analysis of Individual Sports, *Sensors*, 2019, **19**(15), 3310.

208 P. Pandit, M. Y. Chougale, D. Dubal, Y. K. Mishra, G. Kerr and A. K. Pandey, Amplifying Touch Using 3D ZnO Tetrapods for Tactile and Haptic Intelligence, *Small*, 2025, **21**, e2408414.

209 L. Wang, X. Qi, C. Li and Y. Wang, Multifunctional tactile sensors for object recognition, *Adv. Funct. Mater.*, 2024, **34**, 2409358.

210 J. Li, A. Reimers, K. M. Dang, M. G. K. Brunk, J. Drewes, U. M. Hirsch, C. Willems, C. E. H. Schmelzer, T. Groth, A. S. Nia, X. Feng, R. Adelung, W. D. Sacher, F. Schütt and J. K. S. Poon, 3D printed neural tissues with in situ optical dopamine sensors, *Biosens. Bioelectron.*, 2023, **222**, 114942.

211 M. Terracciano, S. Račkauskas, A. P. Falanga, S. Martino, G. Chianese, F. Greco, G. Piccialli, G. Viscardi, L. de Stefano, G. Oliviero, N. Borbone and I. Rea, ZnO Tetrapods for Label-Free Optical Biosensing: Physicochemical Characterization and Functionalization Strategies, *Int. J. Mol. Sci.*, 2023, **24**(5), 4449.

212 R. Viter, I. Tepliakova, M. Drobysh, V. Zbolotnii, S. Rackauskas, S. Ramanavicius, K. Grundsteins, V. Liustrovaite, A. Ramanaviciene and V. Ratautaite, Photoluminescence-based biosensor for the detection of antibodies against SARS-CoV-2 virus proteins by ZnO tetrapod structure integrated within microfluidic system, *Sci. Total Environ.*, 2024, **939**, 173333.

213 V. Myndrul, E. Coy, N. Babayevska, V. Zahorodna, V. Balitskyi, I. Baginskiy, O. Gogotsi, M. Bechelany, M. T. Giardi and I. Iatsunskyi, MXene nanoflakes decorating ZnO tetrapods for enhanced performance of skin-attachable stretchable enzymatic electrochemical glucose sensor, *Biosens. Bioelectron.*, 2022, **207**, 114141.

214 V. Myndrul, I. Iatsunskyi, N. Babayevska, M. Jarek and T. Jesionowski, Effect of Electrode Modification with Chitosan and Nafion® on the Efficiency of Real-Time Enzyme Glucose Biosensors Based on ZnO Tetrapods, *Materials*, 2022, **15**(13), 4672.

215 C.-E. Cheng, S. Tangsuwanjinda, H.-M. Cheng and P.-H. Lee, Copper Oxide Decorated Zinc Oxide Nanostructures for the Production of a Non-Enzymatic Glucose Sensor, *Coatings*, 2021, **11**, 936.

216 X. Li, H. Deng and K. Wu, Sweat-Based Glucose Sensor Based on a Graphene/Au Composite Electrode, *Sci. Adv. Mater.*, 2022, **14**, 55–61.

217 P. Pal, Y. Pratap and S. Kabra, T-ZnO/AlGaN/GaN HEMT uric acid sensor-sensitivity analysis and effect of surface wettability for improved performance, *IEEE Sens. J.*, 2022, **22**, 11819–11826.

218 R. Rawat, S. Roy, T. Goswami, F. S. Mirsafi, M. Ismael, T. Leissner, Y. K. Mishra, J. McLaughlin, K. Kant and A. Mathur, Aptamer-enhanced ultrasensitive electrochemical detection of HER-2 in breast cancer diagnosis using ZnO tetrapod-K4PTC nanohybrids, *Sci. Rep.*, 2025, **15**, 17173.

219 S. Tangsuwanjinda, Y.-Y. Chen, C.-H. Lai, G.-T. Jhou, Y.-W. Chiang and H.-M. Cheng, Microporous Oxide-Based Surface-Enhanced Raman Scattering Film for Quadrillionth Detection of Mercury Ion (II), *Processes*, 2021, **9**, 794.

220 E. Vanags, I. Bite, L. Ignatane, R. Ignatans, A. Trausa, C. F. Tipaldi, K. Vilks and K. Smits, Zinc Oxide Tetrapods Doped with Silver Nanoparticles as a Promising Substrate for the Detection of Biomolecules via Surface-Enhanced Raman Spectroscopy, *ChemEngineering*, 2024, **8**, 19.

221 P.-T. Chen, Y.-C. Lu, S. Tangsuwanjinda, R.-J. Chung, R. Sakthivel and H.-M. Cheng, Irradiation-induced synthesis of Ag/ZnO nanostructures as surface-enhanced Raman scattering sensors for sensitive detection of the pesticide acetamiprid, *Sensors*, 2022, **22**, 6406.

222 Z. Zhao, W. Lei, X. Zhang, B. Wang and H. Jiang, ZnO-based amperometric enzyme biosensors, *Sensors*, 2010, **10**, 1216–1231.

223 A. Sharma, A. Agrawal, G. Pandey, S. Kumar, K. Awasthi and A. Awasthi, Carbon Nano-Onion-Decorated ZnO Composite-Based Enzyme-Less Electrochemical Biosensing Approach for Glucose, *ACS Omega*, 2022, **7**, 37748–37756.

224 S. Anbu, R. Ravishankaran, M. F. C. Da Guedes Silva, A. A. Karande and A. J. L. Pombeiro, Differentially selective chemosensor with fluorescence off-on responses on Cu(2 +) and Zn(2 +) ions in aqueous media and applications in pyrophosphate sensing, live cell imaging, and cytotoxicity, *Inorg. Chem.*, 2014, **53**, 6655–6664.

225 F. Giubileo, E. Faella, A. Kumar, S. de Stefano, L. Viscardi, K. Intonti, O. Durante, A. Pelella, A. Mazzotti, N. Martucciello, E. Beliayev, Y. K. Mishra and M. Passacantando, and A. Di Bartolomeo, Zinc oxide tetrapods as novel field emitters with low turn-on voltage, *Nano Express*, 2024, **5**, 45017.

226 K. Karthick, P. Kathirvel, R. Marnadu, S. Chakravarty and M. Shkir, Ultrafast one step direct injection flame synthesis of zinc oxide nanoparticles and fabrication of p-Si/n-ZnO photodiode and characterization, *Phys. B*, 2021, **612**, 412971.

227 M. Oproescu, A.-G. Schiopu, V.-M. Calinescu and J. D. Fidelus, Enhanced Efficiency of Polycrystalline Silicon Solar Cells Using ZnO-Based Nanostructured Layers, *Crystals*, 2025, **15**, 398.

228 W. Z. Lai, X. Huang, X. F. Wang, Z. H. Wei, Q. T. Wang, L. Sun, L. Zhang, X. Y. Ye and L. A. Ma, Field emission properties of tetrapod-shaped ZnO/TiN point light source with semicircle reflecting anode, *Vacuum*, 2022, **205**, 111408.

229 B. Aziz, A. Majid, L. Ghani and I. Aziz, Photoluminescence effect on phosphorous irradiated zinc oxide (ZnO) nanotetrapods synthesized by simple thermal oxidation method, *J. Phys. Appl.*, 2020, **3**, 107–112.

230 M. Zhang, F. Averseng, J.-M. Krafft, P. Borghetti, G. Costentin and S. Stankic, Controlled Formation of Native Defects in Ultrapure ZnO for the Assignment of Green Emissions to Oxygen Vacancies, *J. Phys. Chem. C*, 2020, **124**, 12696–12704.

231 A. P. Tarasov, C. M. Briskina, V. M. Markushev, L. A. Zadorozhnaya, A. S. Lavrikov and V. M. Kanevskii, Analysis of Laser Action in ZnO Tetrapods Obtained by Carbothermal Synthesis, *JETP Lett.*, 2019, **110**, 739–743.

232 J. Zhao, J. Fan, W. Liu, H. Shi, N. Xiao and M. Hu, Ultra-Broadband Second-Harmonic Generation in ZnO Nano-Tetrapod With Over-One-Octave Bandwidth, *IEEE Photonics Technol. Lett.*, 2019, **31**, 250–252.

233 Y. Yamauchi, M. Tenjimbayashi, S. Samitsu and M. Naito, Durable and Flexible Superhydrophobic Materials: Abrasion/Scratching/Slicing/Droplet Impacting/Bending/Twisting-Tolerant Composite with Porcupinefish-Like Structure, *ACS Appl. Mater. Interfaces*, 2019, **11**, 32381–32389.

234 W. Weng, M. Tenjimbayashi, W. H. Hu and M. Naito, Evolution of and Disparity among Biomimetic Superhydrophobic Surfaces with Gecko, Petal, and Lotus Effect, *Small*, 2022, **18**, e2200349.

235 L.-H. Kao and Q.-H. Chen, An integrated approach for developing a durable and superhydrophobic anti-corrosion coating inspired by biomimetic starfish surface structures, *Prog. Org. Coat.*, 2024, **197**, 108825.

236 Z. Zhang, Preparation of hydrophobic silicone rubber composite insulators and the research of anti-aging performance, *e-Polymers*, 2024, **24**(1), DOI: 10.1515/epoly-2024-0079.

237 R. D. Davidson, T. E. O'Loughlin, T. E. G. Alivio, S.-M. Lim and S. Banerjee, Thermodynamics of Wettability: A Physical Chemistry Laboratory Experiment, *J. Chem. Educ.*, 2022, **99**, 2689–2696.

238 Y. Cao, C. Wang, F. Tie and W. Dong, Superhydrophobic alkoxysilane/T-ZnO/SiO2 nanocomposite coatings enhance mechanical properties of porous building substrates: An experimental and multi-physics simulation study, *Constr. Build. Mater.*, 2025, **467**, 140412.

239 W. Weng, Y. Yu and M. Naito, Antifreeze-Infused Superhydrophobic Surface with Superb Anti-icing and Antifrosting Performance, *Langmuir*, 2025, **41**, 18741–18753.

240 J. Bai, Q. Wang, Y. Zhou, Q. Peng, Q. Fu, Z. Peng, Z. Zhang, J. Long, S. Zhao, G. Li and H. Lei, Preparation and properties of wear resistant thermochromic superhydrophobic coatings, *Colloids Surf., A*, 2025, **707**, 135882.

241 L. Vorotinskienė, A. Antanavičė, R. Skvorčinskienė, S. Račkauskas, M. Urbonavičius, R. Kriūkienė and M. Maziukienė, Effect of hydrophobicity of ZnO tetrapods coating on vapour film formation and friction reduction: A study using complex approach, *Int. J. Therm. Sci.*, 2026, **220**, 110372.

242 H. Zhu, B. Wang, D. Liu, Y. Lei, J. Wen, S. Yang and P. Yu, Preparation of superhydrophobic polyurethane sponge with photodegradation function and study on its oil-water separation performance, *Mater. Today Commun.*, 2024, **41**, 110831.

243 A. Bajpayee, N. Rivera-Gonzalez, E. J. Braham, T. E. G. Alivio, A. Fnu, S. Alvi, C. Li, N. Cool, M. Al-Hashimi, L. Fang and S. Banerjee, Multiscale Textured Mesh Substrates that Glide Alcohol Droplets and Impede Ice Nucleation, *Adv. Eng. Mater.*, 2022, **24**(8), 2101524.

244 W. Weng, M. Tenjimbayashi and M. Naito, Role variability of surface chemistry and surface topography in anti-icing performance, *iScience*, 2024, **27**(11), 111039.

245 W. Weng, X. Zheng, M. Tenjimbayashi, I. Watanabe and M. Naito, De-icing performance evolution with increasing hydrophobicity by regulating surface topography, *Sci. Technol. Adv. Mater.*, 2024, **25**, 2334199.

246 Z. Wang, L. Qian, X. Peng, Z. Huang, Y. Yang, C. He and P. Fang, New Aspects of Degradation in Silicone Rubber under UVA and UVB Irradiation: A Gas Chromatography-Mass Spectrometry Study, *Polymers*, 2021, **13**(13), 2215.

247 R. Lohmann, I. T. Cousins, J. C. DeWitt, J. Glüge, G. Goldenman, D. Herzke, A. B. Lindstrom, M. F. Miller, C. A. Ng, S. Patton, M. Scheringer, X. Trier and Z. Wang, Are Fluoropolymers Really of Low Concern for Human and Environmental Health and Separate from Other PFAS?, *Environ. Sci. Technol.*, 2020, **54**, 12820–12828.

248 C. Yang, J. Wang, J. Li, H. Zhang, C. Shi, Z. Guo and B. Bai, Facile fabrication of durable mesh with reversible photo-responsive wettability for smart oil/water separation, *Prog. Org. Coat.*, 2021, **160**, 106520.

249 Y. Chenxi, W. Jian, L. Juan, Z. Haiou, C. Tianqing, G. Zhen, W. Yingguo and B. Bo, Multibioinspired Design of a Durable Janus Copper Foam with Asymmetric and Cooperative Alternating Wettability for Efficient Fog Harvesting, *ACS Sustainable Chem. Eng.*, 2023, **11**, 3147–3159.

250 D. Li, Y. Fan, G. Han and Z. Guo, Multibioinspired Janus membranes with superwettable performance for unidirectional transportation and fog collection, *Chem. Eng. J.*, 2021, **404**, 126515.

251 Z. Yu, T. Zhu, J. Zhang, M. Ge, S. Fu and Y. Lai, Fog Harvesting Devices Inspired from Single to Multiple Creatures: Current Progress and Future Perspective, *Adv. Funct. Mater.*, 2022, **32**(26), 2200359.

252 H. Qiu, A. Gapeeva, I. Hölken, S. Kaps, R. Adelung and M. J. Baum, Preventing algae adhesion using lubricant-modified polydimethylsiloxane/polythiourethane nanocomposite, *Mater. Des.*, 2022, **214**, 110389.

253 K. Feng, H. Qiu, A. Gapeeva, X. Li, Y. Li, S. Kaps, Y. K. Mishra, R. Adelung, M. Baum and L. Yu, Indole-functionalized polythiourethane/tetrapodal shaped ZnO nanocomposites for eco-friendly marine biofouling control, *Prog. Org. Coat.*, 2023, **185**, 107939.

254 H. Qiu, A. Gapeeva, S. Kaps, R. Adelung and M. J. Baum, Modification of Nylon Nets with Poly(dimethylsiloxane)/Tetrapodal-Shaped ZnO Composite for Aquaculture Biofouling Control, *ACS Appl. Polym. Mater.*, 2021, **3**, 6598–6607.

255 N. Yamamoto, A. Kioka and Y. Yamada, On the deposition and polymorphism of CaCO3 crystals in the presence of the tetrapod-shaped ZnO nanomaterials and polydimethylsiloxane composite, *Results Surf. Interfaces*, 2023, **12**, 100138.

256 F. Liu, M. Yang, B. Han and J. Long, Development of T-ZnOw@Al2O3-incorporated low-temperature curing aluminium phosphate coating on Ti–6Al–4V alloy, *Ceram. Int.*, 2019, **45**, 18406–18412.

257 Z. Zhao, R. Balu, N. R. Choudhury and N. K. Dutta, The effect of tetra-needle-like zinc oxide whisker as additive on the crystallization kinetics of polybutylene adipate terephthalate/polylactic acid blend, *Polym. Eng. Sci.*, 2024, **64**, 4079–4098.

258 R. Brindha, S. S. R. Ajith, M. Nandhini, M. Selvam, K. Subannajui, K. Khotmungkhun and K. Sakthipandi, Evaluation of anticorrosive behaviour of ZnO nanotetra-pods on a AZ91-grade Mg alloy, *Bull. Mater. Sci.*, 2019, **42**, 221.

259 L. Liu, S. Xu, Z. Wang, X. Chen, M. Cao, S. Zhang, Y. Liu and J. Cui, Building of soft-hard compound brush in porous PVA/NH2@TAtZnO plural gel and the high-efficiency anti-interference removal on Pb(II), *Chemosphere*, 2023, **319**, 137990.

260 S. Xu, X. Jiang, L. Liu, Z. Wang, X. Zhang, Y. Peng and M. Cao, Preparation of PVA/tetra-ZnO composite with framework-supported pore-channel structure and the removal research of lead ions, *Environ. Sci. Pollut. Res. Int.*, 2019, **26**, 24062–24074.

261 M. Sharma, M. Joshi, S. Nigam, D. K. Avasthi, R. Adelung, S. K. Srivastava and Y. K. Mishra, Efficient oil removal from wastewater based on polymer coated superhydrophobic tetrapodal magnetic nanocomposite adsorbent, *Appl. Mater. Today*, 2019, **17**, 130–141.

262 F. Wu, B. J. Harper and S. L. Harper, Comparative dissolution, uptake, and toxicity of zinc oxide particles in individual aquatic species and mixed populations, *Environ. Toxicol. Chem.*, 2019, **38**, 591–602.

263 S. W. Y. Wong, P. T. Y. Leung, A. B. Djurisić and K. M. Y. Leung, Toxicities of nano zinc oxide to five marine organisms: influences of aggregate size and ion solubility, *Anal. Bioanal. Chem.*, 2010, **396**, 609–618.

264 E. Iakovleva and M. Sillanpää, The use of low-cost adsorbents for wastewater purification in mining industries, *Environ. Sci. Pollut. Res. Int.*, 2013, **20**, 7878–7899.

265 *2000 years of zinc and brass*, ed. P. T. Craddock, British Museum Press, London, 1998, **vol. 50**.

266 B. de Berardis, G. Civitelli, M. Condello, P. Lista, R. Pozzi, G. Arancia and S. Meschini, Exposure to ZnO nanoparticles induces oxidative stress and cytotoxicity in human colon carcinoma cells, *Toxicol. Appl. Pharmacol.*, 2010, **246**, 116–127.

267 D. Xiong, T. Fang, L. Yu, X. Sima and W. Zhu, Effects of nano-scale TiO2, ZnO and their bulk counterparts on zebrafish: acute toxicity, oxidative stress and oxidative damage, *Sci. Total Environ.*, 2011, **409**, 1444–1452.

268 L. Siebert, E. Luna-Cerón, L. E. García-Rivera, J. Oh, J. Jang, D. A. Rosas-Gómez, M. D. Pérez-Gómez, G. Maschkowitz, H. Fickenscher, D. Oceguera-Cuevas, C. G. Holguín-León, B. Byambaa, M. A. Hussain, E. Enciso-Martinez, M. Cho, Y. Lee, N. Sobahi, A. Hasan, D. P. Orgill, Y. K. Mishra, R. Adelung, E. Lee and S. R. Shin, Light-controlled growth factors release on tetrapodal ZnO-incorporated 3D-printed hydrogels for developing smart wound scaffold, *Adv. Funct. Mater.*, 2021, **31**(22), 2007555.

269 M.-Z. Pan, S.-B. Hua, J.-M. Wu, X. Yuan, Z.-L. Deng, J. Xiao and Y.-S. Shi, Preparation and properties of T-ZnOw enhanced BCP scaffolds with double-layer structure by digital light processing, *J. Adv. Ceram.*, 2022, **11**, 570–581.

270 A. G. Phi-Stone, https://www.phi-stone.de/en/.

271 A. Büter, G. Maschkowitz, M. Baum, Y. K. Mishra, L. Siebert, R. Adelung and H. Fickenscher, Antibacterial Activity of Nanostructured Zinc Oxide Tetrapods, *Int. J. Mol. Sci.*, 2023, **24**(4), 3444.

272 F. M. Collares, I. M. Garcia, M. Klein, C. F. Parolo, F. A. L. Sánchez, A. Takimi, C. P. Bergmann, S. M. W. Samuel, M. A. Melo and V. C. Leitune, Exploring Needle-Like Zinc Oxide Nanostructures for Improving Dental Resin Sealers: Design and Evaluation of Antibacterial, Physical and Chemical Properties, *Polymers*, 2020, **12**(4), 789.

273 H. L. Ong, B. M. Dell'Agnese, Y. Jiang, Y. Guo, J. Zhou, J. Zhang, J. Luo, R. Tao, M. Zhang and L. G. Dover, Controlling bacterial growth and inactivation using thin

film-based surface acoustic waves, *Lab Chip*, 2024, **24**, 4344–4356.

274 P. Schadte, F. Rademacher, G. Andresen, M. Hellfritzsch, H. Qiu, G. Maschkowitz, R. Gläser, N. Heinemann, D. Drücke, H. Fickenscher, R. Scherließ, J. Harder, R. Adelung and L. Siebert, 3D-printed wound dressing platform for protein administration based on alginate and zinc oxide tetrapods, *Nano Convergence*, 2023, **10**, 53.

275 Y. Du, D. Ma, J. Mao, J. Yao, Q. Ma, J. Lu, F. Luo, C. Luo and L. Li, Improving the antistatic and antibacterial properties of polypropylene via tetrapod-shaped ZnO@Ag particles, *Polym. Test.*, 2021, **101**, 107301.

276 F. Qi, X. Gao, C. Wang, Y. Shuai, L. Yang, R. Liao, J. Xin, S. Peng and C. Shuai, In situ grown silver nanoparticles on tetrapod-like zinc oxide whisker for photocatalytic antibacterial in scaffolds, *Mater. Today Sustainability*, 2022, **19**, 100210.

277 J. Vachon, J. Alfurhood, M. Al-Subaie, L. Yang and S. Pierrat, Antibacterial, Antiviral and Antifungal Activity of Zinc Oxide Tetrapod in Polypropylene Compared to Other Zinc Based Additives, *J. Appl. Polym. Sci.*, 2025, **142**(25), e57051.

278 Q. Li, R. Lin, Z. Tang, S. Liang, X. Xue and L. Xing, A flexible self-cleaning/antibacterial PVDF/T-ZnO fabric based on piezo-photocatalytic coupling effect for smart mask, *J. Phys. D: Appl. Phys.*, 2024, **57**, 305106.

279 Z. Zhao, R. Balu, S. Gangadoo, N. K. Duta and N. R. Choudhury, Poly(butylene adipate-*co*-terephthalate)/Polylactic Acid/Tetrapod-Zinc Oxide Whisker Composite Films with Antibacterial Properties, *Polymers*, 2024, **16**, 1039.

280 H. Lee, Y.-J. Kim, Y.-J. Yang, J.-H. Lee and H.-H. Lee, Development of antibacterial dual-cure dental resin composites via tetrapod-shaped zinc oxide incorporation, *Dent. Mater.*, 2024, **40**, 1762–1772.

281 J. Liu, J. Xiong, Q. Huang, T. Lu, W. Chen and M. Li, Eco-friendly synthesis of robust bioinspired cotton fabric with hybrid wettability for integrated water harvesting and water purification, *J. Cleaner Prod.*, 2022, **350**, 131524.

282 J. Gupta, M. Irfan, N. Ramgir, K. P. Muthe, A. K. Debnath, S. Ansari, J. Gandhi, C. T. Ranjith-Kumar and M. Surjit, Antiviral Activity of Zinc Oxide Nanoparticles and Tetrapods Against the Hepatitis E and Hepatitis C Viruses, *Front. Microbiol.*, 2022, **13**, 881595.

283 Y. K. Mishra, R. Adelung, C. Röhl, D. Shukla, F. Spors and V. Tiwari, Virostatic potential of micro-nano filopodia-like ZnO structures against herpes simplex virus-1, *Antiviral Res.*, 2011, **92**, 305–312.

284 T. E. Antoine, S. R. Hadigal, A. M. Yakoub, Y. K. Mishra, P. Bhattacharya, C. Haddad, T. Valyi-Nagy, R. Adelung, B. S. Prabhakar and D. Shukla, Intravaginal Zinc Oxide Tetrapod Nanoparticles as Novel Immunoprotective Agents against Genital Herpes, *J. Immunol.*, 2016, **196**, 4566–4575.

285 M. Hosseini, S. Behzadinasab, A. W. H. Chin, L. L. M. Poon and W. A. Ducker, Reduction of Infectivity of SARS-CoV-2 by Zinc Oxide Coatings, *ACS Biomater. Sci. Eng.*, 2021, **7**, 5022–5027.

286 S. R. Sonntag, S. Gniesmer, A. Gapeeva, R. Adelung, A. Cojocaru, Y. K. Mishra, S. Kaps, A. Tura, S. Grisanti and S. Grisanti, Zinc oxide tetrapods modulate wound healing and cytokine release in vitro—a new antiproliferative substance in glaucoma filtering surgery, *Life*, 2022, **12**, 1691.

287 S. R. Sonntag, S. Gniesmer, A. Gapeeva, K. J. Offermann, R. Adelung, Y. K. Mishra, A. Cojocaru, S. Kaps, S. Grisanti and S. Grisanti, In vitro evaluation of zinc oxide tetrapods as a new material component for glaucoma implants, *Life*, 2022, **12**, 1805.

288 Y. Xu, P. Chen, X. Guo, C. Li, Z. Li, Z. Zhou, M. Li, N. Long and D. Li, Tetraneedlelike ZnO Whiskers/Tetracalcium Phosphate Synergistically Improved the Mechanical, Degradation and Biological Properties of Polycaprolactone Scaffolds, *J. Inorg. Organomet. Polym.*, 2025, 1–13.

289 Q. Zhu, Y. Xuan and X. Liu, Enhancing direct solar thermochemical performance of modified CaCO3 with thermal transport networks composed of tetrapod-shaped ZnO whiskers, *Sol. Energy Mater. Sol. Cells*, 2022, **248**, 111981.

290 B. Kalidasan, A. K. Pandey, F. S. Mirsafi, T. Leissner, H.-G. Rubahn, S. Rahman and Y. K. Mishra, Tetrapod-engineered eutectic salt hydrate composites for advanced thermal energy storage, *J. Energy Storage*, 2025, **124**, 116680.

291 Y. Li, G. Hu, Q. Wang, F. Dong and Y. Xiong, Design of PVA/multilayer hybrid particle composite aerogel skeleton supported form-stable phase change materials with high thermal conductivity and solar-to-thermal conversion efficiency, *J. Energy Storage*, 2024, **77**, 109966.

292 C.-M. Chang, H.-F. Lin, S.-C. Liao, H.-T. Chiu, C.-E. Liu and H.-L. Guo, Effects of Negative Electrodes Coated by ZnO with Different Morphologies on Electrochemical Performances and Safety of Lithium Ion Batteries, *Int. J. Electrochem. Sci.*, 2019, **14**, 1197–1207.

293 M. Jia, S. Yu, D. Li, C. Liu, Y. Bao, X. Yu and K. Chen, Preparation and Photocatalytic Performance of MoS2/ZnS/ZnO-T Heterojunction Photocatalyst for Dye Degradation in Water, *Part. Part. Syst. Charact.*, 2022, **39**, 2200034.

294 J. Tang, Y. Xue, C. Ma, S. Zhang and Q. Li, Facile preparation of BiOI/T-ZnOw p–n heterojunction photocatalysts with enhanced removal efficiency for rhodamine B and oxytetracycline, *New J. Chem.*, 2022, **46**, 13010–13020.

295 Y. He, A. U. Rehman, M. Xu, C. A. Not, A. M. C. Ng and A. B. Djurišić, Photocatalytic degradation of different types of microplastics by TiOx/ZnO tetrapod photocatalysts, *Heliyon*, 2023, **9**, e22562.

296 A. K. Mourya, R. P. Singh, T. Kumar, A. S. Talmale, G. S. Gaikwad and A. V. Wankhade, Tuning the morphologies of ZnO for enhanced photocatalytic activity, *Inorg. Chem. Commun.*, 2023, **154**, 110850.

297 S.-H. Hung and K. McKenna, First-Principles Investigation of the Structure and Properties of Au Nanoparticles Supported on ZnO, *J. Phys. Chem. C*, 2019, **123**, 21185–21194.

298 A. G. Ramu, D. J. Yang, E. M. Al Olayan, O. D. AlAmri, A. S. Aloufi, J. O. Almushawwah and D. Choi, Synthesis of hierarchically structured T-ZnO-rGO-PEI composite and their catalytic removal of colour and colourless phenolic compounds, *Chemosphere*, 2021, **267**, 129245.

299 B. Bachiller-Baeza, A. Iglesias-Juez, G. Agostini and E. Castillejos-López, Pd–Au bimetallic catalysts supported on ZnO for selective 1,3-butadiene hydrogenation, *Catal. Sci. Technol.*, 2020, **10**, 2503–2512.

300 X. Huang, L. Zeng, R. Li, Z. Xi and Y. Li, Manipulating conductive network formation via 3D T-ZnO: A facile approach for a CNT-reinforced nanocomposite, *Nanotechnol. Rev.*, 2020, **9**, 534–542.

301 R. Yan, W. Qin, G. Gong, W. Chen, H. Peng, R. Zhong, C. Mou, C. Huang and B. Zhou, Composite aramid aerogels with anisotropic layered structure reinforced by tetra-needle-like ZnO whiskers for acoustic and thermal insulations, *J. Mater. Sci.*, 2025, **60**, 2344–2362.

302 F. Scherer, S. Wille, L. Saure, F. Schütt, B. Wellhäußer, R. Adelung and M. Kern, Investigation of Mechanical Properties of Polymer-Infiltrated Tetrapodal Zinc Oxide in Different Variants, *Materials*, 2024, **17**(9), 2112.

303 D. Meinderink, K. J. Nolkemper, J. Bürger, A. G. Orive, J. K. Lindner and G. Grundmeier, Spray coating of poly(acrylic acid)/ZnO tetrapod adhesion promoting nanocomposite films for polymer laminates, *Surf. Coat. Technol.*, 2019, **375**, 112–122.

304 Y. Su, Y. Chen, H. Zhang, S. Liu and P. Guo, Synergistic enhancement effect of multi-dimensional nanomaterials on high-damping polyurethane, *J. Rubber Res.*, 2025, **28**, 39–50.

305 X. Jin, J. Strueben, L. Heepe, A. Kovalev, Y. K. Mishra, R. Adelung, S. N. Gorb and A. Staubitz, Joining the unjoinable: adhesion between low surface energy polymers using tetrapodal ZnO linkers, *Adv. Mater.*, 2012, **24**, 5676–5680.

306 T. Peng, J. Wang, W. Chao, S. Zhang, J. Liu and J. Wang, Investigation of Space Charge Characteristics and Deep Charging Effects in T-ZnOw/Polyimide Composites, *IEEE Trans. Dielectr. Electr. Insul.*, 2025, 99.

307 B. Wellhäußer, L. M. Saure, F. Schütt, F. Scherer, S. Wille and M. Kern, The Impact of an MDP-Containing Primer on the Properties of Zinc Oxide Networks Infiltrated with BisGMA-TEGDMA and UDMA-TEGDMA Polymers, *Materials*, 2024, **18**, 137.

308 H. Greijer, N. Mirotta, E. Treossi, F. Valorosi, F. Schütt, L. Siebert, Y. K. Mishra, R. Adelung, V. Palermo and H. Hillborg, Tuneable conductivity at extreme electric fields in ZnO tetrapod-silicone composites for high-voltage power cable insulation, *Sci. Rep.*, 2022, **12**, 6035.

309 X. Zeng, X. Cheng, R. Yu and G. D. Stucky, Electromagnetic microwave absorption theory and recent achievements in microwave absorbers, *Carbon*, 2020, **168**, 606–623.

310 L. Wang, X. Li, Q. Li, X. Yu, Y. Zhao, J. Zhang, M. Wang and R. Che, Oriented Polarization Tuning Broadband Absorption from Flexible Hierarchical ZnO Arrays Vertically Supported on Carbon Cloth, *Small*, 2019, **15**, e1900900.

311 X. Li, L. Yu, W. Zhao, Y. Shi, L. Yu, Y. Dong, Y. Zhu, Y. Fu, X. Liu and F. Fu, Prism-shaped hollow carbon decorated with polyaniline for microwave absorption, *Chem. Eng. J.*, 2020, **379**, 122393.

312 J. Wang, Z. Xiang, Y. Yin, Z. Lu, Q. Ren, B. Yuan and W. Lu, Stomata-Inspired Intelligent High-Performance Hydrogel With on-Demand Gateable Electromagnetic-Interference Shielding, *Small*, 2025, e10156.

313 H. Cai, Y. Chen, C. Feng and Z. Lin, Solvent-controlled synthesis of bimetallic ZIF-coated tetra-needle ZnO whiskers toward hollow Co/C derivatives with enhanced microwave absorption, *J. Mater. Sci.*, 2025, **60**, 18824–18840.

314 X. Guo, X. Zhou, Y. Gao, Y. Qian, G. Wang and L. Lyu, Tetra-needle like ZnO whisker doped graphene composites for radar/infrared compatible stealth properties, *Polym. Compos.*, 2025, **46**, 9383–9399.

315 R. M. Simon, Emi Shielding Through Conductive Plastics, *Polym.-Plast. Technol. Eng.*, 1981, **17**, 1–10.

316 F. Peng, W. Zhu, Y. Fang, B. Fu, H. Chen, H. Ji, X. Ma, C. Hang and M. Li, Ultralight and Highly Conductive Silver Nanowire Aerogels for High-Performance Electromagnetic Interference Shielding, *ACS Appl. Mater. Interfaces*, 2023, **15**, 4284–4293.

317 M. Pérez-Page, E. Yu, J. Li, M. Rahman, D. M. Dryden, R. Vidu and P. Stroeve, Template-based syntheses for shape controlled nanostructures, *Adv. Colloid Interface Sci.*, 2016, **234**, 51–79.

318 C. Orha, M. Nicolaescu, M.-I. Morariu, T. Galatonova, S. Busuioc, C. Lazau and C. Bandas, A Comprehensive Review on Aero-Materials: Present and Future Perspectives, *Coatings*, 2025, **15**, 754.

319 A. Schuchardt, T. Braniste, Y. K. Mishra, M. Deng, M. Mecklenburg, M. A. Stevens-Kalceff, S. Raevschi, K. Schulte, L. Kienle, R. Adelung and I. Tiginyanu, Three-dimensional Aerographite-GaN hybrid networks: single step fabrication of porous and mechanically flexible materials for multifunctional applications, *Sci. Rep.*, 2015, **5**, 8839.

320 C. Orha, M. Nicolaescu, M.-I. Morariu, T. Galatonova, S. Busuioc, C. Lazau and C. Bandas, A Comprehensive Review on Aero-Materials: Present and Future Perspectives, *Coatings*, 2025, **15**, 754.

321 F. Schütt, S. Signetti, H. Krüger, S. Röder, D. Smazna, S. Kaps, S. N. Gorb, Y. K. Mishra, N. M. Pugno and R. Adelung, Hierarchical self-entangled carbon nanotube tube networks, *Nat. Commun.*, 2017, **8**, 1215.

322 L. M. Saure, J. Lumma, N. Kohlmann, T. Hartig, E. E. S. Teotonio, S. Shetty, N. Ravishankar, L. Kienle, F. Faupel, S. Schröder, R. Adelung, H. Terraschke and F. Schütt, Functional light diffusers based on hybrid CsPbBr3/SiO2 aero-framework structures for laser light illumination and conversion, *J. Mater. Sci.*, 2024, **59**, 17382–17393.

323 A. Reimers, A. Bouhanguel, E. Greve, M. Möller, L. M. Saure, S. Kaps, L. Wegner, A. S. Nia, X. Feng, F. Schütt, Y. Andres and R. Adelung, Multifunctional, self-cleaning air filters based on graphene-enhanced ceramic networks, *Device*, 2023, **1**, 100098.

324 T. Braniste, V. Ciobanu, F. Schütt, H. Mimura, S. Raevschi, R. Adelung, N. M. Pugno and I. Tiginyanu, Self-Propelled Aero-GaN Based Liquid Marbles Exhibiting Pulsed Rotation on the Water Surface, *Materials*, 2021, **14**(17), 5086.

325 V. Ciobanu, T. Galatonova, T. Braniste, P. Urbanek, S. Lehmann, B. Hanulikova, K. Nielsch, I. Kuritka, V. Sedlarik

and I. Tiginyanu, Aero-TiO2 three-dimensional nanoarchitecture for photocatalytic degradation of tetracycline, *Sci. Rep.*, 2024, **14**, 31215.

326 A. Reimers, J. Rank, E. Greve, M. Möller, S. Kaps, J. Bahr, R. Adelung and F. Schütt, Graphene-Based Thermopneumatic Generator for On-Board Pressure Supply of Soft Robots, *Soft Robot.*, 2025, **12**, 124–134.

327 F. Rasch, C. Schmitt, L. M. Saure, R. Meyer, V. Adamski, D. Dengiz, R. Scherließ, R. Lucius, M. Synowitz, Y. K. Mishra, K. Hattermann, R. Adelung, J. Held-Feindt and F. Schütt, Macroscopic Silicone Microchannel Matrix for Tailored Drug Release and Localized Glioblastoma Therapy, *ACS Biomater. Sci. Eng.*, 2020, **6**, 3388–3397.

328 K. Siemsen, S. Rajput, F. Rasch, F. Taheri, R. Adelung, J. Lammerding and C. Selhuber-Unkel, Tunable 3D Hydrogel Microchannel Networks to Study Confined Mammalian Cell Migration, *Advanced healthcare*, *Materials*, 2021, **10**, e2100625.

329 J. Li, B. Hietel, M. G. K. Brunk, A. Reimers, C. Willems, T. Groth, H. Cynis, R. Adelung, F. Schütt, W. D. Sacher and J. K. S. Poon, 3D-printed microstructured alginate scaffolds for neural tissue engineering, *Trends Biotechnol.*, 2025, **43**, 447–461.

330 M. Hauck, J. Dittmann, B. Zeller-Plumhoff, R. Madurawala, D. Hellmold, C. Kubelt, M. Synowitz, J. Held-Feindt, R. Adelung, S. Wulfinghoff and F. Schütt, Fabrication and Modelling of a Reservoir-Based Drug Delivery System for Customizable Release, *Pharmaceutics*, 2022, **14**(4), 777.

331 S. Chandrasekaran, W. V. Liebig, M. Mecklenburg, B. Fiedler, D. Smazna, R. Adelung and K. Schulte, Fracture, failure and compression behaviour of a 3D interconnected carbon aerogel (Aerographite) epoxy composite, *Compos. Sci. Technol.*, 2016, **122**, 50–58.

332 S. Garlof, T. Fukuda, M. Mecklenburg, D. Smazna, Y. K. Mishra, R. Adelung, K. Schulte and B. Fiedler, Electromechanical piezoresistive properties of three dimensionally interconnected carbon aerogel (Aerographite)-epoxy composites, *Compos. Sci. Technol.*, 2016, **134**, 226–233.

333 S. Garlof, M. Mecklenburg, D. Smazna, Y. K. Mishra, R. Adelung, K. Schulte and B. Fiedler, 3D carbon networks and their polymer composites: Fabrication and electromechanical investigations of neat Aerographite and Aerographite-based PNCs under compressive load, *Carbon*, 2017, **111**, 103–112.

334 C. Arndt, M. Hauck, I. Wacker, B. Zeller-Plumhoff, F. Rasch, M. Taale, A. S. Nia, X. Feng, R. Adelung, R. R. Schröder, F. Schütt and C. Selhuber-Unkel, Microengineered Hollow Graphene Tube Systems Generate Conductive Hydrogels with Extremely Low Filler Concentration, *Nano Lett.*, 2021, **21**, 3690–3697.

335 M. Hauck, L. M. Saure, B. Zeller-Plumhoff, S. Kaps, J. Hammel, C. Mohr, L. Rieck, A. S. Nia, X. Feng, N. M. Pugno, R. Adelung and F. Schütt, Overcoming Water Diffusion Limitations in Hydrogels via Microtubular Graphene Networks for Soft Actuators, *Adv. Mater.*, 2023, **35**, e2302816.

336 F. Schütt, F. Rasch, N. Deka, A. Reimers, L. M. Saure, S. Kaps, J. Rank, J. Carstensen, Y. Kumar Mishra, D. Misseroni, A. Romani Vázquez, M. R. Lohe, A. Shaygan Nia, N. M. Pugno, X. Feng and R. Adelung, Electrically powered repeatable air explosions using microtubular graphene assemblies, *Mater. Today*, 2021, **48**, 7–17.

337 P. S. Pálvölgyi, D. Sebők, I. Szenti, E. Bozo, H. Ervasti, O. Pitkänen, J. Hannu, H. Jantunen, M. E. Leinonen, S. Myllymäki, A. Kukovecz and K. Kordas, Lightweight porous silica foams with extreme-low dielectric permittivity and loss for future 6G wireless communication technologies, *Nano Res.*, 2021, **14**, 1450–1456.

338 AERO MATERIALS GmBH, https://aero-materials.com/.

339 L. M. Bellan, M. Pearsall, D. M. Cropek and R. Langer, A 3D interconnected microchannel network formed in gelatin by sacrificial shellac microfibers, *Adv. Mater.*, 2012, **24**, 5187–5191.

340 H. Luan, Q. Zhang, T.-L. Liu, X. Wang, S. Zhao, H. Wang, S. Yao, Y. Xue, J. W. Kwak, W. Bai, Y. Xu, M. Han, K. Li, Z. Li, X. Ni, J. Ye, D. Choi, Q. Yang, J.-H. Kim, S. Li, S. Chen, C. Wu, D. Lu, J.-K. Chang, Z. Xie, Y. Huang and J. A. Rogers, Complex 3D microfluidic architectures formed by mechanically guided compressive buckling, *Sci. Adv.*, 2021, **7**, eabj3686.

341 R. Saidur, N. A. Rahim and M. Hasanuzzaman, A review on compressed-air energy use and energy savings, *Renewable Sustainable Energy Rev.*, 2010, **14**, 1135–1153.

342 F. Doyle and J. Cosgrove, An approach to optimising compressed air systems in production operations, *Int. J. Ambient Energy*, 2018, **39**, 194–201.

343 I. Plesco, T. Braniste, N. Wolff, L. Gorceac, V. Duppel, B. Cinic, Y. K. Mishra, A. Sarua, R. Adelung, L. Kienle and I. Tiginyanu, Aero-ZnS architectures with dual hydrophilic–hydrophobic properties for microfluidic applications, *APL Mater.*, 2020, **8**(6), 061105.

344 I. Barg, N. Kohlmann, F. Rasch, T. Strunskus, R. Adelung, L. Kienle, F. Faupel, S. Schröder and F. Schütt, Strain-Invariant, Highly Water Stable All-Organic Soft Conductors Based on Ultralight Multi-Layered Foam-Like Framework Structures, *Adv. Funct. Mater.*, 2023, **33**(21), 2212688.

345 M. Taale, D. Krüger, E. Ossei-Wusu, F. Schütt, M. A. U. Rehman, Y. K. Mishra, J. Marx, N. Stock, B. Fiedler, A. R. Boccaccini, R. Willumeit-Römer, R. Adelung and C. Selhuber-Unkel, Systematically Designed Periodic Electrophoretic Deposition for Decorating 3D Carbon-Based Scaffolds with Bioactive Nanoparticles, *ACS Biomater. Sci. Eng.*, 2019, **5**, 4393–4404.

346 M. Taale, F. Schütt, K. Zheng, Y. K. Mishra, A. R. Boccaccini, R. Adelung and C. Selhuber-Unkel, Bioactive Carbon-Based Hybrid 3D Scaffolds for Osteoblast Growth, *ACS Appl. Mater. Interfaces*, 2018, **10**, 43874–43886.

347 M. Taale, F. Schütt, T. Carey, J. Marx, Y. K. Mishra, N. Stock, B. Fiedler, F. Torrisi, R. Adelung and C. Selhuber-Unkel, Biomimetic Carbon Fiber Systems Engineering: A Modular Design Strategy To Generate Biofunctional Composites from Graphene and Carbon Nanofibers, *ACS Appl. Mater. Interfaces*, 2019, **11**, 5325–5335.

348 C. Shuai, Z. Wang, F. Yang, H. Zhang, J. Liu and P. Feng, Laser additive manufacturing of shape memory

biopolymer bone scaffold: 3D conductive network construction and electrically driven mechanism, *J. Adv. Res.*, 2024, **65**, 167–181.

349 F. Wang, L. M. Saure, F. Schütt, F. Lorich, F. Rasch, A. S. Nia, X. Feng, A. Seekamp, T. Klüter, H. Naujokat, R. Adelung and S. Fuchs, Graphene Oxide Framework Structures and Coatings: Impact on Cell Adhesion and Pre-Vascularization Processes for Bone Grafts, *Int. J. Mol. Sci.*, 2022, **23**(6), 3379.

350 T. S. Karande, J. L. Ong and C. M. Agrawal, Diffusion in musculoskeletal tissue engineering scaffolds: design issues related to porosity, permeability, architecture, and nutrient mixing, *Ann. Biomed. Eng.*, 2004, **32**, 1728–1743.

351 C. D. Devillard and C. A. Marquette, Vascular Tissue Engineering: Challenges and Requirements for an Ideal Large Scale Blood Vessel, *Front. Bioeng. Biotechnol.*, 2021, **9**, 721843.

352 D. A. Oliveira, R. A. Da Silva, M. O. Orlandi and J. R. Siqueira Jr, Exploring ZnO nanostructures with reduced graphene oxide in layer-by-layer films as supercapacitor electrodes for energy storage, *J. Mater. Sci.*, 2022, **57**, 7023–7034.

353 D. Spurling, H. Krüger, N. Kohlmann, F. Rasch, M. P. Kremer, L. Kienle, R. Adelung, V. Nicolosi and F. Schütt, 3D networked MXene thin films for high performance supercapacitors, *Energy Storage Mater.*, 2024, **65**, 103148.

354 R. Yang, H. Du, Z. Lin, L. Yang, H. Zhu, H. Zhang, Z. Tang and X. Gui, ZnO nanoparticles filled tetrapod-shaped carbon shell for lithium-sulfur batteries, *Carbon*, 2019, **141**, 258–265.

355 H. Cavers, H. Krüger, O. Polonskyi, F. Schütt, R. Adelung and S. Hansen, Temperature-Dependent Vapor Infiltration of Sulfur into Highly Porous Hierarchical Three-Dimensional Conductive Carbon Networks for Lithium Ion Battery Applications, *ACS Omega*, 2020, **5**, 28196–28203.

356 H. Kruger, H. Cavers, O. Gronenberg, U. Schurmann, Y. K. Mishra, J. Jacobsen, J. Carstensen, N. Stock, L. Kienle, F. Schutt, R. Adelung and S. Hansen, in *2021 IEEE 11th International Conference Nanomaterials: Applications & Properties (NAP)*, IEEE, 2021, pp. 1–6.

357 N. Wolff, T. Braniste, H. Krüger, S. Mangelsen, M. R. Islam, U. Schürmann, L. M. Saure, F. Schütt, S. Hansen, H. Terraschke, R. Adelung, I. Tiginyanu and L. Kienle, Synthesis and Nanostructure Investigation of Hybrid β-Ga2 O3/ ZnGa2 O4 Nanocomposite Networks with Narrow-Band Green Luminescence and High Initial Electrochemical Capacity, *Small*, 2023, **19**, e2207492.

358 V. Ciobanu, V. V. Ursaki, S. Lehmann, T. Braniste, S. Raevschi, V. V. Zalamai, E. V. Monaico, P. Colpo, K. Nielsch and I. M. Tiginyanu, Aero-TiO2 Prepared on the Basis of Networks of ZnO Tetrapods, *Crystals*, 2022, **12**, 1753.

359 F. Matter and M. Niederberger, The Importance of the Macroscopic Geometry in Gas-Phase Photocatalysis, *Adv. Sci.*, 2022, **9**, e2105363.

360 M. Dragoman, V. Ciobanu, S. Shree, D. Dragoman, T. Braniste, S. Raevschi, A. Dinescu, A. Sarua, Y. K. Mishra, N. Pugno, R. Adelung and I. Tiginyanu, Sensing up to 40 atm Using Pressure-Sensitive Aero-GaN, *Phys. Status Solidi RRL*, 2019, **13**(6), 1900012.

361 Z. Ren, H. Zhang, N. Liu, D. Lei, Q. Zhang, T. Su, L. Wang, J. Su and Y. Gao, Self-powered 2D nanofluidic graphene pressure sensor with Serosa-Mimetic structure, *EcoMat*, 2023, **5**(3), e12299.

362 O. Lupan, V. Postica, M. Mecklenburg, K. Schulte, Y. K. Mishra, B. Fiedler and R. Adelung, Low powered, tunable and ultra-light aerographite sensor for climate relevant gas monitoring, *J. Mater. Chem. A*, 2016, **4**, 16723–16730.

363 I. Plesco, J. Strobel, F. Schütt, C. Himcinschi, N. Ben Sedrine, T. Monteiro, M. R. Correia, L. Gorceac, B. Cinic, V. Ursaki, J. Marx, B. Fiedler, Y. K. Mishra, L. Kienle, R. Adelung and I. Tiginyanu, Hierarchical Aerographite 3D flexible networks hybridized by InP micro/nanostructures for strain sensor applications, *Sci. Rep.*, 2018, **8**, 13880.

364 O. Lupan, V. Postica, J. Marx, M. Mecklenburg, Y. K. Mishra, K. Schulte, B. Fiedler and R. Adelung, Individual hollow and mesoporous aero-graphitic microtube based devices for gas sensing applications, *Appl. Phys. Lett.*, 2017, **110**(26), 263109.

365 I. Hölken, G. Neubüser, V. Postica, L. Bumke, O. Lupan, M. Baum, Y. K. Mishra, L. Kienle and R. Adelung, Sacrificial Template Synthesis and Properties of 3D Hollow-Silicon Nano- and Microstructures, *ACS Appl. Mater. Interfaces*, 2016, **8**, 20491–20498.

366 M. Nicolaescu, T. Braniste, C. Orha, M.-I. Morariu, S. Lehmann, K. Nielsch, I. M. Tiginyanu, R. Faur, V. Zalamai and C. Lazau, Room Temperature UV Photodetector Based on Aero-Titania, *Int. J. Mol. Sci.*, 2025, **26**, 11035.

367 C. Lamprecht, M. Taale, I. Paulowicz, H. Westerhaus, C. Grabosch, A. Schuchardt, M. Mecklenburg, M. Böttner, R. Lucius, K. Schulte, R. Adelung and C. Selhuber-Unkel, A Tunable Scaffold of Microtubular Graphite for 3D Cell Growth, *ACS Appl. Mater. Interfaces*, 2016, **8**, 14980–14985.

368 O. Parlak, Y. Kumar Mishra, A. Grigoriev, M. Mecklenburg, W. Luo, S. Keene, A. Salleo, K. Schulte, R. Ahuja, R. Adelung, A. P. Turner and A. Tiwari, Hierarchical Aerographite nano-microtubular tetrapodal networks based electrodes as lightweight supercapacitor, *Nano Energy*, 2017, **34**, 570–577.

369 E. L. Silva, Y. K. Mishra, A. J. S. Fernandes, R. F. Silva, J. Strobel, L. Kienle, R. Adelung, F. J. Oliveira and M. L. Zheludkevich, Direct Synthesis of Electrowettable Carbon Nanowall–Diamond Hybrid Materials from Sacrificial Ceramic Templates Using HFCVD, *Adv. Mater. Interfaces*, 2017, **4**(10), 1700019.

370 S. Daria, S. Sindu, H. Mathias, H. Luka, M. Janik, D. Jannes, K. Zaho, F. Bodo, K. Holger and A. Rainer, Surface modification of highly porous 3D networks via atmospheric plasma treatment, *Contrib. Plasma Phys.*, 2018, **58**, 384–393.

371 I. Tiginyanu, T. Braniste, D. Smazna, M. Deng, F. Schütt, A. Schuchardt, M. A. Stevens-Kalceff, S. Raevschi, U. Schürmann, L. Kienle, N. M. Pugno, Y. K. Mishra and R. Adelung, Self-organized and self-propelled aero-GaN with dual hydrophilic-hydrophobic behaviour, *Nano Energy*, 2019, **56**, 759–769.

372 J. Strobel, L. Ghimpu, V. Postica, O. Lupan, M. Zapf, S. Schönherr, R. Röder, C. Ronning, F. Schütt, Y. K. Mishra, I. Tiginyanu, R. Adelung, J. Marx, B. Fiedler and L. Kienle, Improving gas sensing by CdTe decoration of individual Aerographite microtubes, *Nanotechnology*, 2019, **30**, 65501.

373 J. Marx, M. Lewke, D. Smazna, Y. K. Mishra, R. Adelung, K. Schulte and B. Fiedler, Processing, growth mechanism and thermodynamic calculations of carbon foam with a hollow tetrapodal morphology – Aerographite, *Appl. Surf. Sci.*, 2019, **470**, 535–542.

374 T. Braniste, M. Dragoman, S. Zhukov, M. Aldrigo, V. Ciobanu, S. Iordanescu, L. Alyabyeva, F. Fumagalli, G. Ceccone, S. Raevschi, F. Schütt, R. Adelung, P. Colpo, B. Gorshunov and I. Tiginyanu, Aero-Ga2O3 Nanomaterial Electromagnetically Transparent from Microwaves to Terahertz for Internet of Things Applications, *Nanomaterials*, 2020, **10**(6), 1047.

375 S. J. Rezvani, A. D'Elia, S. Macis, S. Nannarone, S. Lupi, F. Schütt, F. Rasch, R. Adelung, B. Lu, Z. Zhang, L. Qu, X. Feng, A. R. Vázquez and A. Marcelli, Structural anisotropy in three dimensional macroporous graphene: A polarized XANES investigation, *Diamond Relat. Mater.*, 2021, **111**, 108171.

376 I. Plesco, V. Ciobanu, T. Braniste, V. Ursaki, F. Rasch, A. Sarua, S. Raevschi, R. Adelung, J. Dutta and I. Tiginyanu, Highly Porous and Ultra-Lightweight Aero-Ga2O3: Enhancement of Photocatalytic Activity by Noble Metals, *Materials*, 2021, **14**(8), 1985.

377 J. Ma, C. Liu and C. Song, Hollow MoS2 tetrapods for high-performance potassium-ion storage, *J. Alloys Compd.*, 2022, **898**, 162885.

378 V. Ursaki, T. Braniste, V. Zalamai, E. Rusu, V. Ciobanu, V. Morari, D. Podgornii, P. C. Ricci, R. Adelung and I. Tiginyanu, Aero-ZnS prepared by physical vapor transport on three-dimensional networks of sacrificial ZnO microtetrapods, *Beilstein J. Nanotechnol.*, 2024, **15**, 490–499.

379 V. Ciobanu, T. Galatonova, P. Urbanek, T. Braniste, F. Doroftei, M. Masar, P. Suly, V. Ursaki, B. Hanulikova, T. Sopik, V. Sedlarik, I. Kuritka and I. Tiginyanu, Enhanced solar light photocatalytic degradation of tetracycline by aero-GaN and ZnO microtetrapods functionalized with noble metal nanodots, *Heliyon*, 2024, **10**, e40989.